Thermo-Hydro-Mechanical (THM) coupled simulations of innovative enhanced geothermal systems for heat and electricity production as well as energy storage

Doctoral Thesis

(Dissertation)

to be awarded the Degree of

Doctor of Engineering (Dr.-Ing.)

Submitted by

M.Sc. Muhammad Haris

from Lahore, Pakistan

approved by the Faculty of Energy and Economic Sciences,

Clausthal University of Technology

Date of oral examination

11 July 2022

Dean

Prof. Dr. mont. Leonhard Ganzer

<in case:> Chairperson of the Board of Examiners

Supervising Tutor

Prof. Dr. -Ing. habil. Michael Zhengmeng Hou

Reviewer

Prof. Dr.-Ing. Philip Jaeger

Acknowldgement

I would like to express my sincere gratitude to my supervisor Prof. Dr. -Ing. habil. Michael Zhengmeng Hou for his continuous guidance and motivation. It would be impossible to finish this thesis without his kind support. I have learnd a lot from him and it is my fortune to have worked with him. I am also thankful to Prof. Dr.-Ing. Philip Jaeger for accepting to review this work and valuable suggestions.

I gratefully acknowledge the scholarship "HRDI-MS Leading to Ph.D. Program of Faculty Development for UESTPs/UETs Phase-1 (Batch-V)", from Higher Education Commission Pakistan and also thank DAAD support.

I would like to extend my appreciation to all my colleagues for their cooperation and friendship. Special thanks to Dr. Wentao Feng for his support in solving technical problems and all discussions.

I am grateful to my family and friends for their love in stressful times. Especially, I am thankful to my wife Arooj Baber for her continuous encouragement and emotional support.

Finally, special thanks to my sons Muhammad Hashim Haris and Muhammad Rohaan, who have been a source of pleasure throughout this journey.

Muhammad Haris

Clausthal Zellerfeld, July 2022

Abstract

With the continuous decline in conventional petroleum assets, the exploitation of unconventional energy resources is currently playing a significant role in meeting energy demands. However, due to the finite nature of fossil fuels and environmental concerns, renewable energy resources are inevitable to fulfill increasing energy trends. The exploitation of geothermal energy resources has captivated extensive attention due to its unique features like being stable, efficient, clean, and independent of the weather. Hydraulic fracturing is usually required to create artificial flow channels in tight formations. Yet, the application of multiple hydraulic fracturing through a horizontal well in enhanced geothermal systems (EGSs) is still in the early stage of development. At present, many of the deep geothermal energy projects allow us to get a better understanding of deep geothermal energy exploitation. However, many issues need to be solved for optimizing geothermal energy recovery using multiple hydraulic fractures.

In this dissertation, a workflow is established for EGS exploitation based on the concrete physical performance of the multi-fracture system in a horizontal well. The state-of-the-art software FLAC3D^{plus} and TOUGH2MP-TMVOC are used to develop a coupled thermo-hydro-mechanical (THM) fictive model for constructing multi-fracture schemes and estimating heat extraction performance. By incorporating the actual fracture geometry of newly created subsequent fracture under the influence of stress shadow, cubic law is implemented for fluid flow and geothermal energy production. In addition, energy calculations are performed using a single production well that passes through the center of the created fractures to ensure flow contribution through each fracture in the best economical way. The fictive model studies depict that stress shadow superposition affects the subsequent fracture width based on fracture spacing, which ultimately plays a significant role in geothermal energy production through multiple fractures.

After developing the heat production mechanism through multi-well multi-fracture system, a case study is performed for the MHH-GeneSys region in the North German Basin that integrates the production of heat and electricity using the wellbore data of the GeneSys EGS project. By verifying the generated model through history matching, massive multiple hydraulic fractures are created while incorporating stress superposition effects with different fracture spacing to acquire larger stimulated reservoir volume. It is observed that stress shadow superposition enlarges in massive multiple fracturing, and its impact on individual fracture geometry increases with lower fracture spacing. Furthermore, during sequential fracturing, the newly

created successive fracture's configuration is highly dependent on the previous one. Subsequently, different heat and electricity generation scenarios are analyzed by performing sensitivity analysis through numerous simulations with other parameters such as flow rate and injection/production well spacing. The results show that the influence of flow rate on energy depletion fractured areas is significant under the proposed well arrangement. In other words, high flow rates provide higher energy production results with improved energy aerial sweep efficiency. Furthermore, insufficient well spacing can cause an earlier thermal breakthrough by which larger stimulated fractured volume can be left un-drained. The optimized installed power capacity of the one side of the proposed EGS declines from 7.17 MW to 5.08 MW for 144 L/s in a 12-fracture pattern during 30-years, which satisfies the commercial requirement. A comprehensive economic analysis is performed by adopting different cost factors for various surface and subsurface operations. From optimized energy production results, the levelized cost of electricity (LCOE) is estimated at 5.46 c$/kWh, which is substantially economical compared to Germany's current electricity prices; thus, indicating considerable development potential from an economic perspective. In addition, the generated power potential can be doubled by creating similar fractures to the opposite side using the same injection well.

An innovative concept of regenerative EGS is proposed further that integrates heat and electricity production as well as storage of surplus renewable energy. The energy-depleted massive multi-fractured EGS has been analyzed to efficiently store surplus wind or solar energy and extend the project's life. Numerous simulations are performed using energy storage/recovery cycles for different time durations. The results show that high energy recovery can be achieved by performing continuous cycles with shorter periods. Furthermore, the formation temperature increases with the number of cycles. Consequently, a regenerative EGS could be established in reality compared to standard EGS projects. This regenerative EGS concept can be applied in existing EGS fields as well to make surplus energy usable and keep a geothermal reservoir much renewable by reducing the reservoir temperature reduction rate. In addition, any salt scaling/crystallization in vertical and horizontal sections of wells can be removed using water with high injection pressure and temperature during the energy storage phase.

Contents

List of figures

List of tables

1 Introduction

1.1 Motivation and objectives

The economy and the world's population have resulted in an enormous demand for energy. Since the beginning of the 21st century, the total energy consumption has increased to 60 %. By the end of 2019, it has reached 581.1 exajoules (1 EJ = 10^{18} J), an increment of more than three times during the last fifty years. The increase in energy demand between 2010-2019 is shown in Figure 1.1. The highest consumption was recorded for Asia Pacific, North America, Europe, CIS (Commonwealth of Independent States), Middle East, South & Central America, and Africa. However, due to the Covid-19 pandemic in 2020, the world's energy consumption has declined to 4.5 %, the most significant decline ever recorded since World War II. Due to the imposition of lockdowns and limited transportation, the drop in oil consumption has been recorded around three-quarters of the total decline in energy demand. Nevertheless, the energy demand is expected to rebound by 4.6 % in 2021-22 [1].

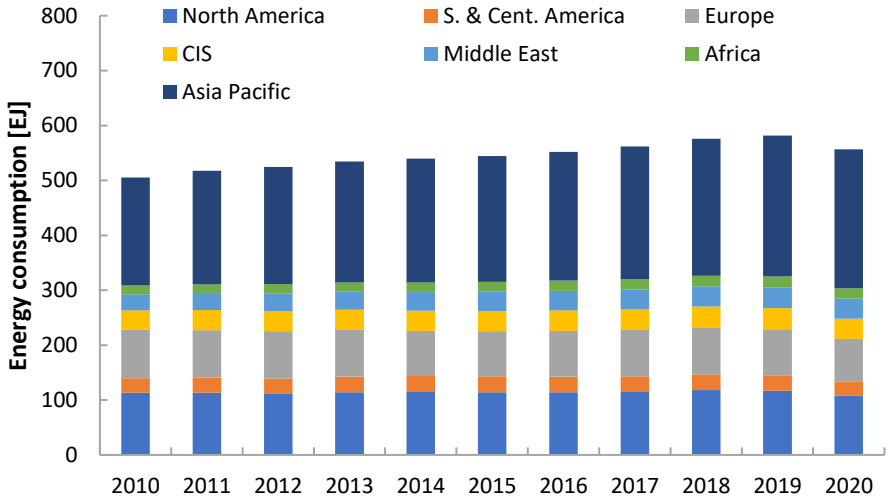

Figure 1.1 World energy consumption by region [2]

Due to the continuous decline in conventional petroleum resources, unconventional energy resources are currently playing an important role in meeting energy demands. In fact, from a broader spectrum, fossil fuels are still contributing a significant share in the total energy supply (Figure 1.2). However, fossil fuels are finite and non-renewable. Once fossil fuels have been produced through natural processes, it takes a long time to replenish them compared to the current consumption rate. In addition, these fuels are creating momentous complications for human health and the global climate.

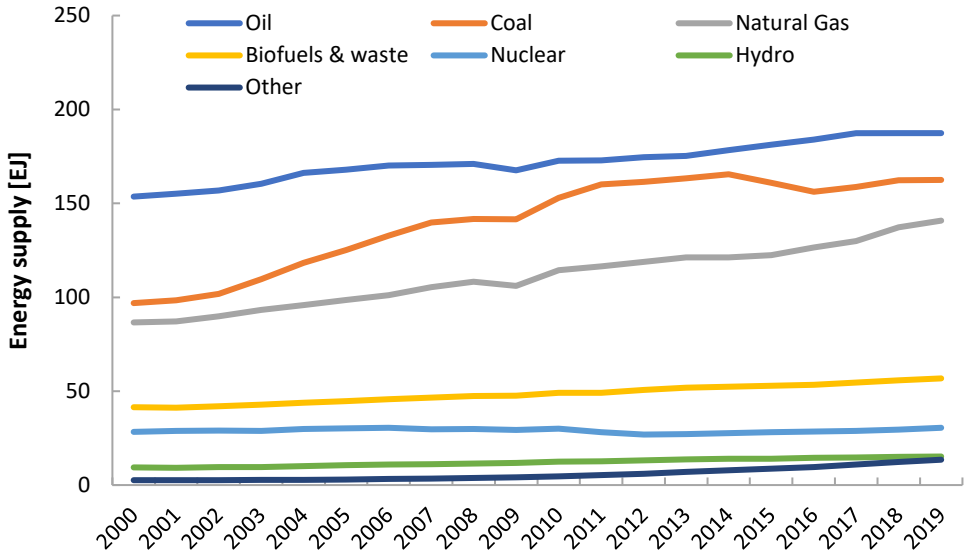

Figure 1.2 World energy supply by source [3]

In the United States, most of the electricity is generated from coal, causing severe industrial pollution. In 2020, coal demand dropped by 220 million tons of coal equivalent (4 %), wherein the advanced economies accounted for more than half of coal's global decline. However, there is still a long way to squeeze out coal from the power sector. According to a survey, burning fossil fuels is responsible for about three-quarters of greenhouse gas emissions globally [4]. China is currently the world's largest energy consumer and accounts for one-third of global CO_2 emissions. However, the Chinese government aims to achieve a CO_2 emissions peak before 2030 and attain carbon neutrality before 2060 [5].

The power, transport, and thermal sectors consume most of the energy each year. It has been recorded that 41% of CO_2 emissions come from the power sector, while the transport and industrial sectors contribute about 42% [6]. These carbon emissions trap solar energy in the atmosphere, raising global temperature. Moreover, extreme weather patterns, adverse effects on food cultivation seasons, severe droughts of water supply, and increasing sea levels are the outcomes of carbon emissions. Therefore, there is an immense need to shift towards zero or low-carbon emission energy sources like renewable technologies.

The energy from natural resources like sun, wind, hydro, and thermal from the earth's crust is categorized as renewable energy. It can replenish itself over a while without exhausting the earth's capital. Renewable energies emit no or low greenhouse gases and air pollutants, which are beneficial for the climate and human health. Promisingly, a tremendous increase in renewable energy generation has been recorded during the last decade (Figure 1.3). In 2020, despite a fall in overall energy demand, energy generation from renewables (excluding

hydroelectricity) recorded its largest-ever increase to 358 TWh. More than 65 % of renewable energy from the Asia Pacific region has been contributed from China, with roughly half of the global rise in wind and solar capacity [2]. Moreover, China, the European Union, and the United States expect to generate 900 TWh, 580 TWh, and 550 TWh from solar PV and wind in 2021, respectively [1]. Figure 1.4 shows the share of electricity that has been produced from renewable technologies in 2020 throughout the world, which portrays that renewables tend to have a sufficient stake in the total electricity mix.

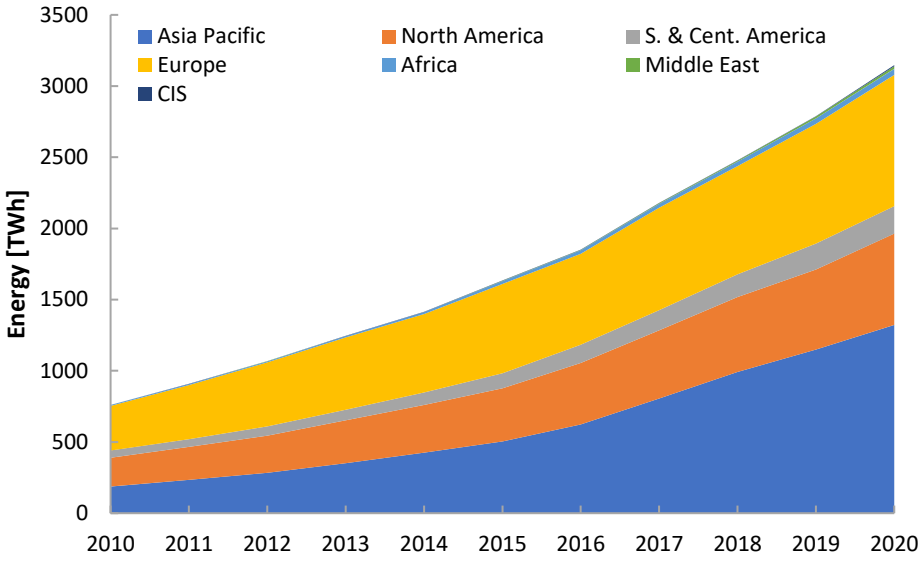

Figure 1.3 Share of renewables in power generation by region [2]

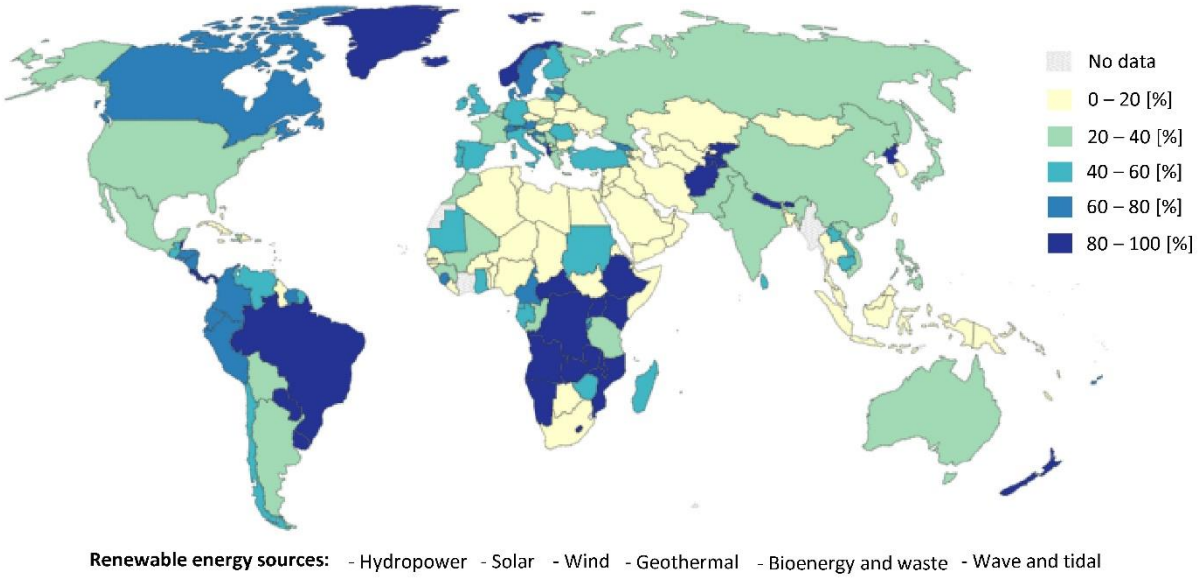

Figure 1.4 Share of electricity production from renewables in 2020 [7]

The primary renewable energy resources such as wind, solar, biomass, and geothermal have acted as suitable alternatives for fossil fuels [8]. Nevertheless, the exploitation of geothermal energy resources has captivated extensive attention due to its unique features like being stable, sustainable, clean, and independent of the weather. In addition, it is available for production for maximum working hours compared to other energy resources. Earth is considered to be a tremendous thermal energy resource. The hot molten core and decay of radioactive minerals are primary heat sources. Besides, the earth crust is a strong absorber of the sun's energy and acts as a solar heat accumulator [9].

The direct utilization of geothermal energy for washing, bathing, cooking, and therapeutic purposes was adopted hundreds of years ago. The first district heating system was installed in France during the fourteenth century, and the first deep well was drilled in Iceland in 1755 [10]. Hot dry rock (HDR) resources with ultra-low porosity and permeability have been exploited through well stimulation techniques and termed enhanced geothermal systems (EGSs) [11] (Figure 1.5). In EGS, cold fluid is injected through the injection well, and heated fluid is produced from the production well [12]. Within the depth of 10 km, more than 13 million exajoules (1 EJ = 10^{18} J) EGS resources have been estimated in the United States, of which 0.2 million EJ can be exploited through current technologies [11].

Similar to the petroleum industry, especially hydrocarbon production through unconventional reservoirs having too small permeability to achieve economic flow rates, reservoir stimulation is also a key technology for HDR development. Different approaches have been developed to enhance the well flow rate through tight formations, including hydraulic fracturing, thermally induced fracturing, and chemical stimulation [13-16]. However, EGSs have been established worldwide by applying hydraulic fracturing with different success rates such as Fenton Hill in New Mexico, Soultz in France, Hijiori in Japan, Paralana in Australia compared with other stimulation methods [17]. In hydraulic fracturing, artificial fractures are created by injecting fluid with high pressure, and fractures are kept open with solid proppants' support. Nevertheless, highly viscous gel and proppants have rarely been used in geothermal field operations [18].

With the rapid developments in petroleum technologies, drilling a horizontal well over 1000 m deep is possible. Multi-stage fracturing through a horizontal well is preferable to acquiring larger stimulated reservoir volume (SRV) for geothermal exploitation. However, individual fracture configuration mainly depends on fracture spacing and orientation of in-situ stresses. Longitudinal and transverse fractures can be obtained by selecting horizontal well trajectories in maximum and minimum in-situ stress direction, respectively (Figure 1.6).

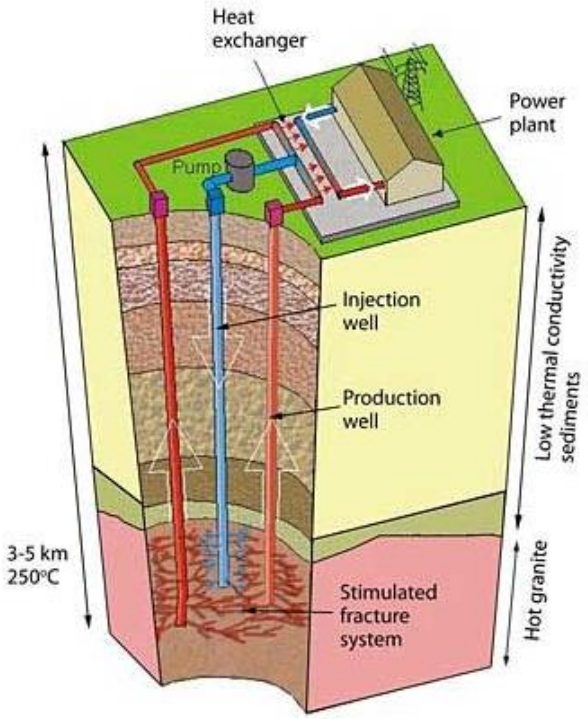

Figure 1.5 Enhanced geothermal system (source:geothermalworldwide.com/egs.html)

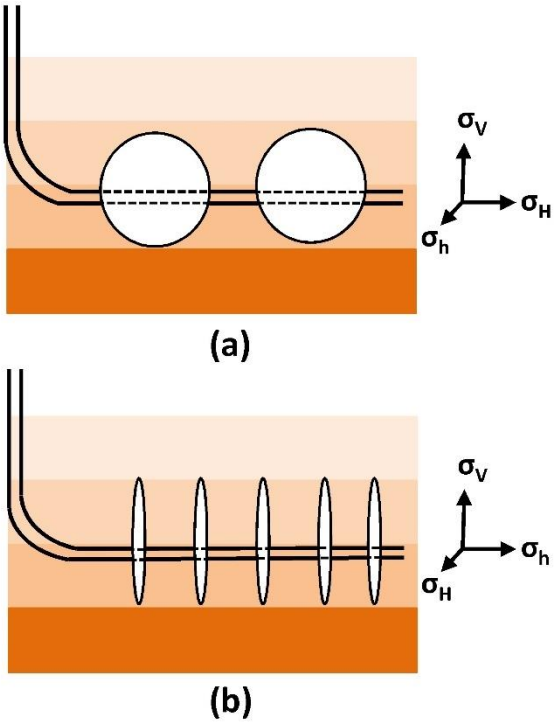

Figure 1.6 Demonstration of multiple fracture system in a horizontal well (a) longitudinal (b) transverse

Currently, many of the conceptual and real EGSs are vertical or sub-vertical, while production performances of horizontal wells are hardly reported. The horizontal well drilling in hard and deep high-temperature formations is a challenging task that involves higher operational costs. In addition, suitable configurations of multiple fractures in connection with preferable flowing paths, maintaining the thermal lifetime of the project with economic fluid production rates and low pumping pressure requirement, are significant issues [11]. However, by combining EGS with horizontal well and multiple hydraulic fractures, many advantages can be obtained: improved well connectivity in tight HDR, adequate SRV, and increased circulation rate with enhanced sweep efficiency.

Therefore, it is imperative to examine and enhance the performance of EGSs using advanced technologies such as multiple hydraulic fracturing through horizontal well, and addressing the related technical issues. In this study, numerical modeling has been conducted to investigate the heat extraction performance of EGSs through multiple hydraulic fractures considering coupled Thermal (T), Hydraulic (H), and Mechanical (M) effects. Moreover, the depleted fractured system has been studied to store surplus renewable energy to extend the EGS project's life.

1.2 Thesis outline

This thesis focuses on the application potential of massive multiple hydraulic fracturing under the influence of stress shadow in EGS to obtain large SRV for heat and electricity generation. In addition, the storage of surplus energy in depleted EGS has also been investigated. The research contents of the thesis are presented in Figure 1.7.

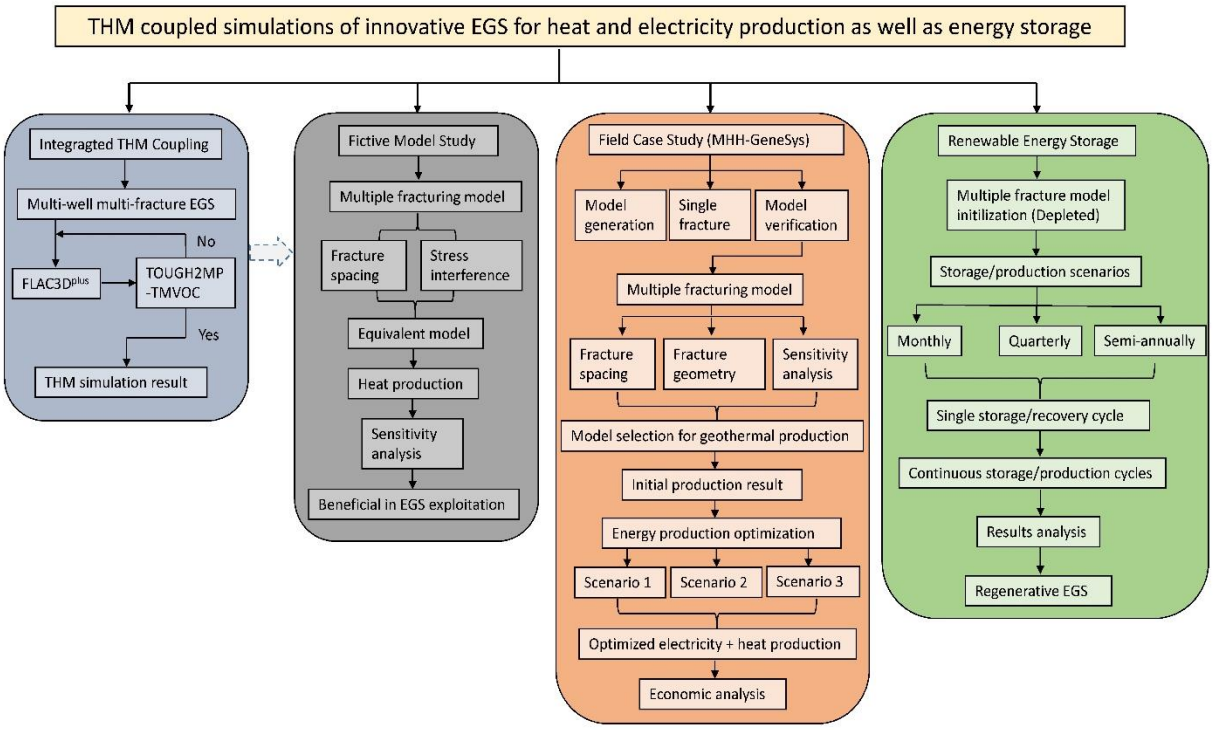

Figure 1.7 Research contents and flow chart of the thesis

In chapter 2, the theoretical background of geothermal reservoirs, their types, use of different geothermal power plants for heat and electricity production, and significant worldwide EGS sites have been briefly discussed. Afterward, governing equations corresponding to geo-processes during stimulation operation are presented. In addition, a comprehensive review of the mathematical models for hydraulic fracturing has been described. Moreover, multistage fracture placement designs and the impacts of stress shadow on fracture configuration are highlighted.

Chapter 3 presents the numerical study performed for geothermal energy production from multiple fractures using a fictive model. Based on the developed powerful simulator FLAC3D^{plus}, fractures are created sequentially through a horizontal well considering stress superposition effects. Subsequently, the fracturing results are imported to the developed simulator TOUGH2MP-TMVOC for energy production. Several recommendations to enhance heat production have been proposed after considering stress shadow effects, fracture spacing, and stimulated fracture areas.

A case study using the field data of the GeneSys-EGS project has been performed after developing the computing scheme during numerical modeling for geothermal energy exploitation, in chapter 4. The generated model has been verified firstly using bottom hole pressure (BHP) history matching. Massive multiple fracturing operations considering different

fracture spacing with stress shadow have been conducted, and based on fracturing results, a suitable multiple fracture scheme for geothermal exploitation is selected. The initial energy production results suggested the need for energy production optimization. Therefore, different optimization scenarios have been studied, and enhanced energy production results have been obtained. In addition, a comprehensive economic analysis has been presented by adopting various cost factors, and the levelized cost of electricity has been compared with Germany's current electricity price.

In chapter 5, an innovative concept of regenerative EGS is proposed further to integrate heat and electricity production as well as storage of surplus renewable energy. This concept can make surplus energy usable and keep a geothermal reservoir much renewable by reducing the reservoir temperature reduction rate. In addition, any salt scaling/crystallization in vertical and horizontal sections of wells could be removed using water with high injection pressure and temperature during the energy storage phase. After performing various energy storage/recovery scenarios based on different periods, suitable strategies for surplus energy storage and production during times of shortage have been proposed concerning the investment perspective. The results depict that together with energy storage, an EGS project can be made regenerative in reality.

2 Fundamentals of geothermal reservoirs and hydraulic fracturing

2.1 Geothermal reservoirs

A geothermal reservoir is a volume of hot rock formations through which heat can be produced economically. The basic requirements of a geothermal system include a significant amount of heat, hot fluid, and fluid flow permeability. Geothermal energy is considered one of the most reliable renewable energy sources because of its stability and weather independence. It evolves due to two sources; (a) transfer of energy from the hot molten core to the exterior of the earth (b) decay of the radio-active elements [19]. The major radio-active elements that increase the earth's temperature are uranium-238, uranium-235, thorium-232, and potassium-40. It has been estimated that the earth's internal energy flows at a rate of 44.2 TW and is restored by the radioactive decay of the minerals at a rate of 30 TW [20-21]. The interior of the earth has a temperature above 5000 K [22] and is considered to be a huge source of geothermal energy [23] (Figure 2.1). An enormous amount of heat energy exists within the earth, but the exact calculation of earth energy varies widely due to different calculation procedures [9]. The tentative estimates suggest that the accumulated heat is about 12.6×10^{24} MJ [19]. While, WEC-2013 estimated the amount about 540×10^{7} EJ (1 Exajoule = 1×10^{18} J). Moreover, it has been predicted that the exploitation of only 1% of geothermal energy is enough to accomplish the global energy demand at a constant consumption rate for 2800 years [9].

Generally, a rise in temperature with increase in depth is observed due to heat flow from the much hotter mantle. The temperature gradient ranges between 25 to 30 ^{o}C/km near the surface throughout the world. Therefore, a geothermal system can exist in a region with a normal or slightly above average temperature gradient. In addition, the feasibility of higher temperature rises in areas along tectonic plate boundaries and volcanic regions, where seismicity has transported hot material from the earth's interior. In the UK, the average geothermal gradient is 26 ^{o}C/km. In contrast, more than 50 ^{o}C has been found in southern Australia, signifying one of the most suitable locations for geothermal power plant installations in the world [24]. The practice of geothermal energy in the forms of hot springs and space heating has an old history that links with ancient Paleolithic and Roman times. The geothermal heating system's inception took place in the 14th century from a French town named Chaudes-Aigues, while the first commercial steam-operated turbines commenced in 1958 in New Zealand for electricity generation [9].

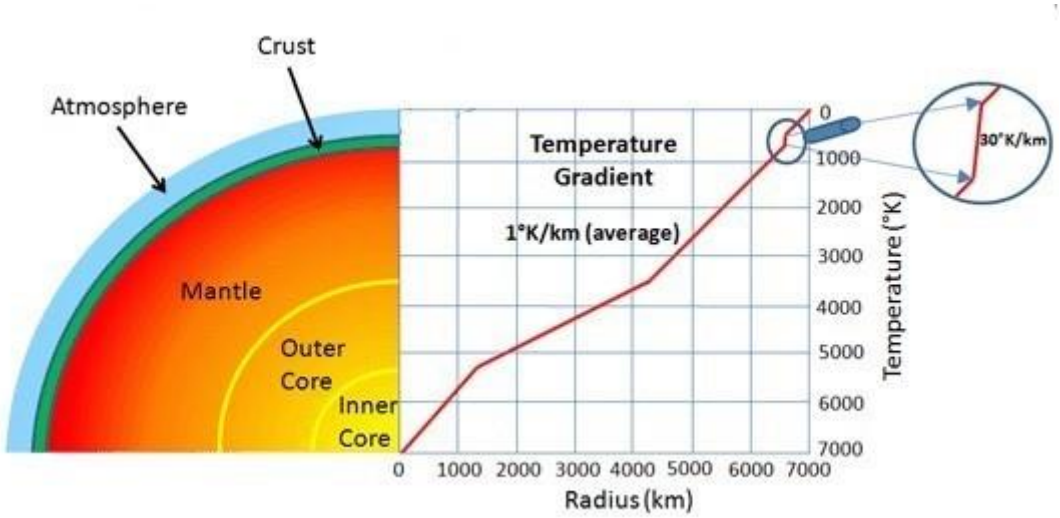

Figure 2.1 Earth's structure and geothermal gradient (modified from source: www.mpoweruk.com/geothermal_energy)

2.1.1 Geothermal reservoir types

Conventional geothermal resources can be either in the form of hydrothermal resources or in the form of petrothermal resources (HDR) [25].

i Hydrothermal systems

The hydrothermal system uses underground fluids (water, steam) present in subsurface formations with adequate permeability to produce geothermal energy. The presence of magmatic intrusions near the earth's crust is helpful for economic geothermal energy developments as these encourage convective circulation of ground water. However, the exact well location to tap the hydrothermal system at industrial levels is vital. The whole system involves one production well and at least one re-injection well to keep the productivity and pressure of the reservoir constant and make a geothermal system sustainable. These systems are further classified based on phase dominance (water or vapor) and formation fluid temperature such as hot (above 100 ^{o}C), warm (between 60 to 100 ^{o}C), and thermal (> 20 ^{o}C) [26]. Water-dominated systems are present throughout the world, such as Olkaria in Kenya, Wairakei in New Zealand, Yangbajing in China, Hatchobaru in Japan. In comparison, vapor-dominated systems are pretty uncommon. Examples include Geysers in the United States, Matsukawa in Japan, and Larderello in Italy [10]. Germany has an abundance of hydrothermal systems, specifically in the regions of the North German Basin, the South German Molasse Basin, and the Upper Rhine Garben [27]. In the North German Basin, many formations contain sandstone strata with a thickness of 20 m, porosity > 20 %, and permeability > 250 mD, making a reservoir suitable for geothermal use. Similarly, the Malm (karstic-dolomotic fractured

carbonate reservoir of the upper Jurassic) in Molasse Basin has very high productivity. It has been used for many research and development activities in Central Europe [27-28].

ii Petrothermal systems / HDR

Rather than conventional hydrothermal resources, petrothermal systems, also known as HDRs, have a high formation temperature range (200 ^{o}C to 350 ^{o}C) but limited porosity and permeability. The earth's energy cannot be extracted through the natural flow of formation fluid. These systems require excessive stimulation techniques to create underground fluid flow channels (artificial fractures) for energy exploitation. EGS technology is deployed mainly in HDR that uses a multi-well arrangement for fluid circulation. Cold fluid (e.g., water) is injected through the injection well that passes through fractures and is produced from the production well carrying the formation heat, as shown in Figure 2.2. The injection and production cycles continue until the formation temperature depletes below the economic limit. The regions in the world having positive temperature irregularities are valuable as high-temperature formations can be exploited from shallow depths with lower drilling expenditures.

Petrothermal systems can also be used to produce energy by utilizing bore hole heat exchangers (BHE's) for various depths ranging from 300 m to 3000 m. These are closed systems with coaxial pipes inside which fluid flow occurs, and fluid is heated by thermal conduction of the surrounding formations. A few examples of BHE's in operation in different parts of Germany include Arnsberg of North Rhine-Westphalia, Prenzlau of Brandenburg, and Heubach of Hesse [26]. However, hydrothermal power plants and thermal applications of geothermal energy are established technologies, whereas EGS projects are still in the development phase.

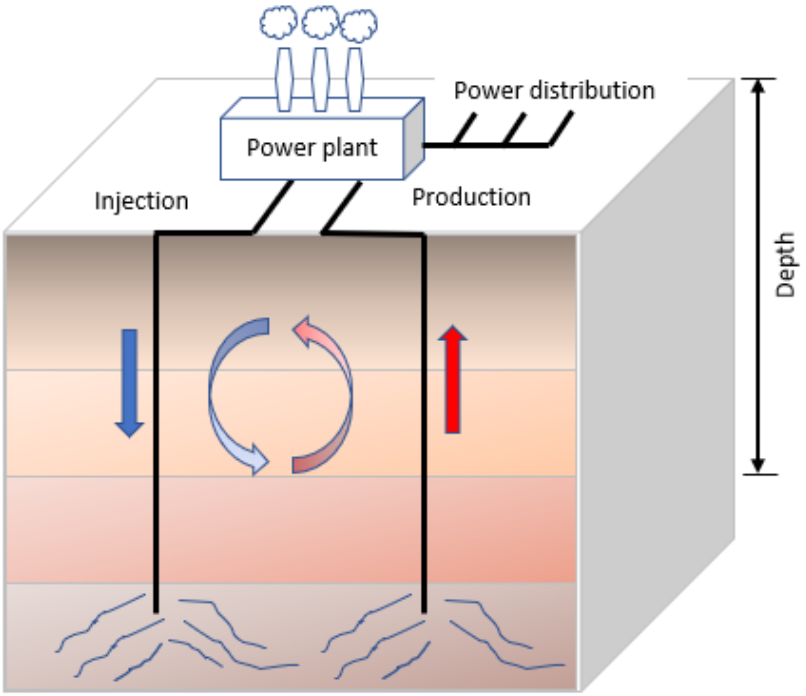

Figure 2.2 Schematic of an enhanced geothermal system

Concerning depth, geothermal energy has two categories: (i) shallow (ii) deep.

- **Shallow geothermal energy**

It refers to the energy stored in the upper layer of the earth's crust (200 m - 300 m), where the temperature is strongly influenced by the air temperature that further depends on the season. However, about 15 m below the earth's crust, the ground temperature remains constant at the mean average annual air temperature throughout the year. Therefore, the ground temperature remains lower and higher than the air temperature during summer and winter. Shallow geothermal systems are used for direct heating or cooling because of the low to moderate temperature range. Generally, ground source heat pumps (GSHP) are installed at the surface for fluid circulation through a variable complex ground loop system (GLS). This is one of the fastest-growing applications to utilize geothermal energy globally [29]. The GLS consists of vertical or horizontal pipes depending on subsurface geology and conditions. Based on the season, hot or cold fluid is circulated through a heat exchanging pipe network, as shown in Figure 2.3.

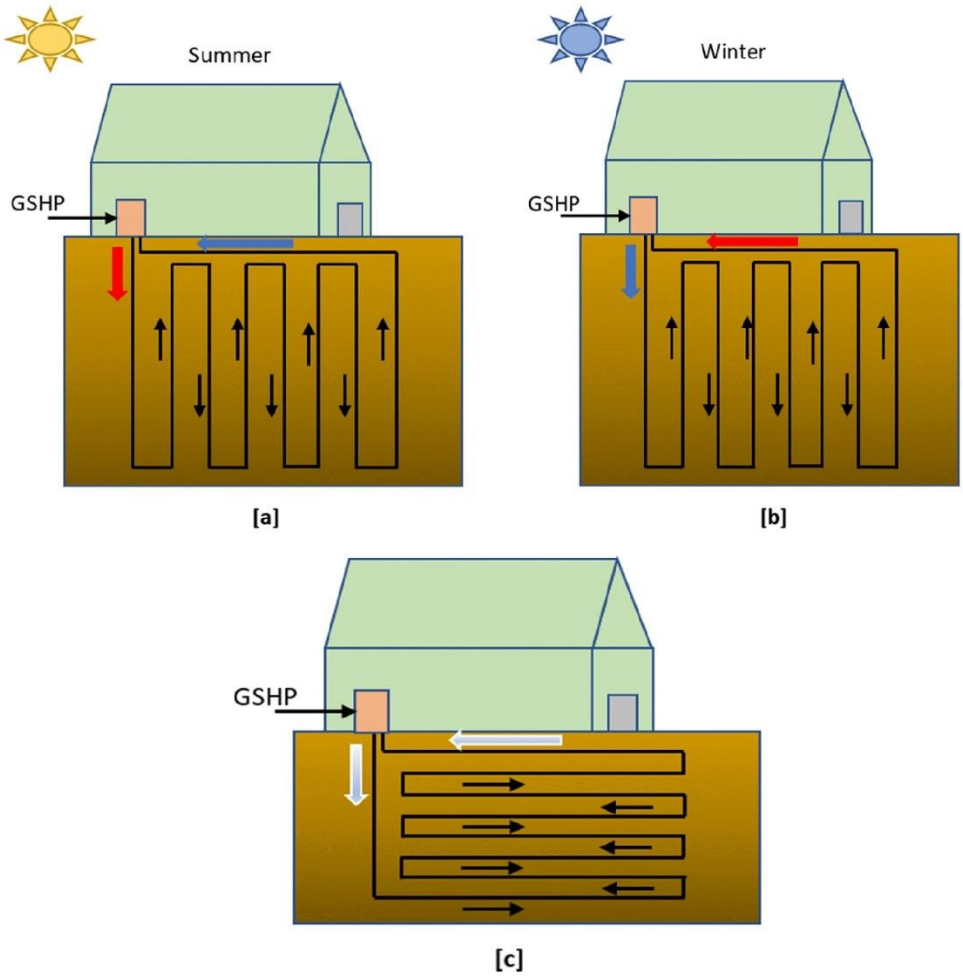

Figure 2.3 Schematic of ground source heat pumps for different seasons & layouts

- **Deep geothermal energy**

These reservoirs are present at a depth greater than 400 m; however, the distinction between shallow and deep geothermal energy is not fixed. Deep geothermal energy is exploited majorly through the application of hydraulic fracturing. Under this category, energy can be produced either from hot sedimentary hydrothermal aquifers having stored hot water or from EGS after stimulation operations. Due to the increase in geothermal gradient, deep geothermal systems are more suitable for electricity generation, producing fluid with higher temperatures. At present, the geothermal wells with more than 3 km depth are limited, but deep drilling for hydrocarbon exploitation encourages the deep drilling for geothermal energy production. The Kola superdeep borehole (KSDB-3), with a depth of 12.261 km, is considered one of the deepest investigation wells in the whole world [30].

2.1.2 Geothermal power plants

Geothermal power plants work similarly to other thermal power plants in which heated fluid is used to generate electricity. In vapor-dominated geothermal systems, steam can be used directly to drive the turbine, whereas, in water-dominated system, the hot fluid needs to be flashed first to produce steam. Since the hot fluid is converted into steam that drives a generator turbine, no or less fuel is required for electricity generation. The condensed steam and water are collected at the outlet and injected into the reservoir through the injection well. The type of conversion technology in power plants mainly depends on producing fluid and its associated temperature. Generally, geothermal power plants are divided into three categories.

- **Dry steam**

Dry steam is the oldest and the simplest type of geothermal power plant that uses hot steam directly to drive the turbine, as shown in Figure 2.4 (a). This type of plant was first built at Lardarello, Italy, in 1904 and is still used in recent years. The working temperature of the pressurized steam is in the range of 180 ^{o}C to 350 ^{o}C, limiting its usage due to the lower number of high-temperature hydrothermal resources in the world. However, dry steam power plants contribute more than 40 % to geothermal electricity production in the United States [31].

- **Flash steam**

Flash steam power plants are also known as “wet steam power plants” because hot water is firstly converted into steam (Figure 2.4 (b)). The high-pressure hydrothermal fluid is directed to a tank having much lower pressure that creates rapid vaporization of the produced fluid. These vapors rotate the turbine to produce electricity. The unused and condensed water is collected at the outlet and re-injected into the reservoir. Due to technological advancement, steam can be generated at different working temperatures. Therefore, flash steam power plants are categorized as single flash and multiple flash power plants. Typically, double flash systems are 20 to 30 % more efficient than single flash systems [33]. These plants can work above 182 ^{o}C and are the most common power plants.

- **Binary power plant**

Binary power plants are designed to produce electricity from low to intermediate temperature reservoirs with fluid in the range of 85 ^{o}C to 175 ^{o}C [34]. These power plants differ from others due to the utilization of binary fluid (organic compound) as primary working fluid, with a lower boiling point than produced water. The produced hot water is sent initially to a heat exchanger, where working fluid with a low boiling point is converted into steam and rotates the turbine (Figure 2.4 (c)). The condensed working fluid and hot brine are sent again to the heat exchanger

to extract maximum energy, and, in the end, cold brine is re-injected into the reservoir through the injection well. At the same time, condensed steam of working fluid is prepared for the next cycle. The main advantages, such as; the use of binary fluid having a low boiling point for steam conversion, high reservoir sustainability, and high reliability of operation, make this power plant category more applicable to produce electricity, especially in countries having lack of high-temperature geothermal resources.

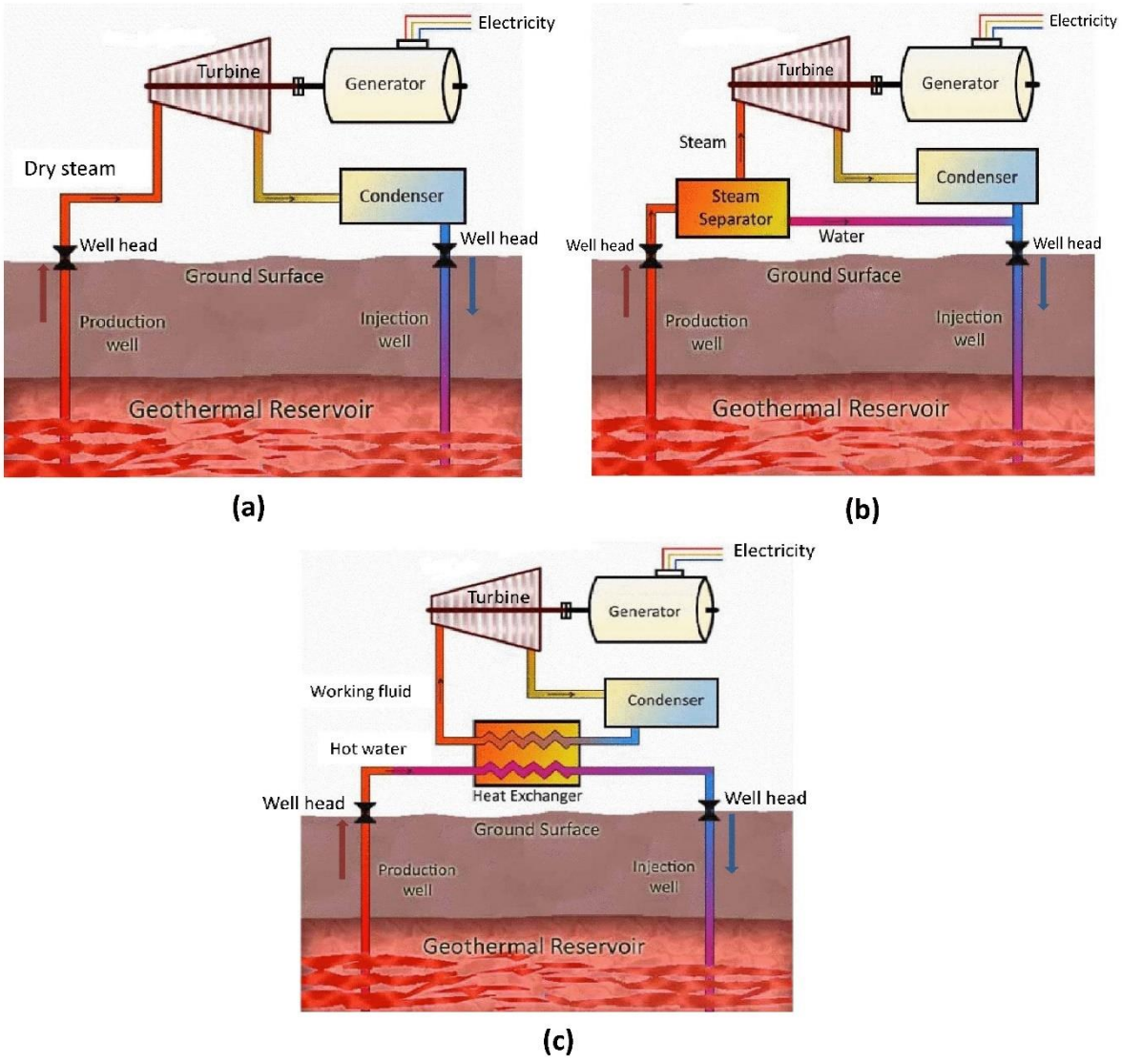

Figure 2.4 Schematic of geothermal power plant (a) dry steam (b) flash steam (c) binary (modified from Daware [32])

2.2 Worldwide EGS projects

The EGS concept was first implemented at the Fenton Hill site in 1974 by the Los Alamos National Laboratory (LANL) in the US. Since then, many developed countries like the US, Australia, and Europe have invested in researching and expanding EGS projects. The development of the EGS is considered highly risky due to ultra-low porosity and permeability. The US has categorized the EGS into three types: in-field EGS, near-field EGS, and greenfield EGS, depending upon the degree of difficulty for EGS development. The early projects like Fenton Hill, Rosemanowes, Ogachi were problematic greenfield EGS. However, the improvements in hydraulic fracturing technology and experience of oil & gas fields have aided a lot in recent developments of EGS, and the success rate has progressively increased. Figure 2.5 shows some critical EGS projects globally, while Table 2.1 describes some important features of ongoing EGS projects.

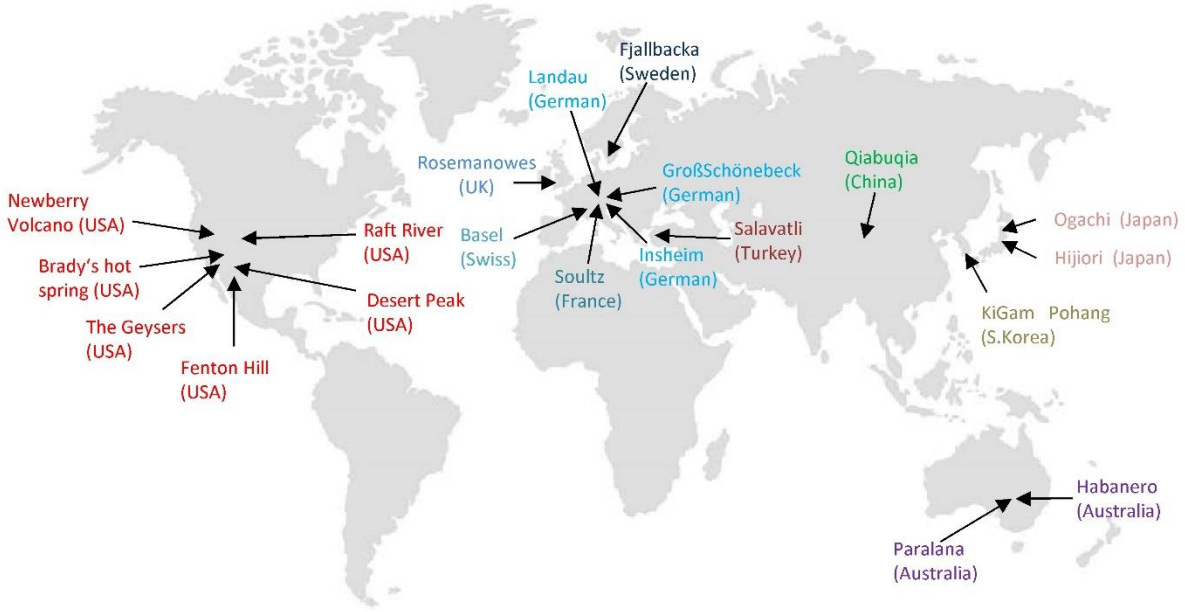

Figure 2.5 Illustration of some EGS sites in the world (modified from Lu [17] and Han et al. [35])

Table 2.1 Features of some ongoing EGS projects for electricity generation in the world [17, 35, 36]

Site name	Country	Geothermal capacity / in progress (MWe)	Reservoir lithology	Stimulation method
Landau	Germany	1.8	Granite	Hydraulic
Bruchsal	Germany	0.55	Sandstone	Hydraulic

Insheim	Germany	4.8	Granite	Hydraulic
Groß Schönebeck	Germany	1	Sandstone/conglomerate	Hydraulic and chemical
Soultz	France	1.5	Granite	Hydraulic and chemical
Desert Peak	USA	1.7	Metamorphic tuff	Hydraulic and chemical
Cooper Basin	Australia	1	----	Hydraulic
Coso	USA	240	Granite	Hydraulic and chemical
Salavatli	Turkey	17 (In-progress)	----	Chemical
Bradys hot spring	USA	2-3	Rhyolite, metamorphic substrate	Hydraulic
The Geysers	USA	1500	Metasandstone	Explosive
Paralana	Australia	3.75	Sedimentary/metamorphic	Hydraulic and chemical
Newberry	USA	35 (In-progress)	Marl, quartz porphyry, granite	Hydraulic
Pohang	South Korea	1.5 (In-progress)	Granodiorite	Hydraulic
Habanero	Australia	1 (40 MW targeted)	Granite	Hydraulic
Raft river	USA	5	Granite	Hydraulic and thermal
Qiabuqia	China	----	Monzonitic granite	Thermal and hydraulic

- **Fenton Hill**

The first EGS effort was attempted in 1974 at Fenton Hill in the US by creating a natural tank reservoir having 300 ^{o}C temperature at a depth between 4 to 5 km. The site was located at the edge of the Valles Caldera in north-central New Mexico and was selected due to its high temperature and rock characteristics [37]. The project was initiated by LANL and divided into two phases with deep drilling of two wells during different periods to test the geothermal capacity using a binary cycle power generation system. The project lasted for 21 years due to low capacity and economic constraints. The results showed that heat could be produced from the low-permeable hot formation by creating fractures with hydraulic fracturing technology; however, forming the connection between wells was crucial. In addition, results proposed the development of high-temperature downhole equipment to achieve precise information of subsurface stresses, pressure, and temperature [17].

- **Rosemanowes**

In 1977, the Camborne School of Mines initiated an experimental EGS project at Rosemanowes Quarry UK funded by the Department of Energy and the Commission of the European Communities. The intention was to perform large-scale experiments and address the stimulation issues for adequate fracture networks. The estimated power potential was approximately 3 GWe due to hot granite formations. The project continued in several phases and ceased to operate in 1991 due to excess fluid leak-off and inability to acquire the expected geothermal capacity [11, 38].

- **Hijiori**

Hijiori's HDR project in Japan was carried out by NEDO (New Energy and Industrial Technology Development Organization) in the 1980s by utilizing the experience of the Fenton-Hill project due to similar geological conditions. This project provided new aspects of knowledge and concepts that contributed to international HDR development. The project was divided into two stages depending on the heat extraction area. One injector (named as SKG-2) and three producers (named as HDR-1, HDR-2, HDR-3) were drilled at a shallow depth of about 1800 m, while the distance between the wells was within several tens of meters. Hydraulic fracturing operation was performed during each developmental stage; however, the project faced the severe problem of fluid loss due to the presence of natural fissures. The Hijiori project highlighted the importance of understanding the natural fracture system by mapping the acoustic emission during stimulation job, which can predict the orientation and growth of stimulated fractures and help establish a better well connection [37].

- **Basel**

Basel EGS has been known as failed geothermal project due to the severe issue of induced seismicity. This EGS site was located in Basel, the third-largest city in Switzerland, having more than 70,000 inhabitants. Despite a history of natural seismic activity (the highest of about 6.7 magnitude earthquake in 1356 in this area [39]), it was planned to develop a commercial EGS in 2006 at a depth of 5000 m with a temperature of approximately 200 ^{o}C. A seismic monitoring system comprising of six borehole seismometers was installed near the injection well. Hydraulic fracturing was performed in granite layers that induced seismic events and eventually, fracturing was stopped. A seismic event of magnitude 3.4 was recorded during post fracturing period, which caused damage to local property and structures. The problem of induced seismicity raised public concerns, and the project was abandoned in 2009 [38].

- **Soultz-sous-Forets**

The Soultz-sous-Forets (geothermal site in France) is located within the central part of the Upper Rhine Graben basin. The geology is characterized by highly fractured granite with a reservoir temperature over 180 ^{o}C. In 1987, the European Commission selected the Soultz site for geothermal exploitation on a commercial scale after comparing the suitability with other EGS sites of Rosemanowes and Bad Urach. Several wells have been drilled at different locations and depths. Currently, there exist three wells that are approximately 5000 m deep [40]. Many hydraulic stimulation operations have been performed to increase the subsurface heat exchange area. More than 114,000 seismic events have been detected during hydraulic stimulation operations on the local seismic network with magnitudes between -2.0 and +2.9. However, after the most significant magnitude (+2.9) in 2003, the modification in stimulation strategy was implemented using low flow rates and volumes [41]. The ORC binary power plant is in operation to produce electricity of about 1.5 MW. In order to reduce the re-injection pressure and increase production, submerged pumps have been installed at the site [17].

Landau

The Landau EGS project is located in the Upper Rhine Graben region of Germany. Compared to the normal value of thermal gradient (about 30 ^{o}C/km), the Upper Rhine Plain possesses a temperature gradient of about 80 ^{o}C/km at some places. Therefore, Landau offers good temperature conditions for EGS development. However, it is the first project in Germany facing similar problems to Basel, i.e., seismicity. A seismic event of 2.7 in magnitude caused the project's suspension in 2009. Nevertheless, the project was restarted with a reduced injection rate and pressure, which ultimately decreased the power generation capacity.

- **The Geysers**

The Geysers is considered one of the world's largest geothermal fields, having an installed capacity of about 1500 MW [42]. It is located in the Mayacamas Mountains of California, approximately 72 miles north of San Francisco. Steam has been produced for power generation from more than 350 wells. The first commercial power plant started operation in 1960 and since then, about 22 power plants have been installed. Most of the power plants are owned by Calpine, while the rest are operated by the US Renewables Group, Northern California Power Agency and Silicon Valley Power. An EGS demonstration project was launched in 2009 at one northwestern part of the Geysers site to exploit the high-temperature reservoir (280 ^{o}C – 400 ^{o}C) having low permeable rocks. Previously abandoned exploration wells P-32 and P-31 were

successfully re-opened, deepened, and re-completed to produce high-quality steam. Due to significant thermal effects, the cold fluid fracturing technique successfully provided artificial fractures near the wellbore area without high injection pressure. Therefore, the largest recorded earthquake is less than 2.87 [17].

- **Cooper Basin Project**

The whole Australian continent contains regional overthrust tectonic stress that can hinder the development of geothermal fields using hydraulic fracturing. However, a large amount of field data obtained through hydrocarbon exploration in the Cooper Basin helped in characterizing the geothermal resource [37]. In 1983, hot granite rock beneath the Cooper Basin was explored during petroleum exploration well named "McLeod 1". The granite in Cooper Basin contains significant radioactive elements such as uranium, resulting in high reservoir temperature at shallow depths. The purpose of the project was to exploit hot granite formation to achieve 100 MW electricity using a binary cycle power generation system. The first geodynamic well (Habanero-1) was completed in 2003 to a depth of 4421 m, and since then, three additional wells have been drilled in the Habanero area, near the original McLeod well. At Habanero, the maximum temperature recorded was 243 ^{o}C [43]. In 2013, Habanero EGS was successfully commissioned with a power capacity of 1 MWe. However, the project's ultimate goal is to increase the power production to 450 MWe. The field experience showed that overthrust stress environments could be ideal for stimulation, which can aid in horizontal drilling for reservoir development [17].

- **Desert Peak in the US**

The Desert Peak EGS project was started in 2002 to produce 2 to 5 MWe using a binary power plant. The field is located about 50 miles northeast of Reno, Nevada, northwest Churchill County. The Desert Peak area is one of the several geothermal areas in the region, while others include Bradys Hot Springs, Soda Lake, Stillwater, and Dixie Valley. During the first stage of the project, the study results of the well DP23-1 showed difficulties in well stimulation operation due to fragile rock characteristics. Therefore, the project proceeded to the second stage with the drilling of DP27-15 because of favorable temperature and stimulation conditions. The Desert Peak geothermal field currently has a generation capacity of 1.7 MWe from around 30 geothermal wells [17, 44].

2.3 Geomechanics involved during hydraulic fracturing

Hydraulic fracturing (HF), known by many names such as fracking, fracing, hydrofracturing, etc., is a process in which a fracture initiates and propagates with the application of hydraulic loading of injection fluid [45, 46]. HF operations have been used to enhance the productivity of oil or gas wells. It is a challenging technique involving large volumes of injection fluid (e.g. water), heavy-duty pumps, multiple types of proppants, and polymetric additives to acquire specific fluid rheology [47]. A hydraulic fracture is generated in two stages. First is the "pad stage", in which a clean fluid is injected into the formation, and a fracture is initiated once the down-hole pressure exceeds the formation breakdown pressure. Second is the "slurry stage", in which a mixture of fluid containing certain additives and proppant is pumped into the formation for fracture extension and to keep the fracture open under the influence of closure stress. The geometry of the created fracture depends on in-situ stresses, mechanical properties of the formation, formation heterogeneities (natural fissures or faults), and the rheological properties of the fracturing fluid [14, 46].

2.3.1 Stresses and strain

In 1828, Cauchy introduced linear elasticity theory that describes the deformation of an object under the influence of loading conditions. He provided the definition of stress and strain and established a system of partial differential equations to describe these processes [48]. Stress is defined as the force that acts on an infinitesimal area and can be described in terms of stress tensor as it varies with the surface orientation on which it is applied. Mathematically it can be written as Eq. (2.1).

$$\vec{\sigma} = \lim_{\Delta S \to 0} \frac{\Delta \vec{F}}{\Delta S} \tag{2.1}$$

where $\vec{\sigma}$ is the stress vector [Pa], $\Delta\overrightarrow{F}$ is the vector of internal force [N], ΔS is the corresponding area to the internal force [m^2].

The internal force can be disintegrated into one normal and two shear directions of a surface that ultimately yields in three normal stresses (σ_{xx}, σ_{yy}, σ_{zz}) and six shear stresses (τ_{xy}, τ_{yz}, τ_{zx}, τ_{xz}, τ_{zy}, τ_{yx}) as shown in Figure 2.6 (a). Due to symmetry of shear stresses ($\tau_{xy}= \tau_{yx}$, $\tau_{yz}= \tau_{zy}$, $\tau_{zx}= \tau_{xz}$), the total number of stress components can be reduced to six.

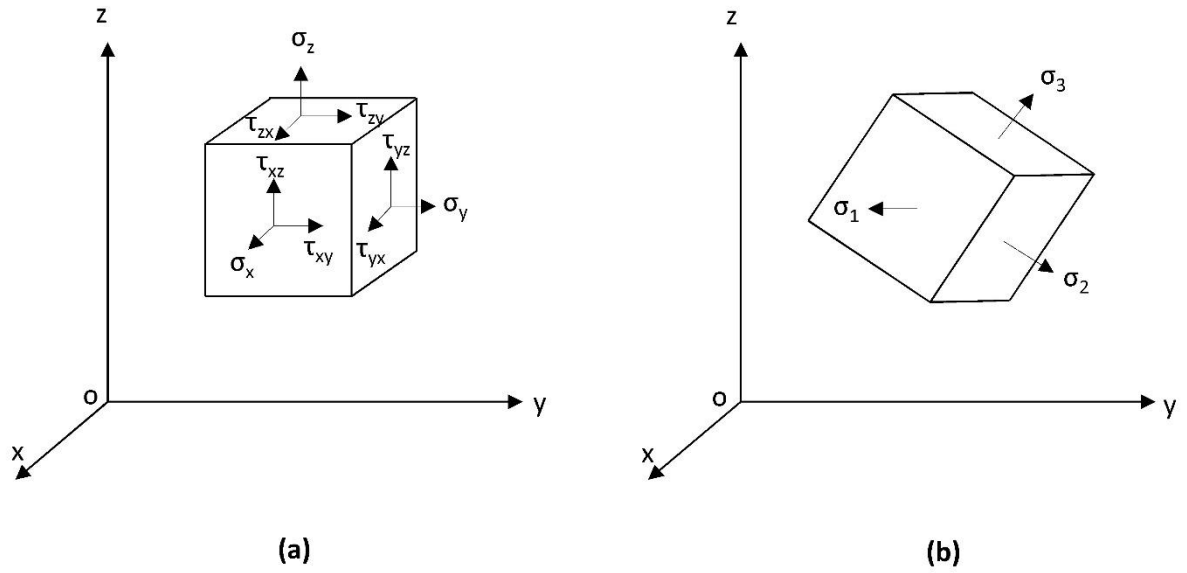

Figure 2.6 Schematic of (a) stresses in a cartesian coordinate system (b) principal stresses

The stress and strain are second-order tensors and can be described in a 3 x 3 matrix, which has three principal directions that are fixed, i.e., not change with the orientation of the axis. There are three principal values of stress and strain tensors, and the characteristic equation of stress state (Eq. 2.2) can be used for the principal stress estimations.

$$\sigma^3 - I_1\sigma^2 - I_2\sigma - I_3 = 0 \tag{2.2}$$

where σ is the stress [Pa], I_i are the invariants of stress tensor [Pa], i = 1, 2, 3, which are independent of the coordinate system and can be expressed as follows;

$$I_1 = \sigma_{ii} = \sigma_{xx} + \sigma_{yy} + \sigma_{zz} \tag{2.3}$$

$$I_2 = \begin{vmatrix}\sigma_{xx} & \tau_{xy}\\ \tau_{yx} & \sigma_{yy}\end{vmatrix} + \begin{vmatrix}\sigma_{yy} & \tau_{yz}\\ \tau_{zy} & \sigma_{zz}\end{vmatrix} + \begin{vmatrix}\sigma_{zz} & \tau_{zx}\\ \tau_{xz} & \sigma_{xx}\end{vmatrix} = \sigma_{xx}\sigma_{yy} + \sigma_{yy}\sigma_{zz} + \sigma_{xx}\sigma_{zz} - \tau_{xy}^2 - \tau_{yz}^2 - \tau_{zx}^2 \tag{2.4}$$

$$I_3 = det(\sigma_{ij}) = \sigma_{xx}\sigma_{yy}\sigma_{zz} + 2\tau_{xy}\tau_{yz}\tau_{zx} - \tau_{xy}^2\sigma_{zz} - \tau_{yz}^2\sigma_{xx} - \tau_{xz}^2\sigma_{yy} \tag{2.5}$$

where σ_{ii} is the normal component of the stress vector above the section i, i = x,y,z, τ_{ij} is the shear component of the stress vector above section i on different axes, i, j = x,y,z, and i ≠ j.

In addition, the three principal stresses of a stress state can be calculated using Eq. (2.5).

$$\begin{cases} \sigma_1 = \frac{1}{3} I_1 + \frac{2}{\sqrt{3}} \sqrt{J_2} \sin\left(\theta + \frac{2}{3}\pi\right) \\ \sigma_2 = \frac{1}{3} I_1 + \frac{2}{\sqrt{3}} \sqrt{J_2} \sin\theta \\ \sigma_3 = \frac{1}{3} I_1 + \frac{2}{\sqrt{3}} \sqrt{J_2} \sin\left(\theta - \frac{2}{3}\pi\right) \end{cases} \tag{2.6}$$

where σ_i is the principal stress of a stress state [Pa], J_i is the invariant of the stress deviator tensor [Pa], i = 1, 2, 3, θ is the Lode's angle [°].

Analogous to principal stress, there exist three invariants of stress deviator tensor (Eq. (2.7)-(2.9)). Deviatoric stress describes the changes in distortion and is important in the creep process.

$$J_1 = S_{ii} = 0 \tag{2.7}$$

$$\begin{aligned} J_2 &= -\left[\begin{vmatrix} \sigma_{xx} & \tau_{xy} \\ \tau_{yx} & \sigma_{yy} \end{vmatrix} + \begin{vmatrix} \sigma_{yy} & \tau_{yz} \\ \tau_{zy} & \sigma_{zz} \end{vmatrix} + \begin{vmatrix} \sigma_{zz} & \tau_{zx} \\ \tau_{xz} & \sigma_{xx} \end{vmatrix}\right] \\ &= \frac{1}{6}\left[\left(\sigma_{xx} - \sigma_{yy}\right)^2 + \left(\sigma_{yy} - \sigma_{zz}\right)^2 + \left(\sigma_{zz} - \sigma_{xx}\right)^2\right] + \tau_{xy}^2 + \tau_{yz}^2 \end{aligned} \tag{2.8}$$

$$J_3 = det\left(S_{ij}\right) = \left(\sigma_{xx} - \sigma_m\right)\left(\sigma_{yy} - \sigma_m\right)\left(\sigma_{zz} - \sigma_m\right) \tag{2.9}$$

where $S_{ij}$is the component of the stress deviator tensor [Pa], i = x, y, z.

For practical purposes, the equilibrium equations are required to express the relation between external forces and stress under a dynamic state. Based on the unit element in Figure 2.8, the dynamic equilibrium equations in x, y and z directions can be expressed as;

$$\begin{cases} \frac{\partial \sigma_{xx}}{\partial x} + \frac{\partial \tau_{xy}}{\partial y} + \frac{\partial \tau_{xz}}{\partial z} + F_x - \rho \frac{\partial^2 u}{\partial t^2} = 0 \\ \frac{\partial \sigma_{xx}}{\partial x} + \frac{\partial \tau_{xy}}{\partial y} + \frac{\partial \tau_{xz}}{\partial z} + F_y - \rho \frac{\partial^2 v}{\partial t^2} = 0 \\ \frac{\partial \sigma_{xx}}{\partial x} + \frac{\partial \tau_{xy}}{\partial y} + \frac{\partial \tau_{xz}}{\partial z} + F_z - \rho \frac{\partial^2 w}{\partial t^2} = 0 \end{cases} \tag{2.10}$$

where F_i is the component of the force in i direction [N], i = x, y, z, ρ is the density of object [kg/m^3], u, v, w are the components of object's displacement on x, y and z axis [m], t is the time [s].

To describe the relationship between displacement and strains, geothermic equations are introduced. Three normal strains ($\varepsilon_{xx}, \varepsilon_{yy}, \varepsilon_{zz}$) and three shear strains ($\varepsilon_{xy}, \varepsilon_{yz}, \varepsilon_{zx}$) can be used to describe the 3D strain state in Cartesian coordinate system. The geometric equations are expressed as Eq. (2.11).

$$\begin{cases} \varepsilon_{xx} = \dfrac{\partial \mathrm{u}_x}{\partial \mathrm{x}}, & \varepsilon_{xy} = \dfrac{1}{2}\left(\dfrac{\partial \mathrm{u}_x}{\partial y} + \dfrac{\partial \mathrm{u}_y}{\partial x}\right) \\ \varepsilon_{yy} = \dfrac{\partial \mathrm{u}_y}{\partial \mathrm{y}}, & \varepsilon_{yz} = \dfrac{1}{2}\left(\dfrac{\partial \mathrm{u}_z}{\partial y} + \dfrac{\partial \mathrm{u}_y}{\partial z}\right) \\ \varepsilon_{zz} = \dfrac{\partial \mathrm{u}_z}{\partial \mathrm{z}}, & \varepsilon_{zx} = \dfrac{1}{2}\left(\dfrac{\partial \mathrm{u}_z}{\partial x} + \dfrac{\partial \mathrm{u}_x}{\partial z}\right) \end{cases} \tag{2.11}$$

2.3.2 Constitutive model

The relationship between stress and strain can be further elaborated using constitutive equations. The typical stress-strain curve having two major sections, i.e., elastic and plastic, is shown in Figure 2.7.

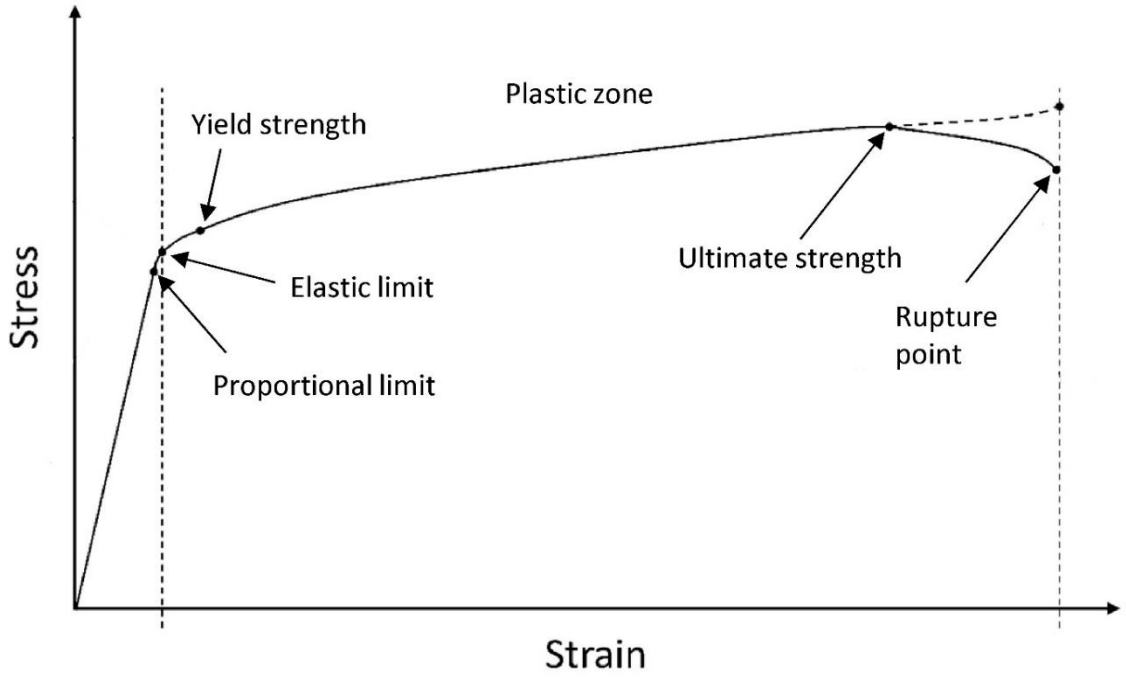

Figure 2.7 Typical stress-strain curve

A linear relation exists between stress and strain until the proportional limit is reached. During this stage, the deformation is reversible. However, deformation becomes irreversible once the stress state reaches or exceeds the yield strength of the material. Elastic theory can calculate elastic strain as in Eq. (2.12).

$$\begin{cases} \varepsilon_{xx} = \frac{1}{E}\left[\sigma_{xx} - \upsilon\left(\sigma_{yy} + \sigma_{zz}\right)\right], \ \ \varepsilon_{xy} = \frac{\tau_{xy}}{2G} \\ \varepsilon_{yy} = \frac{1}{E}\left[\sigma_{yy} - \upsilon(\sigma_{xx} + \sigma_{zz})\right], \ \ \varepsilon_{yz} = \frac{\tau_{yz}}{2G} \\ \varepsilon_{zz} = \frac{1}{E}\left[\sigma_{zz} - \upsilon\left(\sigma_{xx} + \sigma_{yy}\right)\right], \ \ \varepsilon_{zx} = \frac{\tau_{zx}}{2G} \end{cases} \tag{2.12}$$

where E is Young's modulus [Pa], υ is the Poisson ratio [-], G is the shear modulus [Pa].

In the plastic zone, micro fractures begin to appear in the object. Two famous failure criterions exist to quantify the plastic strain, i.e., Mohr failure criterion and Tensile criterion. In Mohr failure criterion, shear stress exceeds the shear strength and is expressed as;

$$F^p = \sigma_1 - \sigma_3 N_\varphi - 2c\sqrt{N_\varphi} \tag{2.13}$$

where σ_1 is the maximum principal stress [Pa], σ_3 is the minimum principal stress [Pa], c is the cohesion [Pa], N_φ is a constant and can be calculated using Eq. (2.14);

$$N_\varphi = \frac{1 + sin\varphi}{1 - sin\varphi} \tag{2.14}$$

where φ is the friction angle [°].

In tensile failure criterion, plastic failure takes place when tensile stress exceeds the tensile strength and is expressed as;

$$F^p = -\sigma_3 - \sigma_T \tag{2.15}$$

where σ_T is the tensile strength [Pa].

The plastic deformation can be calculated as;

$$\mathrm{d}\varepsilon_{ij}^P = \ \mathrm{d}\lambda . \frac{\langle F^P \rangle}{|F^P|} . \frac{\partial Q^P}{\partial \sigma_{ij}} \tag{2.16}$$

$$\langle F^P \rangle = \begin{cases} 0 & F^P \leq 0 \\ F^P & F^P > 0 \end{cases} \tag{2.17}$$

where ε_{ij}^P is plastic stain [-], λ is the plastic strain multiple [-], Q^P is the potential function [-], F^P is the failure function.

The potential functions related to Mohr and Tensile failure criteria are expressed in Eq. (2.18) and Eq. (2.19), respectively.

$$Q^p = \sigma_1 - \sigma_3 N_\varphi \tag{2.18}$$

$$Q^p = -\sigma_3 \tag{2.19}$$

2.4 Modeling of hydraulic fracturing

Dow Chemical Company introduced hydraulic fracturing in the 1930s with the observation that downhole fluid pressure can crack the formation rock [46]. However, the first hydraulic fracturing treatment was performed in 1947 in Kansas on a gas well in the Hugoton field [49]. Since then, millions of treatments have been performed in low permeable fields with various geological environments. Hydraulic fracturing is a complex process that involves multiple coupled processes such as mechanical deformation of rock caused by fluid pressure change on the fracture surface, the fluid flow inside the fracture and formation along with their interactions, fracture propagation, proppant movement inside the fracture, and its settlement. A mathematical model is necessary to propose and investigate the hydraulic fracturing treatment. Therefore, the race for developing theoretical models began in the 1950s gradually for 2-dimension (KGD & PKN) and 3-dimension such as cell-based pseudo-3D (P3D) and planar 3D models. A review of these models has been presented in the subsequent section.

2.4.1 Penny-shaped fracture's modeling

The leading analytical solution for a penny-shaped fracture (Figure 2.8) was found by Sneddon and Elliot [50] in 1946 with fixed fracture length and under the influence of constant loading at plain strain state. They proposed an expression for the width of a penny-shaped crack having radius 'R' that defines an ellipsoid as given in Eq. (2.20).

$$w(r) = \frac{8P_{net}R(1-v^2)}{\pi E}\sqrt{1-\frac{r^2}{R^2}} \tag{2.20}$$

Whereas the volume of the crack is expressed in Eq. (2.21).

$$V = \frac{16(1-v^2)R^3}{3E}P_{net} \tag{2.21}$$

where R is the radial fracture length [m], r is the radial coordinate [m], E is the Young's modulus [Pa], v is the Poisson ratio [-], $P_{net} = p_f - \sigma_c$ is the net pressure [Pa], p_f is the pressure inside the fracture [Pa] and σ_c is the fracture closure pressure [Pa].

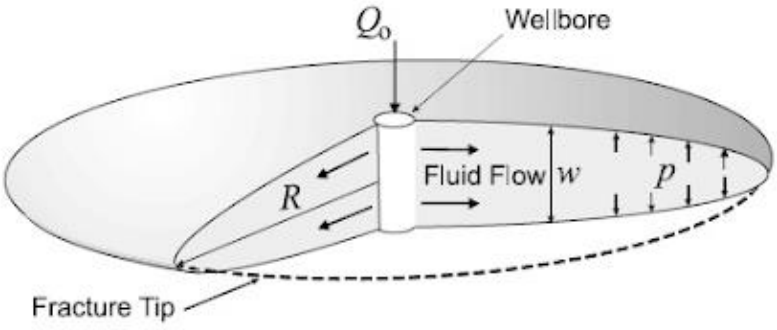

Figure 2.8 Schematic of radial fracture geometry [46]

Sack [51] in 1946, described the net pressure for fracture propagation under constant pressure loading as:

$$P_{net} = \sqrt{\frac{\pi \gamma_F E}{2(1-v^2)R}} \tag{2.22}$$

where γ_F is the fracture surface energy [J/m^2].

The radial fracture length can be calculated in terms of injection rate and time by assuming no leak-off as described in Eq. (2.23).

$$R = \left[\frac{9EQ^2t^2}{128\pi\gamma_F(1-v^2}\right]^{1/5} \tag{2.23}$$

Carter (1957) introduced the fundamental equation (Eq. 2.24) to define fluid leak-off during hydraulic fracture modeling, neglecting the fluid viscosity and solid mechanics effects.

$$u_L = \frac{C_L}{\sqrt{t - t_{exp}}} \tag{2.24}$$

where u_L is the leak-off velocity at a point on fracture wall [m/s], C_L is the leak-off coefficient [m/s$^{1/2}$], t is the current time of injection [s], t_{exp} is the beginning time of leak-off [s].

Sneddon and Elliot (1946) also proposed an analytical solution to solve the stress interference phenomenon during hydraulic fracturing. The stress components are described as follows:

$$\frac{1}{2}\left(\Delta\sigma_x - \Delta\sigma_y\right) = P_{net}\left\{\frac{r}{\sqrt{r_1 r_2}}\cos\left(\theta - \frac{1}{2}\theta_1 - \frac{1}{2}\theta_2\right) - 1\right\} \tag{2.25}$$

$$\frac{1}{2}(\Delta\sigma_y - \Delta\sigma_x) = P_{net}\frac{rsin(\theta)}{c}\left(\frac{c^2}{r_1 r_2}\right)^{\frac{3}{2}} sin\frac{3}{2}(\theta_1 + \theta_2) \quad (2.26)$$

$$\Delta\tau_{xy} = P_{net}\frac{rsin(\theta)}{c}\left(\frac{c^2}{r_1 r_2}\right)^{\frac{3}{2}} cos\frac{3}{2}(\theta_1 + \theta_2) \quad (2.27)$$

where *c* is the fracture half-length and the other symbols are explained in Figure 2.9.

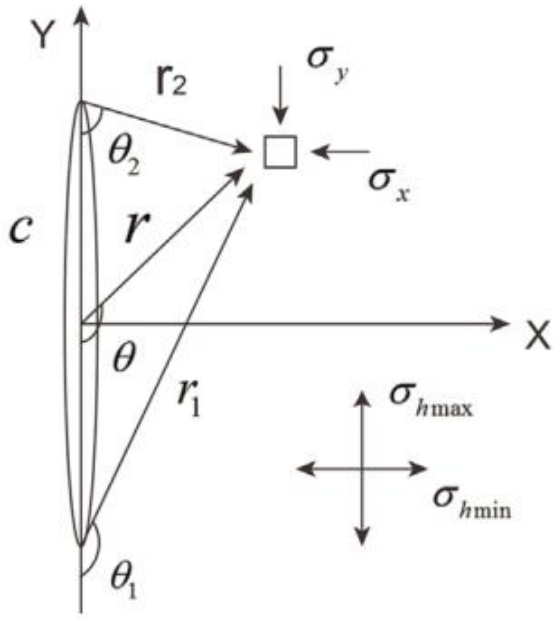

Figure 2.9 Schematic of 2D fracture parameters in Eqs. (2.25) to (2.27) [52]

2.4.2 Two-dimensional models (2D)

Two models, namely PKN model (developed by Perkens, Kern and Nordgren), and KGD model (developed by Khristianovich, Zheltov, Geertsma and de Klerk), are considered as basic hydraulic fracturing models that include volume balance and solid mechanics. These models have relatively simple geometries converting a 3D solid and fracture mechanics problem into 2D (i.e., plane strain) problem. The details of these models are presented in the following section.

2.4.2.1 The PKN model

Perkin and Kerin (1961) [53] assumed that the stresses above and below the pay zone are sufficiently large enough to allow the fracture propagation only in the pay zone with fixed vertical height. Furthermore, the fracture cross-section is elliptical and has a limited height h_f (Figure 2.10). This is valid if the fracture half-length is much bigger than fracture height

(L>>hf). The fluid flow rate in an elliptical section is governed by 1D Newtonian flow and can be written as in Eq. (2.28).

$$\frac{dp}{dx} = -\frac{64q\mu}{\pi h_f w^3} \tag{2.28}$$

where p is the pressure [Pa], x is the distance along the fracture [m], μ is the fluid viscosity [cp].

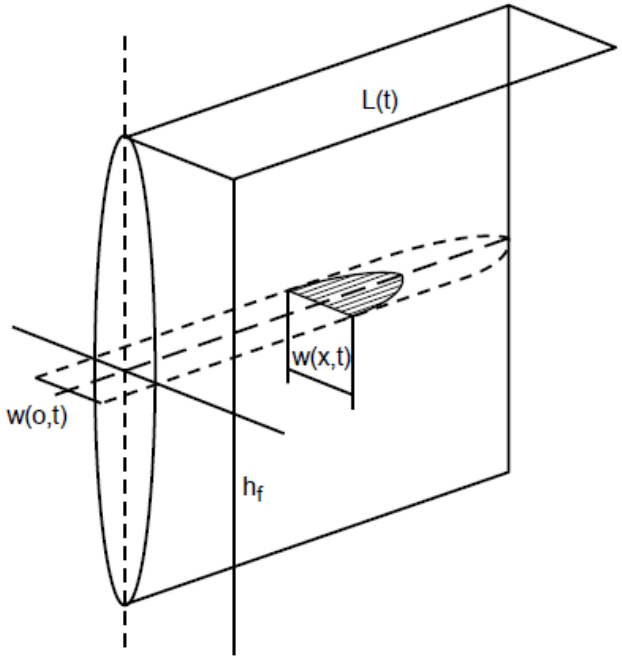

Figure 2.10 Schematic of a PKN fracture model [14]

For the fixed fracture height, maximum fracture width can be described in terms of net pressure (Sneddon and Elliot (1946) as:

$$w = \frac{2p_{net}h_f(1-v^2)}{E} \tag{2.29}$$

By substituting Eq. (2.29) in Eq. (2.28), replacing flow rate q by one-half of the injection rate ($q_i/2$), and neglecting both leak-off and fluid storage in fracture, Eq. (2.30) can be obtained.

$$p_{net}^3 dp_{net} = -\frac{4}{\pi}\frac{\mu q_i E'^3}{h_f^4}dx \tag{2.30}$$

where $E' = \frac{E}{1-v^2}$ is the plane strain modulus [Pa].

By integrating the above expression along the fracture half-length L and $p_{net} = 0$ at the fracture tip, net pressure can be described in Eq. (2.31).

$$p_{net} = \left[\frac{64\mu q_i E'^3}{\pi h_f^4} L\right]^{1/4} \tag{2.31}$$

Maximum fracture width in terms of injection rate can be obtained (Eq. (2.32)) by inserting Eq. (2.31) back in Eq. (2.29).

$$w(x) = 3\left[\frac{\mu q_i (L-x)}{E'}\right]^{1/4} \tag{2.32}$$

Nordgren (1972) [54] added the leak-off and fluid storage relations into the initial Perkins and Kern model, and optimized the fracture model known as PKN model. The equation of continuity (i.e., conservation of mass) is described as:

$$\frac{\partial q}{\partial x} + q_L + \frac{\partial A}{\partial t} = 0 \tag{2.33}$$

where q is the volume flow rate through a cross-section [m^3/s], A is the cross-sectional area of the fracture (which is $\pi wh_f/4$ for PKN model) [m^2], q_L is the leak-off rate per unit length [m^2/s].

q_L can be expressed according to Carter model (1957) as:

$$q_L = 2h_f \mu_L \tag{2.34}$$

where u_L is the leak-off velocity at a point on the fracture wall and is expressed in Eq. (2.24).

By substituting Eq. (2.28) and Eq. (2.34) into Eq. (2.33), the following expression is obtained.

$$\frac{E'}{128\mu h_f}\frac{\partial^2 w^4}{\partial x^2} = \frac{8C_L}{\pi\sqrt{t - t_{exp}(x)}} + \frac{\partial w}{\partial t} \tag{2.35}$$

Using the numerical methods, the above partial differential equation can be solved.

2.4.2.2 The KGD model

Khristianovich and Zhelo (1955) [55] developed the hydraulic fracturing model by assuming the fracture width independent of fracture height at any distance from the well. This assumption is valid for a fracture with a much higher height than half-length (hf>>L). Figure 2.11 shows KGD model having fixed fracture height. KGD width calculations can be used for short fractures where plane strain assumptions are applicable to horizontal sections. Moreover, the radial model is appropriate for analogous reservoir conditions considering the injection section practically a point source. They included the solution of fracture mechanics' aspects of the

fracture tip by assuming the flow rate in the fracture as constant. In addition, the pressure inside the fractured body can be approximated as constant, except for a small region near the fracture tip with no fluid pressure.

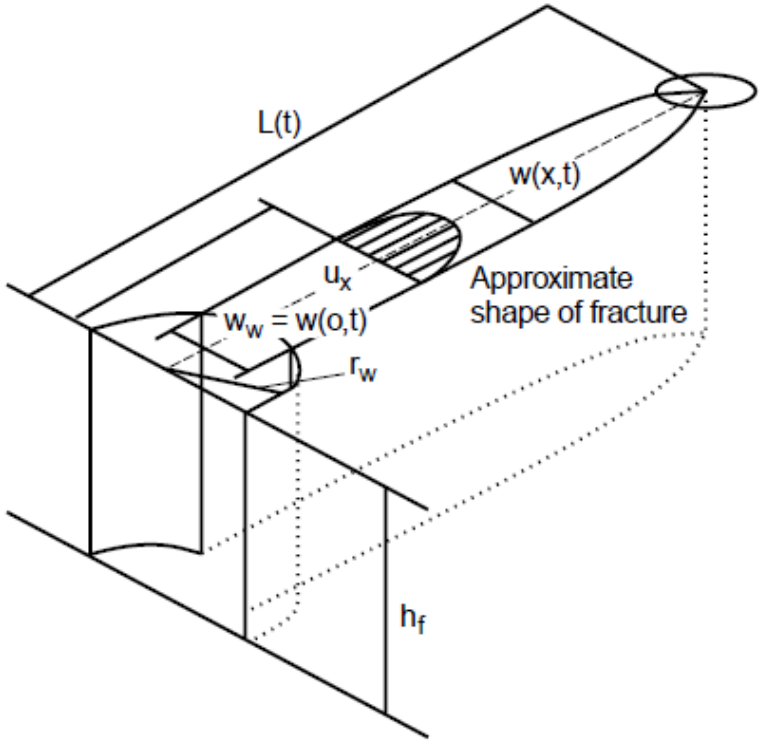

Figure 2.11 Schematic of a KGD fracture model [14]

Geertsma and de Klerk (1969) [56] adopted the Khristianovich and Zheltov's work and provided a more straightforward solution for the tip region. For the rectangular cross-section, 1D flow can be presented as:

$$\frac{\partial p}{\partial x} = -\frac{12q\mu}{h_f w^3} \tag{2.36}$$

The above equation can be written in integral form

$$P_{net} = \frac{6\mu q_i}{h_f} \int_0^L \frac{dx}{w^3} \tag{2.37}$$

By adopting Barenblatt's (1962) [57] tip condition (which suggests that the fracture tip must close smoothly, Figure 2.12), the stress intensity factor is zero and stated as in Eq. (2.38).

$$\int_0^L \frac{p_{net}(x)dx}{\sqrt{1-(x/L)^2}} = 0 \tag{2.38}$$

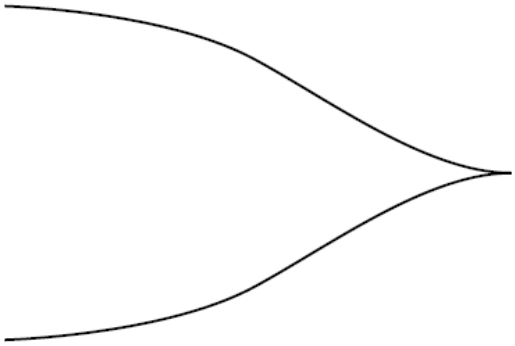

Figure 2.12 Barenblatt's tip condition [14]

The fracture width profile near the unpressured region is almost the same as that acquired with constant net pressure over the entire fracture and can be written as:

$$w_w = \frac{4}{E'} L p_{net} \tag{2.39}$$

By solving Eq. (2.37) through Eq. (2.39), expressions for the well bore net pressure (Eq. 2.40) and wellbore width (Eq. (2.41)) can be obtained.

$$p_{net} \approx \left[\frac{21\mu q_i}{64\pi h_f L^2} E'^3\right]^{1/4} \tag{2.40}$$

$$w_w = \left[\frac{84}{\pi}\frac{\mu q_i L^2}{E' h_f}\right]^{1/4} \tag{2.41}$$

In case of no leak-off, fracture length and width can be calculated in terms of injection time.

$$L(t) = 0.38\left[\frac{E' q_i^3}{\mu h_f^3}\right]^{1/6} t^{2/3} \tag{2.42}$$

$$w_w = 1.48\left[\frac{\mu q_i^3}{E' h_f^3}\right]^{1/6} t^{1/3} \tag{2.43}$$

Geertsma and de Klerk (1969) extended the model to include a leak-off term according to Carter's (1957) method. They incorporated fluid loss, assuming no effect on fracture shape or pressure distribution. The volume of two-wing KGD fracture is:

$$V_f = \frac{\pi}{2} h_f L w_w \tag{2.44}$$

By applying volume balance and Laplace transformation, Eq. (2.45) is obtained.

$$L = \frac{q_i w_w}{64 C_L^2 h_f}\left(e^{s^2} erfc(S) + \frac{2}{\sqrt{\pi}} S - 1\right) \tag{2.45}$$

where $S = \frac{8 C_L \sqrt{\pi t}}{\pi w_w}$.

2.4.3 Three-dimensional models (3D)

The above-mentioned 2D models contain several assumptions and significant limitations as these work on the fixed fracture height or radial fracture propagation. However, fracture width generally varies from the well to the tip of the fracture. The 3D models have been developed to overcome this limitation.

2.4.3.1 Planar 3D model

The Planar 3D model is a physical-based model that assumes the fracture as planar and oriented normal to the far-field minimum in-situ stress. During fluid flow inside the fracture, both the width at any point and the shape of fracture vary with time. The relation between pressure gradient and flow rate is sensitive to the fracture width. This model considers a coupling between the fracture geometry and fluid flow. The fracture width at any point (x,y) can be determined by an integral of the net pressure over the entire fracture as:

$$w(x,y) = \iint_S f(x - x', y - y')\big(p(x',y') - \sigma(x',y')\big) dx' dy' \tag{2.46}$$

where σ is the stress, f is the elastic influence function of an arbitrary point (x',y') to the point (x,y).

The boundary element method can be used to generate the mesh in each layer with a couple of variants. The triangular mesh (moving) and quadrilateral mesh (fixed) are shown in Figure 2.13 and Figure 2.14, respectively. The propagation criterion differs for each mesh strategy.

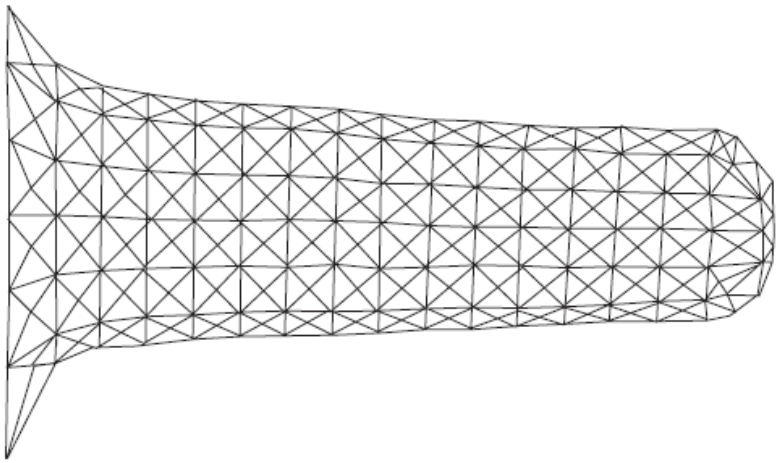

Figure 2.13 Representation of planar 3D fracture geometry based on moving mesh system of triangular elements [46]

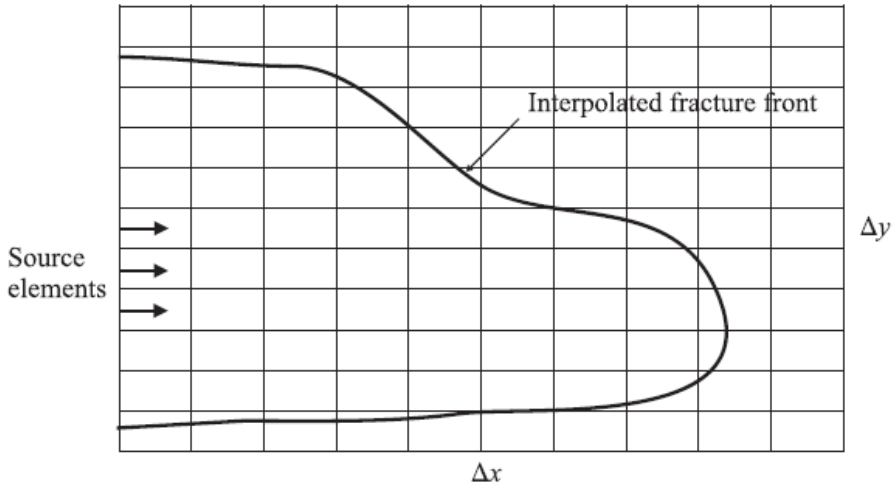

Figure 2.14 Representation of planar 3D fracture geometry based on regular (fix) system of quadrangular elements [46]

The fluid flow is presented using equations for conservation of mass and the leak-off effect as:

$$\left(\frac{\partial(\rho w u_x)}{\partial x}\right) + \left(\frac{\partial(\rho w u_y)}{\partial y}\right) + \frac{\partial(\rho w)}{\partial t} + 2\rho u_L = 0 \tag{2.47}$$

Due to the difficulty of complex coupling of fluid flow, solid deformation, relation between width and pressure, and the complexity of the moving-boundary problem, this model is only numerically solvable.

2.4.3.2 Pseudo-3D model (P3D)

Pseudo-3D models attempt to apprehend the physical behavior of a planar 3D hydraulic fracture with minimal computational complexity. The basic assumptions to build these models include

homogeneous reservoir elastic properties and averaged over all fracture height layers. There are two main P3D models, i.e., cell-based and lumped.

- **Cell-based pseudo-3D model**

Cell-based P3D models adopt the fracture as a series of connected cells (Figure 2.15). Each cell behaves as a planar fracture and does not contribute in fluid flow in a vertical direction, same as the PKN model. Therefore, it is valid only if the fracture length is higher than the fracture height. The fluid flow occurs along the fracture length and the pressure in the cross-section is calculated using Eq. (2.48).

$$p = p_{cp} + \rho g y \tag{2.48}$$

where p_{cp} is the pressure along a horizontal line through the center of the perforations, y is the vertical distance from the center of the perforations.

The above expression is valid for sufficiently slow vertical fracture extension and assumes negligible pressure gradient resulting from the vertical flow.

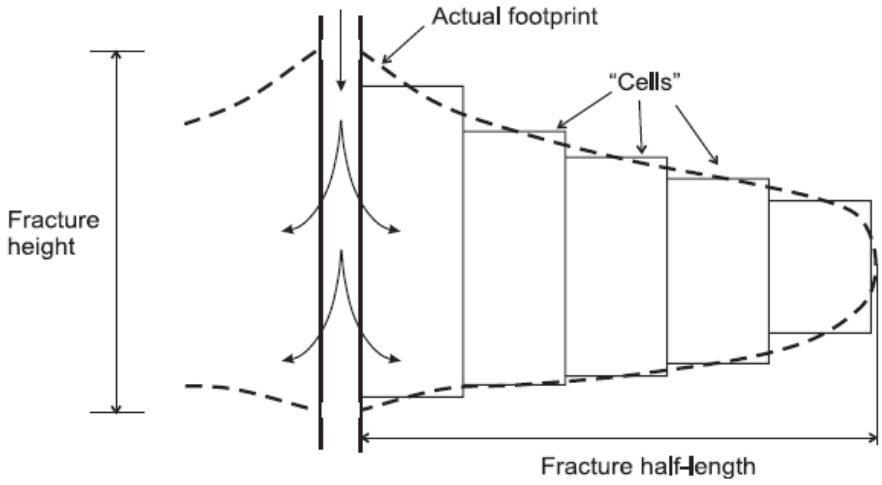

Figure 2.15 Schematic of facture geometry based on cell-based pseudo-3D model [46]

Fung et al. (1987) [58] provided a general solution for asymmetric multi-layer cases. They proposed that the stress intensity factor at the top (K_{Iu}) and bottom tips (K_{Il}) can be expressed in terms of pressure at the center of the perforation and the closure stress in each layer.

$$k_{Iu} = \sqrt{\frac{\pi h_f}{2}}\left[p_{cp} - \sigma_n + \rho_f g\left(h_{cp} - \frac{3}{4}h_f\right)\right] + \sqrt{\frac{2}{\pi h_f}}\sum_{i=1}^{n-1}(\sigma_{i+1} - \sigma_i)\left[\frac{h_f}{2}\cos^{-1}\left(\frac{h_f - 2h_i}{h_f}\right) - \sqrt{h_i - (h_f - h_i)}\right] \quad (2.49)$$

$$k_{Il} = \sqrt{\frac{\pi h_f}{2}}\left[p_{cp} - \sigma_n + \rho_f g\left(h_{cp} - \frac{1}{4}h_f\right)\right] + \sqrt{\frac{2}{\pi h_f}}\sum_{i=1}^{n-1}(\sigma_{i+1} - \sigma_i)\left[\frac{h_f}{2}\cos^{-1}\left(\frac{h_f - 2h_i}{h_f}\right) - \sqrt{h_i - (h_f - h_i)}\right] \quad (2.50)$$

where k_{Iu} and k_{Il} are the stress intensity factors [Pa.m$^{1/2}$], ρ_f is the fluid density [kg/m^3]; h_f, h_i, h_{cp} are relevant heights [m] (Figure 2.16).

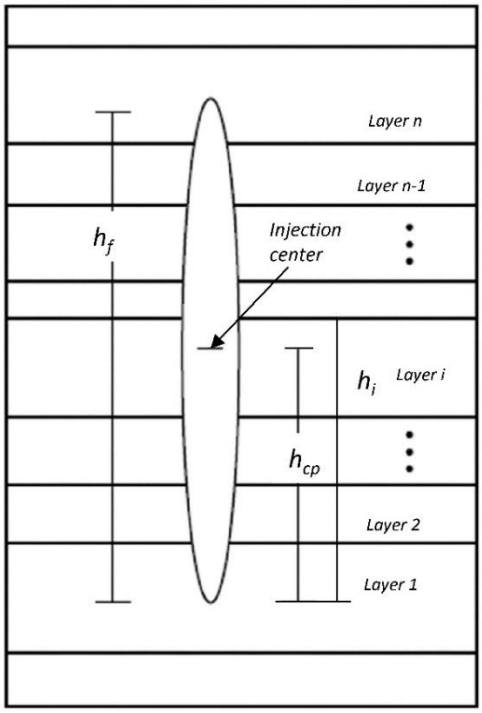

Figure 2.16 Definition of the variable for fracture containment problem (modified from Economides & Nolte [14])

With the known pressure at the center of the perforation (p_{cp}) and incremental height growth, the fracture width can be presented as in Eq (2.51).

$$w(y) = \frac{4}{E'}\left(p_{cp} + \rho_f g\left(h_{cp} - y\right) - \sigma_n\right)\sqrt{y\left(h_f - y\right)} + \frac{4}{\pi E'}\sum_{i=1}^{n-1}(\sigma_{i+1} - \sigma_i)\left[(h_i - \mathrm{y})\cosh^{-1}\left(\frac{y}{|y - h_i|}\,\frac{h_f - 2h_i}{h_f} + \frac{h_i}{|y - h_i|}\right) + \sqrt{y\left(h_f - y\right)}\cos^{-1}\left(\frac{h_f - 2h_i}{h_f}\right)\right] \quad (2.51)$$

where *y* is the elevation measured from the bottom tip of the fracture.

- **Lumped pseudo-3D model**

In the lumped P3D approach, a fracture is divided into two half ellipses joined to their centers in the fracture length direction, as shown in Figure 2.17. The three variables, i.e., the top ellipse, the bottom ellipse, and fracture length, are calculated at each time step. At the same time, fluid follows fixed streamlines from the perforation to the ellipse edge. This approach was firstly introduced by Clearly (1980) [59] and was based on the mass conservation equation and the relation between the distribution of crack opening over fracture length. The net pressure distribution is expressed as:

$$P_{net}(x) = \int_{-L}^{L} I(x, x')w(x')dx' \quad (2.52)$$

While momentum conservation is stated as:

$$\tilde{q}q^{m-1} = \frac{-\gamma_4 w^{2n-m+1}\tilde{\nabla}p}{\mu} \quad (2.53)$$

where γ_4 is channel factor, *m* is for turbulence, *n* enables consideration for both non-Newtonian fluids and turbulent flow.

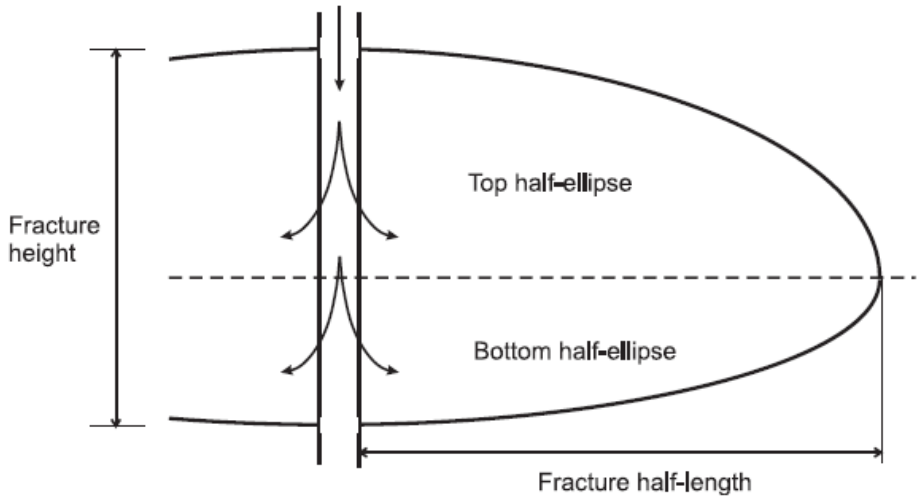

Figure 2.17 Schematic of facture geometry based on pseudo-3D lumped elliptical model

The further developed PKN and KGD models are generally used to determine fracture propagation in vertical and horizontal directions. The mass balance can be obtained by averaging over the fracture length.

$$\rho(q\bar{w} - Lq_L) = d(\gamma_3 \rho \bar{w} L)/dt \tag{2.54}$$

Where

$$\bar{w} \approx \frac{\gamma_1 p_{net}}{E} L \tag{2.55}$$

And power law flow equation:

$$q^m \bar{w}^m \approx \frac{\gamma_5^m (\bar{w})^{2n+2}}{L^2} \tag{2.56}$$

Where

$$\gamma_5^m = \frac{\gamma_2 \gamma_4 E}{\gamma_1 \mu} \tag{2.57}$$

The above expressions are similar to the KGD model and relatively simple, but "γ" coefficients may not be constant. Laboratory experiments or field studies can help to determine these coefficients.

In order to achieve a fully 3D hydraulic fracturing model while incorporating coupled processes, significant attempts have been made in recent decades. Zhou and Hou (2013) [60]

have developed an advanced approach for simulating hydraulic fracturing. In this approach, a fracture can propagate under a three-dimensional stress state with hydro-mechanical coupling effects among the fracture and the matrix mediums using software FLAC3D. In addition, the settling effect of proppants during fluid transport was also implemented. In 2016, Feng [61] extended the model by taking the heat transport in fracture and heat exchange effects between fracture and surrounding rocks during the hydraulic fracturing process in tight sandstones. By introducing a set of plug-in components in FLAC3D, the modified software is named FLAC3D^{plus}. To model the fully THM coupled processes, two numerical simulators FLAC3D and TOUGH2 were coupled to exchange data with non-linear coupling functions [62, 63]. Afterward, the modified version FLAC3D^{plus} has been coupled with TOUGH2MP to model the hydraulic fracturing process in different reservoirs [64, 65].

2.5 Significance of wellbore orientation on hydraulic fracturing

The wellbore orientation concerning in-situ stresses significantly impacts the propagation of multiple fractures in a horizontal well. Longitudinal and transverse fractures are formed parallel and perpendicular to the horizontal wellbore direction (Figure 2.18). Vertical wellbores have been used to perform stimulation operations throughout history. However, with the development in drilling technology, alternative wellbore designs have emerged as efficient fluid/heat extraction methods.

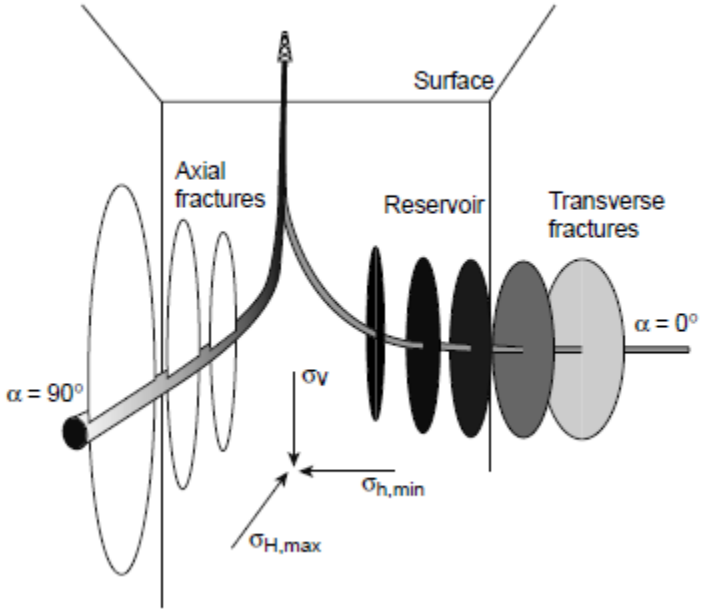

Figure 2.18 Longitudinal and transverse fractures [14]

- **Deviated wellbore**

In deviated wellbores, the drill bit is deflected at a specified angle from vertical to intersect the targeted formations. These wellbores are commonly drilled from fixed drilling locations and deflected with the help of special drilling tools such as mud turbines and steerable rotary assembly [66].

- **Horizontal wellbores**

These are the wellbores in which the targeted formations are anticipated with a high trajectory angle within the specific zone of interest. Horizontal drilling provides the advantage of accessing a more extensive reservoir section that may have limited formation thickness. In addition, practices of multiple fracturing operations using horizontal wellbore in tight hydrocarbon formations and geothermal reservoirs have become inevitable in recent times. However, horizontal wellbores are more likely to face stability issues due to high vertical stress.

- **Multilateral**

These wells have more than one lateral radiating from the main borehole. This helps in connecting several reservoirs from the single surface platform. Multilaterals are suitable to apply in locations where separate well drilling is not possible and economical. These are also beneficial to reduce the surface footprints, particularly in the case of land operations.

2.5.1 Multistage fracture placement design

The selection of wellbore orientation is further helpful in planning the multiple fracture placement design. The multistage fracturing through a single or multiple horizontal well is generally done simultaneously or sequentially. In the case with multiple wells, this is known as "zipper" fracturing technique. The "zipper-frac" approach aims to generate a network of closely spaced fractures so that an improved stimulated reservoir volume is achieved. Zipper stimulation is divided into three categories.

(a) Simultaneous zipper stimulation

This technique performs simultaneous stimulation in both parallel wellbores (Figure 2.19 (a)). During the propagation of simultaneous multiple fractures, these can interact with each other and some may not initiate due to the stress shadow effect [67]. Numerical methods performing fluid flow for fracture deformation and principles of fracture mechanics can help and improve the fracture system. This technique is applicable in shale formations using slick water [68].

(b) Sequential zipper stimulation

In this method, fractures are created sequentially with time difference between two consecutive fracturing stages as shown in Figure 2.19 (b). This concept can anticipate residual stress field of well-1 to enhance the fracturing operation from well-2. Although, most operators have adopted this stimulation technique due to its operational efficiency, improved hydrocarbon production has been observed in very few cases [69].

(c) Modified-zipper stimulation

In this method, stimulation stages are performed like sequential zipper but the wellbores have initial offset among them (Figure 2.19 (c)). Theoretically, it has been observed that both the sequential and the modified-zipper provide almost same stimulated reservoir volume. However, the reactivation of preexisting fractures due to stress shadow in modified-zipper method potentially increase the complexity and the stimulated volume [67, 70].

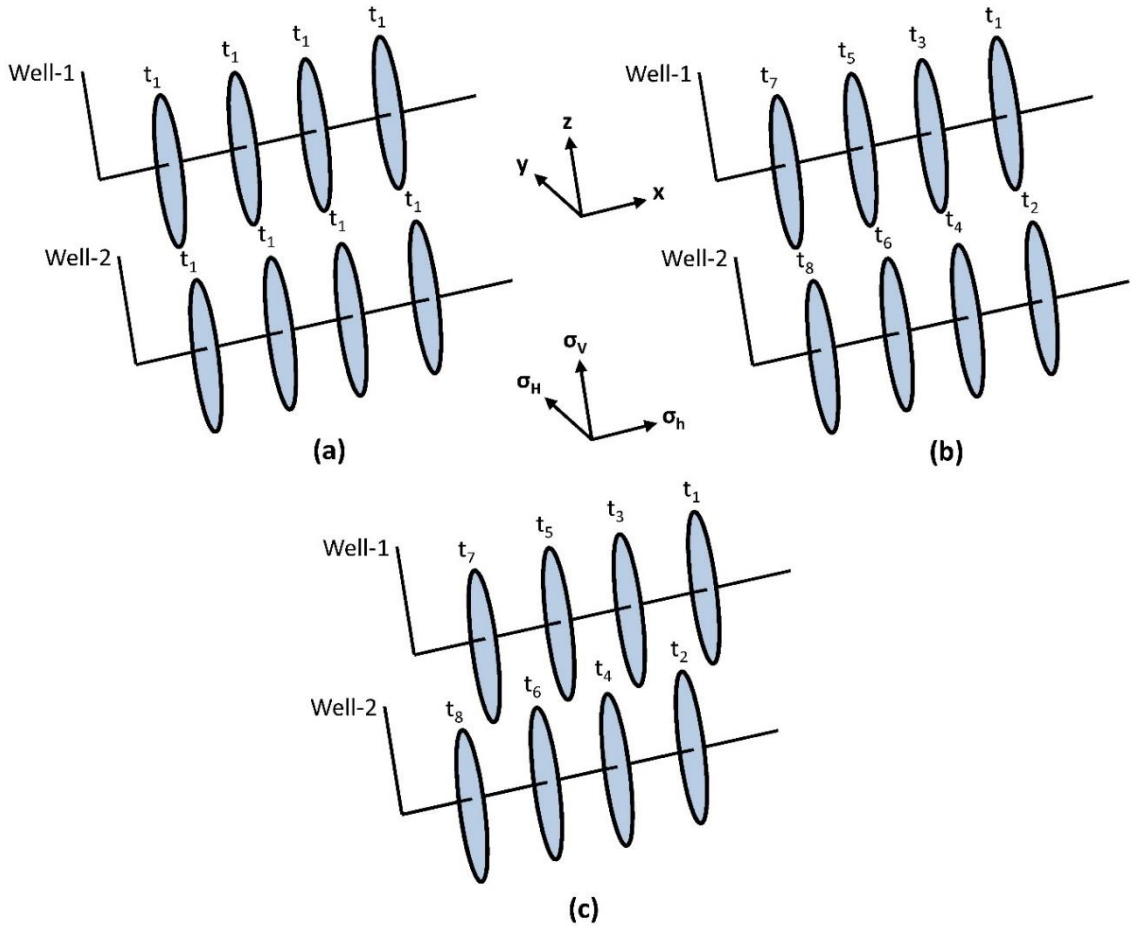

Figure 2.19 Simplified illustrations of (a) simultaneous (b) sequential and (c) modified zipper stimulation at parallel wellbore with time sequence (t1 to t8)

2.5.2 Stress shadow during multiple fracturing

The application of horizontal drilling in unconventional reservoirs with multiple transverse fractures has achieved considerable recognition in recent times. The multiple transverse fractures can be created once the horizontal wellbore is drilled parallel to the direction of minimum horizontal stress. In fracturing operation, significant amount of fluid is injected through injection perforations that not only pressurize the formation but also changes the in-situ stresses. During multiple fracturing, the increase in pressure is dependent on fracture spacing, the net pressure and the overlap area between the fractures. Such increase in pressure or stress is frequently termed as "stress shadowing" [71]. The stress shadow effect was first reported in Green et al. [72] and Snedon et al. [50] during the study of stress distribution of a semi-infinite two-dimensional fracture. The stress shadow can alter the orientation of two horizontal principal stresses. Ideal transverse fractures can be obtained without stress shadowing; however, the propagation of middle fracture is quite restricted while considering stress shadowing effect (Figure 2.20).

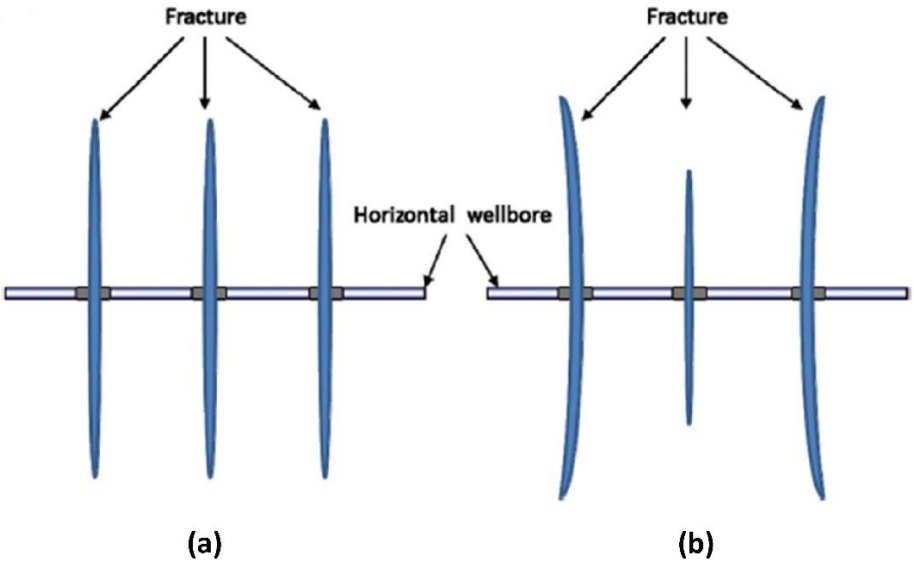

Figure 2.20 Multiple fracturing operation in the horizontal wellbore (a) without stress shadow (b) with stress shadow [71]

Soliman and Addams [73] investigated multiple transverse fractures by adopting analytical solutions for semi-infinite 2D fractures. They concluded that the stress shadow effect increases with the increase in fractures and with the decrease in fracture spacing. It has been found that fracture spacing and the sequence of fracturing operations (simultaneous, sequential, alternative) greatly influence fracture geometry. The fractures present in the middle usually have shorter fracture lengths during simultaneous operation. In contrast, during sequential

fracturing, the effects of preceding fractures may cause reduced reorientation of the succeeding fractures [74]. In addition, the fracturing sequence also plays a significant role in the degree of stress reorientation.

It has been noted that stress perturbation ahead on the subsequent fractures increases until it reaches a maximum value depending upon the fracture spacing. If an alternate fracturing sequence is adopted, fractures can be placed closer to each other, which can help in efficient drainage of the reservoir (Figure 2.21). However, special tools may need to be developed for ensuring fracturing sequence [75].

In this thesis, the stress shadowing effect during multiple fracturing operations is analyzed using consecutive fracturing sequence.

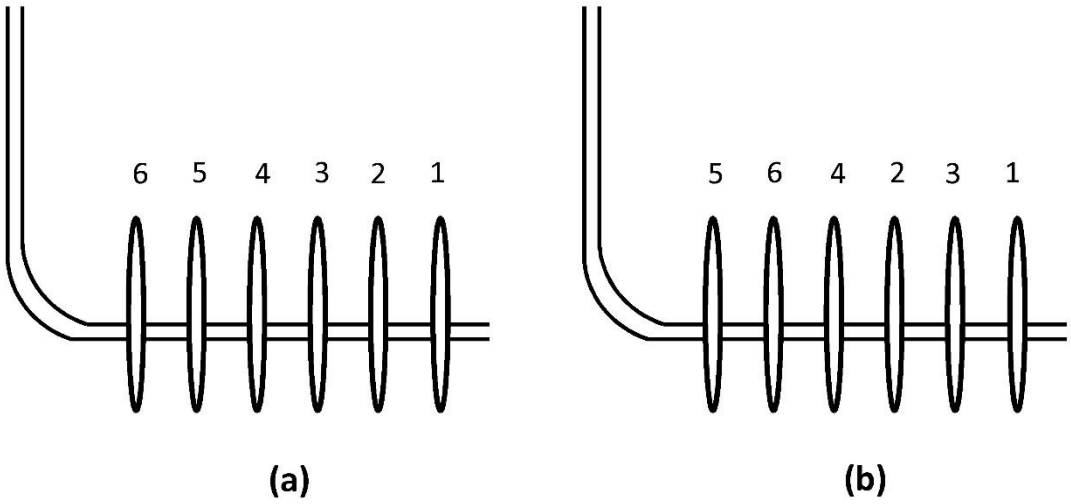

Figure 2.21 Fracturing sequence (a) consecutive (b) alternative

3 Numerical study of geothermal heat production through multiple hydraulic fractures in a horizontal well in consideration with stress shadow effects

In this chapter, thermo-hydro-mechanical (THM) coupled processes are integrated based on numerical computational methods, and a fictive model study is carried out for geothermal energy production through multi-well multi-hydraulic fractures. It is hard to find an in-depth analysis incorporating the stress shadow impact while designing multiple fractures in enhanced geothermal systems. A couple of prominent features exemplifies the uniqueness of this study. The effect of the previous fracture on each newly created fracture has been analyzed based on configured fracture geometry during multiple hydraulic fracturing, combining the stress shadow effect. Afterward, fluid flow calculations for geothermal utilization are performed using cubic law while integrating the changes during fracturing operations. This concept can provide a good understanding of reckoning out the preferable flowing paths and a fair estimation of geothermal energy production. The main contents of this chapter have been published in the following research paper (Haris et al. 2020)[76]: Investigative coupled Thermo-Hydro-Mechanical modelling approach for geothermal heat extraction through multistage hydraulic fracturing from hot geothermal sedimentary systems. *Energies* 13, 3504.

3.1 Overview of the role of hydraulic fracturing in EGS Exploitation

Hydraulic fracturing is a well-known and widely accepted stimulation technique that is generally applied in low to ultra-low permeable reservoirs, i.e., tight or shale gas, to create flow channels (artificial fractures) to enhance flow rate from the reservoir to the wellbore [14]. Utilizing horizontal well technology with multiple transverse fractures has gained acknowledgment to deal with tight unconventional resources. However, it is still at the investigative stage for EGS exploitation. Plenty of work has been done in the past for appropriate designing of hydraulic fracturing to increase oil or gas production based on reservoir permeability, porosity, number of fractures, fracture spacing, conductivity, and half-length. Many in-situ factors are responsible for fluid conduction through single or multiple fractures, which cannot be fully controlled from an engineering point of view [77]. While working on geothermal energy systems, these issues become more significant as the thermal breakthrough measurement in a multiple fracture system is quite complex [78]. Based on different geothermal field studies, such as Soultz, Fenton Hill and Rosemanowes, insufficient

hydraulic connection and short cut issues were major causes of failure in obtaining optimal flow rates [79, 81].

Due to the limitations of time consumption and expenditures involved, laboratory tests for EGS have been neglected and rely on numerical simulations, which have made great progress in the recent era [82, 83]. Extraction of geothermal energy is a composite phenomenon that involves coupled thermal, mechanical, and hydraulic processes [84-86]. Moreover, to better understand suitable mass flow rates, heat production life span ,and heat extraction efficiency, numerical methods can be the only option to provide viable solutions. It has been estimated that the low permeability geothermal reservoir can be utilized with at least 20 kg/s production rate considering economic constraints [87]. Cao et al. [88] researched developing a fully coupled THM model for heat extraction through an idealized quintuplet EGS system. They suggested that temperature gradient induces thermal stress in the reservoir, which affects the formation permeability and heat extraction performance. Salimzadeh et al. [89] worked on deformable fractured geothermal systems and analyzed the impacts of cold fluid flow on the fracture aperture. They pointed out that cold fluid creates volumetric deformation and amends the overall distribution of stresses.

The significant designing constraints for multiple fracture systems include appropriate placement of well, fracture spacing, wellbore completion, fracture geometry, and conductivity. Li et al. [90] worked on multiple transverse fractures based on fixed fracture geometry and highlighted the importance of interaction between the wellbore and geothermal reservoir. They concluded that wellbore radius and production rate are the main influential factors during fluid flow. Several studies have been conducted by considering the geothermal reservoir as an equivalent porous medium or pipe network model, but hydro-mechanical coupling was overlooked [91-92]. The study of Zhao et al. [93] on a geothermal field in Tengchong, China, depicted that fluid flow increases due to strong mechanical effects during heat extraction over time. Zeng et al. [94] investigated electricity generation potential through a naturally fractured granite formation. They concluded that energy production is mainly dependent on injection rate and injected fluid temperature, while an increased number of horizontal wells can significantly enhance the production rate compared to vertical well. Roussel et al. [75] worked on optimizing the fracture spacing and sequencing in the Barnett shale formation. They concluded that alternate fracture sequencing and zipper fractures could enhance the stimulation treatment in the horizontal well. Fish et al. [95] verified the presence of stress shadow with the use of micro-seismic measurements during field tests and found that the growth of middle fracture is highly

attenuated by the surrounding fractures during simultaneous fracture propagation, as compared to the corner fractures. The working results of Soliman et al. [73] suggested that stress contrast increases as the fracture spacing decreases.

Although some researchers [95-97] have studied and analyzed the geometry and propagation of fractures employing a simultaneous multi-stage hydraulic fracturing technique for economical production of fossil fuels through tight formations, the impact of stress shadow on multiple fracture configuration and consequently for geothermal energy production especially incorporating THM coupling effects still needs critical investigation, which is therefore carried out in this study.

3.2 Application of FLAC3D^{plus} for modeling hydraulic fracturing

The numerical simulator FLAC3D (Itasca), the extension of the two-dimensional program FLAC (Fast Lagrangian Analysis of Continua), was initially designed to solve the soil or rock-related geotechnical engineering problems with the consideration of coupled hydraulic, mechanical, and thermal effects. It utilizes the finite difference method (FDM) for performing numerical simulations. However, its uses in the petroleum industry, especially to simulate hydraulic fractures, are limited due to fundamental design modules. The advancements of Zhou et al. (2013) [60] and Zhou et al. 2014 [98] in FLAC3D for simulating hydraulic fracture propagation in three-dimensions under fully hydro-mechanical coupled effects has made it more practical. Furthermore, heat transport within fracture and heat exchange between fracturing and surrounding rocks has also been supplemented in the extended model developed by Feng et al. [61].

3.2.1 Hydro-mechanical coupled governing equations

The consequences of hydraulic fracturing include complex coupled HM processes in the formations that take place instantaneously. The mechanical deformation is measured by solving a combination of equations such as the equation of motion (Eq. 3.1) that incorporates displacement increment dynamically at a certain time interval, the continuum equation (Eq. 3.2), and the constitutive equation (Eq. 3.3) for strain and stress increment.

$$\sigma_{ij,j} + \rho\left(b_i - \frac{dv_i}{dt}\right) = 0 \tag{3.1}$$

$$\Delta\varepsilon_{ij} = \frac{1}{2}\left(\Delta u_{i,j} + \Delta u_{j,i}\right) \tag{3.2}$$

$$\Delta\sigma' = D\Delta\varepsilon \tag{3.3}$$

where σ is the total stress [Pa], ρ is the rock density [kg/m^3], bi is the volumetric acceleration [m/s^2], v_i is the rock mass velocity [m/s], t is the time [s], $\Delta\varepsilon$ is the strain increment [-], u is the displacement [m], $\Delta\sigma'$ is the effective stress increment [Pa], D is the physical matrix, i, j ϵ (x,y,z).

The pressure inside fracture changes during fluid injection or leak-off [98]. At this moment, it is considered that the elements within the fracture distort while the residual elements remain stagnant (Figure 3.1). The erratic behavior of fracture can be elaborated by adding an extra strain increment in the total strain increment, which is the response of pressure change in fracture. Furthermore, the pressure change in fracture only creates strain change normal to the fracture plane and is defined in an equation (Eq. 3.4).

$$\Delta\varepsilon_f = \frac{P_f\,(t+1) + \sigma_n(t)}{\alpha_1} \tag{3.4}$$

where ε_f is the induced strain [-], P_f is the fluid pressure in fracture [Pa], σ_n is the normal stress perpendicular to the fracture [Pa], α_1 = K + 4/3 G is the material constant based on shear modulus G [Pa] and bulk modulus K [Pa].

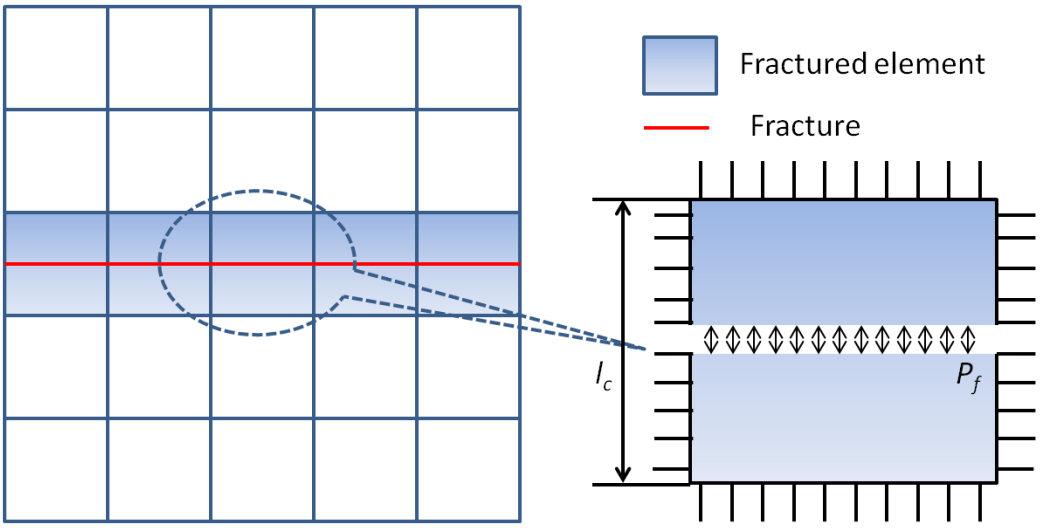

Figure 3.1 Presentation of the fracture element and load condition in a geometric model [98]

Using the induced strain, the change of fracture width for small elements normal to the fracture plane can be calculated as Eq. (3.5).

$$\Delta w = \Delta\varepsilon_f l_c \tag{3.5}$$

where w is the fracture width [m], l_c is the element length normal to the fracture [m].

Physically, a fracture can never be closed, and some fracture width always exists due to the prevention caused by surface roughness and proppant concentration in the fracture. To consider the proppant compaction or fracture wall contact, the contact stress is added in Eq. (3.4), which becomes Eq. (3.6).

$$\Delta\varepsilon_f = \frac{P_f\,(t+1) + \sigma_{con}(t) + \sigma_n(t)}{\alpha_1} \tag{3.6}$$

where σ_{con} is the contact stress [Pa] with

$$\begin{cases} \sigma_{con}(t+1) = 0 & if\ C \le C_{max}\ and\ w \ge w_{res} \\ \sigma_{con}(t+1) = \sigma_{con}(t) + \alpha_1 \cdot \Delta\varepsilon_0 & if\ C > C_{max}\ or\ w < w_{res} \end{cases}$$

where ε_0 is the over reduced strain [-], C is the proppant concentration [-], C_{max} is the maximum proppant concentration [-], w_{res} is the residual fracture width [m].

By applying induced strain induced due to the change of fluid pressure in fracture, the new stress increments can be calculated according to Hook's law.

$$\sigma_n(new) = \sigma_n(old) - \alpha_1\Delta\varepsilon_f \tag{3.7}$$

$$\sigma_{1,2}(new) = \sigma_{1,2}(old) - \alpha_2\Delta\varepsilon_f \tag{3.8}$$

where $\sigma_{1,2}$ are the stresses in another two principal directions (Pa), α_2= K – 2/3 G.

Zhou et al. [98] improvised the fracture propagation criteria by introducing multiple divisions of elements, as shown in Figure 3.2. The sub-elements in the partially fractured element are much sensitive to applied effective stress and convert into fully fractured elements once the effective stress exceeds the tensile strength. Hence, the fracture tip proceeds and the successive unfractured elements alter into partially fractured elements.

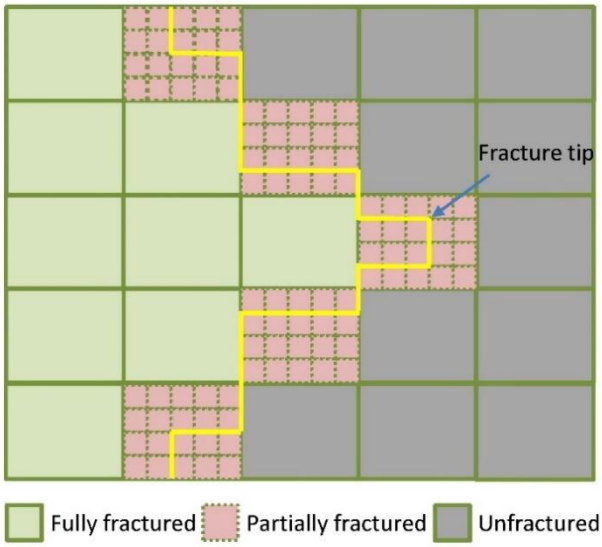

Figure 3.2 Categorization of fully fractured, partially fractured and unfractured elements

3.2.2 Two-phase flow in fracture (solid + liquid)

The combination of solid proppant and liquid based on different compositions, including certain additives and chemicals, forms a fluid slurry used during the hydraulic fracturing operation. The fluid flow in fractures highly depends on the volumetric concentration of the proppant as its concentration can change the rheological properties of the fluid. Based on the experimental findings, Barree et al. [99] derived a mathematical correlation that describes the relation between proppant concentration and slurry viscosity.

$$\mu_a = \mu_0 \left(1 - \frac{C}{C_{max}}\right)^{-a} \tag{3.9}$$

where μ_a is the apparent viscosity of the slurry [Pa.s], μ_0 is the effective Newtonian viscosity of clean fluid [Pa.s], C_{max} is the maximum proppant concentration [kg/m^3], C is the proppant concentration [kg/m^3], a is the correlation coefficient [-].

This correlation suggests that fluid starts to behave more like a solid with the increase in proppant concentration. The lower shearing region corresponds to Newtonian fluids, while the higher shear rate region is comparable to the shear-thinning fluid. To compensate these effects, Eissa et al. [100] developed a model that describes the relationship between slurry viscosity and proppant concentration and is expressed in Eq. (3.10).

$$\mu_a = \mu_0 \left(1 - \frac{C}{C_{max}}\right)^{-a} \frac{tan^{-1}\left(\frac{\gamma}{\gamma_L}\right)^{n-1}}{tan^{-1}\left(\frac{\gamma}{\gamma_H}\right)^{n-1}} \tag{3.10}$$

where γ is apparent shear rate [l/s], γ_L and γ_H are the parameters [1/s], n is the power law coefficient [-].

The two-phase flow (solid + liquid) in the fracture is generally treated as the flow between two parallel planes. With this assumption, the Navier-Stokes equation (Eq. (3.11)) can be used to derive the average velocity for slurry flow considering gravity as well. For incompressible slurry, the mass conservation equation can be reduced to the volume conservation equation (Eq. (3.12)). By putting the value of Eq. (3.11) into Eq. (3.12), Eq. (3.13) can be obtained that considers the influence of fracture aperture, pressure gradient slurry density alteration, and apparent slurry viscosity.

$$v_s = -\frac{w^2}{12\mu_a}\frac{\partial\left(P_f + \rho_s g z\right)}{\partial x} \tag{3.11}$$

$$\frac{\partial(w)}{\partial t} + \nabla \cdot (v_s w) + w Q_s = 0 \tag{3.12}$$

$$w\left(Q_{inje.} + Q_{leak}\right) + \frac{\partial w}{\partial t} = \nabla \cdot \left[\frac{w^3}{12\mu_a}\nabla\left(P_f + \rho_s g z\right)\right] \tag{3.13}$$

where v_s is the slurry velocity [m/s], w is the fracture width [m], P_f is the fluid pressure in fracture [Pa], $\rho_s = C\,\rho_p + (1 - C)$ is the slurry density [kg/m^3], ρ_p is the proppant density [kg/m^3], g is the gravity acceleration [m/s^2], z is the elevation [m], t is the time [s], Q_s is the source [1/s], $Q_{inje.}$ is the injection source [1/s], Q_{leak} is the leak-off source [1/s].

FLAC3D^{plus} utilizes Eq. (3.14) to evaluate the proppant transport.

$$\frac{\partial(Cw)}{\partial t} + \nabla \cdot \left(C v_p w\right) + w C_{inje} Q_{inje} = 0 \tag{3.14}$$

where C is the proppant concentration [%], v_p is the proppant velocity [m/s], C_{inje} is the proppant injection concentration [%].

3.2.3 Fluid flow interaction between the fracture and the rock formation

Some of the injected fluid enters into the rock formations during the hydraulic fracturing process. It is due to the pressure difference between the fracture and formation. This process is known as “leak-off” and during this pore pressure is changed. The combination of fracture

propagation, surrounding stress distribution and final proppant placement depends on the leak-off rate. In FLAC3D^{plus}, leak-off is modeled numerically using the method introduced by Zhou et al. [60], which describes the leak-off term at each time step (Eq. 3.15) considering the stationary Darcy flow between the fracture wall and the formation.

$$Q_{leak}^{t+1} = \frac{K_m S}{\mu V_i} f\left(P_p^t - P_f^t\right) \tag{3.15}$$

K_m is the permeability of the matrix [m^2], S is the exchange area [m^2], μ is the viscosity [Pa.s], V_i is the volume of the element [m^3], f is the infiltration coefficient [l/s], P_f and P_p is the fluid pressure in the fracture and formation pores [Pa], respectively.

3.3 Governing equations for heat transmission

The knowledge of reservoir stimulation remains incomplete without discussing the thermal process. Heat transmission between the fracture and the rock is a complex phenomenon that can be characterized into different transmission mechanisms. The details are provided in this section.

3.3.1 Heat conduction

Due to the difference in temperature between the two parts of the same medium, the thermal energy exchange is known as heat conduction. By integrating the heat flow equation (Fourier 1878, Eq. (3.16)), continuity equation (Eq. (3.17)), and thermal constitutive equation (Eq. (3.18)), the heat conduction process can be described mathematically as in Eq. (3.19).

$$q_i = -\lambda \frac{\partial T}{\partial i} \tag{3.16}$$

$$-\left(\frac{\partial q_x}{\partial x} + \frac{\partial q_y}{\partial y} + \frac{\partial q_z}{\partial z}\right) + q_v = \frac{\partial H}{\partial t} \tag{3.17}$$

$$\frac{\partial H}{\partial t} = \rho c_v \frac{\partial T}{\partial t} \tag{3.18}$$

$$\lambda \frac{\partial^2 T}{\partial x^2} + \lambda \frac{\partial^2 T}{\partial y^2} + \lambda \frac{\partial^2 T}{\partial z^2} + q_v = \rho c_v \frac{\partial T}{\partial t} \tag{3.19}$$

where q_i is the heat flow in the i direction [W/m^2](i = x, y, z), λ is the rock thermal conductivity [W/(m·°C)], T is the rock temperature [°C], q_v is the heat source of volume [W/m^3], H is the stored heat per unit volume [J/m^3], ρ is the density [kg/m^3], c_v is the specific heat capacity [J/(kg·°C)].

3.3.2 Heat convection

The heat exchange due to fluid movement from one place to another is categorized as heat convection. It is dominant form of heat transfer in liquids and gases. The driving force is the temperature gradient, while heat exchange is influenced by other factors such as flow rate, surface roughness, etc. These factors can be incorporated using the heat transfer coefficient and described in Eq. (3.20).

$$q_n = h(T_s - T_e) \tag{3.20}$$

where q_n is the heat flux component normal to the boundary in the direction of the exterior normal [W/m^2], h is the convective heat-transfer coefficient [W/(m·°C)], T_s is the temperature at the surface of the solid body [°C], T_e is the temperature of the surrounding fluid [°C].

Feng et al. (2016) [61] implemented the new thermal module in FLAC3D^{plus} into the simulator using the finite volume method and implicit Euler method to incorporate heat conduction and convection between flowing fluid and solid rock formation. In this improved model, the impact of advective heat transfer and temperature on the material properties is measured distinctly. The combination of heat conduction and advection is expressed as in Eq. (3.21).

$$\lambda\frac{\partial^2 T}{\partial x^2} + \lambda\frac{\partial^2 T}{\partial y^2} + \lambda\frac{\partial^2 T}{\partial z^2} + \rho c_V v_x\frac{\partial T}{\partial x} + \rho c_V v_y\frac{\partial T}{\partial y} + \rho c_V v_z\frac{\partial T}{\partial z} + q_v = \rho c_V\frac{\partial T}{\partial t} \tag{3.21}$$

where v_i is the fluid flow velocity in the i direction [m/s] (i = x, y, z), q_v is the heat source of volume [W/m^3].

3.4 Fluid flow in rock formation (TOUGH2MP-TMVOC)

TOUGH2MP-TMVOC are massively parallel versions of TOUGH2 code, specially designed for efficient parallel simulation for multi-phase multi-component fluid flow under both isothermal and non-isothermal conditions in porous as well as in fractured media. Furthermore, the use of the TMVOC version has the added advantage of solving the problems dealing with a multi-component mixture of volatile organic chemicals in multi-dimensional heterogeneous porous media.

Gaseous, aqueous and hydrate phases generally exist in pores of hydrocarbon rock formations and obey Darcy law during flow in a porous medium. The proportion of each phase is defined as the average mole fraction in the phase over all phases in the specific zone. Therefore, the sum of all mobile phases is equal to 1.

$$\sum_\beta S_\beta = 1 \tag{3.22}$$

where S_β is the mole fraction in phase β [-], β is the mobile phase of gas, aqueous and hydrate.

The proportion of each component in these phases can be described in terms of average mole fraction and the sum of all component in all phases is equal to 1.

$$\sum_k x_\beta^k = 1 \tag{3.23}$$

where x_β^k is the mole fraction of component k in phase β [-].

In order to simplify multi-fluid flow in a porous medium, the whole model can be discretized into small blocks, as shown in Figure 3.3, using the integral finite difference method [101]. The small blocks having a sub-domain V_n in a flow system are bounded by a closed surface Γ_n. The general mass and energy balance equation can be written in integral form as Eq. (3.24) [102];

$$\frac{d}{d_t}\int_{V_n} M^k \, dV_n = \int_{\Gamma_n} F^k . n d\Gamma_n + \int_{V_n} q^k \, dV_n \tag{3.24}$$

where V_n is the volume of arbitrary subdomain in the flow system [m^3], Γ_n defines the closed surface of V_n [m^2], n is the normal vector on a surface element Γ_n pointing inward into V_n, M shows the mass or energy per volume [mol/m^3], k is the mass components or energy component, F denotes the mass or heat flux [$mol/m^2/s$], q denotes sinks and sources [$mol/m^3/s$].

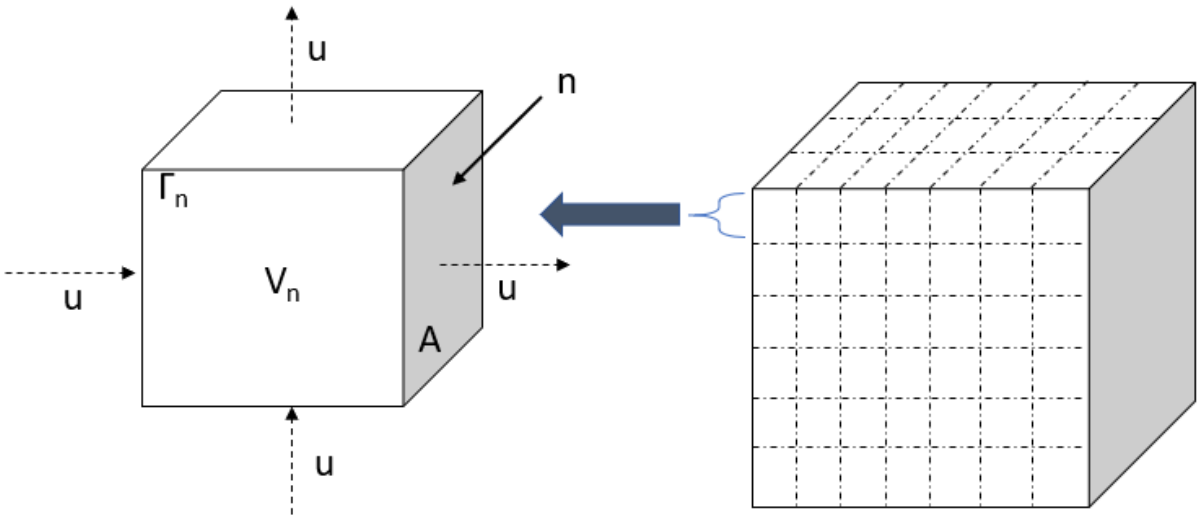

Figure 3.3 Schematic of discreate blocks

The general mass accumulation term and advection mass flux term, which are the sum of phases, can be written in Eq. (3.25) and Eq. (3.26), respectively.

$$M^k = \phi \sum_{\beta} S_\beta \rho_\beta X_\beta^k \tag{3.25}$$

$$F^k = \sum_{\beta} X_\beta^k F_\beta \tag{3.26}$$

where ϕ is the porosity [-], ρ_β is the density of phase β.

According to Darcy law, multiphase multicomponent fluid flow in fracture and reservoir is presented by fluid flow equation (Eq. (3.27)) and mass conservation equation (Eq. (3.28)).

$$F_\beta = -k \frac{k_{r\beta}\rho_\beta}{\mu_\beta} \left(\nabla p_\beta - \rho_\beta g\right) \tag{3.27}$$

$$\frac{\partial(\phi \sum_\beta S_\beta \rho_\beta x_\beta^k)}{\partial t} = -\nabla . (\sum_\beta F_\beta x_\beta^k) + q^k \tag{3.28}$$

where k is the absolute permeability [m^2], $k_{r\beta}$ is phase relative permeability [-], μ_β is phase viscosity [Pa.s], p_β phase pressure [Pa], g is gravitational acceleration [m/s^2].

The absolute permeability of phase β can be expressed using the work of Klinkenberg (1941) [103] as in Eq. (3.29).

$$k = k_\infty \left(1 + \frac{b}{p}\right) \tag{3.29}$$

where k_∞ is the permeability at infinite pressure [m^2], b is the Klinkenberg parameter [-].

Several correlations exist in the literature that defines the relative permeability and capillary pressure functions related to phase saturation. Among them, the widely accepted and used correlations for two-phase (gas and liquid) flow are Corey's relative permeability function (1954) and Van Genuchten's capillary pressure function (1980) [102].

$$k_{rl} = \hat{S}^4 \tag{3.30}$$

$$k_{rg} = (1 - \hat{S})^2 (1 - \hat{S}^2) \tag{3.31}$$

where $\hat{S} = (S_l - S_{lr}) / (1 - S_{lr} - S_{gr})$, S_{lr} is the residual liquid saturation [-], S_{gr} is the residual gas saturation [-].

$$P_{cap} = -P_o [(S^*)^{-\frac{1}{m}} - 1]^{1-m} \tag{3.32}$$

where P_o is the strength coefficient [Pa], m is the van genuchten's shape parameter [-].

The permeability of each fractured zone can be calculated using cubic law (Eq. (3.33)), as the fluid flow through the fracture plane can be treated as flow between parallel plates.

$$k = \frac{(fw)^2}{12} \tag{3.33}$$

where k denotes the fracture permeability [m^2], w corresponds to fracture width [m] and f is categorized as fracture roughness value [-].

The numerical stability needed for an efficient calculation for multiphase flow requires the dealing of flux and sink/source terms for the next time level, i.e., t^{k+1}. The time discretization results as a set of coupled non-linear equation (Eq. (3.34)).

$$R_n^{\kappa,k+1} = M_n^{\kappa,k+1} - M_n^{\kappa,k} - \frac{\Delta t}{V_n}\{\sum_m A_{nm} F_{nm}^{\kappa,k+1} + V_n q_n^{\kappa,k+1}\} = 0 \tag{3.34}$$

where $R_n^{\kappa,k+1}$ and $M_n^{\kappa,k+1}$ are the residuum and mass of component κ per unit volume in the n-th element at time $k+1$ [mol/m^3], respectively. Δt is the time step [s], A_{nm} is the cross-section area between the n-th and m-th element [m^2], $F_{nm}^{\kappa,k+1}$ is the flow term between elements at time step k+1 [mol/m^2/s], $q_n^{\kappa,k+1}$ is the sink or source term in the n-th element at time step k+1 [mol/m^3/s].

By introducing an iteration index p and expanding the residuum term of Eq. (3.34) at iteration step p+1, Eq. (3.35) is achieved. Eq. (3.34) and Eq. (3.35) are solved by Newton-Raphson iteration, which leads to Eq. (3.36).

$$R_n^{\kappa,k+1}(x_{i,p+1}) = (R)_n^{\kappa,k+1}(x_{i,p}) + \sum_i \left(\frac{\partial R_n^{\kappa,k+1}}{\partial x_i}\right)_P (x_{i,P+1} - x_{i,P}) + \cdots \ldots . = 0 \tag{3.35}$$

$$-\sum_i \left(\frac{\partial R_n^{\kappa,k+1}}{\partial x_i}\right)_P (x_{i,P+1} - x_{i,P}) = R_n^{\kappa,k+1}(x_{i,P}) \tag{3.36}$$

where $x_{i,p}$ is the value of i-th primary variable at p-th Newton-Rapshson iteration step.

3.5 Numerical study of multiple hydraulic fracturing and heat production through a fictive model

This section presents and applies the mechanism of multiple fracturing in a fictive model using FLAC3D^{plus}. In addition, stress shadow effects on subsequent hydraulic fracture geometry are analyzed. Afterward, geothermal utilization through multiple tensor fractures is analyzed using fluid flow simulator TOUGH2MP-TMVOC. The workflow of the numerical simulations is shown in Figure 3.4.

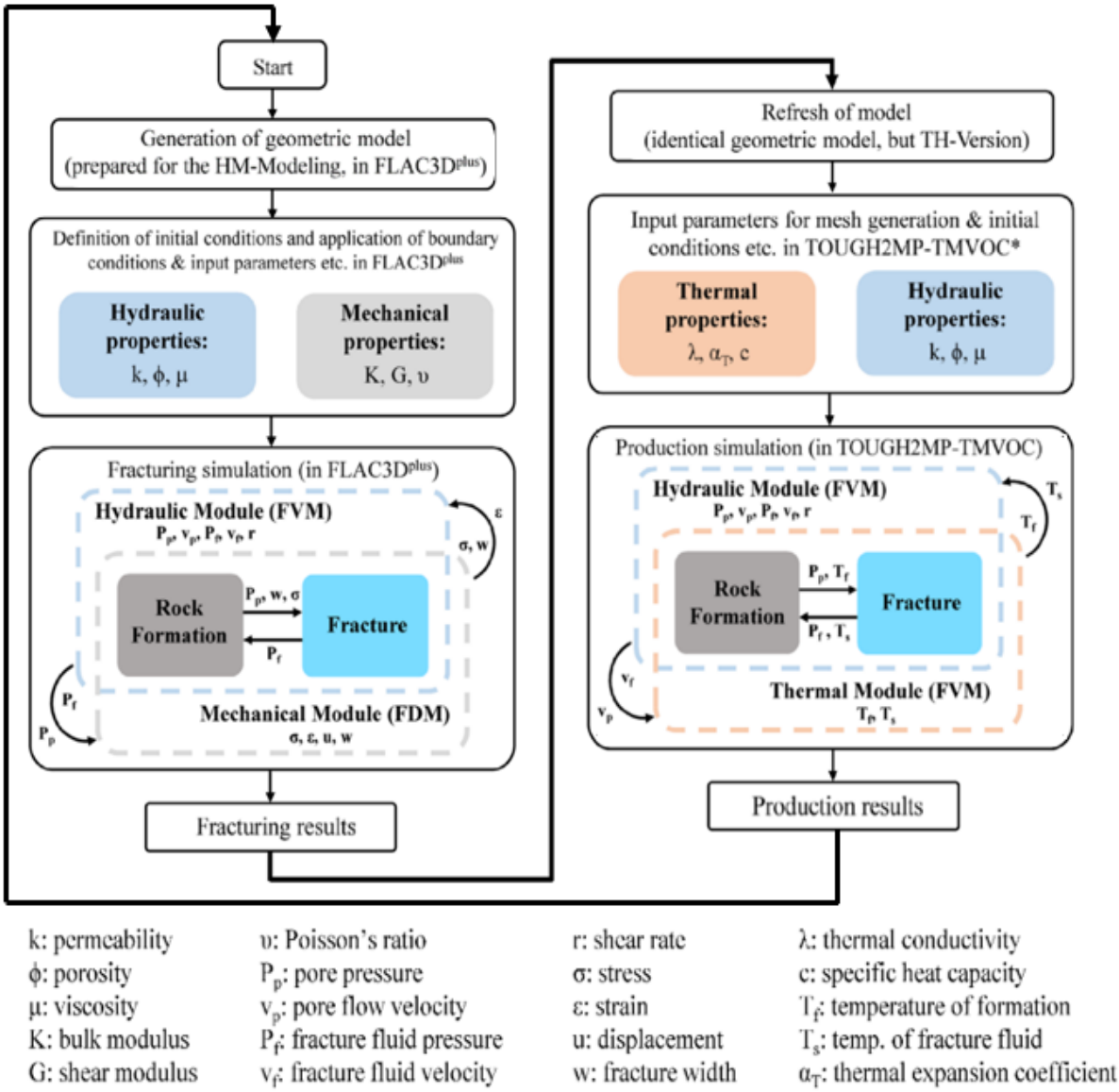

Figure 3.4 Flow chart of the computing scheme during the numerical modeling [76]

3.5.1 Fictive model generation

A fictive ½ 3D model with three rock formations is generated considering the symmetrical geological conditions as shown in Figure 3.5. The pay-zone section (sandstone) of 100 m height

is present between the cap rock (siltstone) and the basement (siltstone), having 50 m each in vertical height/thickness. The ½ 3D model has dimensions of 250 m (x) × 450 m (y) × 200 m (z) and is distributed into 105,000 rectangular elements. The cap and basement layers have very low permeability, which provides support as good hydraulic boundaries. The initial stress and pore pressure conditions are shown in Figure 3.6, while details of the mechanical and the hydraulic properties of layers are given in Table 3.1.

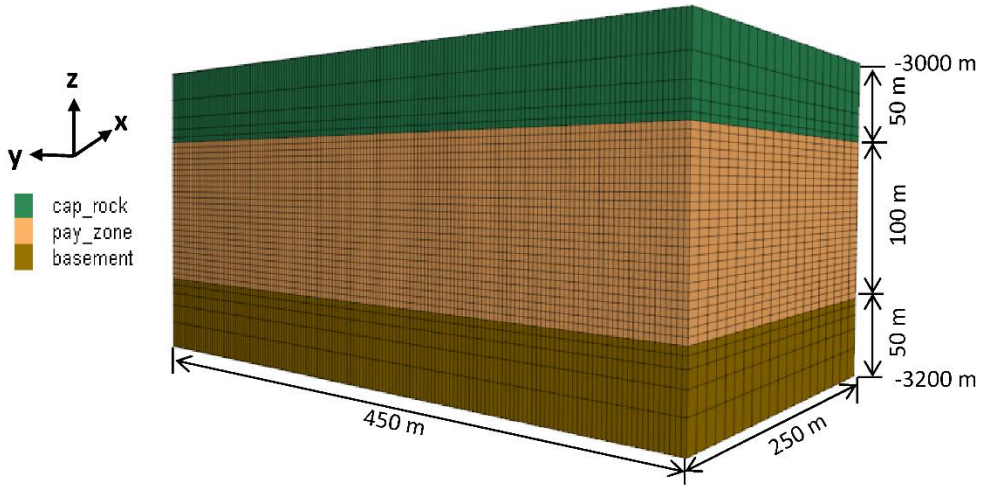

Figure 3.5 Schematic of the stratigraphy and ½ 3D geometric model of the fictive reservoir

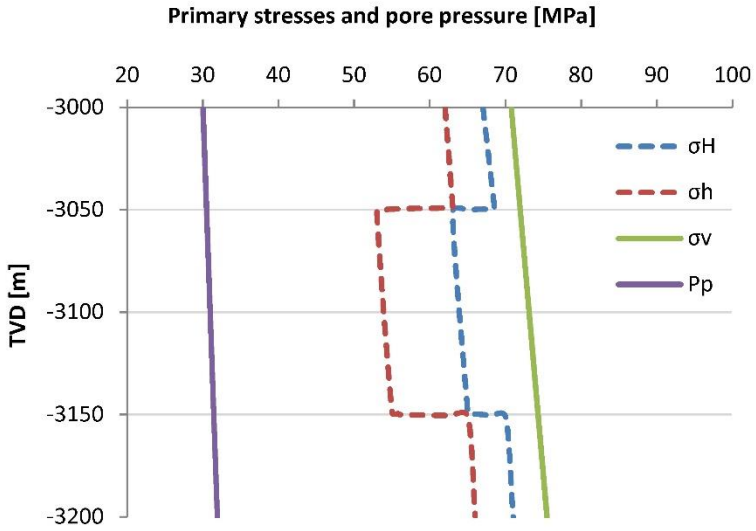

Figure 3.6 Variation of primary stress and pore pressure with depth in the fictive reservoir model

Table 3.1 Hydraulic & mechanical properties of the model

Zones	Porosity [-]	Permeability [m^2]	Density [kg/m^3]	Poisson's ratio [-]	Young's modulus [Pa]
Cap rock	0.025	1×10^{-18}	2650	0.3	2.5×10^{10}
Pay-zone	0.1	1×10^{-15}	2600	0.25	3.5×10^{10}
Basement	0.025	1×10^{-18}	2650	0.3	2.5×10^{10}

A horizontal well is located at the center of the reservoir layer at a depth of -3100 m, and the direction of the horizontal well is along with the minimum horizontal stress (along the y-axis) to facilitate the development of multiple tensile fractures. The first fracturing treatment is done at a distance of about 36 m from one side of the geometric model (Figure 3.7(a)). A fluid volume of about 650 m^3 is injected to create a fracture at a 7.2 m^3/min injection rate with a water density of 1040 kg/m^3. The initial and the final changes that occurred in minimum horizontal stress ($FLAC3D^{plus}$ uses negative (-ve) sign values for stress presentation) are shown in Figure 3.7(b) & (c). Due to the hydraulic fracturing operation, the minimum horizontal stress value has increased from 52 MPa to 66 MPa, decreasing perpendicular to the fracture surface plane and changing in the whole reservoir model. After the injection period of 90 minutes, the configuration of fracture width is shown in Figure 3.7(d). It is noticed that, due to strong hydraulic barriers of upper and lower formations, the fracture remains in the pay-zone layer having a height and half-length of 100 m.

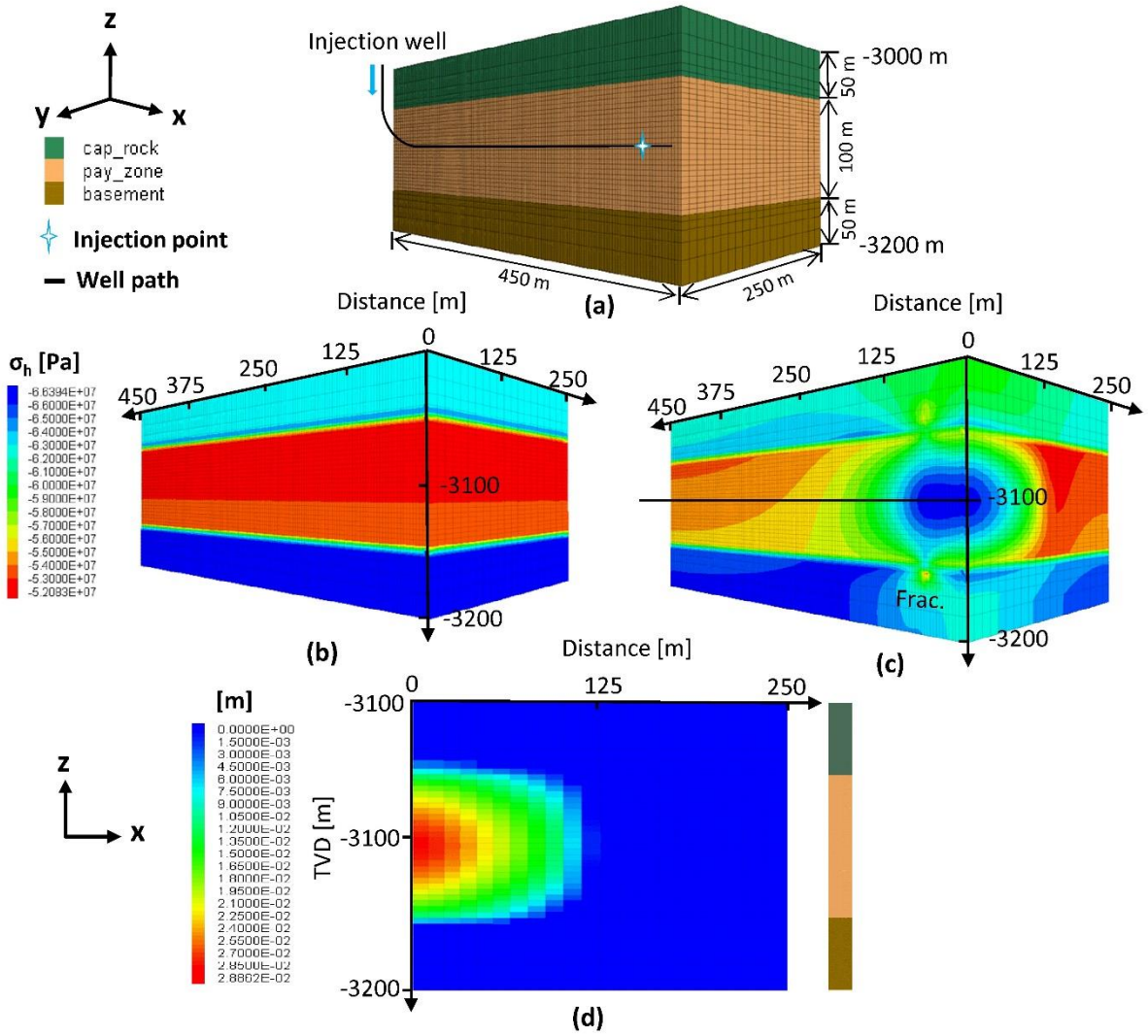

Figure 3.7 Representation of (a) injection point in horizontal well of model (b) minimum horizontal stress before hydraulic fracturing (c) minimum horizontal stress after hydraulic fracturing (d) fracture width

In order to improve the performance of multiple fractures for geothermal energy production through a horizontal well, a numerical study to investigate fracture deviation during propagation is of vital importance. After the results of the first hydraulic fracture, the further simulations are done in such a way that the changes occurred in the model after each fracture treatment (sequentially) are engaged so that the performance of multiple hydraulic fracturing under the influence of stress shadow of each subsequent fracture is analyzed. Thus, the influence of stress shadow on each fracture geometry is investigated precisely. However, an appropriate selection of fracture spacing is necessary. Normally, shorter fracture spacing is preferred due to the greater chances of higher production rate and lower horizontal well cost. According to Rossel

and Sharma [75], minimum fracture spacing for transverse fracture growth is defined beyond the S5 contour, the region with a stress reorientation angle < 5°. This approach is adopted here, and minimum fracture spacing is measured. Figure 3.8 shows the minimum horizontal stress reorientation angle at the end of the injection period at injection depth. It can be seen that the minimum fracture spacing under prevailing conditions is 52 m to acquire a denser multiple fracture system.

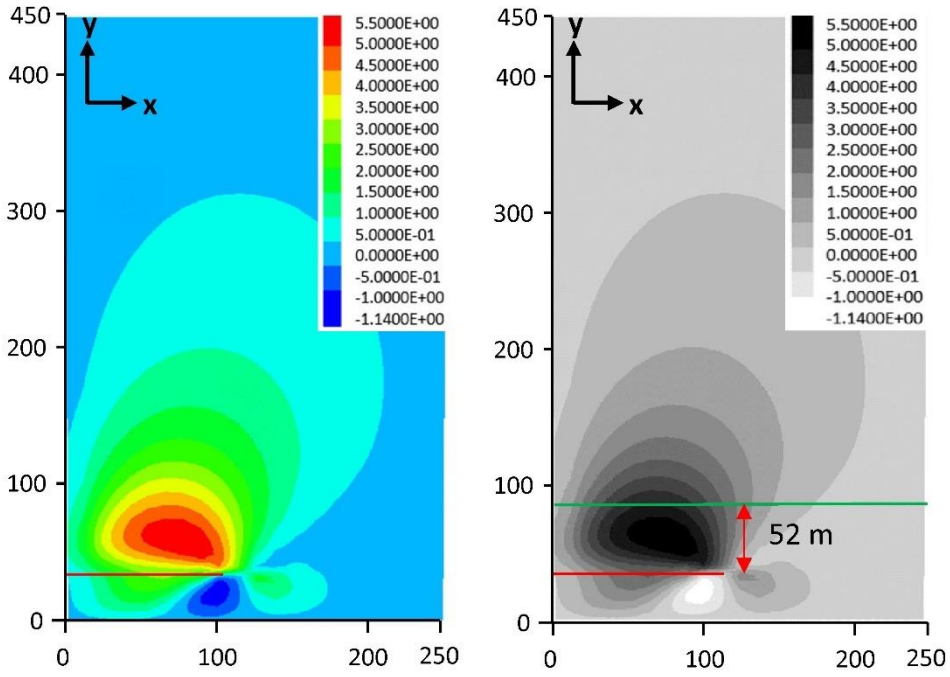

Figure 3.8 Angle of minimum principal stress reorientation at the end of injection at the injection depth (z=-3100 m). Red lines represent the position of first fracture and green line for the minimum subsequent fracture spacing

The sequential fracturing operation is conducted initially with the fracture spacing of 80 m as a base case having the same injection plan as the first created fracture in the geometric model. The corresponding configured four fracture model is shown in Figure 3.9 (a). It is observed that the length and height of each created fracture are the same, i.e., 100 m, while the difference exists in each fracture width. The minimum horizontal stress shadow at the end of four fracturing operations is presented in Figure 3.9 (c). It is clearly observed that the stress shadow interference exists among four fractures with variable intensity.

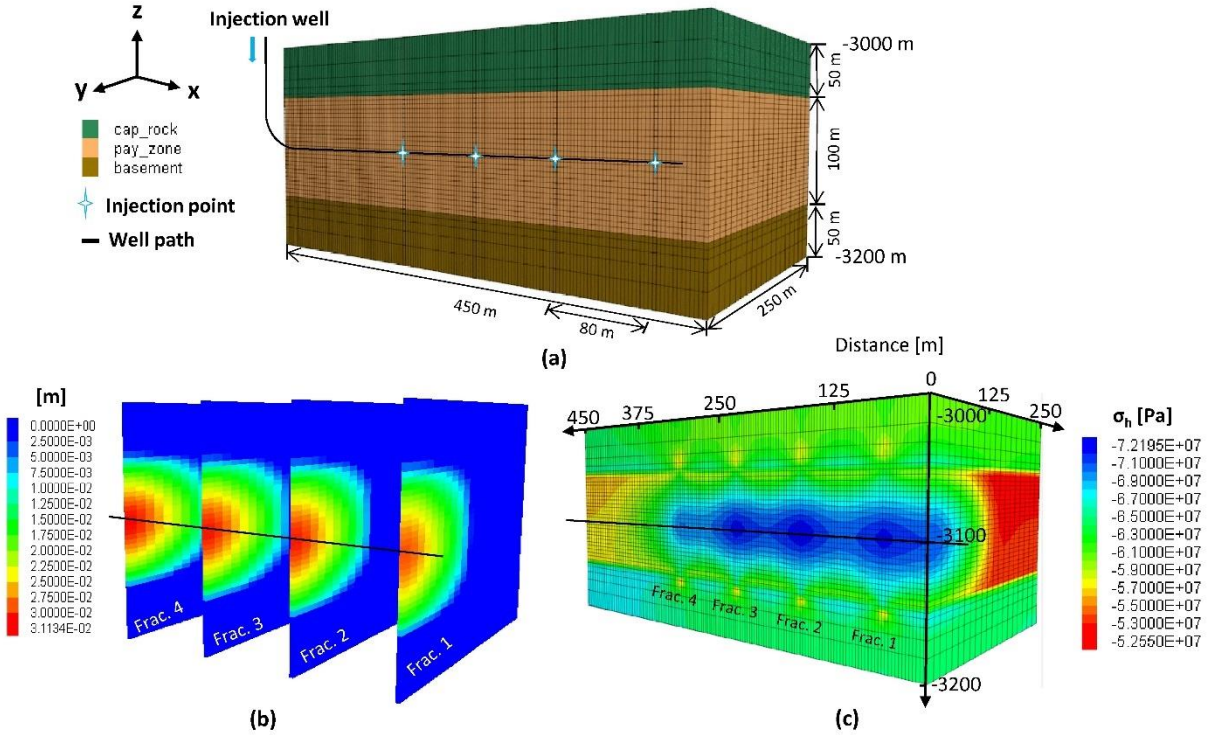

Figure 3.9 Illustration of the four created fracture results (a) ½ 3D model having four fracture planes of 80 m fracture spacing (b) fracture widths (c) minimum horizontal stress shadow (modified from Haris et al. [76])

In order to investigate the stress shadow effects on each fracture width with different fracture spacing, two simulations are conducted with 60 m and 120 m fracture spacing using the same injection strategy as of the base case, i.e., 80 m. The ½ 3D fictive model boundary and injection plan for each hydraulic fracture are also kept the same. The only difference is the spacing among fractures.

The comparative modeling results are shown in Figure 3.10. In the case of 60 m fracture spacing, it is observed that the stress shadow interference has increased, and fracture width changes radically. The results are rather opposite in the case of double fracture spacing (i.e., 120 m). The stress distribution is fair enough to reduce the stress interference effect on each fracture, and thus similar fracture geometry exists. Therefore, stress shadow has become a source of fracture width variation in a multiple fracture system.

According to cubic law, the permeability of the created fracture directly depends on fracture width. With the variation in individual fracture width, the flow conductivity of each fracture cannot be the same. This analysis is adopted in fluid flow calculations among fractures for energy production.

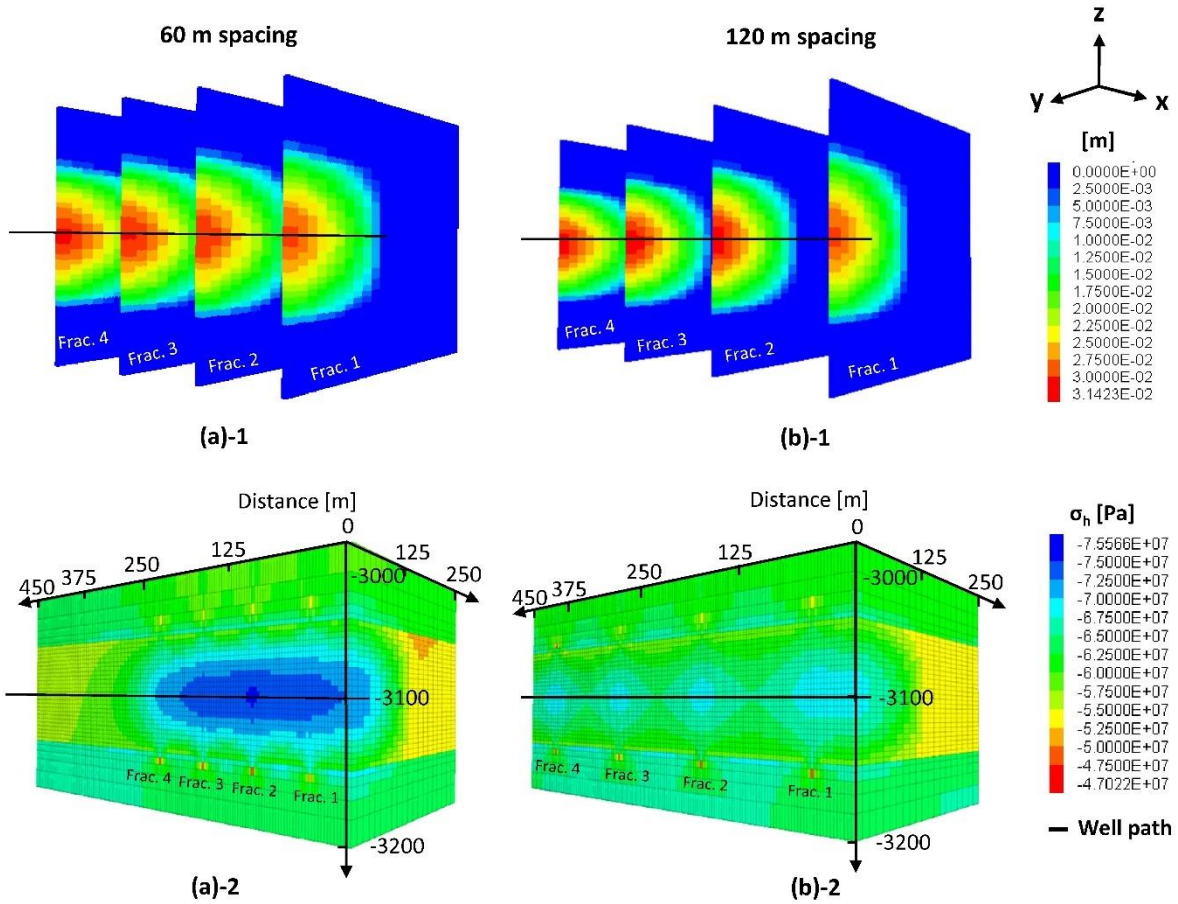

Figure 3.10 Comparison of fracture width and stress shadow based on fracturing results with fracture spacing (a) 60 m and (b) 120 m (modified from Haris et al. [76])

3.5.2 Modeling for geothermal energy production

After fracturing operations, energy production is analyzed. The model is imported to TOUGH2MP-TMVOC for heat production estimations. This approach provides benefits for accounting coupled thermo-hydro-mechanical effects in a time-efficient manner, especially in the case of multiple fracture systems. Moreover, TOUGH2MP-TMVOC provides the ability of multiphase, multi-component fluid flow through fractures and reservoir formations, facilitating the temperature and pressure-dependent enthalpy, as well [104]. A geothermal doublet system with one injection and one production well considering an innovative approach is used for energy production modeling, as shown in Figure 3.11. Single production well located at the center of fracture can provide the fluid flow from both sides of the created fracture wings, eliminating the utilization of the second production well. Moreover, the production well's connection through the center of each created fracture provides the surety of fluid flow from each fracture; thus, limiting the tendency of facing the problem of non-connected fractures to the production well.

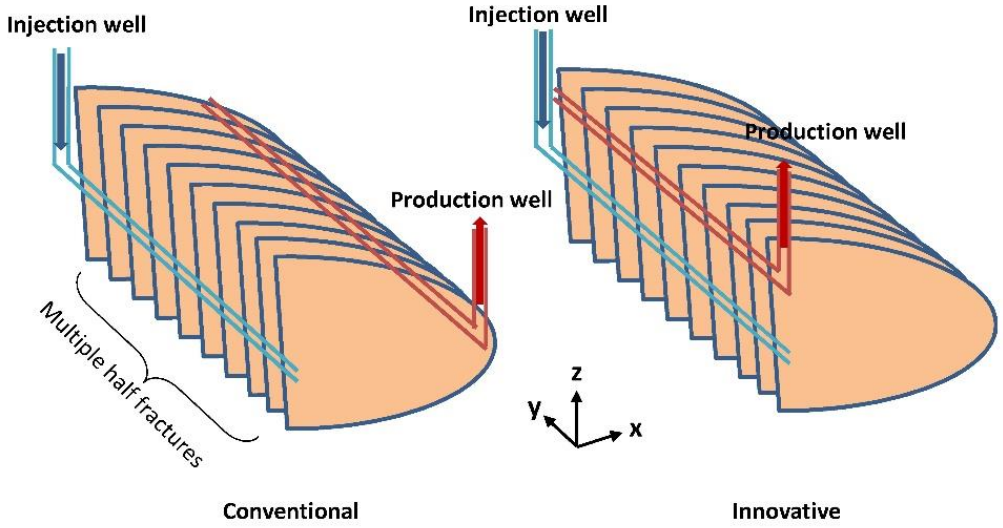

Figure 3.11 Half model of injection & production wells arrangement passing through multiple fractures (a) conventional approach (b) innovative approach

From fracturing results, each fracture zone has a height and length of 100 m. The distance between the injection and the production well in the equivalent model is 40 m (Figure 3.12). Injected fluid properties and rock parameters are provided in Table 3.2. The temperature from top to bottom of the model varies from 204 ^{o}C to 213 ^{o}C using a geothermal gradient of 0.05 ^{o}C/m with surface temperature adjustment. Furthermore, to have good fracturing conditions in the flow model, nearby zones are created along the fracture planes with smooth permeability decrease in x, y, and z directions.

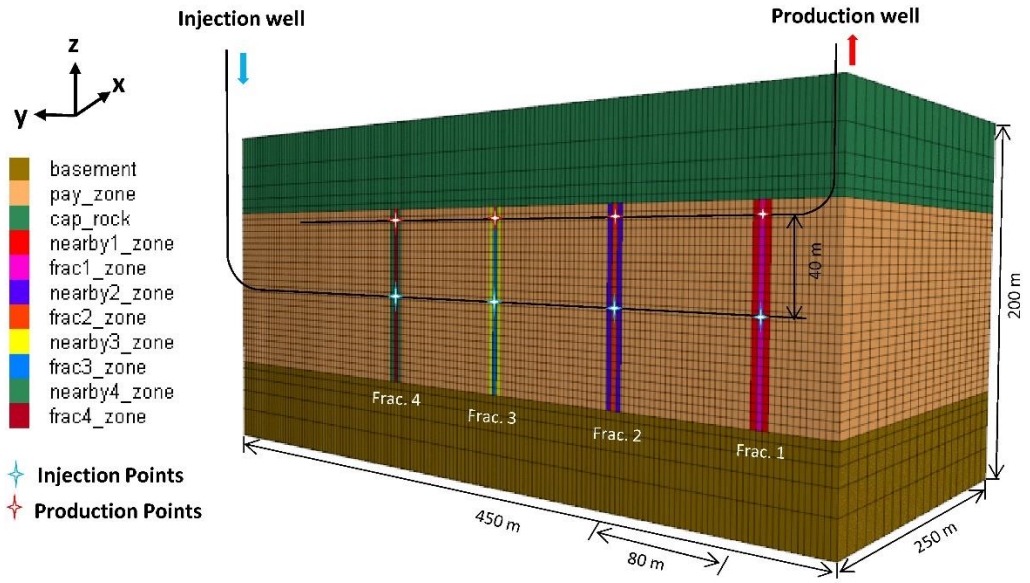

Figure 3.12 Schematic of equivalent model showing four fracture planes after fracturing in combination of injection and production wells with 80 m fracture spacing (modified from Haris et al. [76])

Table 3.2 Rock and fluid parameters

Properties	**Values**
Injected Fluid	Water
Fluid injection temperature	55 [^{o}C]
Thermal conductivity of rock formations	2.8 [W/m ^{o}C]
Specific heat of formations	965 [J/kg ^{o}C]
Bottom hole pressure of production well	30 [MP]

3.5.2.1 Case 1

Firstly, geothermal energy production results are analyzed with 80 m fracture spacing base case. Water with an injection rate of 2.5 kg/s is injected through each injection point for 20 years. The corresponding production rate and enthalpy, which fundamentally depend on the flow conductivity of individual fractures, are measured. During simulations, the production is taken against a constant bottom hole pressure, i.e., 30 MP. Figure 3.13 shows the spatial distribution of temperature variation at different times in the whole developed model. With the increase in production period, the cold fluid temperature envelope expands both inside and outside of the fracture planes due to heat conduction and convection.

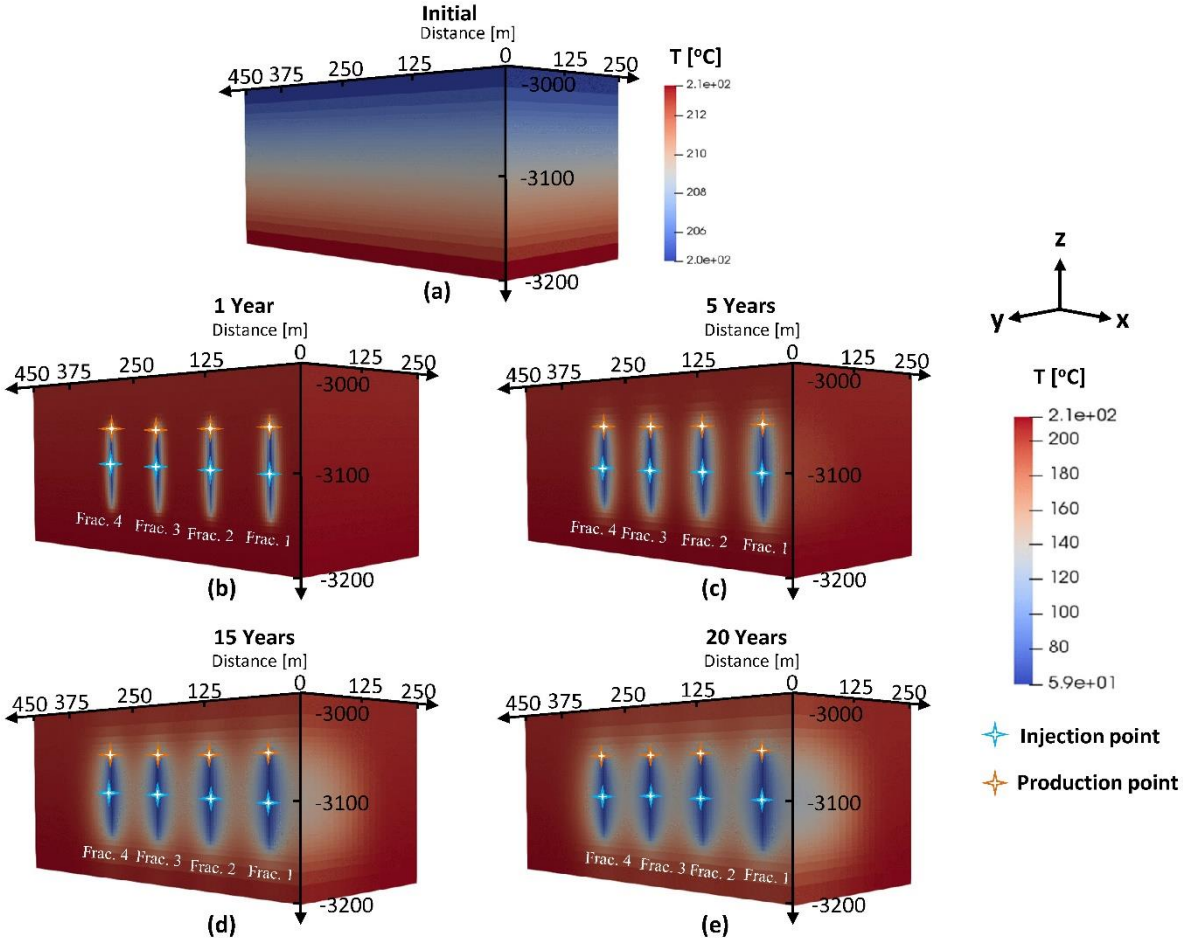

Figure 3.13 Spatial distribution of temperature variation at time (a) 0 year (b) 1 year (c) 5 years (d) 15 years and (e) 20 years of production with 80 m fracture spacing in the developed model

The temporal evolution of temperature decline in four fracture planes after 1, 5, and 20 years of production is shown in Figure 3.14. With the start of injection, the temperature near the injection perforation zones declines to 55 ^{o}C, and the reduced temperature area reaches the production point within one year of the production period. While comparing the results during 20 years of production, the lower portion of each fracture plane depletes initially, and the upper part depletes afterward. It is due to the fluid movement under the gravitational effect and higher cold water density [90]. The arrangement of injection from lower points and production from upper points provides an added advantage for harnessing energy from the lower hot section of the model.

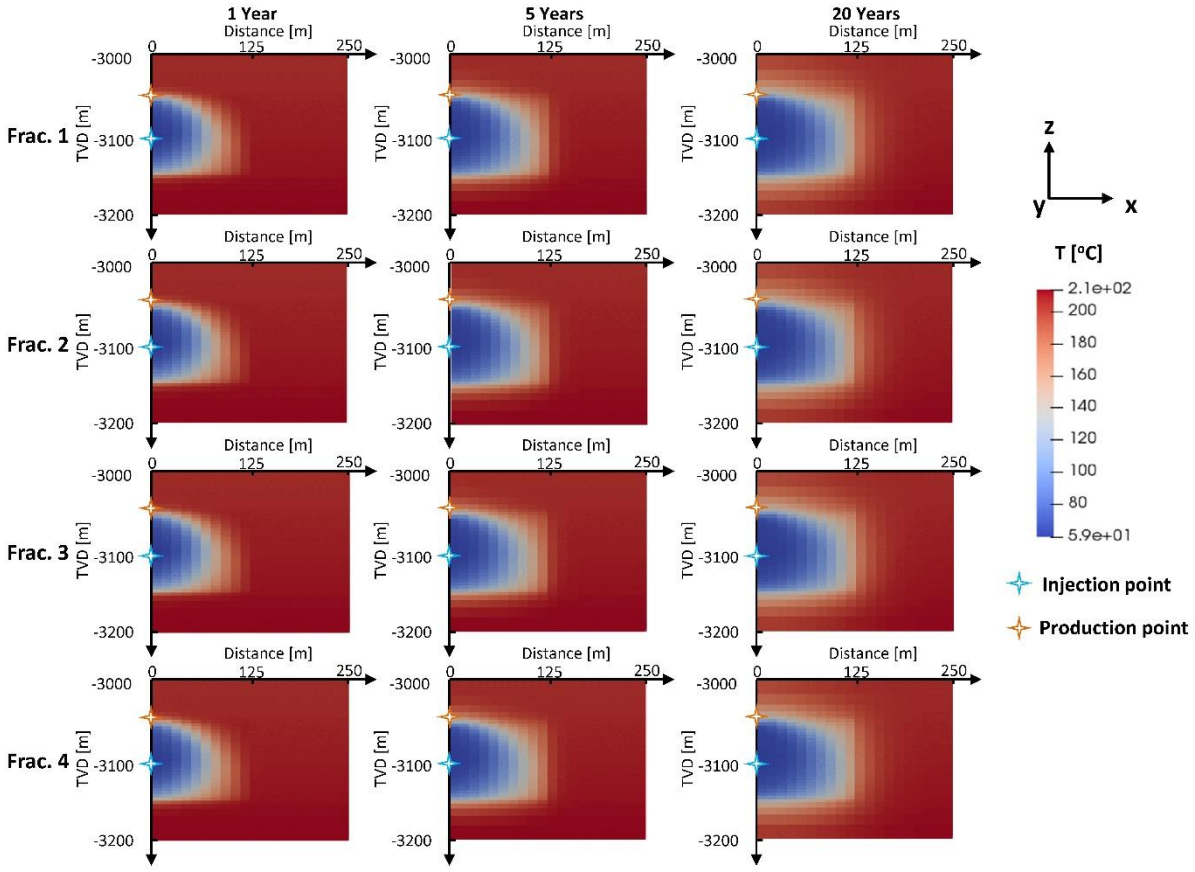

Figure 3.14 Temporal evolution of temperature decline in four fracture planes after 1, 5 and 20 years of production with 80 m fracture spacing

3.5.2.2 Case 2

Case 2 represents the energy production based on the fracturing results of 60 m fracture spacing. All four fractures have the same 100 m length and height but different fracture widths. The injection and production wells are at the same depth as in case 1.

Figure 3.15 shows the spatial distribution of temperature variation at different times in the developed model. The temperature declines in x, y, and z directions over time, while the rate of temperature decline is more between the fracture planes. The lower fracture spacing has caused more temperature decline of rock formation between the two fracture planes than the 80 m fracture spacing results (see Figure 3.13). The temporal evolution of temperature decline in four fracture planes after 1, 5, and 20 years of production with 60 m fracture spacing is shown in Figure 3.16. The temperature decline inside the fracture planes is somewhat similar to case 1 but with variable intensity.

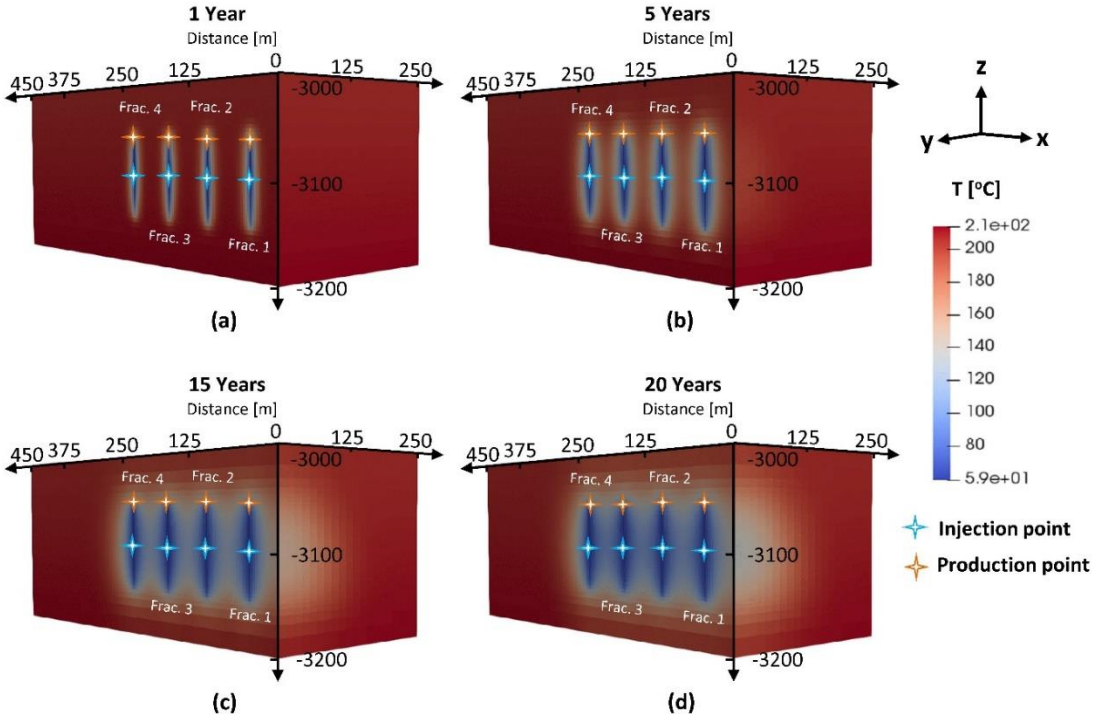

Figure 3.15 Spatial distribution of temperature variation with 60 m fracture spacing in the developed model at time (a) 1 year (b) 5 years (c) 15 years and (d) 20 years

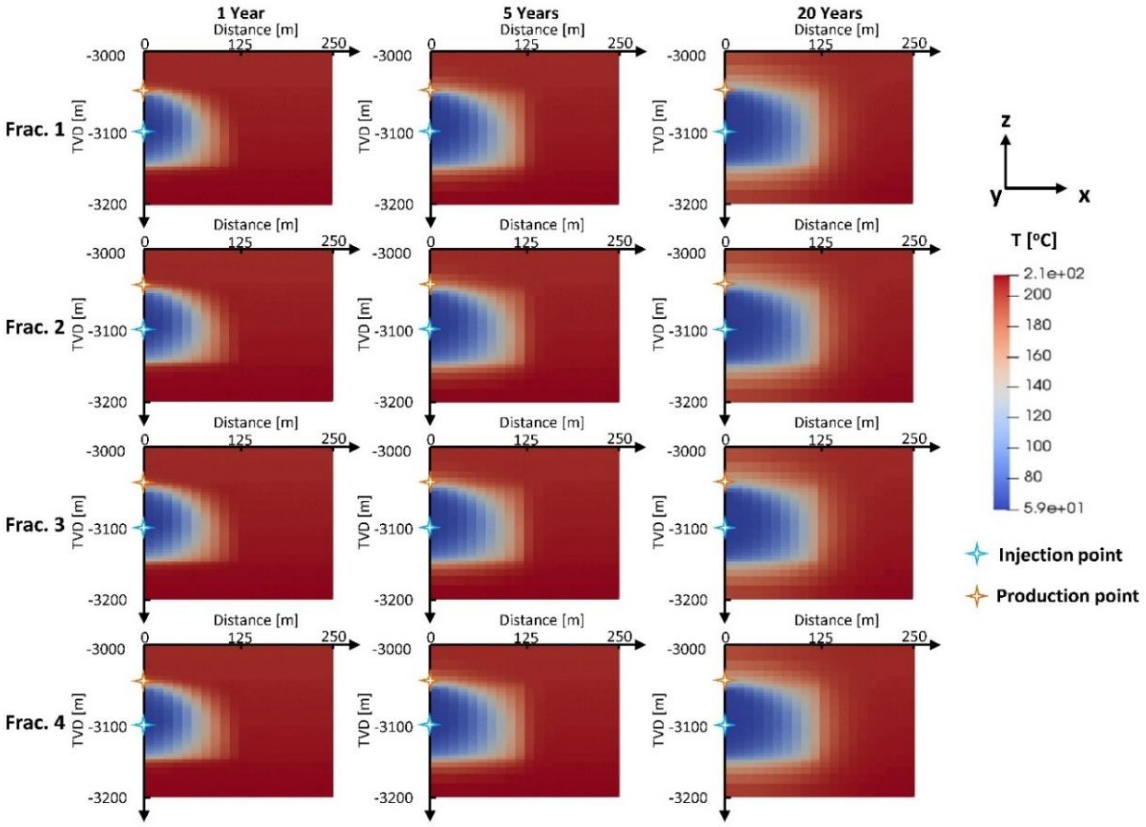

Figure 3.16 Temporal evolution of temperature decline in four fracture planes after 1, 5 and 20 years of production with 60 m fracture spacing

3.5.2.3 Case 3

Case 3 is based on fracturing results of 120 m fracture spacing where stress shadow effects are minimum, while all other geometric modeling parameters for the model are same as in case 1. Furthermore, all four fractures have the same 100 m length and height but different stress-dependent fracture widths.

The temperature reduction envelope expands with time, but due to the greater spacing among two fractures in case 3, the less temperature depletes at the middle of fracture spacing (Figure 3.17). Whereas the temperature decline inside the four fracture planes is rather similar to case 1, but with variable intensity, as shown in Figure 3.18.

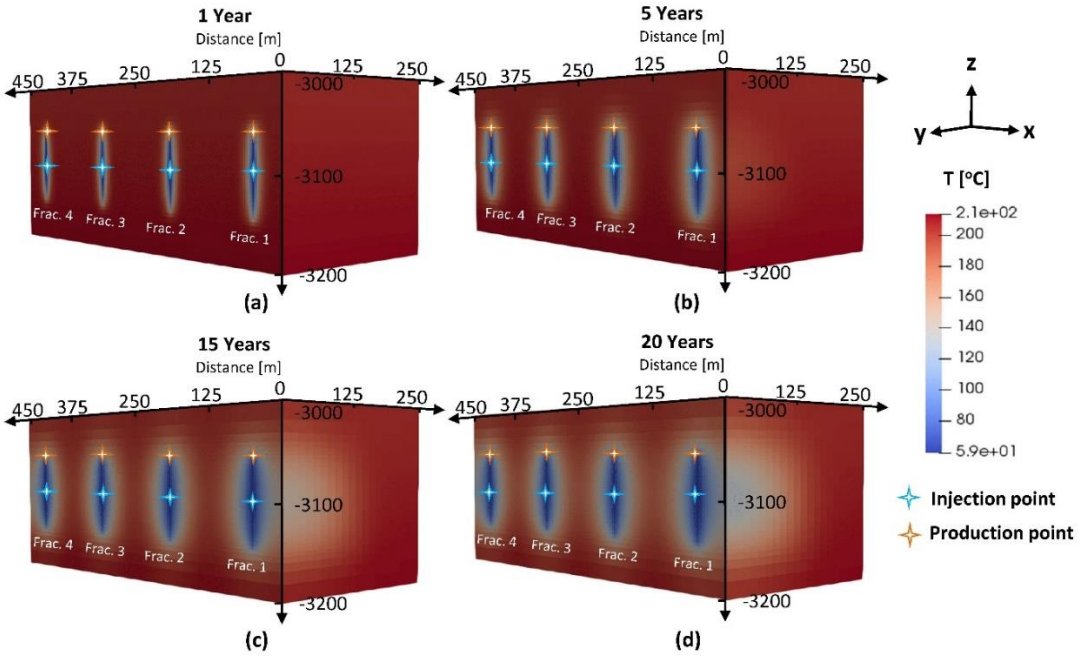

Figure 3.17 Spatial distribution of temperature variation with 120 m fracture spacing in the developed model at time (a) 1 year (b) 5 years (c) 15 years and (d) 20 years

Figure 3.19 shows the comparison of temperature decline trends within 20 years of time period in four individual fractures with different fracture spacing. It is observed that variations in temperature decline exist in fractures due to the different fracture configurations despite the same injection plan. The sharp drop in temperature at an early time is due to the short distance of only 40 m between injection and production perforation, which causes an early water breakthrough at production perforation. In case with 60 m fracture spacing, the produced fluid temperature from the first and second fracture decreases more quickly compared to the third and fourth fracture due to the large variation of fracture geometries.

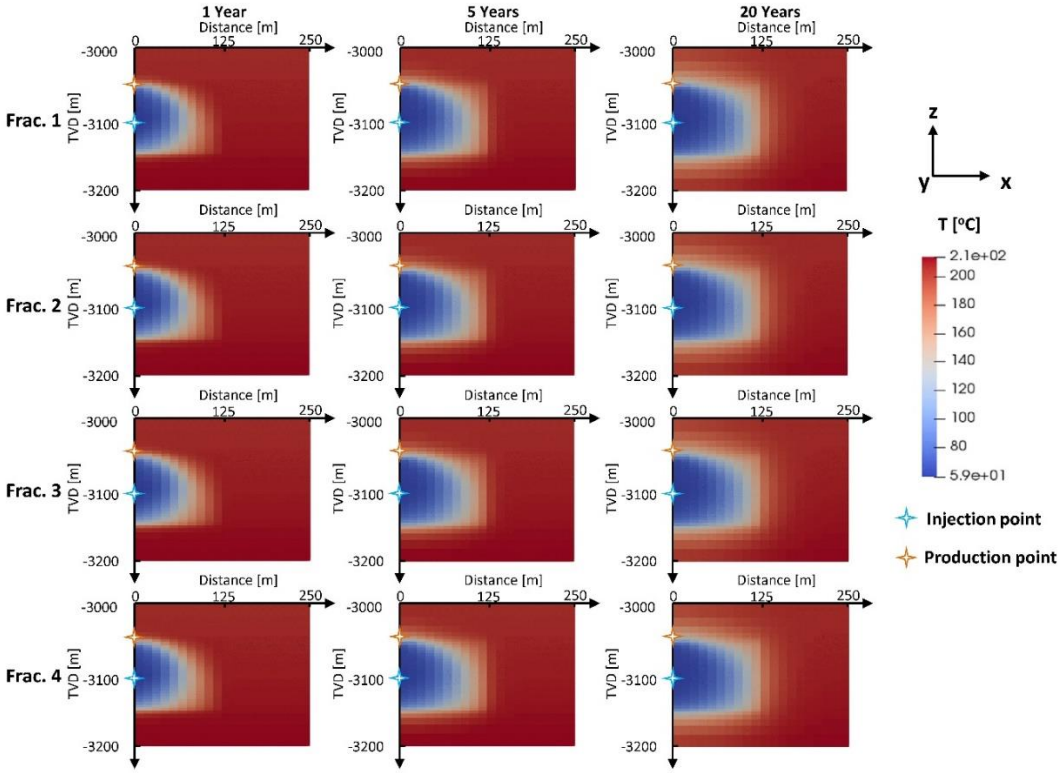

Figure 3.18 Temporal evolution of temperature decline in four fracture planes after 1, 5 and 20 years of production with 120 m fracture spacing

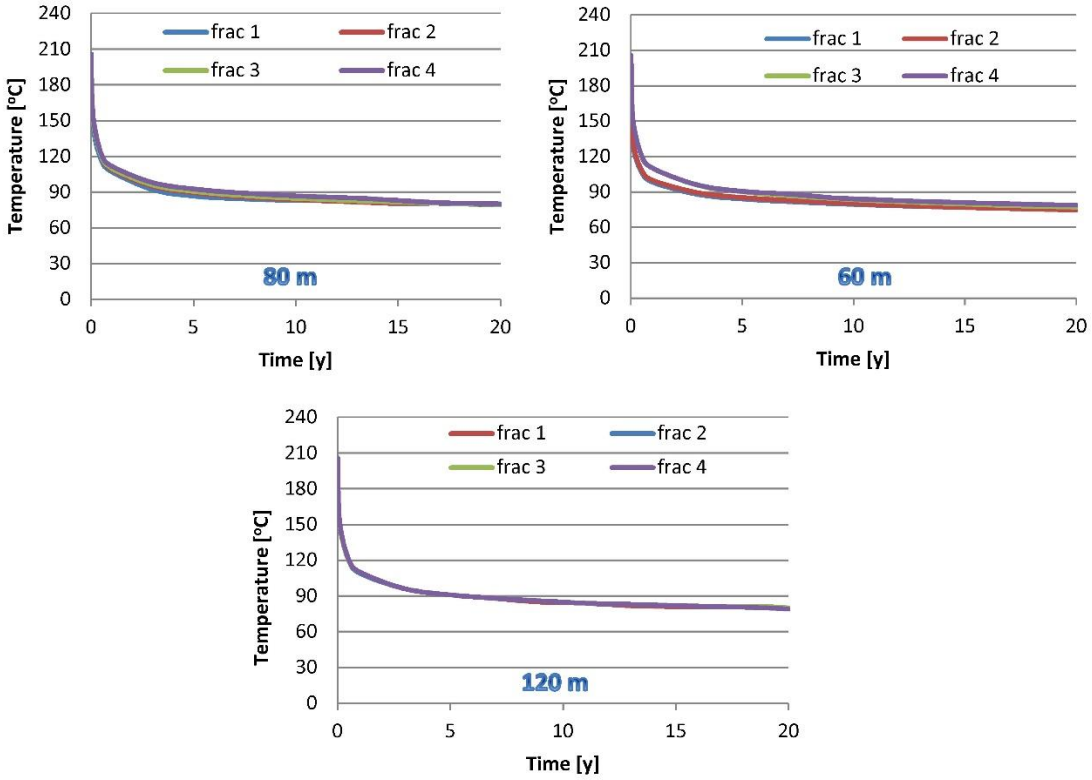

Figure 3.19 Temperature decline trends within 20 years of time period in four fractures with 60 m, 80 m and 120 m fracture spacing [76]

As the individual fracture configuration is least affected by stress shadow in the case of 120 m fracture spacing, the temperature decline is quite similar in each fracture plane. It is conceivable that the breakthrough at the production end can be delayed with the increase in distance of injection and production location.

Figure 3.20 illustrates cross-sectional views of the temperature decline in the model at injection depth of -3100 m during different times of energy production with different fracture spacing. It can be clearly observed that the temperature reduction envelope between fractures increases over time. In addition, with 120 m fracture spacing, the whole model experiences the temperature decline in an equal proportion during 20 years of production.

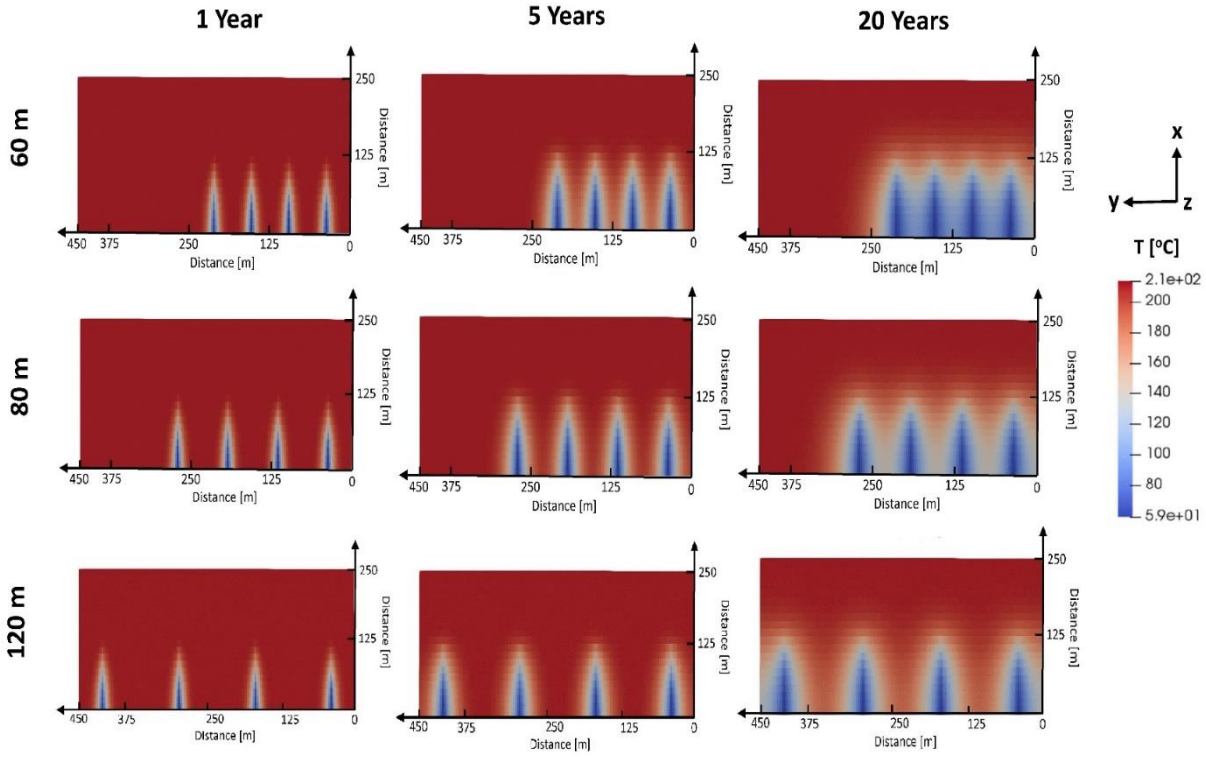

Figure 3.20 Cross-sectional view of the temperature decline inside the model at injection depth i.e. -3100 m with different fracture spacing after (a) 1 year (b) 5 years and (d) 20 years of production

3.5.2.4 Comparative analysis & discussion

This section compares the obtained energy results through numerical modeling of the fictive model with different fracture spacing. The difference in injection and production enthalpies provides a good measure of heat production through the simulated model. The produced net energy can be calculated using the following relationship [105];

$$H = q\,(h_i - h_o) \tag{3.37}$$

where q is the production rate [kg/s], h_i is the enthalpy of injected water [J/kg] and h_o is the produced fluid enthalpy [J/kg].

A comparison of net-energy contribution (%) for each fracture after 1, 5, and 20 years of production with variable spacing is illustrated in Figure 3.21. It can be seen that, with 60 m spacing, the first fracture is contributing least, while the fourth fracture is contributing maximum in terms of energy production. This trend remains the same throughout the 20 years of life span. In the case with 80 m fracture spacing, the contribution rate somewhat becomes homogenous compared to the 60 m spacing case. However, the first and second fractures are still contributing less than the third and fourth fractures. An analogous heat contribution is observed with 120 m spacing, which identifies enough spacing for homogeneous heat production through each fracture. It is observed that the unevenness of energy contribution through each fracture is amplified due to the shorter distance among fractures in the case of 60 m spacing. Furthermore, the shortcut in energy contribution in a multiple fracture system becomes more prominent with the lower fracture spacing.

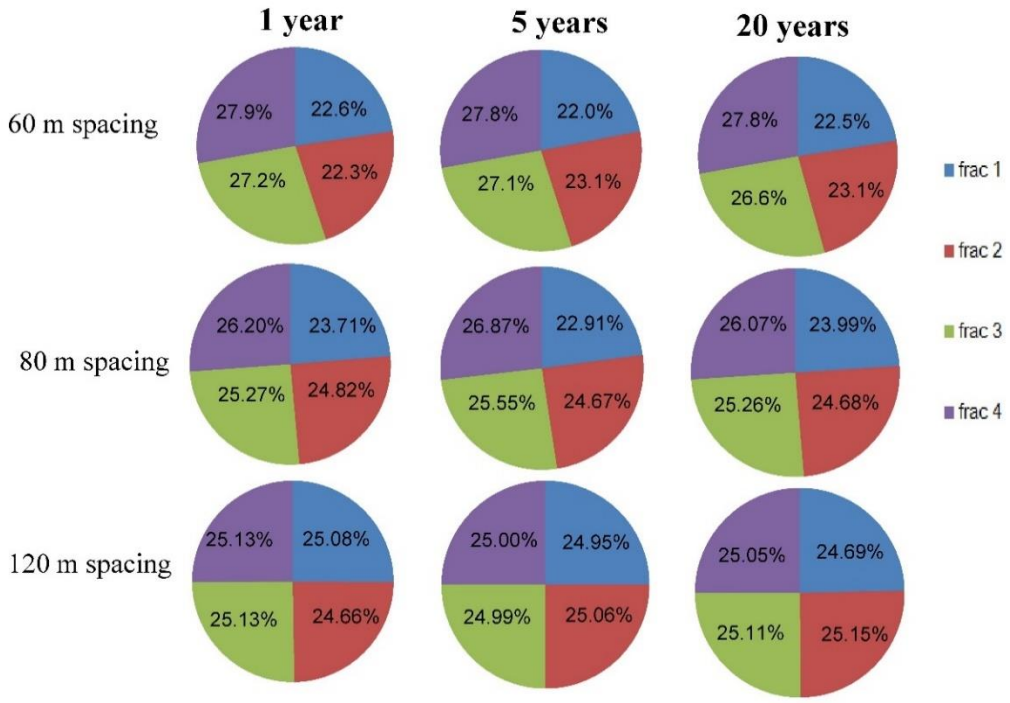

Figure 3.21 Net energy contribution (%) through each fracture after 1, 5 and 20 years of production with 60 m, 80 m and 120 m fracture spacing [76]

The rise in fluid temperature depends on the time duration it spends inside the fracture before production. If the fluid stays in fracture for a longer period, the fluid temperature rises more due to heat conduction through the hot surrounding environment. Higher fracture permeability allows fluid to flow further away from the injection point parallel to the fracture plane before reaching the producing end, absorbing more reservoir heat. The comparative results of cumulative energy produced and heat production power with time through individual fracture with different spacing are presented in Figure 3.22. In the case of 60 m spacing, fluid is produced too early without spending much time in the first and second fracture compared to the third and fourth fractures. Energy trends become closer for each fracture in the case of 80 m distance. However, 120 m spacing is quite enough to compensate the fracture's permeability variations in terms of less interference among fracture fluid flow area to contribute to heat production.

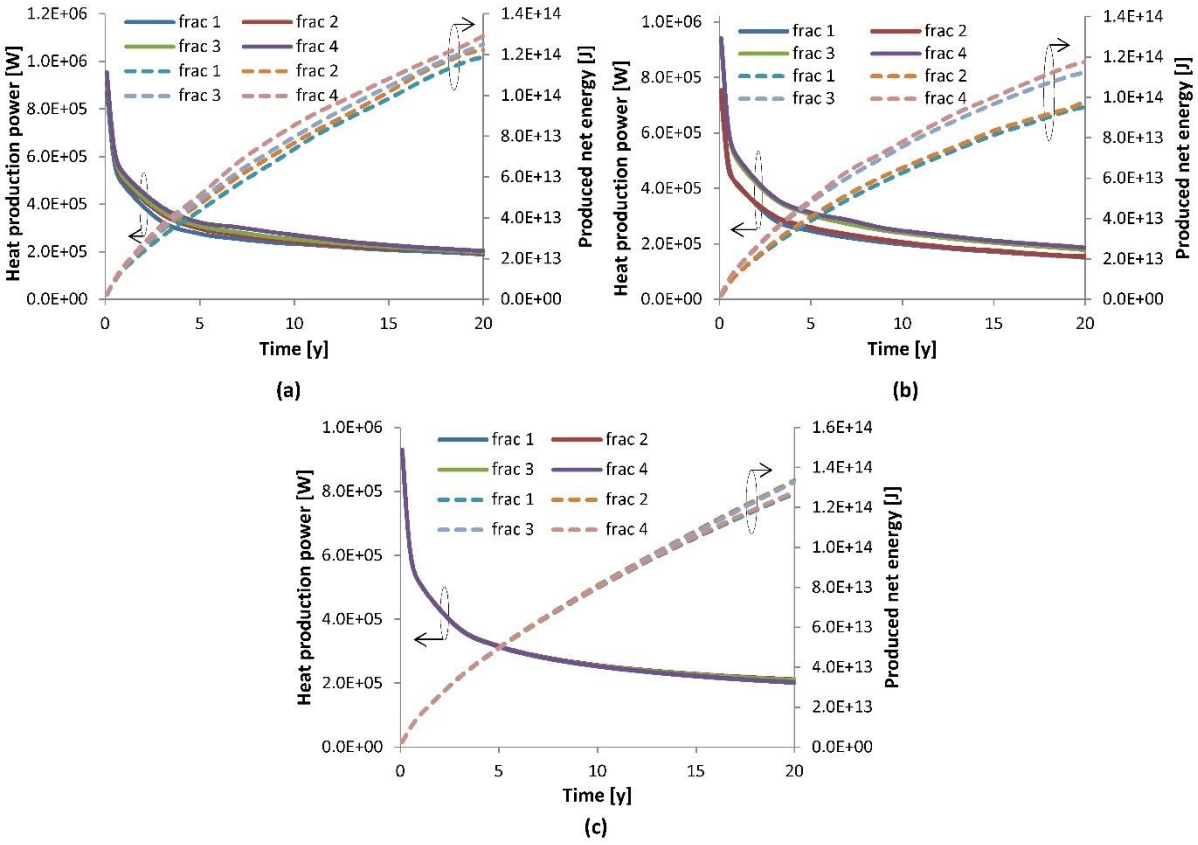

Figure 3.22 Comparative results of produced net heat and heat production power within 20 years with fracture spacing of (a) 80 m (b) 60 m and (c) 120 m [76]

Figure 3.23 shows the cumulative energy produced from combined four half fracture areas during 20 years of production with different fracture spacing. It can be seen that the rate of energy production is high at the early times of production and decreases with time due to

depletion of in-situ thermal energy. But the difference in energy contribution through multiple fractures with variable spacing remain consistent.

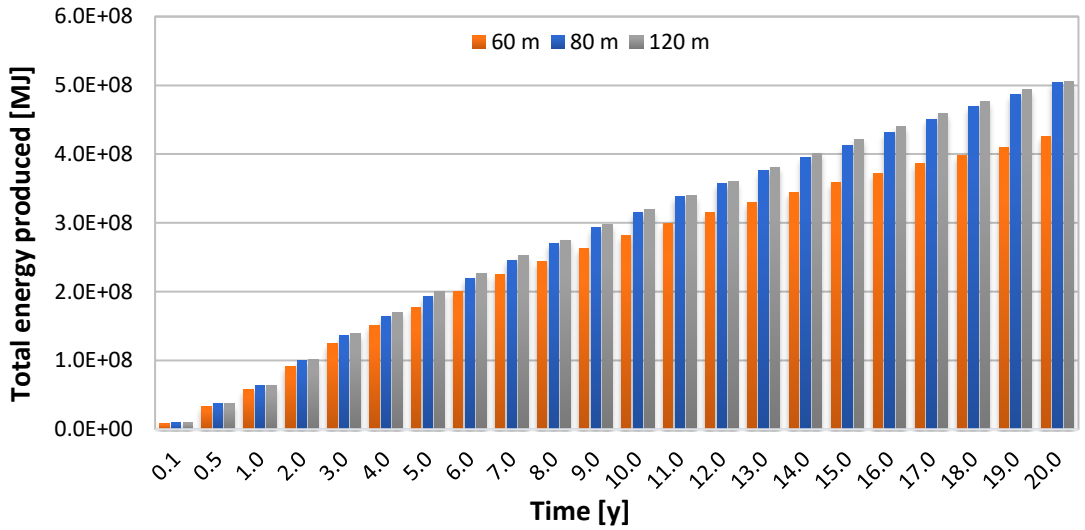

Figure 3.23 Schematic of cumulative energy produced during 20 years through combined four half fracture model with 60 m, 80 m and 120 m fracture spacing [76]

Figure 3.24 shows the total production power from combined four half fracture areas during 20 years of production with different fracture spacing. From the beginning, maximum energy is produced with 120 m fracture spacing, which corresponds to maximum thermal production power of 3.7 MW compared to 80 m and 60 m spacing, while the difference in this contribution rate becomes less till the end of 20 years of production.

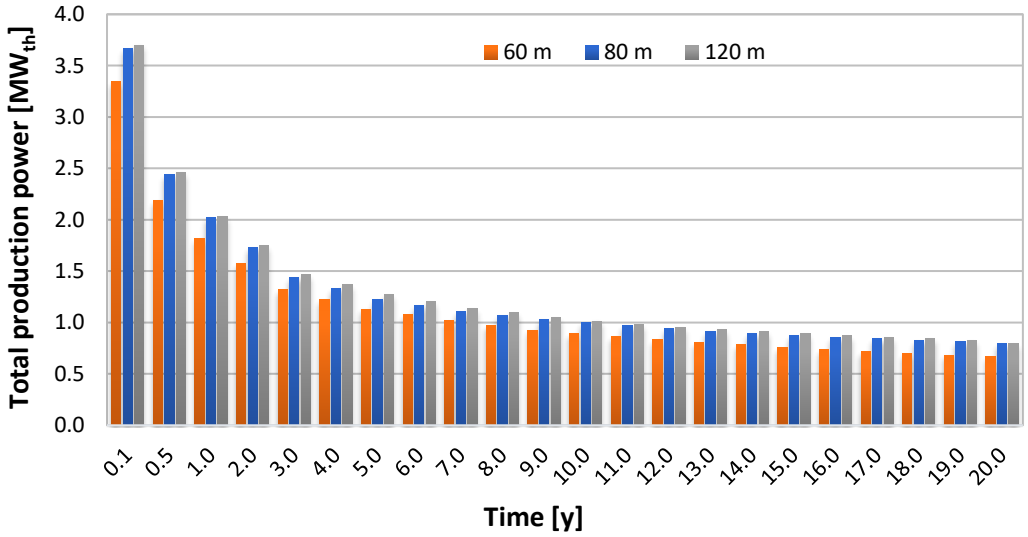

Figure 3.24 Schematic of heat production power during 20 years through combined four half fracture model with 60 m, 80 m and 120 m fracture spacing [76]

3.5.3 Impact of variable fracture area on energy production

In previous cases with 60 m, 80 m and 120 m fracture spacing, the resultant fracture length and height were same for each fracture, while stress shadow only affected the fracture widths. In this section, numerical modeling is done with variable fracture areas as their impact on geothermal energy production is still un-explained and in realistic situation, the chances of similar fracture areas are very less.

In order to investigate the impact of variable fracture areas on geothermal energy production, a fictive ½ 3D model having three rock formations is generated as shown in Figure 3.25 (a). The model dimensions are same as of previous cases and the fracture spacing is taken as 120 m. Numerical simulation of four hydraulic fracturing is conducted with same injection rate but with variable injection time for different fractures to facilitate the generation of variable fracture areas. The fluid volume of about 540 m^3, 420 m^3, 300 m^3 and 180 m^3 is injected to create first, second, third and fourth fracture, respectively. The individual fracture geometry with width is shown in Figure 3.25 (b), while the corresponding minimum horizontal stress shadow is shown in Figure 3.25 (c). All four fractures attain the available vertical height quickly and remain in pay zone due to strong upper and lower hydraulic barriers. By lowering the injection volumes, fractures having lower areas are created.

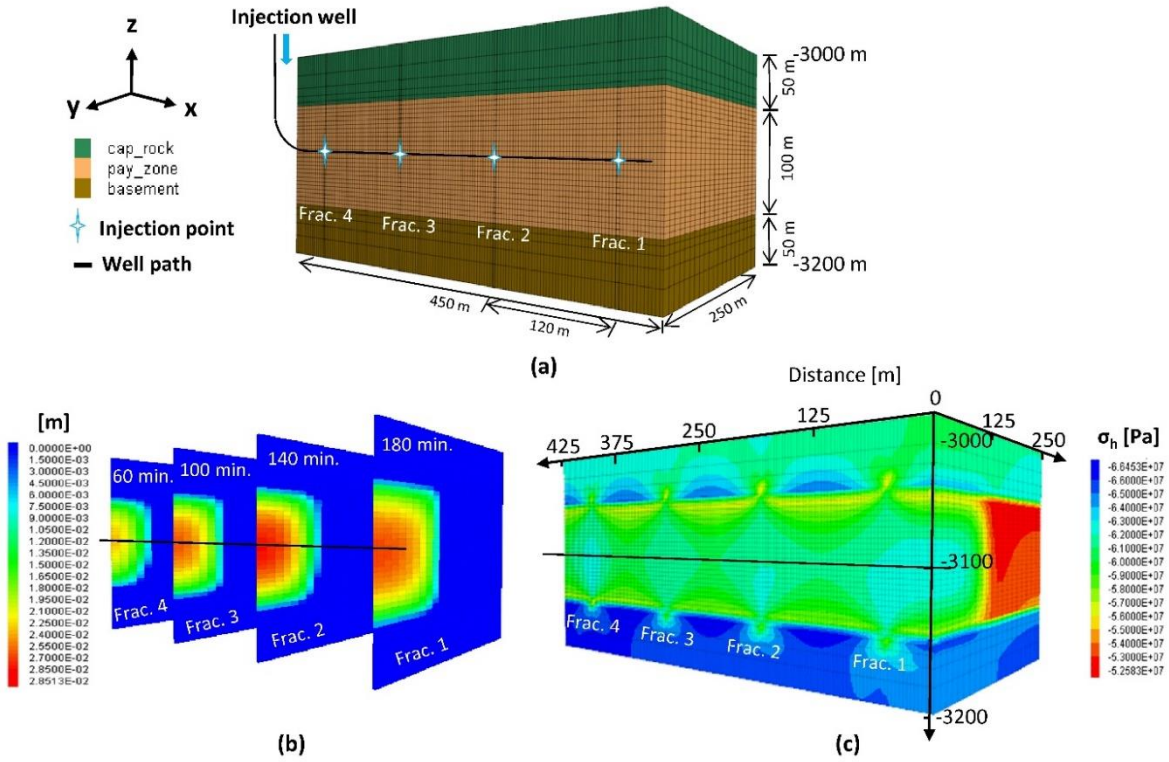

Figure 3.25 Illustration of generated fracture with (a) ½ 3D model having four fracture planes of 120 m fracture spacing (b) widths (c) minimum horizontal stress shadow.

3.5.3.1 Geothermal energy production through variable fracture areas

After obtaining fracturing results, geothermal energy production through variable fracture areas are calculated. The distance between the injection and the production well is taken as 40 m (Figure 3.26). Each fracture zone has the height of 100 m but with variable fracture half-length as shown in Figure 3.26 (b). Moreover, nearby zones are created with smooth permeability reduction in x, y and z directions along the fracture planes.

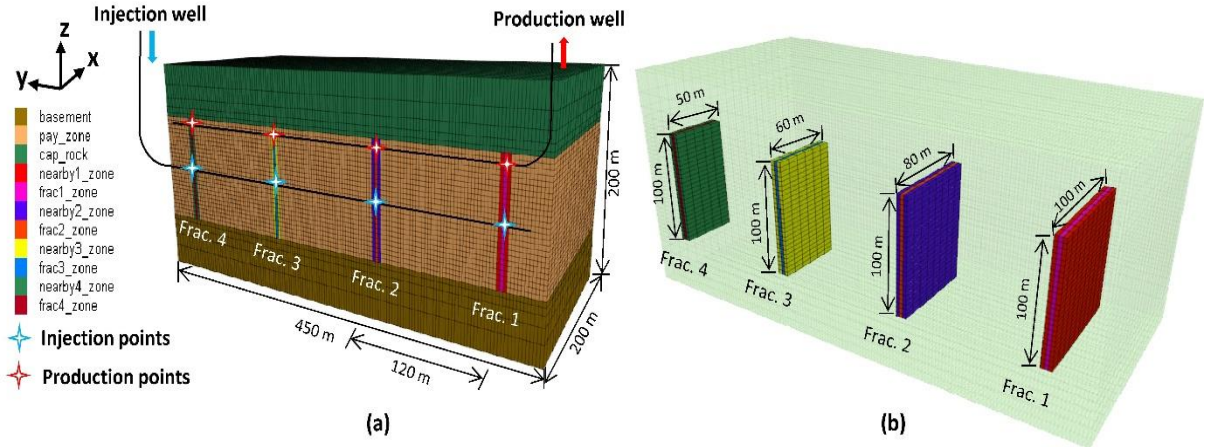

Figure 3.26 Schematic of equivalent model (a) after fracturing in combination of injection and production wells (b) having variable fracture areas

It is observed that due to variable fracture areas, all four fractures behave differentially for energy production (Figure 3.27). The first fracture being the largest one depletes more in terms of fracture area as compared to other three fracture planes. While, in fourth fracture plane having the least fracture area, the cold temperature envelope remains somewhat within the fracture plane and the smallest area around the plane depletes in comparison with other fracture planes (Figure 3.28).

Figure 3.29 (a) shows temperature decline through four fractures. As the fracture area reduces from first to fourth fracture, the rate in temperature reduction increases. The fourth fracture shows an early water breakthrough compared to other fractures. Furthermore, fluid from least fracture area is produced more quickly and spends less time in fracture. It carries low geothermal energy compared to larger fracture areas (Figure 3.29 (b)). Therefore, it is concluded that fracture area has direct impact on geothermal energy production. Larger fracture areas are required to harness maximum thermal energy from geothermal reservoir and to make a geothermal project feasible under economic constraints.

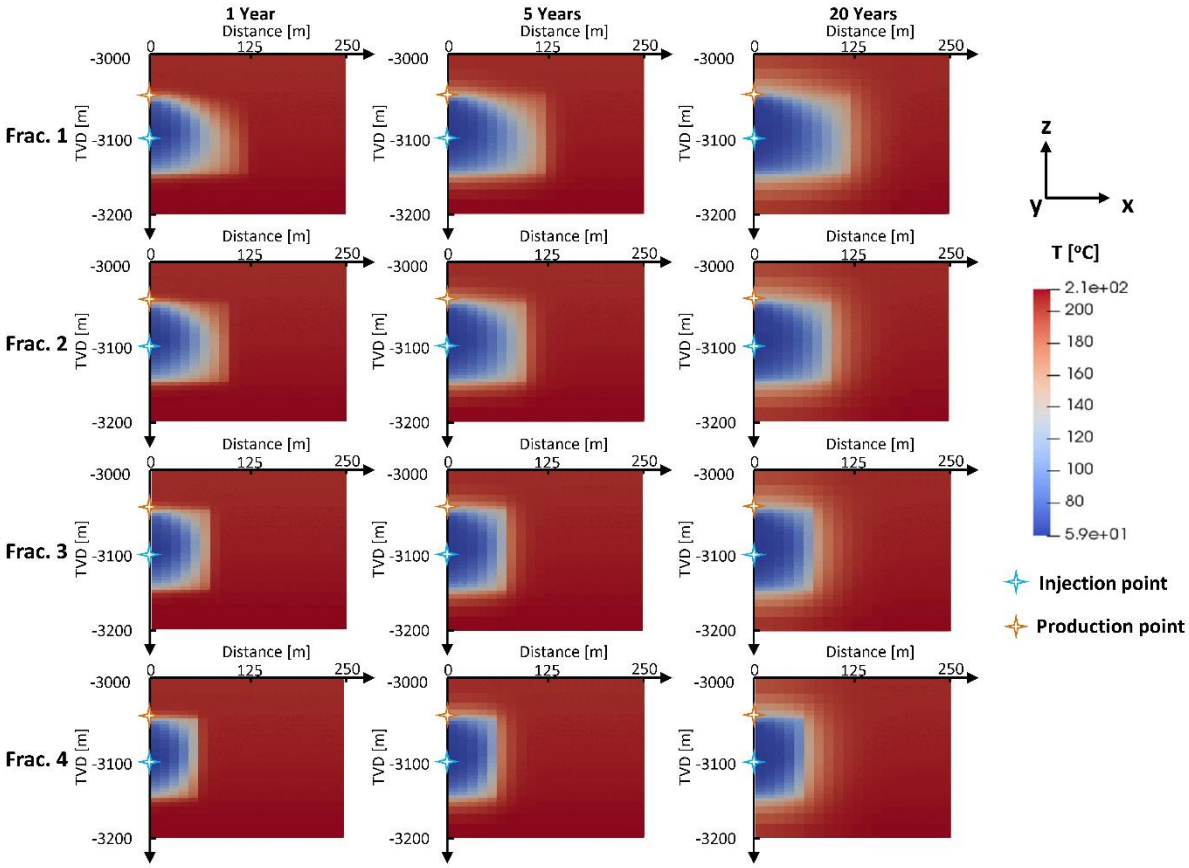

Figure 3.27 Temporal evolution of temperature decline in four fracture planes after 1, 5 and 20 years of energy production

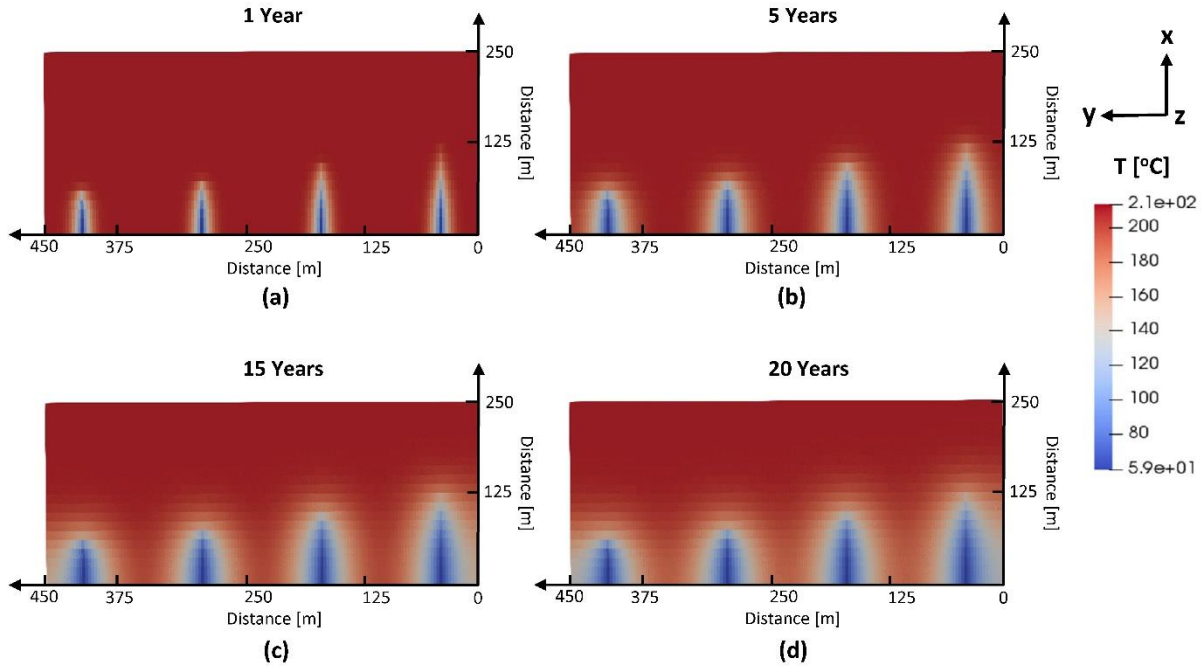

Figure 3.28 Cross-sectional view of the temperature decline in the model having variable fracture areas at injection depth i.e. -3100 m with 120 m fracture spacing after (a) 1 year (b) 5 years (c) 15 years and (d) 20 years of energy production

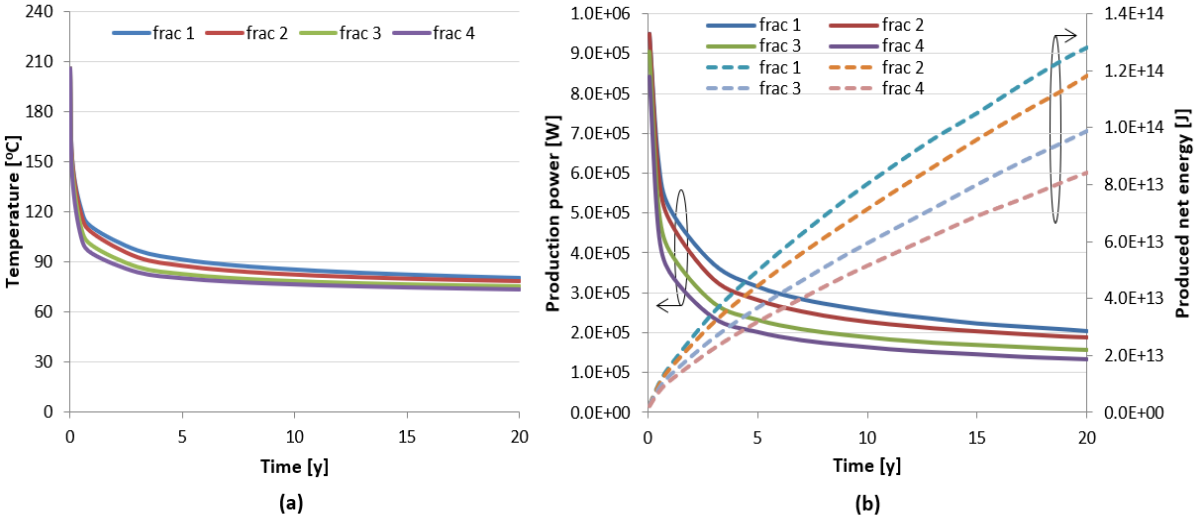

Figure 3.29 Trends of (a) temperature decline in four fractures having variable areas (b) produced net energy and heat production power

Summary

In this chapter, numerical study for heat exploitation is carried out through tight geothermal formations by employing state-of-the-art software FLAC3D^{plus}-TOUGH2MP-TMVOC. Multiple sequential hydraulic fracturing operations through horizontal well are conducted to investigate the influence of stress shadow on individual fracture geometry by adopting different

fracture spacing cases. The fracturing results show that fracture spacing has significant effect on the final configuration of individual fractures. With the decrease in fracture spacing, stress shadow effect is significant, which ultimately changes the fracture width and fluid flow performance. However, this effect is considerably reduced with the increase in fracture spacing. Afterward, multiple fracturing results are used for heat production simulations. By adopting an innovative approach with a single production well that passes through the center of each fracture, heat from both sides of fracture wings can be produced. In addition, this well arrangement provides the confirmation of each fracture connection to the production well. However, due to differences in individual fracture geometry, the energy contribution through multiple fractures is not equal even though the injection plan for each case is the same. An earlier and sharp decline in production temperature for each fracture is observed due to small fracture areas and less distance between the injection and production wells, i.e., 40 m. It is pragmatic that the distance between injection and production wells can set the time for a thermal breakthrough at producing end.

The analysis of fluid flow through variable fracture areas shows low energy contribution from lower fracture areas. Higher production temperature and energy contribution is observed as the fracture area increases. Therefore, larger stimulated fracture areas are required for higher energy production. The assumption of considering similar fracture shapes and widths for energy production from multiple fracture system without analyzing stress dependent fracture's configuration may lead to erroneous results.

The fictive model study having multiple hydraulic fractures is conducted with small fracture areas having maximum half-lengths and heights of 100 m. The stress shadow effects are unknown for gigantic multiple fracturing operations as large quantities of fluid may need to be injected for massive multiple hydraulic fracturing. The further analysis has been carried out in the next chapter.

4 Geothermal exploitation through massive multiple hydraulic fractures; a case study of a geothermal field in the North German Basin (MHH-GeneSys)

Geothermal resources in Germany are limited to intermediate and low enthalpy ranges. The total geothermal resources available to generate electricity have been estimated at 2100 EJ (1 EJ = 1 x 10^{18} J). In addition, these resources are bound to petrothermal reservoirs (about 96 %), faults (about 4 %), and hydrothermal resources (about 1 %). However, the exploitation of hydrothermal reservoirs has been more successful than petrothermal reservoirs so far [106]. In addition, more than 180 geothermal installations are in operation for direct heat utilization that has cumulative heat production of about 1259.9 GWh [27]. In Germany, significant geological settings for geothermal energy are found in the Upper Rhine Graben, the North German Basin (NGB), and the South German Molasse Basin, as shown in Figure 4.1. The Upper Muschelkalk and Bunter formations in the Upper Rhine Graben, Mesozoic sandstone units in the NGB, and the Malm in the South German Molasse Basin have been identified as noteworthy geothermal potential horizons [107, 108].

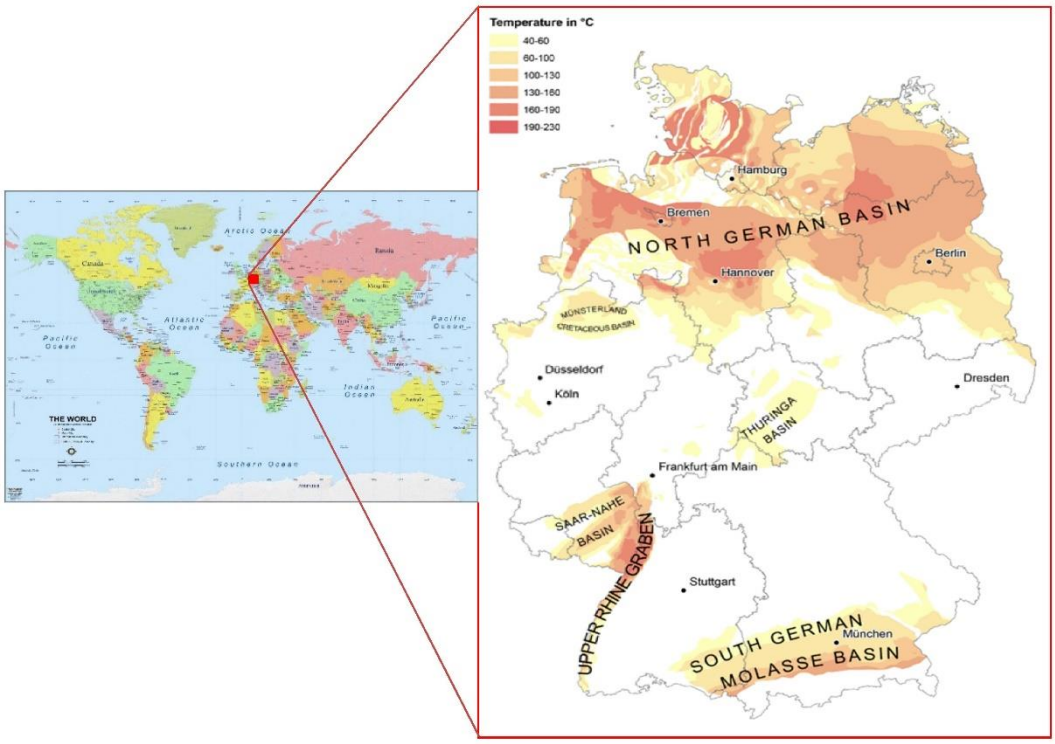

Figure 4.1 Regions and temperature ranges of hydrothermal resources in Germany (adapted and modified from Suchi et al. [109])

The geothermal potential of the NGB has been estimated more than 13000 EJ as heat in place. However, it has been exploited by few localities so far [106]. In the 1980s, several wells were drilled in the NGB to utilize deep hot water resources at different locations (e.g., Waren, Neustadt-Glewe, etc.). Since 1995, the Neustadt-Glewe geothermal plant had been used for heat production, but in 2003 it was converted into combined heat and power system with an installed working capacity of 0.2 MW_{el}. This plant is considered a pilot electricity generation plant from a low enthalpy reservoir in Germany. However, due to low working capacity and economic reasons, the power production was shut down in 2012 [26, 110]. Currently, different power plants such as Dürrhaar, Insheim, Kirchstockach, Traunreut, Sauerlach, and Taufkirchen are in operation with variable working capacity in different basins of Germany [111].

Among other renewable energy resources, Geothermal energy has a significant role in making the environment "greener," and Germany is expanding its energy transition capability towards geothermal energy production. Figure 4.2 (a) shows the installed capacity and annual production of major geothermal fields operating in Germany, while Figure 4.2 (b) shows the maximum operating flow rates. Primary uses of produced energy vary from electricity generation to district heating based on the working capacity and temperature of the produced fluid. The installed capacity for electricity generation through geothermal power has been increased from 6 MW to 37 MW during 2010-2019. At the same time, annual production has been increased from 23 GWh to 168 GWh (Figure 2 (c)). Based on these statistics, it is conceivable that the role of geothermal energy production and especially for electricity generation will be quite dynamic in the future.

In this chapter, a comprehensive investigation of heat and electricity production through a geothermal region in Hannover (Germany) has been performed by conducting massive multiple hydraulic fracturing operations through a horizontal well using the field data of the GeneSys EGS project. Moreover, the performance optimization through configured fractures geometries for energy contribution is analyzed. The case study has been performed well with the help of post-developed numerical simulators FLAC3D^{plus} and TOUGH2MP-TMVOC.

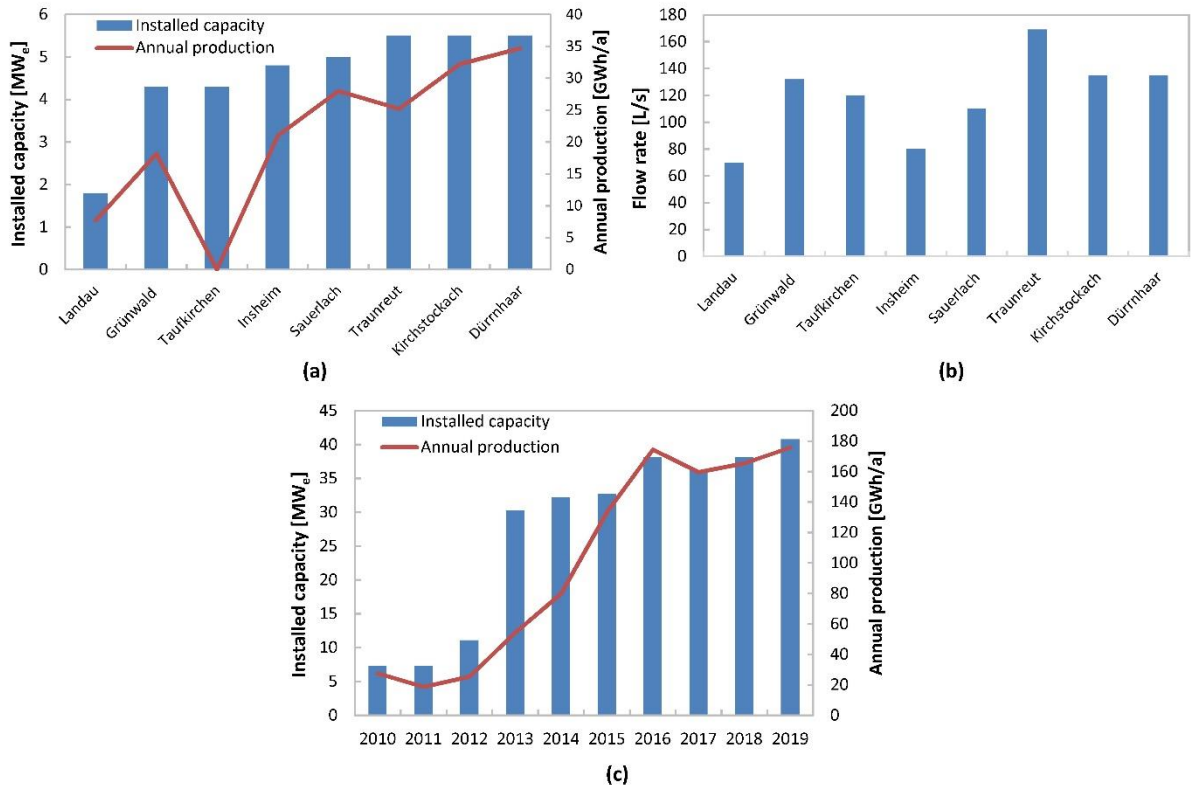

Figure 4.2 Geothermal power statics in Germany (a) installed capacity & annual production of major geothermal fields in year-2019 (b) operational flow rate in different fields (c) cumulative generation capacity & production during 2010-2019

4.1 Overview of the EGS project – (GeneSys)

The EGS project- GeneSys is located in the North German Basin Hannover area with moderate temperatures ranging from 130 ^{o}C to 190 ^{o}C. The GeneSys project was started after the successful results obtained from the initial test well in the nearby area "Horstburg" under similar subsurface geological conditions, where massive fracturing operation was performed using fresh water due to the existence of low permeable sedimentary formations. The experience of the Horstburg project gave the confidence to use fresh water alone for massive hydraulic fracture in the GeneSys project as well. In this geothermal project, a single borehole was used to obtain the geothermal energy from the sedimentary rock formations. The stratigraphic sequence along with the temperature gradient is shown in Figure 4.3.

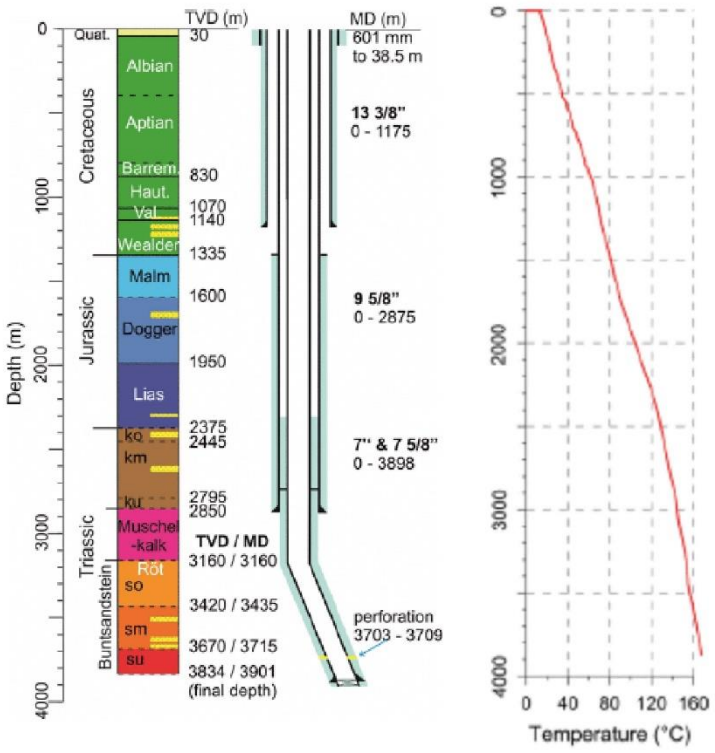

Figure 4.3 Geological profile, well completion and formation temperature of the GeneSys borehole [112]

The purpose of this project was to produce 2 MW thermal energy to fulfill the energy requirement of surrounding residents. A massive single hydraulic fracturing operation was performed on the targeted formation of Buntsandstein at a depth of -3660 m by injecting 20,000 m^3 of fresh water carrying no proppant to acquire the fracture area of 1.1 km^2. The whole fracturing operation was performed in 5 days with several injection pauses. Several tests were also performed to check stress levels and fracture development, and it was found that the fracture had retained its high conductivity without any proppant usage [111-112]. In addition, no large magnitude of seismic event was recorded. After six months of shut-in, a significant amount of water was recovered with low production rate. However, regained water was oversaturated with salt at surface conditions and high-temperature reduction caused the formation of a salt plug inside the tubing due to cooling-induced precipitation. One year later, the salt plug was removed using the coil tubing technique; however, high temperature reduction and extreme water salinity were major reasons for project breakdown (Figure 4.4). Therefore, geothermal exploitation through the GeneSys EGS using a single well with low flow rates could not provide acceptable results [112].

Figure 4.4 Local media of Hanover reported that the Genesys geothermal facility had ceased operation, with the title "Geothermal energy project in Hanover put on hold". briefly stated as: At the Stilleweg in Groß-Buchholz, 20 million euros have been buried – Because salt clogs the borehole, the geothermal project cannot be continued

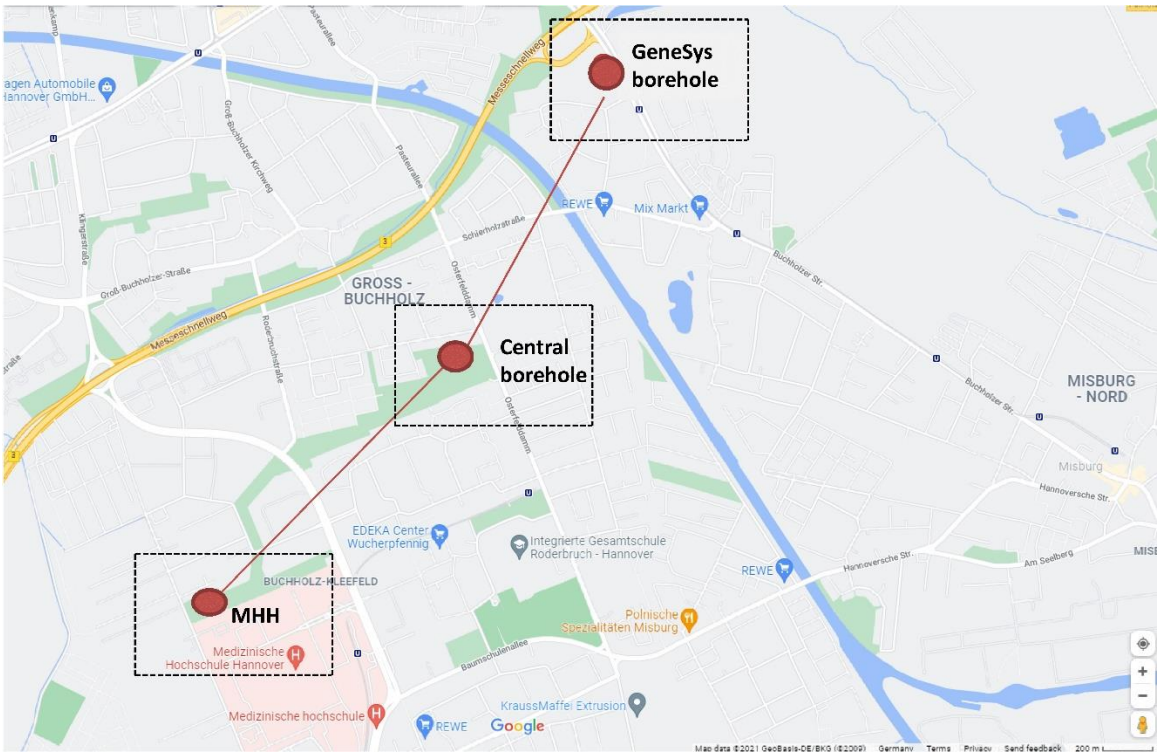

Figure 4.5 Overview of an innovative project area in Hannover (MHH-GeneSys-EGS)

In this case study, an enhanced geothermal system for a region in Hannover MHH-GeneSys is proposed to integrate heat and electricity production, as shown in Figure 4.5. Furthermore, geothermal exploitation from multi-well multi-fracture systems can solve the salt production problem due to the continuous circulation of fluid. Using the engineering data of the GeneSys project, a single hydraulic fracture is created to verify the simulated model firstly. Afterward, the state-of-the-art software FLAC3D^{plus} and TOUGH2MP-TMVOC are used to design the gigantic multi-fracture schemes in this particular area while considering stress superposition effects. Correspondingly, the heat extraction performance for heat and electricity production is evaluated.

4.1.1 Model generation and parameters

The true representation of the reservoir model is depicted by the actual prevailing geological and strati-graphical conditions. The reservoir consists of several layers of sandstone formations sandwiched between rock salt formations. Considering symmetrical geological state, a ¼ 3D model is generated that lies at a depth between -3287 m and -4100 m and discretizes into 36,520 rectangular blocks having dimensions of 1300 m (x) × 100 m (y) × 813 m (z), respectively (Figure 4.6). The injection perforation is located at a depth of -3660 m in volpriehausen-sandstone formation, while the temperature of the model varies according to the geothermal gradient of 0.03 °C/m. The mechanical and hydraulic parameters of rocks and fluid are presented in Table 4.1 and Table 4.2. Furthermore, the three-dimensional stresses at initial conditions are shown in Figure 4.7.

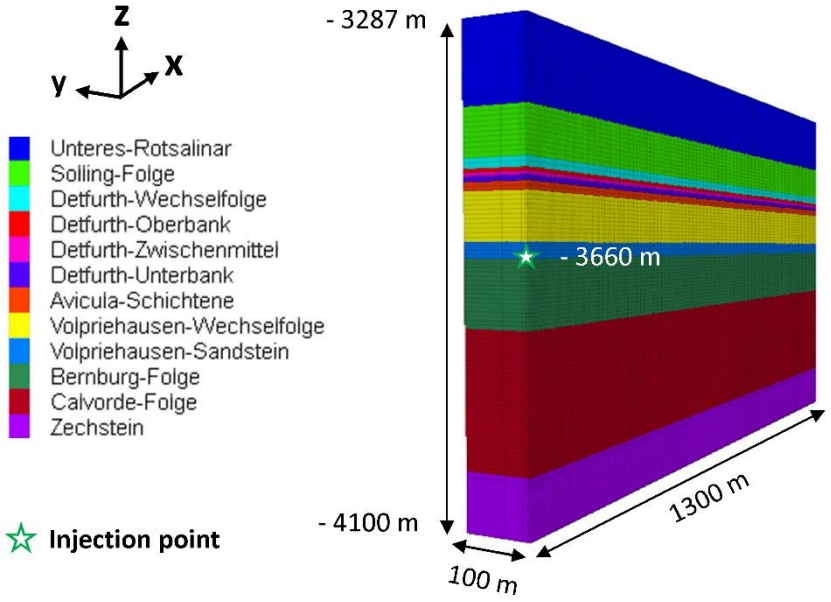

Figure 4.6 Schematic of ½ 3D reservoir model along with stratigraphy

Table 4.1 Mechanical parameters of the model [114]

Depth (top)	**Layer**	**Density, ρ**	**Young Modulus, E**	**Poisson ratio, v**	**Bulk Modulus, K**	**Shear Modulus, G**	**Tensile strength, σ_t**	**Tectonic stress, σ_{tec}**
		[g/cm^3]	**[GPa]**	**[-]**	**[GPa]**	**[GPa]**	**[MPa]**	**[MPa]**
-3287	Unteres Rötsalinar	2.19	39.15	0.226	23.84	15.96	0.5	0
-3424	Solling-Folge	2.71	33.55	0.236	21.20	13.57	2.61	25.3
-3504	Detfurth Wechselfolge	2.72	46.11	0.228	28.21	18.78	2.61	
-3521	Detfurth-Oberbank	2.72	59.08	0.220	35.15	23.21	2.61	25.3
-3527	Detfurth-Zwishcnmittel	2.71	70.92	0.207	40.40	19.37	2.61	25.3
-3533	Detfurth-Unterbank	2.69	55.35	0.200	30.72	23.07	2.61	25.3
-3542	Avicula-Schichten	2.67	65.38	0.215	38.17	26.92	2.61	25.3
-3556	Volpriehausen-Wechselfolge	2.71	63.90	0.222	38.34	26.14	2.61	25.3
-3636	Volpriehausen-Sandstein	2.70	61.83	0.213	35.89	25.49	2.61	25.3
-3662	Bernburg-Folge	2.72	64.09	0.225	38.87	26.16	2.61	25.3

-3773	Calvörde-Folge	2.72	64.09	0.232	39.90	26.01	2.61	25.3
-4000	Zechstein	2.25	39.15	0.226	23.84	15.96	0.5	0

Table 4.2 Hydraulic parameters of the model [114]

Depth (top)	**Layer**	**Permeability, k (x, y, z)**	**Porosity, ϕ**	**Viscosity, μ**	**Biot coefficient horizontal, α_h**	**Biot coefficient vertical, α_v**
		[m^2]	**[%]**	**[Pa/s]**	**[-]**	**[-]**
-3287	Unteres Rötsalinar	1.00^{-21}	10.0	0.001	0.0	0.0
-3424	Solling-Folge	2.00^{-17}	11.4	0.001	0.6	0.6
-3504	Detfurth Wechselfolge	2.00^{-17}	9.7	0.001	0.6	0.6
-3521	Detfurth-Oberbank	1.02^{-16}	7.9	0.001	0.6	0.6
-3527	Detfurth-Zwishcnmittel	2.04^{-16}	6.7	0.001	0.6	0.6
-3533	Detfurth-Unterbank	2.00^{-17}	5.7	0.001	0.6	0.6
-3542	Avicula-Schichten	2.40^{-17}	5.6	0.001	0.6	0.6
-3556	Volpriehausen-Wechselfolge	2.00^{-17}	7.1	0.001	0.6	0.6
-3636	Volpriehausen-Sandstein	2.00^{-17}	6.1	0.001	0.6	0.6
-3662	Bernburg-Folge	2.55^{-18}	5.7	0.001	0.6	0.6
-3773	Calvörde-Folge	2.00^{-17}	5.7	0.001	0.6	0.6
-4000	Zechstein	1.00^{-21}	0.1	0.001	0.6	0.6

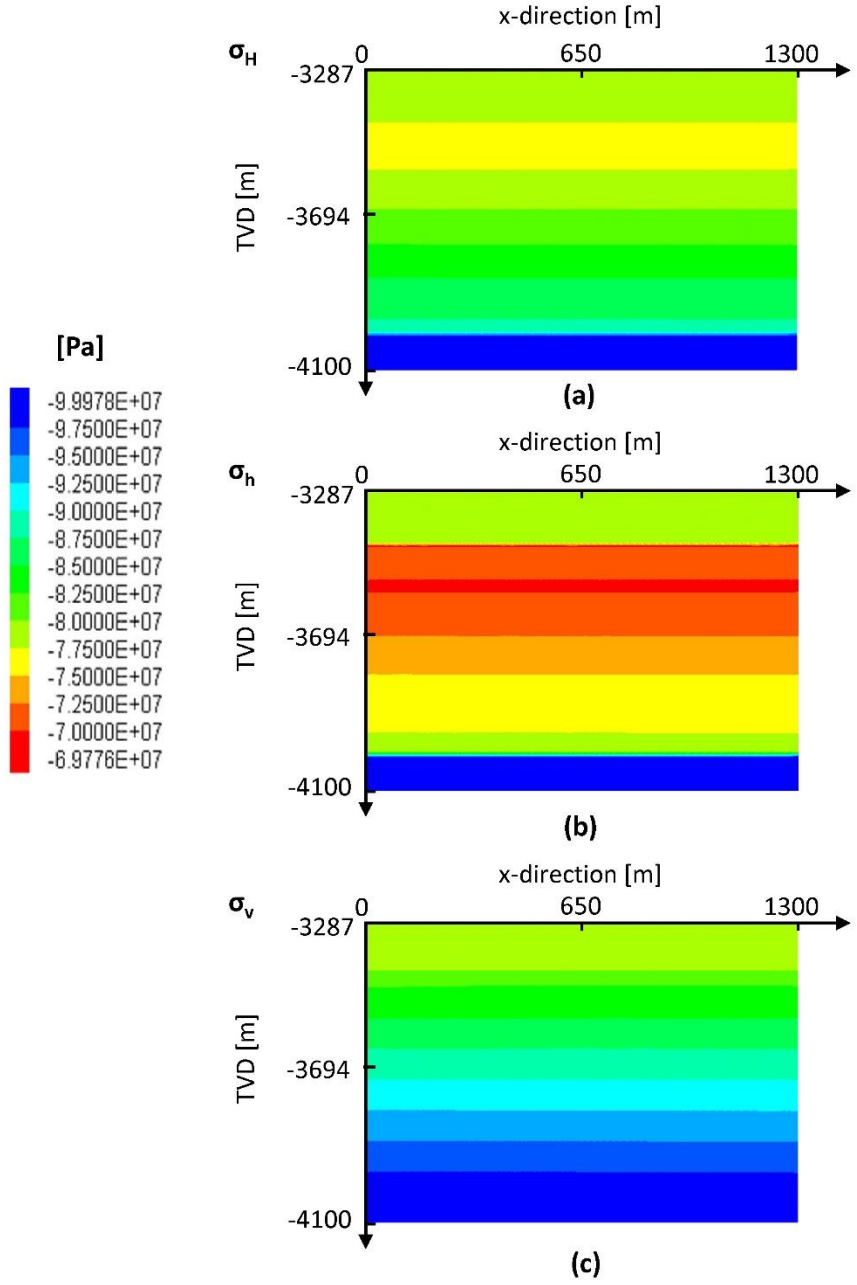

Figure 4.7 Variation of (a) maximum horizontal stress (b) minimum horizontal stress and (c) vertical stress

While defining initial conditions, the pore pressure is assumed to be hydrostatic, having a hydraulic gradient of 0.01 MPa/m at the top of the sandstone layer. The minimum horizontal stress (σ_h) exists in the y-direction, while maximum principal stress is taken along the vertical z-direction. The vertical stress (σ_v) can be calculated using Eq. (4.1), which is the integral of density over depth for each formation. Eq. (4.2) can be used for computing the minimum horizontal stress values using pore pressure and vertical stress. The maximum horizontal stress

is usually considered intermediate stress and is calculated by averaging the vertical and minimum horizontal stress values (Eq. (4.3)).

$$\sigma_v = \sum_{i=1}^{n} \rho_i \ g \ \Delta h_i \tag{4.1}$$

$$\sigma_h = \frac{v}{1-v}(\sigma_v - \alpha_v \,.P) + \alpha_h \,.P \ + \sigma_{tec} \tag{4.2}$$

$$\sigma_H = \frac{\sigma_v + \ \sigma_h}{2} \tag{4.3}$$

where, ρ is the density of layer [kg/m^3], g is the gravity [m/s^2], h is the layer thickness [m], α_v is the vertical Biot-coefficient [-], α_h is the horizontal Biot-coefficient [-], v is the Poisson ratio [-].

4.1.2 Verification of simulation model

The study results of Tischer et al. [112] are used to verify the simulation model based on pressure history matching. A total volume of 20,000 m^3 of pure water is injected with a 5.4 m^3/min maximum injection rate. Fracturing operation is continued for around 110 hours with several injection pauses. Initially, fracture propagates faster vertically until it intersects with the strong upper boundary barrier and, latterly, in the horizontal direction. At the end of the injection, a large fracture with a half-length of about 1160 m and a fracture height of 390 m is obtained (Figure 4.8 (a)). Figure 4.8 (b) shows the half fracture geometry at the end of the injection period. The maximum half width of 1.85 cm is obtained opposite to the formation having the least value of minimum horizontal stress at the end of injection.

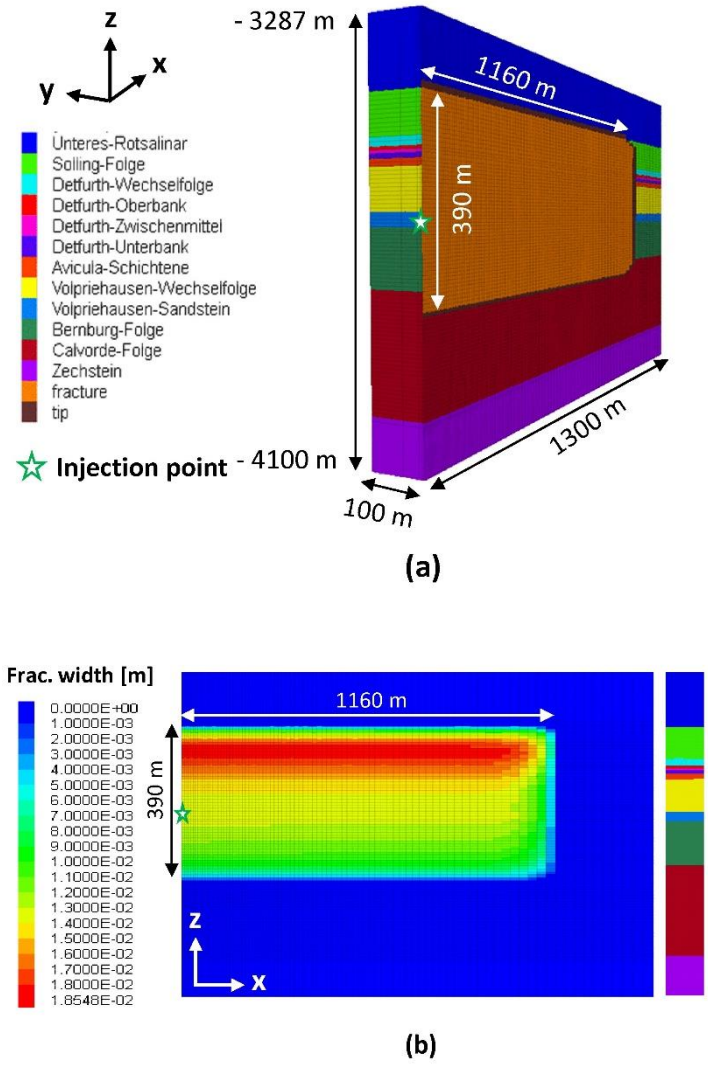

Figure 4.8 Illustration of (a) fracture geometry by hydraulic fracturing at the end of injection (b) fracture width along the horizontal & vertical directions in reservoir

Figure 4.9 shows injection volume and fracture volume evolution throughout the injection period. At earlier intervals of the injection phase, fracture volume increases almost linearly with the injection volume. During the shut-in phases, the fracture volume reduces and the reduction rate increases with time, while the leak-off volume rises. Generally, higher permeability of formations causes a higher leak-off rate. However, the leak-off volume is very less due to the lower permeability of formations, and hence the created fracture retains its volume and shape.

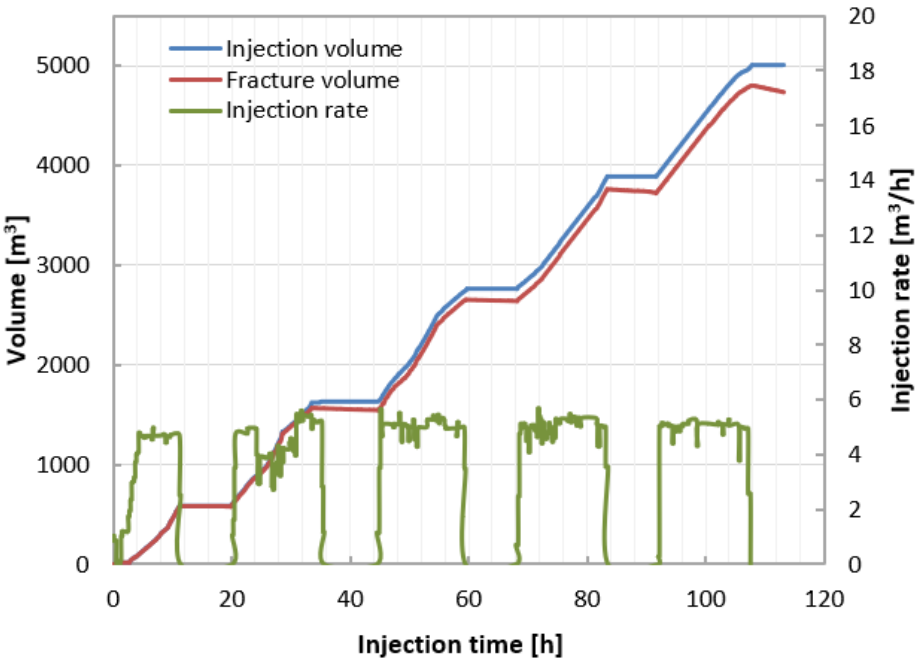

Figure 4.9 Evolution of injection and fracture volume over time

In field operations, well head pressure is measured during hydraulic fracturing. Depending on the well depth, hydrostatic pressure of the water column can be calculated and added in well head pressure to obtain the bottom hole pressure. Furthermore, friction and fluid flow pressure losses along the well path as well as in perforation are also added to well head pressure [14]. Mathematically, it can be described as in Eq. (4.4).

$$BHP = WHP + \rho_{fluid} g h - \Delta p_{near\ wellbore} - \Delta p_{flow} \quad (4.4)$$

where *BHP* is the bottom hole pressure [Pa], *WHP* is the well head pressure [Pa], ρ is the fluid density [kg/m^3], $\Delta p_{near\ wellbore}$ is the near-wellbore friction pressure loss [Pa], Δp_{flow} is the fluid flow pressure loss in the wellbore [Pa].

After converting surface treating pressure to bottom hole pressure encompassing hydrostatic pressure and frictional losses, the comparison of the simulated BHP and measured BHP is shown in Figure 4.10. Due to many uncertainties, an exact match is not possible. However, the simulated result matches the measured one well, proving the suitability and acceptability of used parameters and stresses to model fracturing operations.

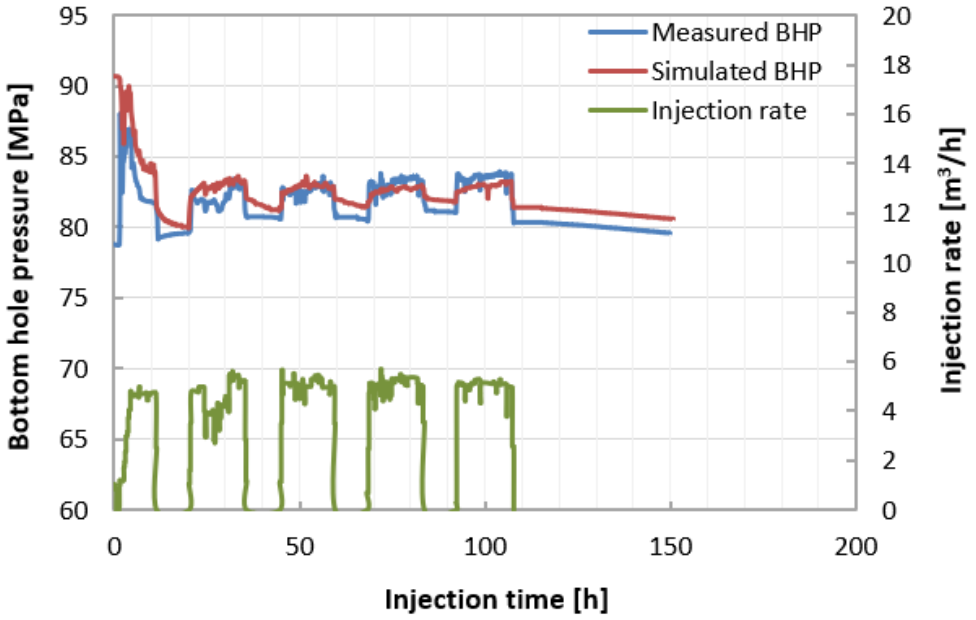

Figure 4.10 Comparison of the simulated BHP with measured BHP over time

4.2 Multiple hydraulic fracturing

After validating the geometric/numerical model, an innovative idea is implemented to analyze the large geothermal area by creating 10 – 12 hydraulic fractures to one side of the well having approximately 5 km^2 fractured area based on the schematic fracture pattern, as shown in Figure 4.11. It depicts the combination of multistage hydraulic fracturing with three vertical wells. It is planned to create each fracture sequentially with lower injection fluid volumes. This approach can provide extra advantages of exploiting a larger geothermal area with lesser seismic activity and reduce the drilling investment cost compared to energy production.

In order to investigate the influence of stress shadow on each fracture geometry, suitable fracture spacing is crucial. As discussed in chapter 3, minimum fracture spacing for transverse fracture growth is defined beyond the S5 contour, the region with a stress reorientation angle < 5^o [75]. Figure 4.12 shows the minimum horizontal stress reorientation angle at the end of the injection period at -3660 m injection depth. It can be seen that the minimum fracture spacing under the prevailing conditions is 57 m to acquire a denser multiple fracture system.

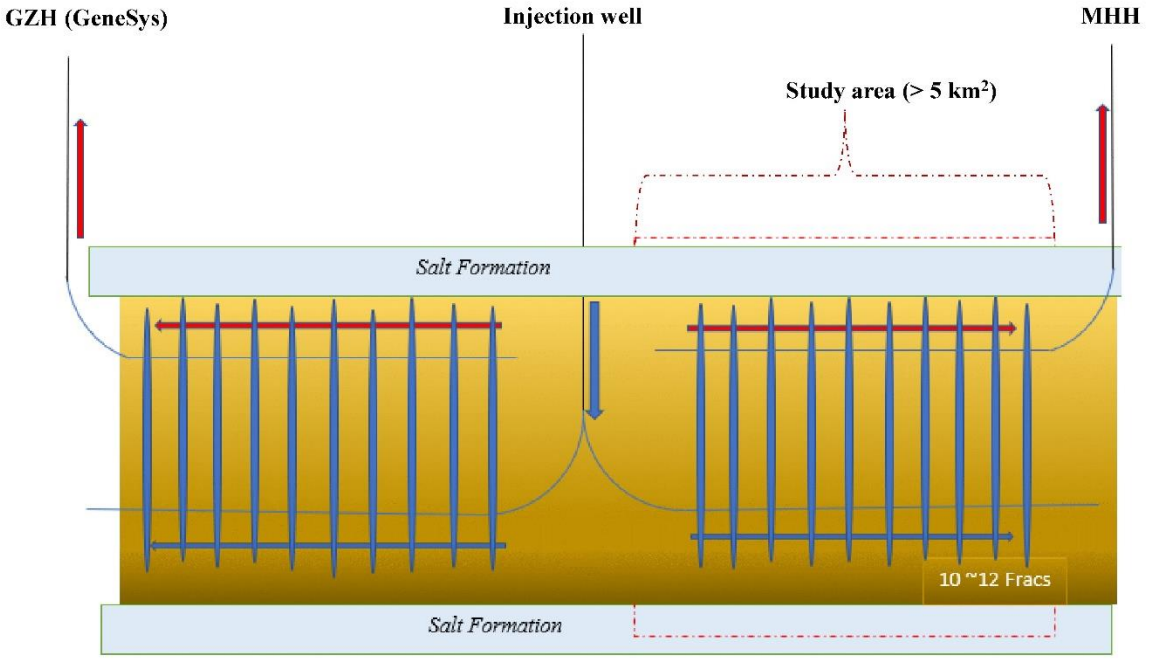

Figure 4.11 Schematic of the proposed multiple fracture pattern through multi-wells of water injection and production

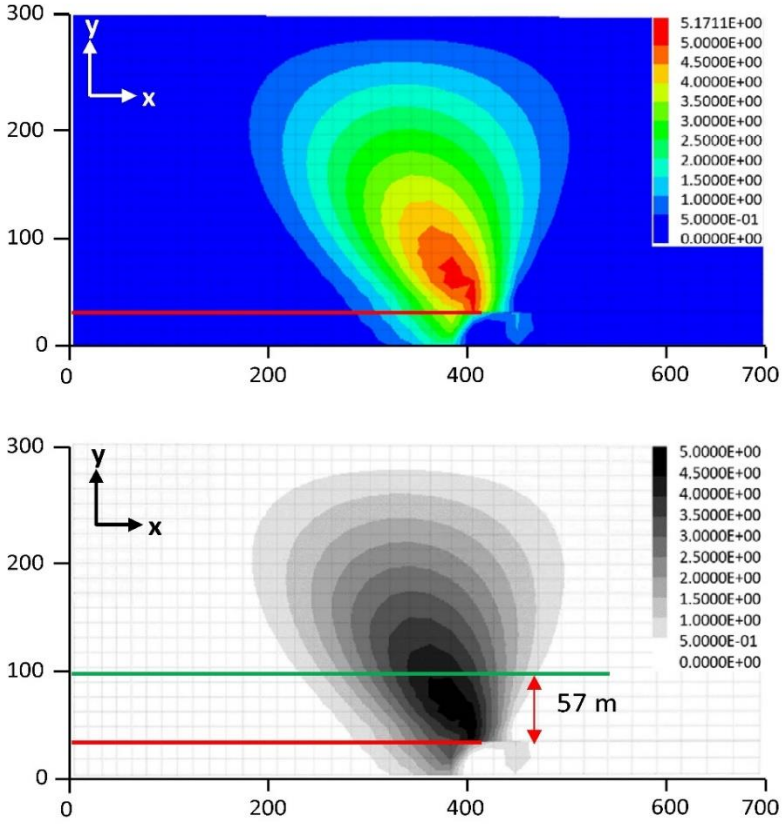

Figure 4.12 Angle of minimum principal stress reorientation at the end of injection at the injection depth (z=-3660 m). Red lines represent the position of first fracture and green line for the minimum subsequent fracture spacing

Furthermore, the accuracy and time consumption for the numerical modeling of multiple fracturing operations are highly dependent on the simulated model's geometry and the number of elements. After conducting numerous simulations, a model with three massive fractures is adopted due to multiple-fracture geometry constraints. The 3D ½ geometric model with three injection points to create three sequential fractures is shown in Figure 4.13 (a). The horizontal length of the model is reduced to 700 m, while 60 m fracture spacing in the y-direction is used as a base case. The lateral size of the model in the y-direction is 183 m. Three fractures are generated through the sequential fracturing technique after injecting 21,600 m^3 of total fluid volume. Table 4.3 provides information about injection parameters and model properties. All three fractures are created following the same injection parameters and conditions with pure water having no proppant. It is observed that minimum horizontal stress has drastically increased from 69 to 95 MPa, especially at the middle region of the geometric model (Figure 4.13 (b) & (c)).

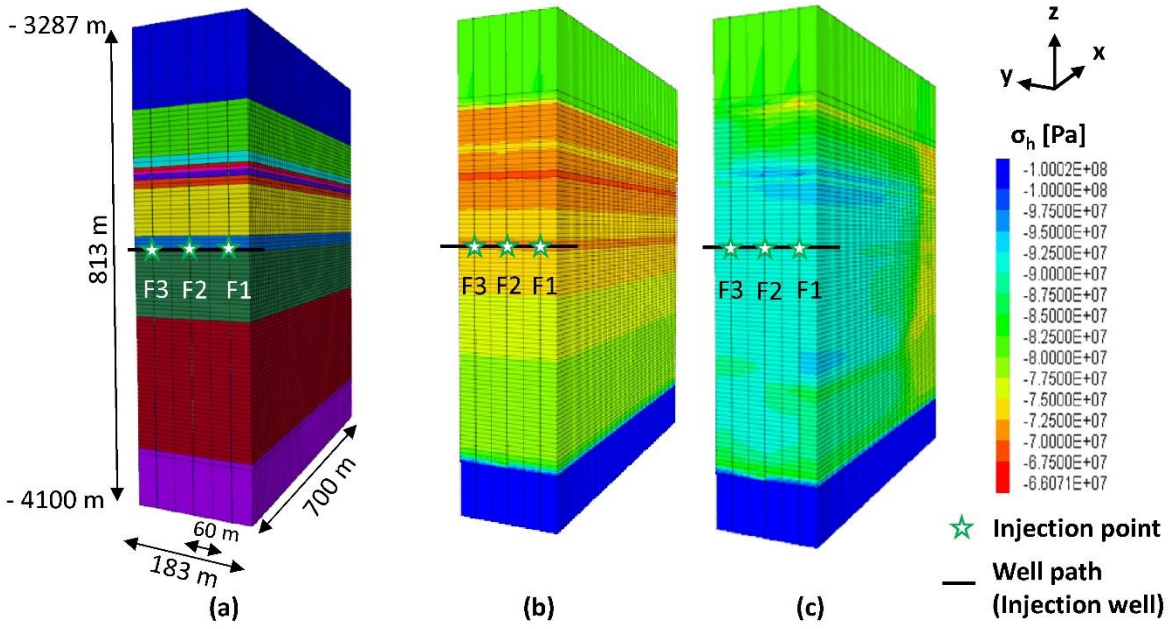

Figure 4.13 3D ½ geometric model showing three fractures injection points with (a) 60 m fracture spacing, (b) prevailing minimum horizontal stress before fracturing, and (c) minimum horizontal stress after fracturing

Table 4.3 Injected fluid and rock parameters for multi-fracture modeling

Parameter	**Value**
Injected fluid	Water
Injected fluid volume per half fracture	3600 [m^3]
Injection rate per fracture	5.4 [m^3/min.]
Specific heat of formations	1200 [J/kg °C]
Thermal conductivity of rock formations	2.5 [W/m °C]

The minimum horizontal stress at the cross-section along the x-z plane (y = 0) of each generated fracture provides valuable information related to individual fracture geometry, shown in Figure 4.14 (b). The highest increase in horizontal stress is observed in the third fracture, which is created at the end. The variations in fracture width and shape can be more prominent in massive fracturing operations as higher fluid volumes are used to create large fractures. This can be seen by analyzing the obtained results of fracture geometries, as illustrated in Figure 4.14 (c). The highest fracture width in the first fracture is present at the upper section of the formation opposite to the least minimum horizontal stress. The shape, width, and area of second and third consecutive fractures significantly depend on the stress shadow of the first and second fractures, respectively. Higher fracture width at the upper side of the first fracture restricts the propagation of the second fracture at the upper side. Therefore, the maximum fracture width of the second fracture exists at the lower depth. In addition, the height of the second fracture is increased, while fracture half-length is reduced. It is important to recognize that the minimum horizontal stress value is larger at greater depths than the lower depth (upper side of the model) at initial conditions. The maximum width of the second fracture at the lower portion is due to the stress shadow effect of the first fracture, which provides hindrance in the fracture propagation at the upper side. A similar trend is observed for the third fracture as well but in the opposite manner. The stress shadow of the second fracture forces the propagation of the third fracture with maximum fracture width at the upper side. Furthermore, the configuration of the third fracture is highly distorted with increased fracture half-length compared to the other two fractures.

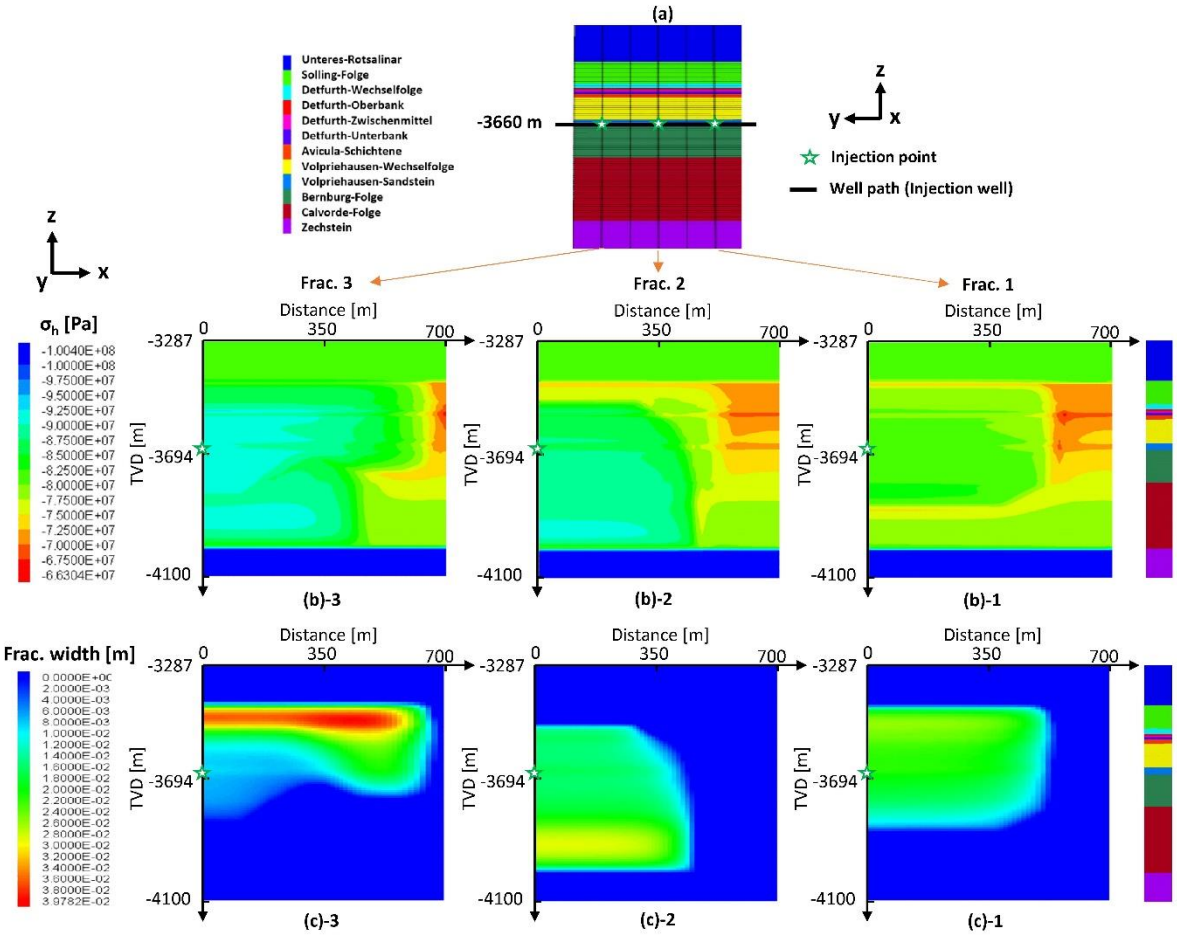

Figure 4.14 Minimum horizontal stress along three fracture planes and fracture widths with 60 m spacing

To comprehend the stress shadow influence concerning fracture spacing in this particular area, fracturing simulations are performed further with 80 m, 120 m, 140 m, and 200 m fracture spacings successively. The corresponding results of three fracture widths and configurations are shown in Figure 4.15. The results of 80 m spacing are somewhat similar to 60 m spacing (base case) but with a smooth increase in the third fracture height. Moreover, the maximum width of the third fracture reduces and occurs at the short middle portion of the fracture. It will allow the fracture to propagate in the lower formations as well. As the fracture spacing increases from 80 m to 200 m, the homogeneity in the second and third fractures also increases. However, even with 200 m fracture spacing, a similar fracture pattern is still not achieved due to stress interference among the fractures. The comparison also depicts that the propagation of the third fracture is highly dependent on the configuration of the second fracture. The geometry of the third fracture is somewhat inverse to the second fracture. Therefore, it can be concluded that the continuation of the second and third fracture patterns may occur alternately in the case of a

larger number of fracturing operations. Although, with more fracture spacing, chances of similar fracturing patterns increase. However, increased fracture spacing requires a longer horizontal section that can cause an extra burden in drilling, completion, and well operation costs [115].

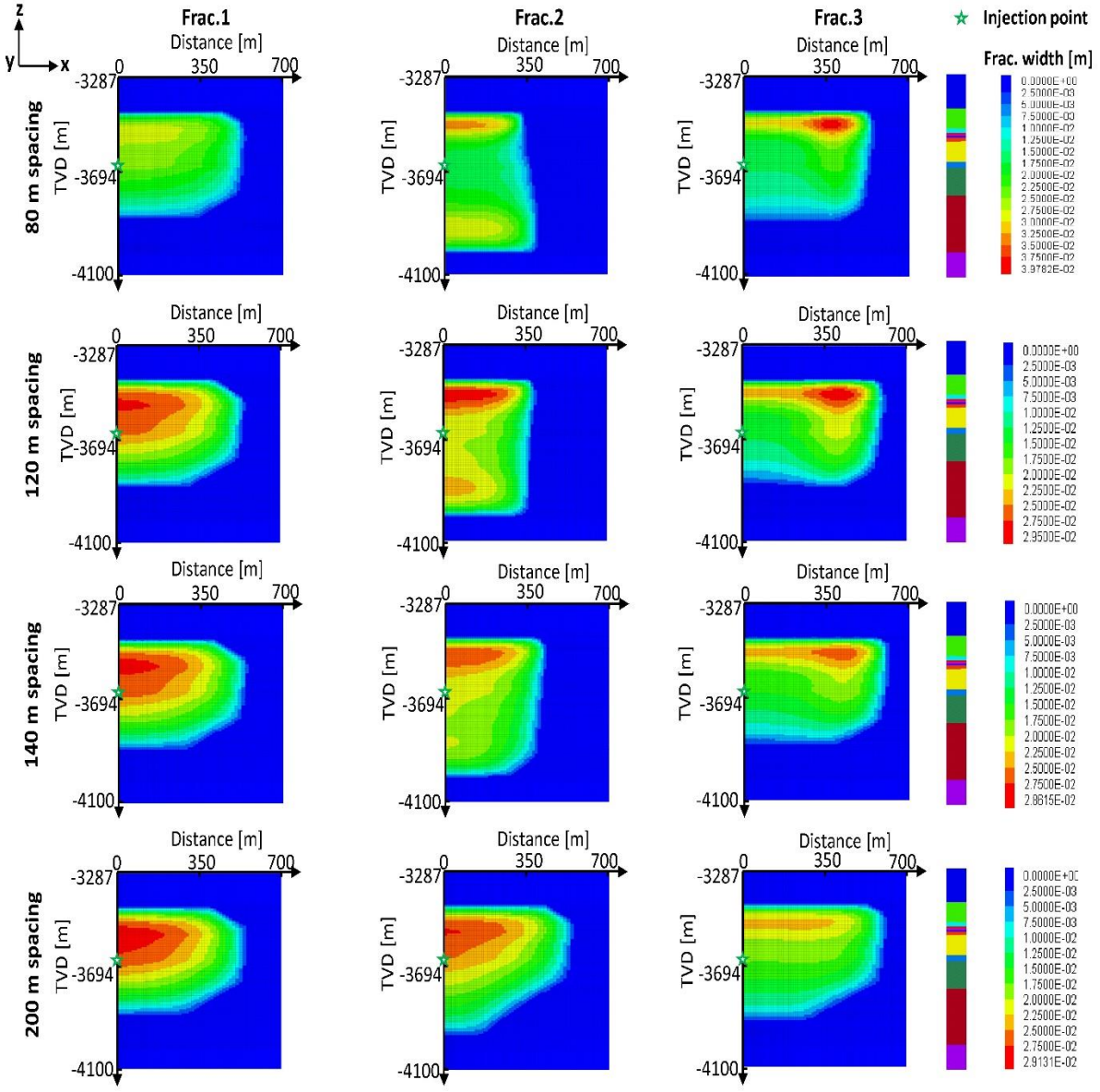

Figure 4.15 Comparative configurations of three fractures with corresponding widths over 80, 120, 140, and 200 m fracture spacing (modified from Haris et al. [76])

Stress shadow effects in the geometric model can be further elaborated by mapping iso-surface contours inside the geometric model. Figure 4.16 demonstrates the comparison of minimum horizontal stress iso-surface contours between 60 m, 140 m, and 200 m fracture spacing with

front views (a), top views at the injection depth (b), and side views (c). The horizontal well and clip location are highlighted as well. In the case of 60 m spacing, the stress shadow is compacted due to the large interference of three fracturing operations that have created a significant distortion in respective fracture shapes. In the case of 140 m spacing, contours are fairly distributed in the model showing less intrusion of stress shadow among fracture planes. While, for 200 m spacing, the smoothness among the fracture is highest.

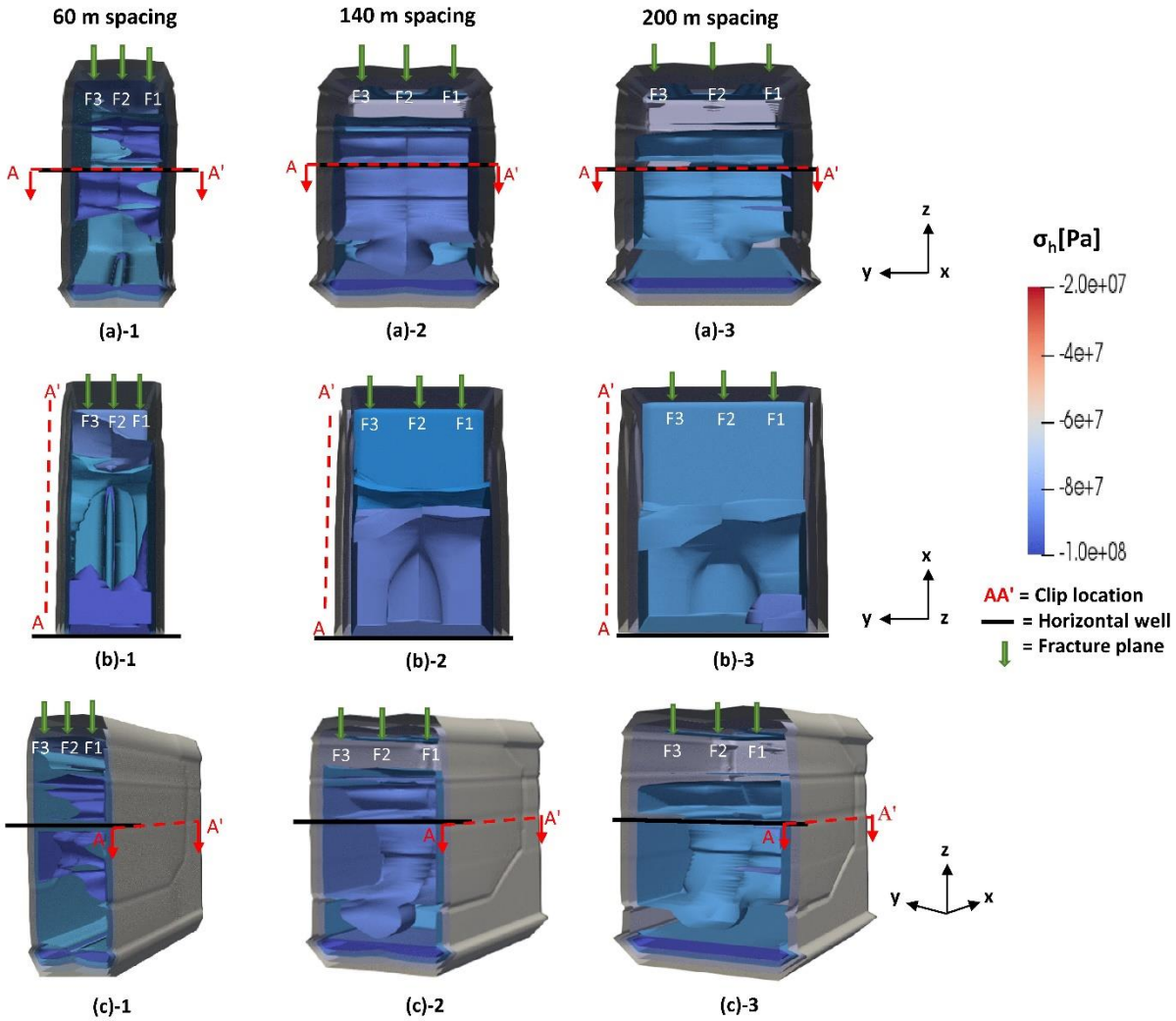

Figure 4.16 Iso-surface contours of different minimum horizontal stress values (a) front view (b) top view at the injection depth and (c) side view in the simulated model for 60 m, 140 m and 200 m fracture spacing

As the objective of this case study is to achieve about 5 km^2 fractured area after hydraulic fracturing for geothermal energy production, 140 m qualifies for desired results. Based on the 3-fracture results, a model of the 12-fracture pattern with the same fracture spacing and stress

shadow is designed. The half model is shown in Figure 4.17 (b), which will be further used to investigate geothermal energy production in the next section.

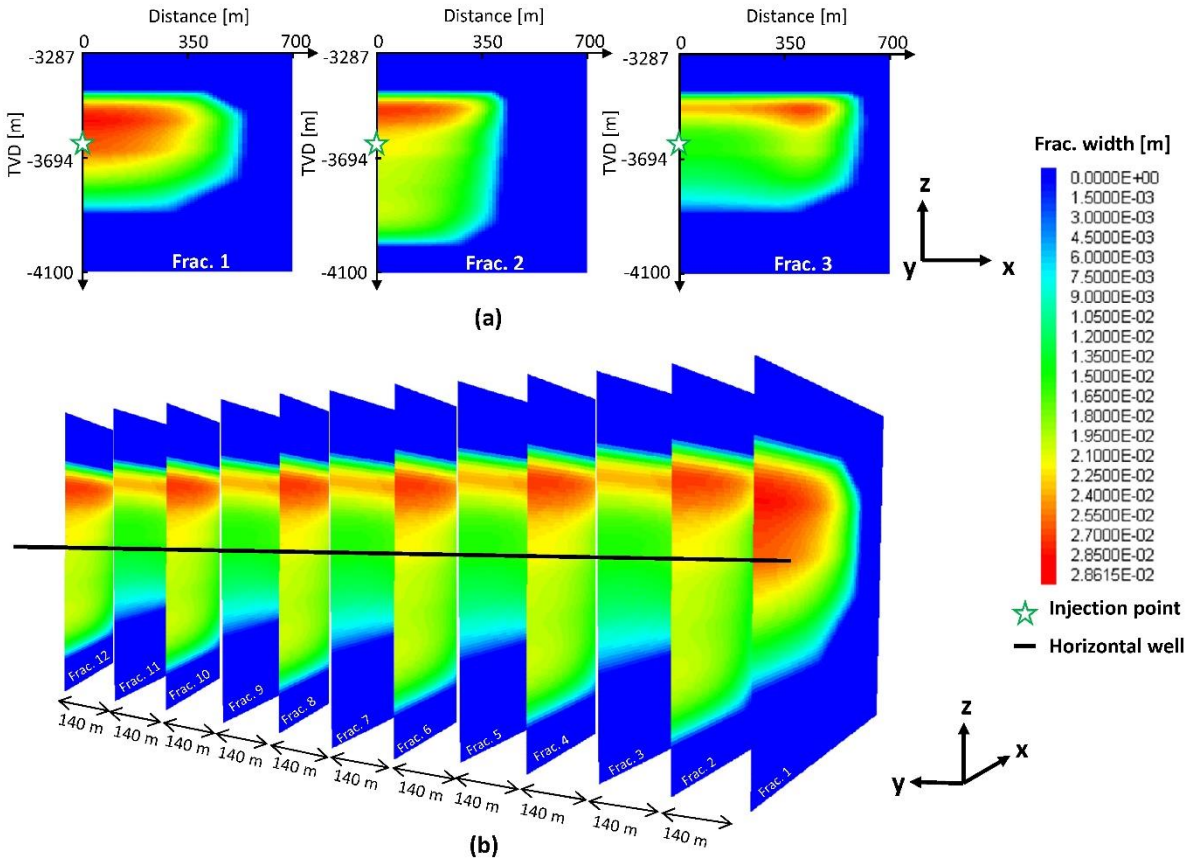

Figure 4.17 Schematic of (a) three fractures and (b)12-fracture pattern for geothermal exploitation with 140 m fracture spacing

4.3 Geothermal exploitation through configured multiple fracture model

Firstly, an equivalent model of three fracture patterns is used to investigate each fracture's coupled fluid flow and heat transfer. For this purpose, the model is represented in Figure 4.18 (a), and the dimensions of the model are the same as of the fracturing model. The fluid flow and heat transfer equations have already been presented in chapter 3. The temperature from top to bottom of the model increases from 152 ^{o}C to 177 ^{o}C by considering a geothermal gradient of 0.03 ^{o}C/m with surface temperature adjustment, which also corresponds to the reservoir temperature of the GeneSys geothermal site [112]. The second horizontal well is drilled at a depth of -3500 m to produce heated water, which is at a quarter (1/4) depth of the least fracture height. The purpose of using this depth for production well is to make sure the flow contribution

through each fracture and enough upper height from the salt bearing formation. Water is injected at a rate of 12 L/s through the injection well, and it is assumed that flow is distributed equally among three fractures, i.e., 4 L/s, by adopting the limited entry completion technique [35]. The corresponding production rate at the specified bottom hole pressure is measured. The rock and fluid parameters used for geothermal exploitation are expressed in Table 4.4.

Table 4.4 Rock and fluid parameters for geothermal exploitation

Parameters	Values
Injection fluid temperature	60 [^{o}C]
Production well depth	-3500 [m]
Injection fluid	Water
Distance between injection & production wells	160 [m]
Injection rate per fracture	4 [L/s]
Specific heat of formations	1200 [J/kg ^{o}C]
Thermal conductivity of rock formations	2.5 [W/m ^{o}C]

Figure 4.18 (c) shows the 3-dimensional temporal evolution of temperature decline in fractures with a green horizontal line as an injection well and a red horizontal line as a production well. In addition, the injection and production points are highlighted with the corresponding colors. It can be observed that during continuous cold-water injection, the temperature inside the fractures decreases with time.

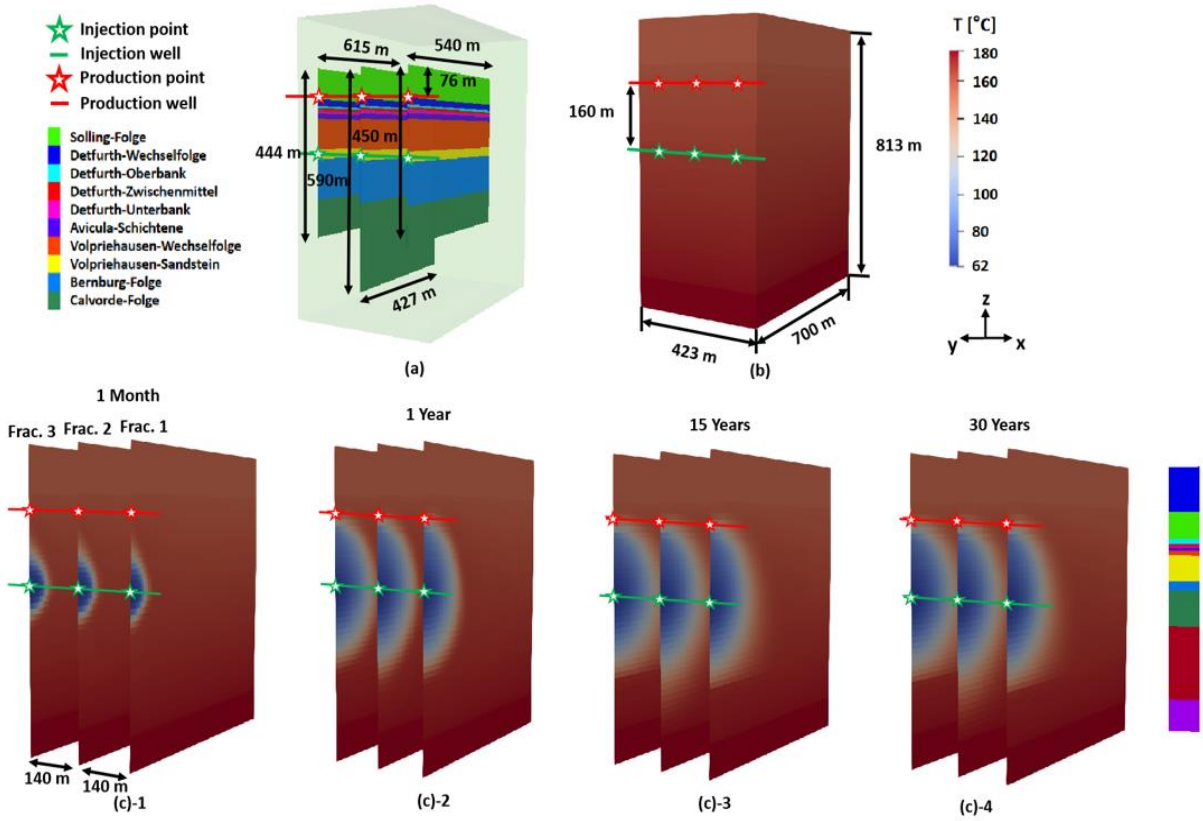

Figure 4.18 Schematic of (a) an equivalent model having three fracture patterns with 140 m spacing (b) model temperature before production (c) temperature variation inside fractures at the different time interval

A further elaborated view in 2D (y = 0) of the spatial distribution of temperature decline inside the fracture planes is shown in Figure 4.19. As the injection begins from the injection point, the low-temperature region is formed around the injection perforation interval. The cold front increases outside and follows a circular shape in expansion. The cold front almost reaches the production point within one year of production with a temperature greater than 60 ^{o}C. Afterward, the rate of lateral expansion of cold front movement along the x-direction reduces and increases in the y-direction. The first and third fractures, having lower fracture heights compared to the second fracture, contribute fully through vertical dimension. However, the lower portion of the second fracture contributes less due to earlier connection development between injection and production points. The lower portion of the second fracture plane still has a higher temperature even after 30 years of production. It is also observed that even after 30 years of production, the cold front is unable to produce the energy from all of the fracture areas. Only about ½ of each fracture's half-fracture area contributes to energy production until the end of 30 years.

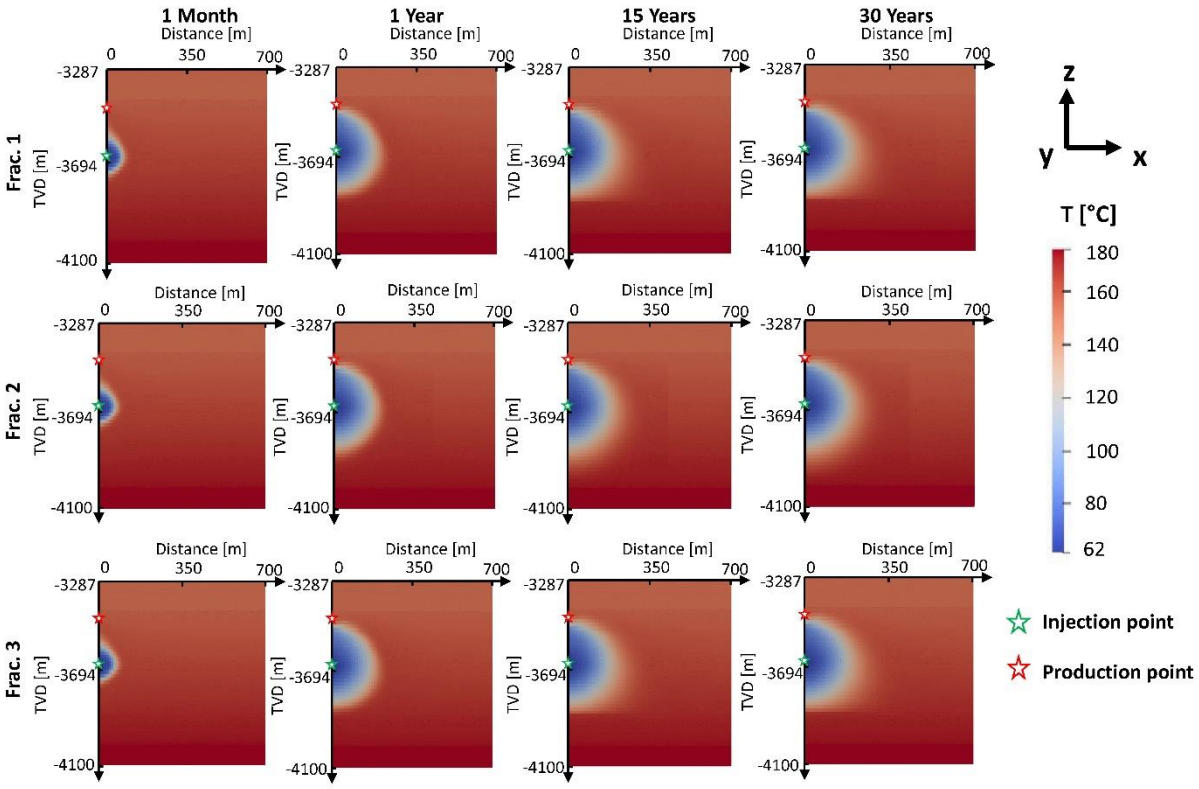

Figure 4.19 Temporal evolution of temperature decline in three fracture planes after 1 month, 1 year, 15 years and 30 years of production

Figure 4.20 shows the temperature decline of the produced fluid through each fracture. Initially, the fluid is produced at the formation temperature of about 160 ^{o}C, and a little rise in temperature is observed due to heat conduction. Subsequently, the temperature drops sharply. Within six months of production, the temperature has dropped to 125 ^{o}C. This is due to the fact that during early period of injection, heat transfer is manily through heat convection between cold & hot fluids. Heat conduction between injection fluid and surrounding rock is relatively slow that takes place at the later stage. After ten years of production, the rate of temperature decline becomes smooth for the rest of the production period. It is noted that, even with different fracture dimensions and configurations, each fracture shows quite a similar temperature decline trend through this huge fracture system. Depending on injection and production fluid enthalpies, the heat production power can be calculated using Eq. (3.37).

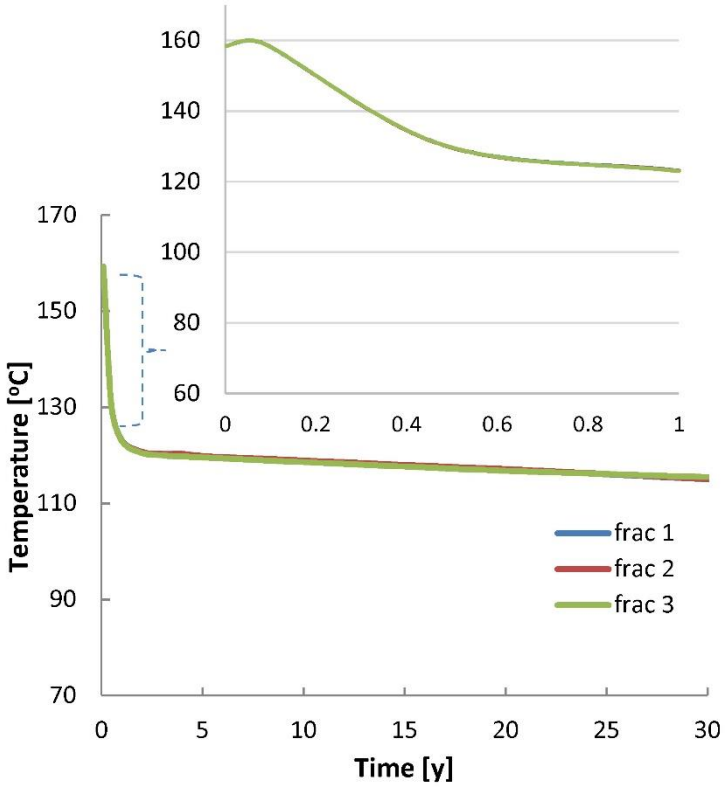

Figure 4.20 Production temperature decline trends within 30 years in three fractures

Based on the three fracture results, an equivalent model of the 12-fracture pattern is designed for geothermal energy production, as shown in Figure 4.21. The distance between the injection and production wells is 160 m, while the distance between the fracture is 140 m.

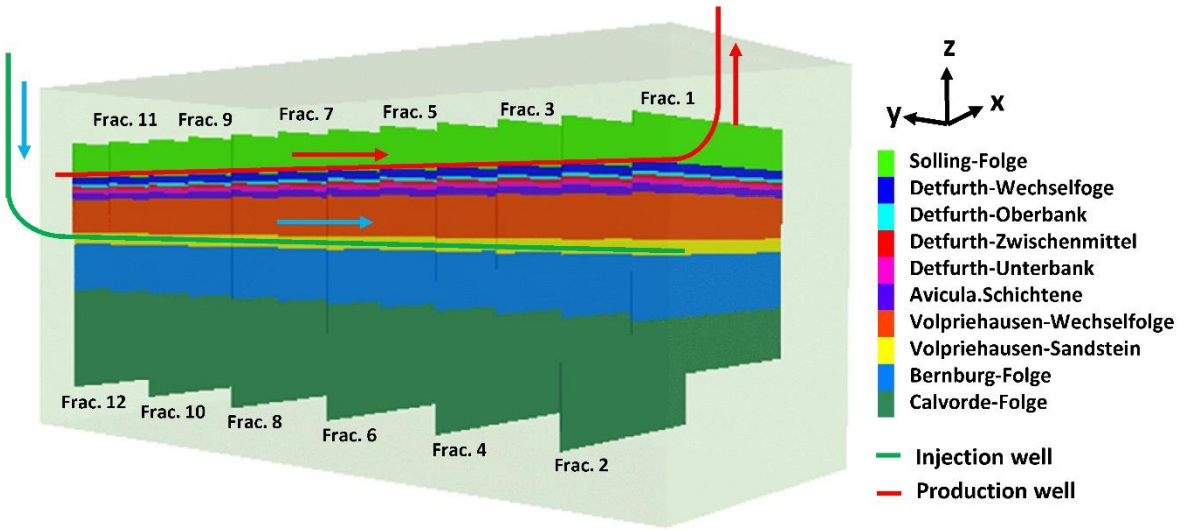

Figure 4.21 Schematic of equivalent model for 12-fracture pattern after fracturing in combination of injection and production wells

For the 12-fracture pattern, a total of 48 L/s is injected through the injection well, and the production rate is measured at the producing end accordingly at the fixed bottom hole pressure. Figure 4.22 (a) shows that the geothermal capacity decreases sharply from 31 MW_t to 15 MW_t during one year of production due to the sharp decline in production temperature. Later, the declining trend of geothermal capacity slows down and finally reaches 13 MW_t after 30 years of operation. Furthermore, Figure 4.22 (b) shows the produced net energy reaching about 12 PJ ($1PJ = 1*10^{15}J$) during 30 years of operation.

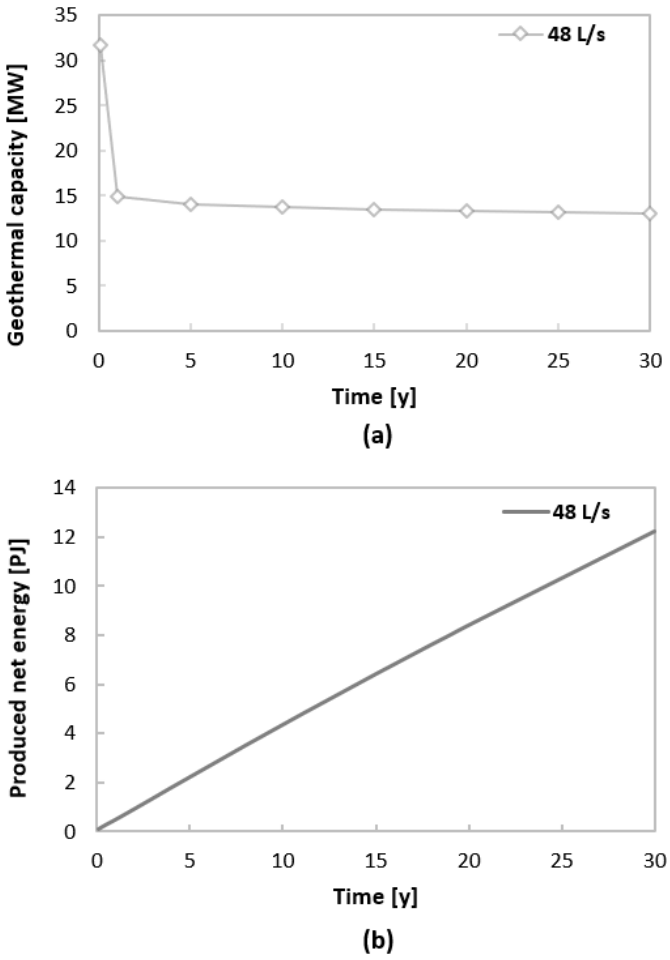

Figure 4.22 Schematic of (a) geothermal capacity and (b) net energy production through 12 fractures

The initial production results based on temperature decline in fracture planes show that, even though a gigantic fractured area is available in tight formations, the current combination of injection/production wells arrangement and fluid flow plan cannot produce the energy fully through each fracture. Therefore, energy production optimization through the multiple fractured model is required.

4.3.1 Geothermal energy production optimization

Figure 4.23 shows the optimizing scenarios for energy production. Each scenario is explained comprehensively in the subsequent section, and in the end, the scenario will be selected that provides the best production results.

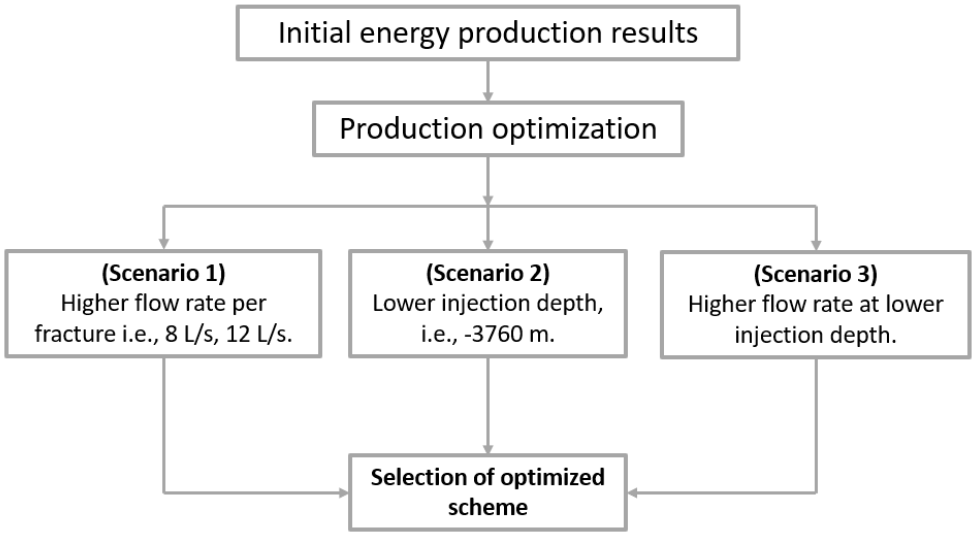

Figure 4.23 Flow chart of selecting the optimized production scenario

4.3.1.1 Scenario 1

Currently, geothermal installations in Germany have been dealing with variable flow rates, i.e., 30 L/s to 168 L/s for geothermal energy production [111]. Therefore, analysis for heat extraction optimization in scenario one is performed with higher flow rates such as 8 L/s and 12 L/s per fracture, successively. In addition, high flow rates can reduce the salt scaling rate in vertical and horizontal sections of wells. The remaining reservoir/injection parameters are the same as of the initial production case. Moreover, the spacing between injection and production well is also the same as in the initial case, i.e., 160 m. The results of cold-water injection with increased rates are shown in Figures 4.24 & 4.25. It can be observed that the impact of increased flow rate is quite prominent in comparison to Figure 4.19. From the start of injection, the cold temperature envelope covers more fracture area, and this trend remains same during the whole 30-year production period. Each fracture contributes more to energy production both in horizontal and vertical directions. At the end of 30 years, the temperature is declined to about 60 ^{o}C in more than ½ of the half-fracture areas.

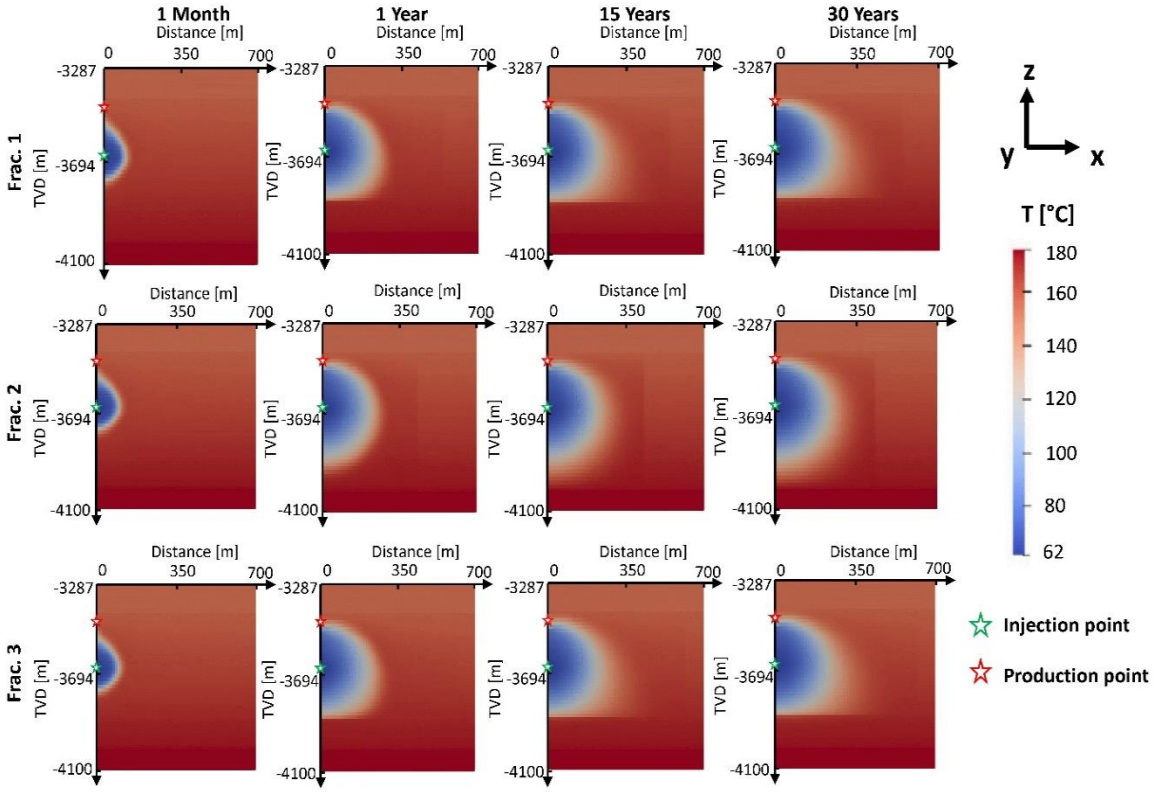

Figure 4.24 Temporal evolution of temperature decline in three fracture planes after 1 month, 1 year, 15 years, and 30 years of production at rate of 8 L/s per fracture

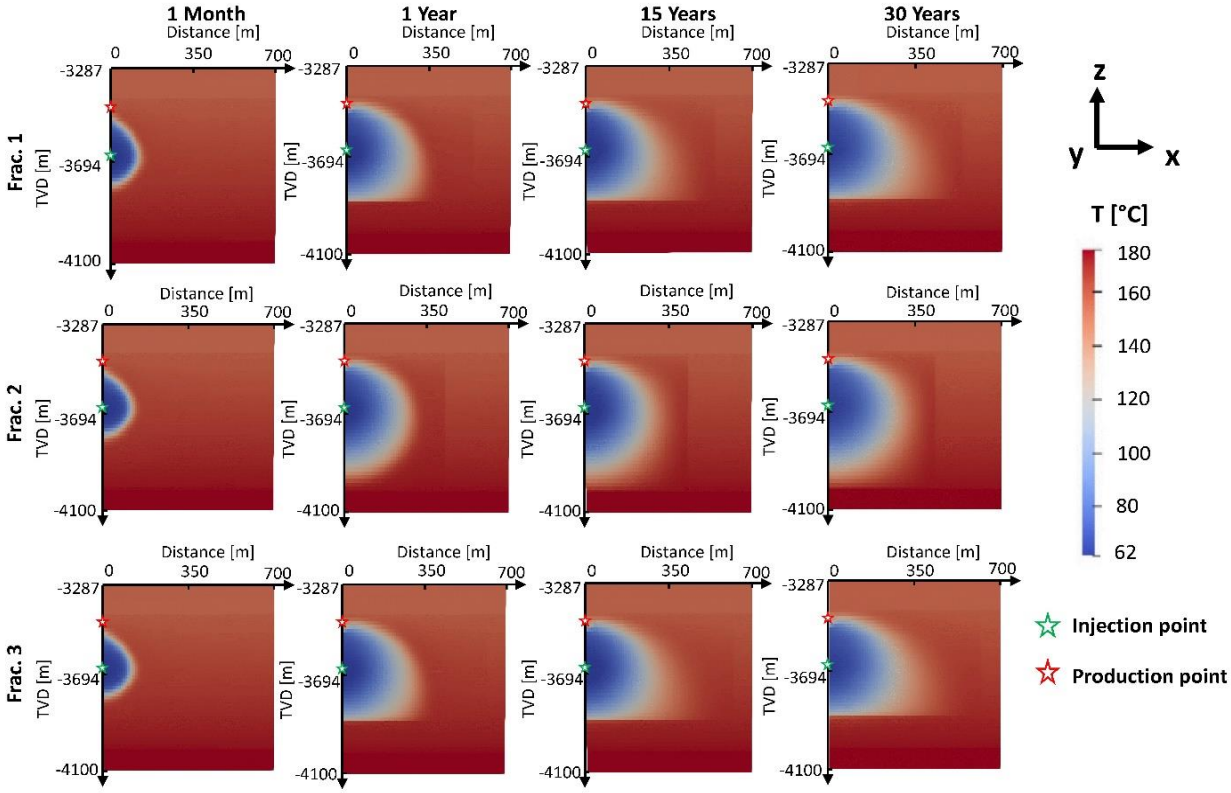

Figure 4.25 Temporal evolution of temperature decline in three fracture planes after 1 month, 1 year, 15 years and 30 years of production at flow rate of 12 L/s per fracture

Figure 4.26 shows comparative results of the temporal evolution of temperature decline in three fracture planes after 30 years of production with different flow rates. The impact of an increased rate is quite noticeable on the energy harnessing fracture area. Less than ½ of the half fracture areas for 4 L/s injection rate per fracture in energy contribution are changed into more than ¾ of the half fracture areas for 12 L/s per fracture.

It is observed that with the higher flow rates, a sharp decline in temperature at the production end occurs (Figure 4.27). The reason is the quick flow of fluid towards the production end. For 12 L/s, the temperature decreases quickly from 160 ^{o}C to 100 ^{o}C and finally reaches about 96 ^{o}C for each fracture. Although binary power plants can operate for temperature range from 80 ^{o}C -170 ^{o}C, for commercial energy production, the production temperature should be greater than 100 ^{o}C.

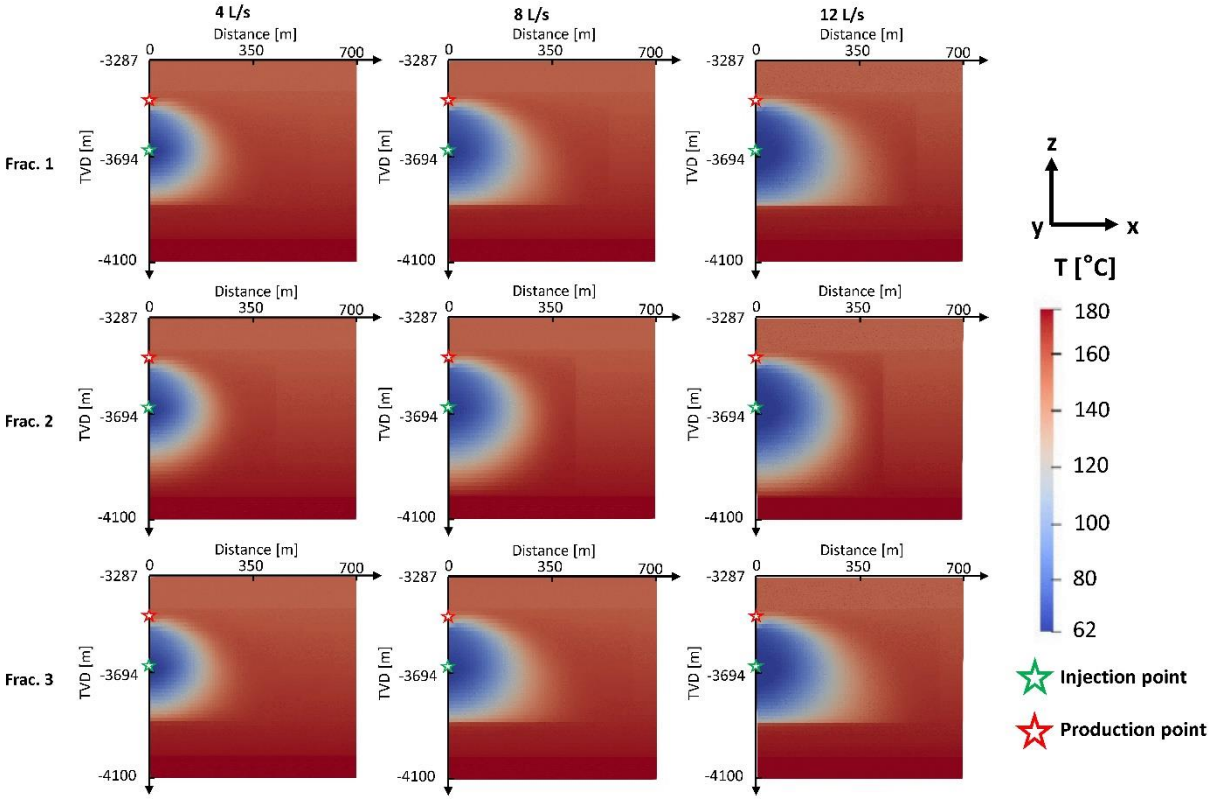

Figure 4.26 Temporal evolution of temperature decline comparison in three fracture planes after 30 years of production with different flow rates per fracture

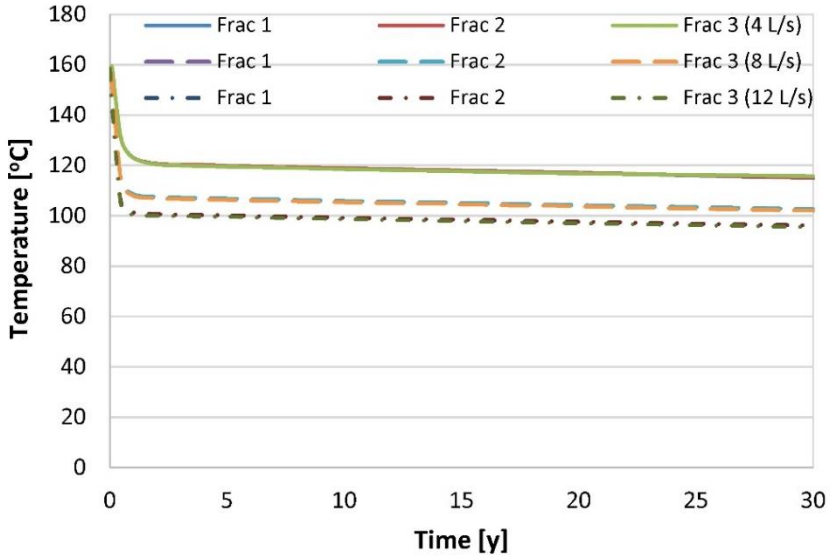

Figure 4.27 Production temperature decline trends within 30 years of period in three fractures with different flow rates

Besides, with the curb of quicker and significant temperature decline for higher flow rates, more energy can be produced due to increased energy contribution area through the stimulated

fractures. Figure 4.28 compares geothermal capacity results with different flow rates for the 12-fracture pattern. The geothermal capacity has increased from 31 MW_t to 44 MW_t and 53 MW_t for 48 L/s, 96 L/s, and 144 L/s, respectively. The increased flow rates also show similar decreasing trends of geothermal capacity as of 48 L/s. The cumulative produced energy has also been increased to 20 PJ and 26 PJ for 96 L/s and 144 L/s, respectively. Furthermore, the geothermal heat capacity can be converted into electrical power using Eq. (4.5) [115].

$$W_e = \eta\, W_h \tag{4.5}$$

where W_e is electricity generation power [W], η is conversion efficiency [-] and W_h is the heat production power [W].

The conversion efficiency η mainly depends on the type of geothermal power plant used for electricity generation. Generally, it is lower than conventional thermal power plants' efficiency and varies due to differences in heat losses, turbine efficiency, and generator efficiency of geothermal power plants [116]. From the results of 94 geothermal power plants, the conversion efficiency is reported between 12 % to 21%. Among different types of geothermal power plants, the efficiency of the binary power plant is normally lower than 10 % due to lower geothermal reservoir temperature. In literature, different models have been used for geothermal binary power plants but Carnot and Triangular cycles are generally considered as ideal models. The efficiency of the Carnot cycle and Triangular cycle can be calculated using Eq. (4.6) and Eq. (4.7) [117].

$$\eta_{th}^{C} = 1 - \frac{T_L}{T_H} \tag{4.6}$$

$$\eta_{th}^{TRI} = \frac{T_H - T_L}{T_H + T_L} \tag{4.7}$$

where T_L is the absolute temperature of heat sink and T_H is the absolute temperature of heat source, while units of temperature are in Kelvin or degree Rankine [^{o}R].

Based on the statistical results of the conversion efficiency in literature, 10 % of conversion efficiency is adopted in this work for electricity power calculation [115]. Figure 4.28 (c) shows the evolution of heat production power (W_h) and electricity generation power (W_e) during 30 years of production with a 144 L/s flow rate. The decline trends of W_h and W_e are according to the production temperature decline. W_h decreases from 53.4 MW_t to 30 MW_t, reducing 43.8 % in geothermal capacity. Therefore, W_e decrease from 5.34 MW to 3.0 MW, correspondingly.

In order to meet the commercial feasibility, the electricity generation power must be above 3 MW [115].

Although the results of scenario 1 somewhat correspond to the commercial requirement, further energy production optimization is carried out to acquire enhanced results.

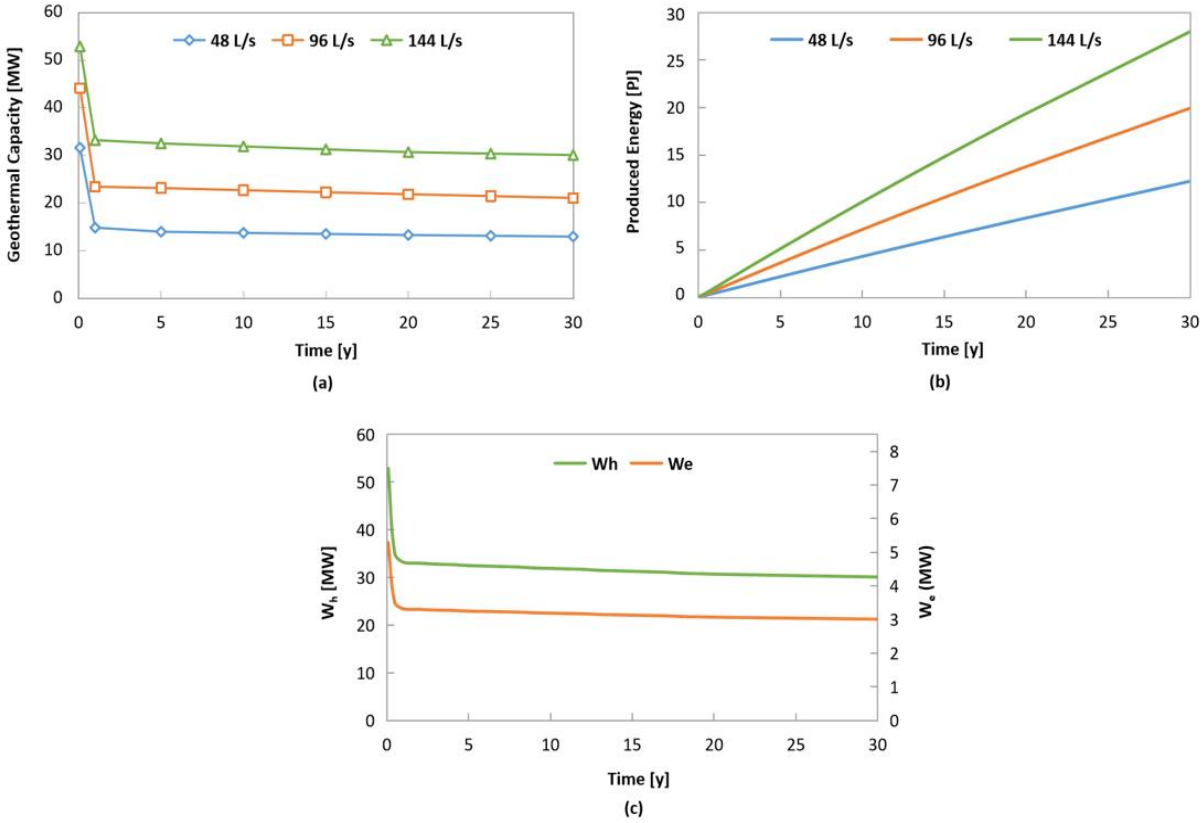

Figure 4.28 Comparative schematics of energy production results through different flow rates (a) geothermal capacity (b) net energy production and (c) heat production and electricity generation power at 144 L/s flow rate

4.3.1.2 Scenario 2

The effect of distance between injection and production wells on heat extraction is analyzed in the second scenario. For this purpose, the horizontal injection well is placed 100 m below, i.e., -3760 m, compared to the initial case. Due to the change in injection well location, the previously generated model of multiple hydraulic fractures at -3660 m cannot satisfy the proposed second scenario. In addition, the three-fracture pattern may not be the same as in the previous case due to the changes in stress shadow. Therefore, the fracturing model has been generated again for the new injection depth.

The 3D ½ geometric model with three injection points is shown in Figure 4.29. The horizontal length of the model is 700 m, while 140 m fracture spacing in the y-direction is used, similar to the previous case. The lateral size of the model in the y-direction is 423 m. Through the sequential fracturing technique, three fractures are generated after injecting 21,600 m^3 of total fluid volume, while all the injection parameters and model properties are the same as provided in Table 4.3. All three fractures are created by following the same injection parameters and conditions with pure water having no proppant.

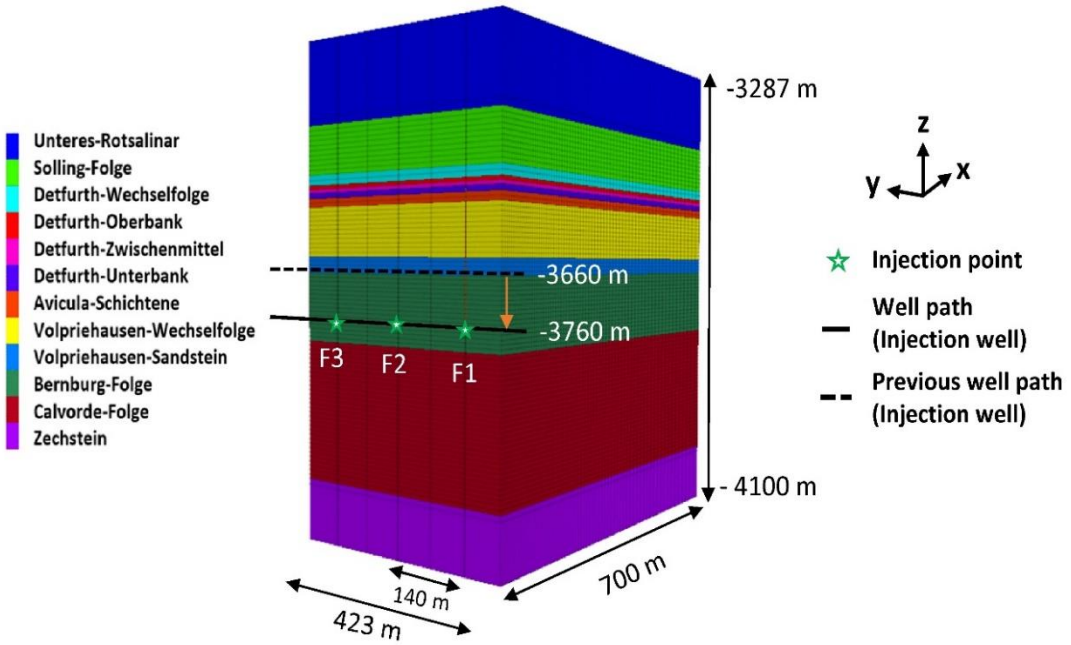

Figure 4.29 3D ½ model showing injection points of three fractures with 140 m fracture spacing having injection well at -3760 m depth

Figure 4.30 (a) shows the model's y-z plane (x = 0) with injection points in fracture planes and the well path. The minimum horizontal stress at the cross-section along the x-z plane of each generated fracture is shown in Figure 4.30 (b). The highest increase in minimum horizontal stress is quite similar in all three fracture planes, while the variations in fracture width and shape of each fracture depend on the stress shadow. This can be observed by analyzing the obtained results of fracture geometry, as illustrated in Figure 4.30 (c). All three fractures show the highest fracture widths at the upper section of the formation against the least minimum horizontal stress. Although the injection plan for each fracture is the same; however, the width of the third fracture is expressively reduced compared to the other two fracture planes. The reason is that the third fracture has attained significant fracture height with the reduced half-length. Therefore, in

comparison with Figure 4.17, the geometry of each fracture is considerably altered due to a change in injection depth.

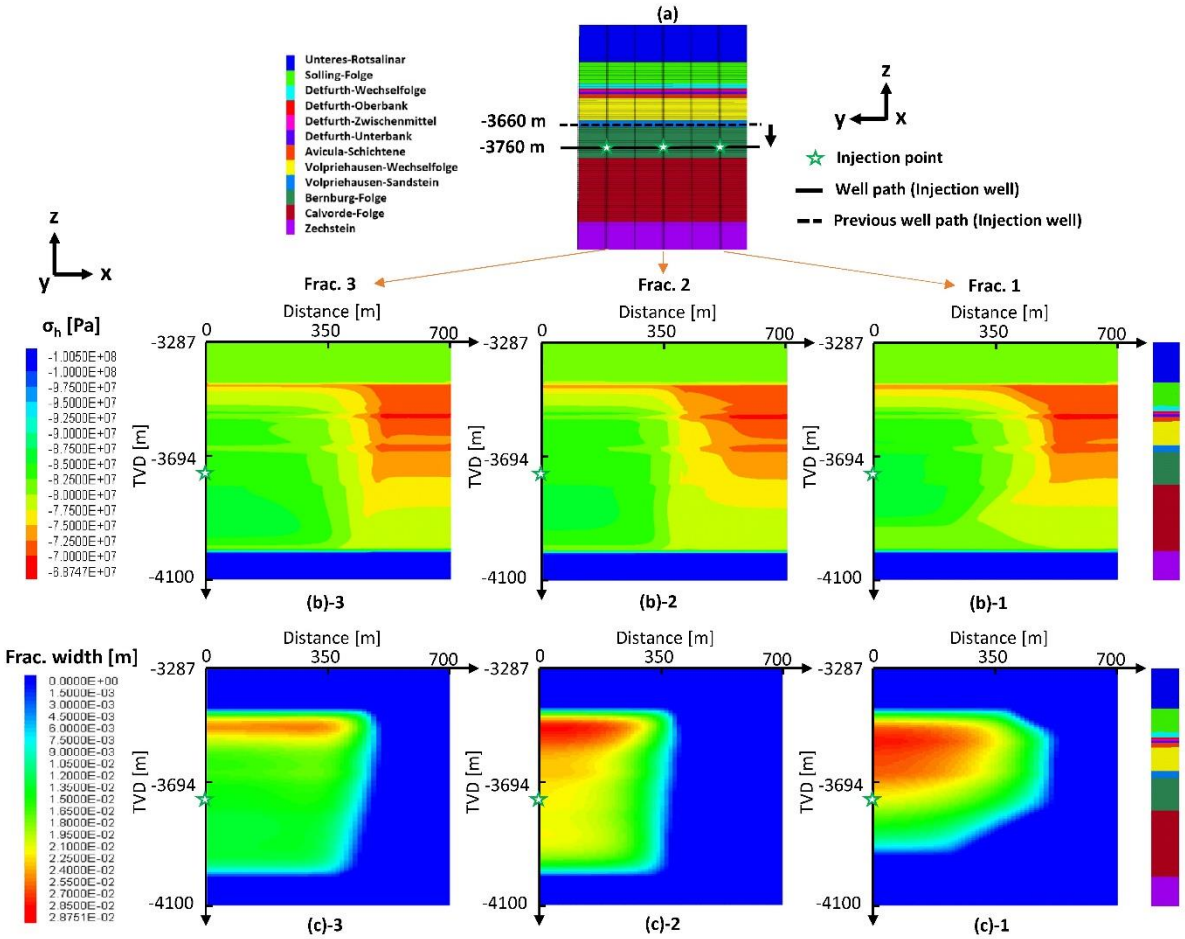

Figure 4.30 Minimum horizontal stress along three fracture planes and fracture widths with 140 m spacing at -3760 m injection depth

Figure 4.31 demonstrates the comparison of stress shadow iso-surface contours inside the geometric model with 140 m fracture spacing for different well depths with front views (a), top views at the injection depth (b), and side views (c). The contours are fairly distributed in the model in connection with each fracture shape. In the case of -3760 m well depth, second and third fractures have attained full available fracture height. Therefore, the lower section of iso-surface contours is changed compared with -3660 m well depth.

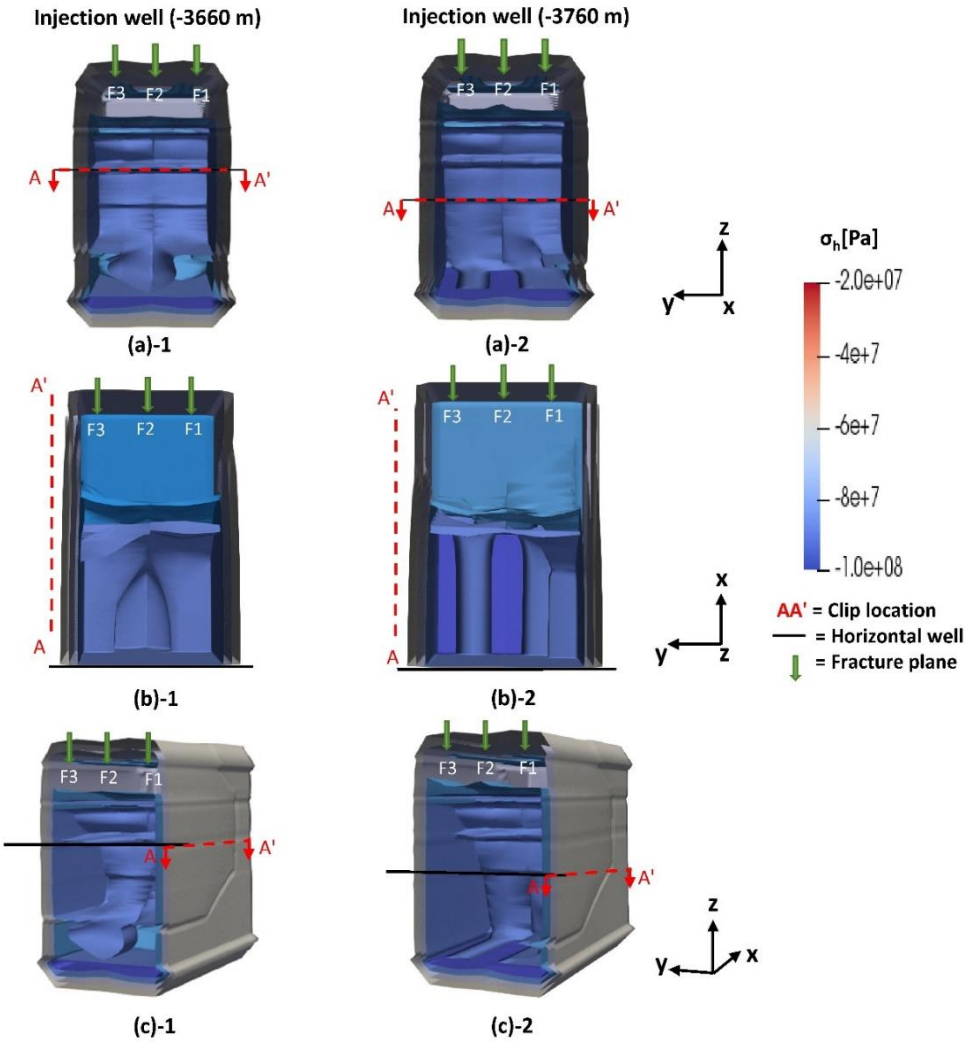

Figure 4.31 Iso-surface contours of different minimum horizontal stress values inside the simulated model for 140 m fracture spacing for different well depths (a) front views (b) top views at the injection depth and (c) side views

After achieving a 3-fracture configuration from injection well depth of -3760 m under the influence of stress shadow, an equivalent model is generated for energy production. In the second scenario, geothermal energy is produced using an injection rate of 4 L/s per fracture through the injection well at -3760 m depth. All the injection and rock parameters are the same as the initial case. Furthermore, the depth of production well is also the same as in the initial case, i.e., -3500 m. Therefore, the distance between the injection and production well is now 260 m.

The comparative schematic of the spatial distribution of temperature decline inside fracture planes is shown in Figure 4.32. In the case of injection well at -3660 m depth, the cold front increases outside and follows a circular shape in expansion, but, in the case with injection well

at -3760 m, the circular shape of expansion is changed into elliptical. The lower injection depth has caused the initial fluid movement in the lower section of the model and then towards the production end. It can be seen that after one year of production, more fracture area of the lower section has been depleted in terms of temperature decline at - 3760 m injection depth. This trend remains similar till the end of 30 years of production. However, it is also observed that even with the current well arrangement and flow rate, the energy is not produced entirely through each fracture.

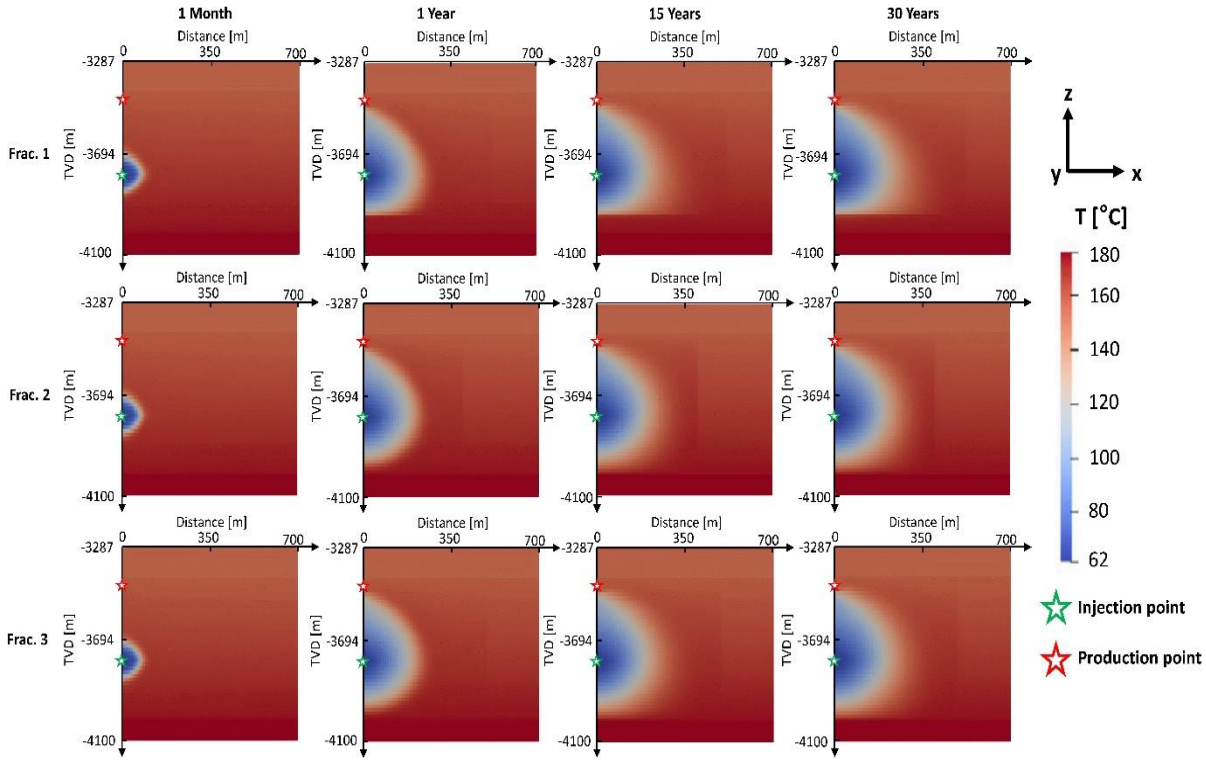

Figure 4.32 Temporal evolution of temperature decline in three fracture planes after 1 month, 1, year, 15 years and 30 years of production from -3760 m injection depth

Figure 4.33 shows the production temperature decline trends within 30 years in three fractures from - 3760 m well depth. After 1 year of production, the production temperature is declined to 140 ^{o}C, while all three fractures produced at the temperature of 133 ^{o}C at the end of the production period.

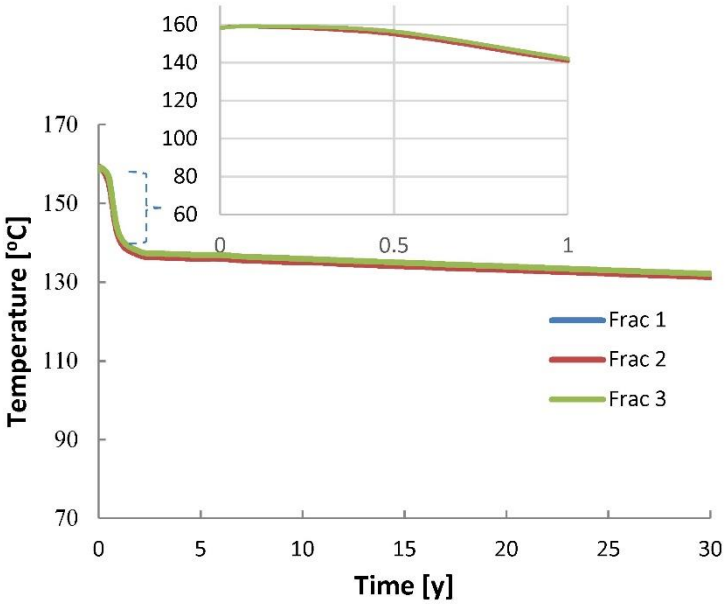

Figure 4.33 Production temperature decline trends within 30 years of period in three fractures at -3760 m injection depth

For the 12-fracture pattern, a total of 48 L/s is injected through the injection well and produced at a fixed bottom hole pressure. Figure 4.34 (a) shows that the geothermal capacity decreases sharply from 35 MW_t to 30 MW_t during six months of the production period due to the sharp decline in production temperature. Later, the declining trend of geothermal capacity slows down and finally reaches 20 MW_t after 30 years of operation. Furthermore, Figure 4.34 (b) shows the produced net energy reaching about 20 PJ during 30 years of operation.

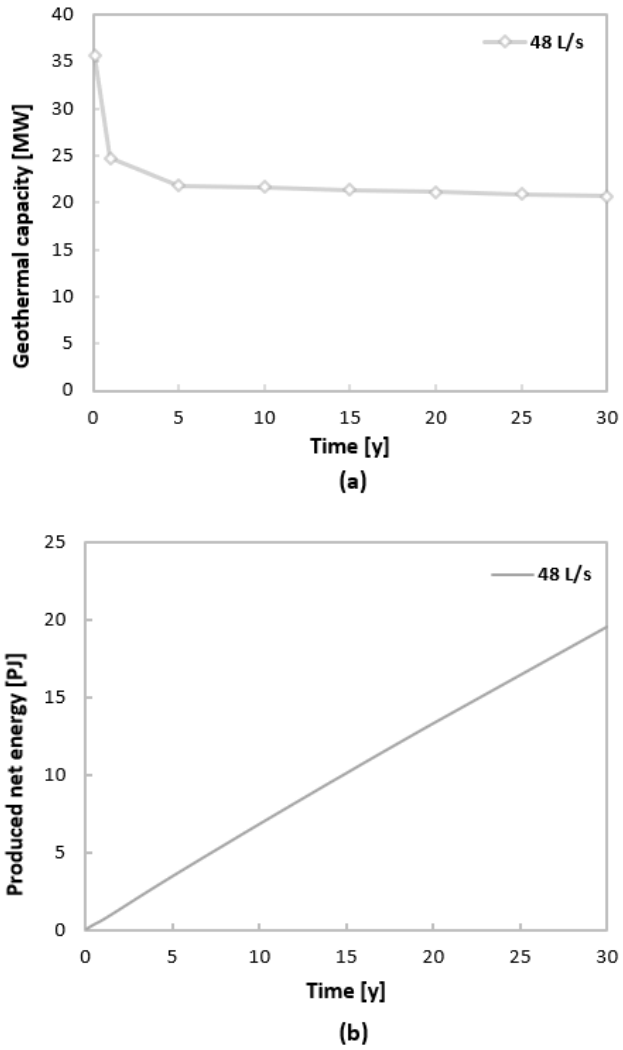

Figure 4.34 Representation of (a) geothermal capacity and (b) net energy production through 12-fracture pattern

4.3.1.3 Scenario 3

In third scenario, energy production estimations have been conducted using higher flow rates, i.e., 8 L/s and 12 L/s per fracture from the lower injection well (-3760 m). It has already been observed from the second scenario that by increasing the distance between injection and production well, water with higher temperature is produced, which ultimately relates to the higher energy production. Therefore, if the flow rate is increased, the chances of more energy production are high. Figure 4.35 compares the temporal evolution of temperature decline in three fracture planes with different flow rates after 30 years of operation. It can be seen that with the increase in flow rates, cold-front areas inside the fractures have been increased, and the maximum areal sweep through each fracture is achieved with a 12 L/s flow rate per fracture.

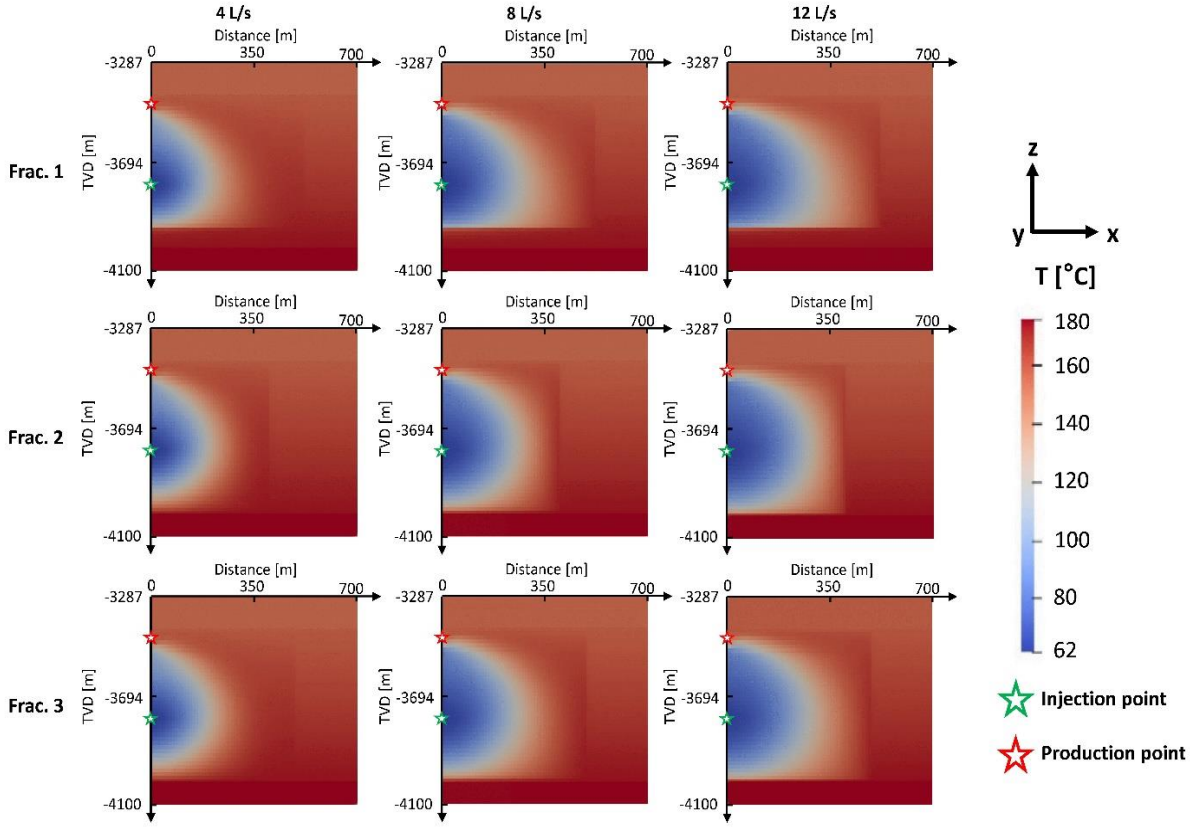

Figure 4.35 Temporal evolution of temperature decline comparison in three fracture planes after 30 years of production with different flow rates per fracture

Figure 4.36 shows the temperature decline trend in the configured model (a) side view (b) front view, and (c) top view at the injection depth, after 30 years of production with 12 L/s flow rate per fracture. Due to the heat conduction, not only fractures are contributing towards energy production, but also the temperature between the area of fracture planes has decreased with production.

For the 12-fracture pattern, a total of 48 L/s, 96 L/s, and 144 L/s is injected successively. Figure 4.38 (a) compares the geothermal capacity decline trends for different flow rates. During 30 years of heat production, the geothermal capacity has decreased from 36 MW_t to 20 MW_t, 53 MW_t to 35 MW_t, and 71 MW_t to 51 MW_t for 48 L/s, 96 L/s and 144 L/s, respectively. The respective decreases are 44.4 %, 33.9 % and 28.1 %. Furthermore, the produced net energy reaches about 20 PJ, 33 PJ, and 48 PJ for 48 L/s, 96 L/s and 144 L/s, respectively (Figure 4.38 (b)).

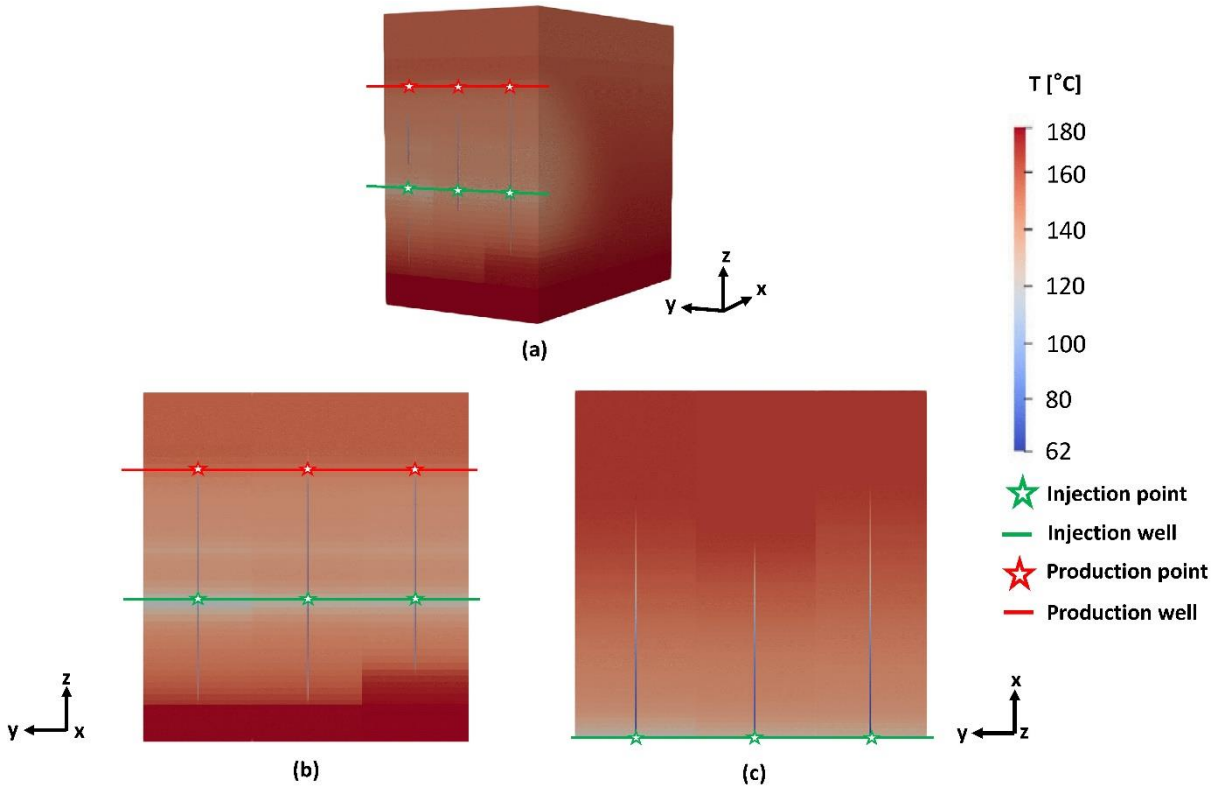

Figure 4.36 Schematic of temperature decline trend in the configured model (a) side view (b) front view and (c) top view at the injection depth, after 30 years of production with 12 L/s flow rate

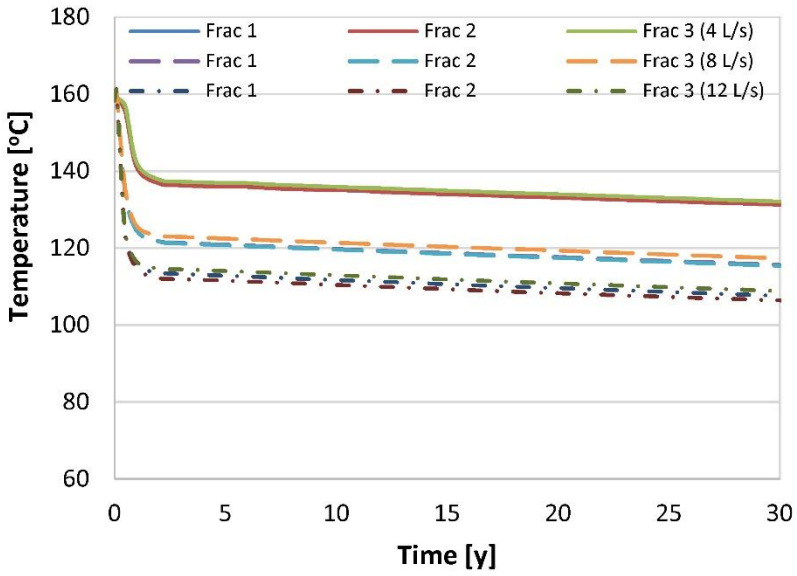

Figure 4.37 Production temperature decline trends within 30 years of period in three fractures with different flow rates

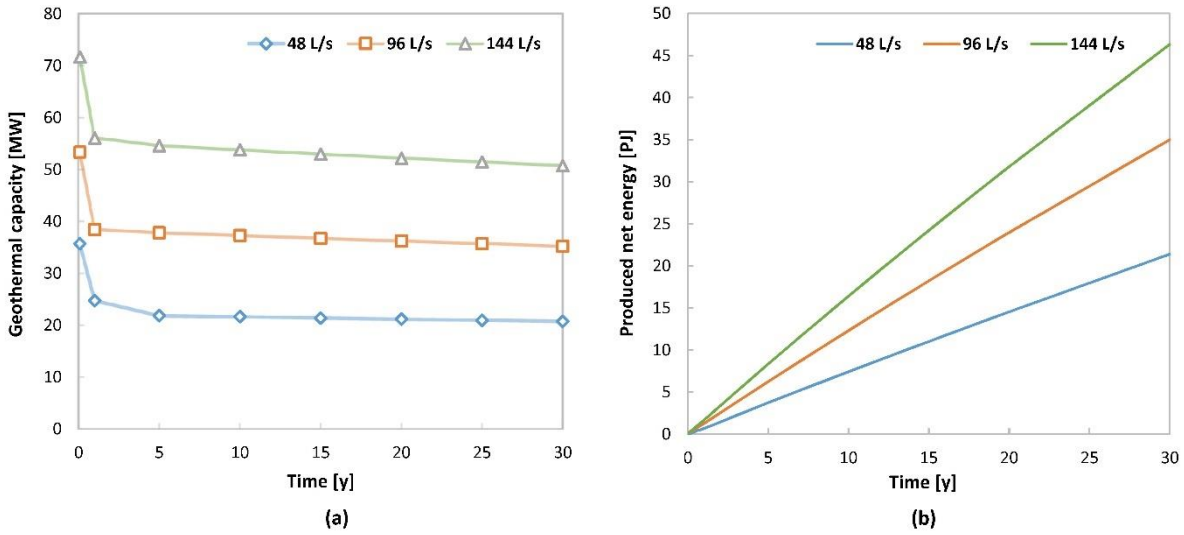

Figure 4.38 Comparative schematic of energy production results through different flow rates from -3760 m injection depth (a) geothermal capacity (b) net energy production

The power generation of a geothermal power plant significantly depends on its working capacity throughout the year. While considering a working capacity of 90 % (10 % tolerance for shut-in), the cumulative power generation at different flow rates is shown in Figure 4.39. The cumulative power generation reaches 1200 GWh for 144 L/s rate compared to 820 GWh and 470 GWh for 96 L/s and 48 L/s rates.

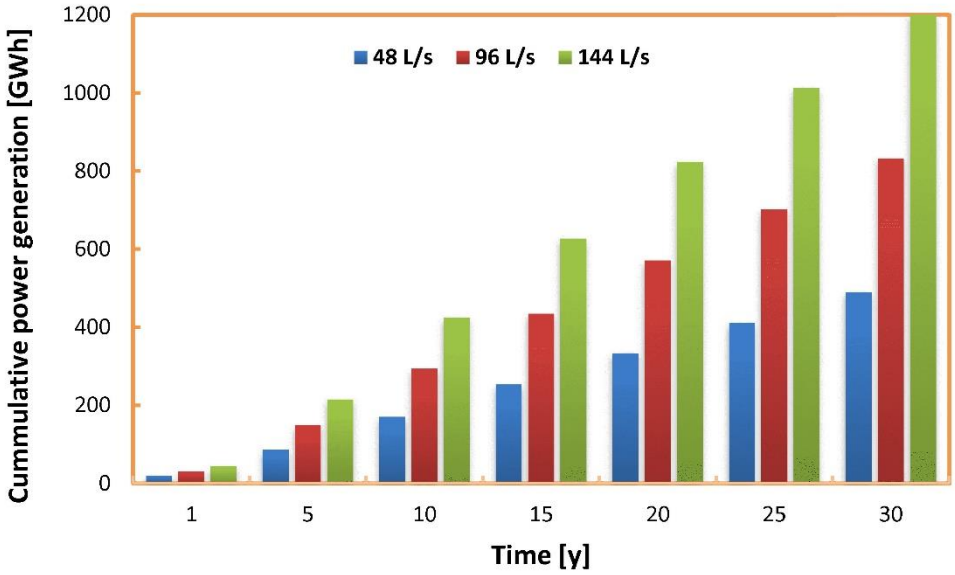

Figure 4.39 Comparison of total power generation during 30 years at different flow rates

Figure 4.40 compares heat production power (W_h) for different flow rates, times, and depths. The solid curves represent heat production power at -3660 m injection depth, while dotted lines show the results of -3760 m injection depth. The increment of only 100 m distance between injection and production wells has shifted the heat production power curves significantly upwards. In addition, for 144 L/s rate, W_h has increased from 30 MW_t to 51 MW_t and W_e from 3.0 MW to 5.1 MW, correspondingly at the end of the production period (Figure 4.41).

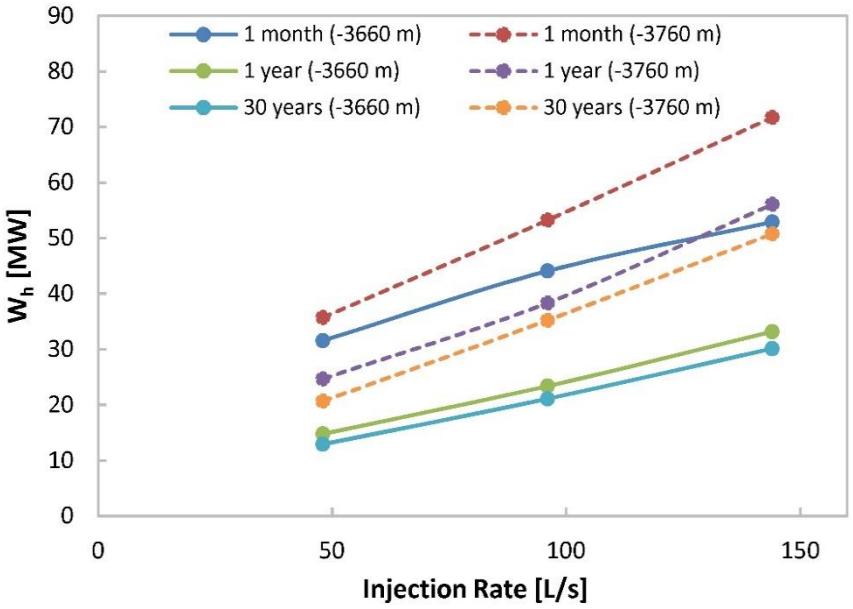

Figure 4.40 Comparison of heat production power (W_h) for different flow rate, time and depth

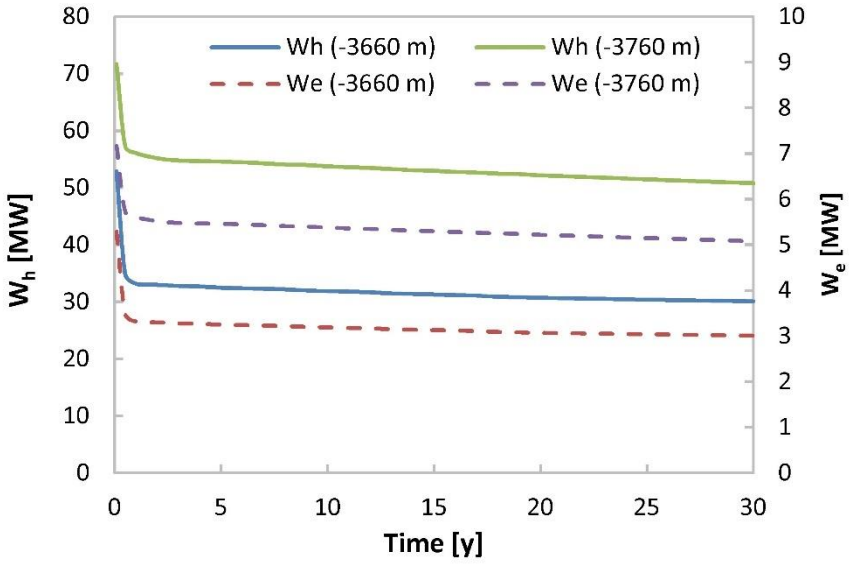

Figure 4.41 Comparison of heat production power (W_h) and electricity generation power (W_e) during 30 years of production at 144 L/s flow rate from different injection depths

The percentage increase in electricity generation at different depths and rates is shown in Figure 4.42. After one month of production, electricity generation has increased to 12.9 %, 20.8 %, and 35.5 % for 48 L/s, 96 L/s, and 144 L/s rates. At the end of 30-year, electricity generation has increased to 60.4 %, 66.8 %, and 68.7 % for 48 L/s, 96 L/s, and 144 L/s rates, respectively. These increasing numbers clearly depict that geothermal energy production is enhanced with the increase in flow rate and distance between injection and production well. Although the results of 96 L/s from the injection depth of -3760 m agrees with geothermal energy production's commercial requirement; however, with 144 L/s rate, geothermal energy production is further improved. Hence the optimized energy production with scenario 3 is achieved.

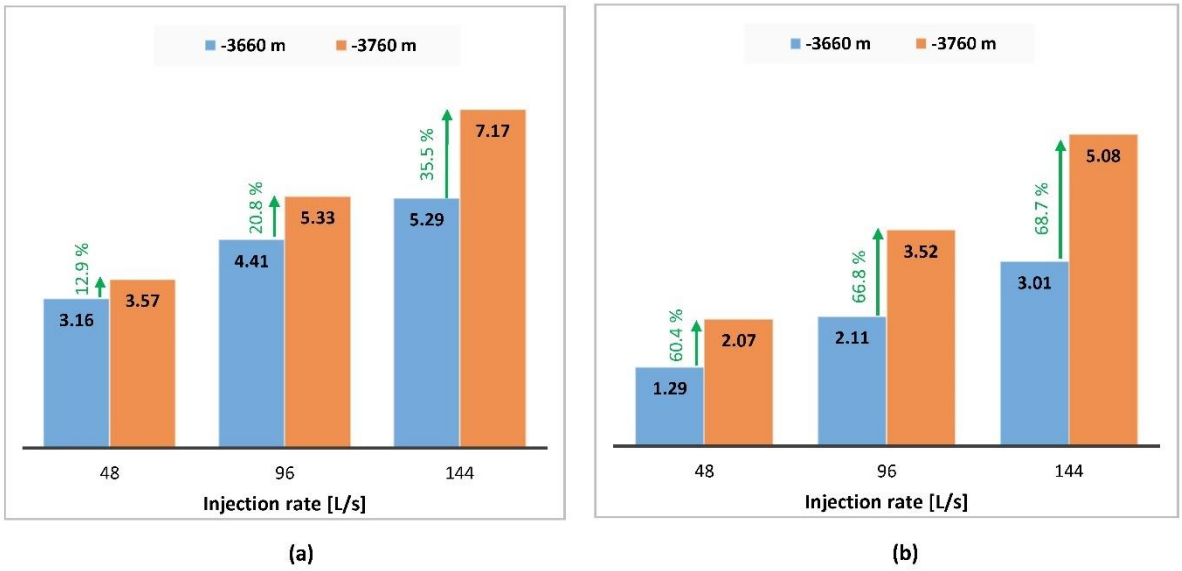

Figure 4.42 Comparison of electricity generation in (MW) for different injection rate and depth after (a) 1 month (b) 30 years of heat production

4.4 Economic analysis

One of the most important aspects of any geothermal field project is utilizing the field in an optimized way so that the project can be executed under economic limitations. In conventional hydrothermal systems, in-situ fluid is produced from the production without excessive drilling and fracturing operations. On the contrary, EGS systems typically involve injection/production of water or any suitable fluid at higher depths to come across the higher rock temperature along with fracturing operations. Due to these reasons, the cost of an EGS project is relatively high.

The economic evaluation for a geothermal project is usually done based on oil or gas projects' field experience due to a lower level of literature details than hydrocarbon projects. Even over 4000 geothermal wells drilled worldwide, their costs are hardly found due to secrecy [118]. The levelized cost of electricity (LCOE) is a simplified and the most common approach used to estimate the economic feasibility of a geothermal power generation system. In this approach, the cost per unit of electricity is calculated by dividing the total investment cost by the total power generation (Eq. (4.8)) [119].

$$LCOE = \frac{Total\ investment\ cost}{Total\ power\ generation} \tag{4.8}$$

Three main categories contribute to the investment cost of an EGS project, i.e., surface costs, subsurface costs, and operation and maintenance costs (O&M). The following sub-sections briefly describe cost estimations of different geothermal fields by considering different cost factors in the currency of dollar ($), and the LCOE for this case study is calculated in the end.

4.4.1 Surface costs/ Surface installation costs

The surface costs mainly include geothermal exploration and equipment installation costs. Geothermal exploration employs the same sort of equipment needed for hydrocarbon exploration, and the cost varies with geological strata and depth of investigation. For about 4000 m depth, the exploration cost is estimated at $ 4.5 million [120]. The surface equipment cost, including personnel wages, can be estimated with the same accuracy as other construction projects such as buildings, roads, etc. The initial investment cost directly related to equipment installation is considered proportional to the installed power plant capacity. For the proposed EGS power plant having a 3 MW capacity in the Daqing oilfield, the surface installation cost was estimated to be $ 6 million [115]. The surface installation costs of five power plants in Iceland were estimated to be 1000 $/kW for the power plant ranging 20-60 MW, and it was concluded that the surface equipment cost varies linearly with plant size [121]. However, unit capital cost decreases exponentially with increased power capacity due to economy of scale. More precisely, it varies from 2000 $/kW for a 5 MW power plant to 1000 $/kW for a 150 MW power plant [115, 122]. Therefore, the total surface cost based on installed geothermal power capacity can be calculated using Eq. (4.9).

$$C_{surf} = C_{exp} + 2000 * P_t \tag{4.9}$$

where C_{surf} is the surface cost [$], C_{exp} is the exploration cost [$], P_t is the installed power capacity [MW].

4.4.2 Subsurface costs

The highest ambiguity in cost estimations is mainly related to subsurface uncertainties. For instance, the field study of the Namafjall field in Iceland estimated subsurface cost of about $ 13 million out of total project cost of $ 35 million for a 20 MW geothermal power plant [121]. For the single flash model geothermal power plant, Chamorro et al. [122] assumed subsurface cost as 50 % of the total initial cost, corresponding to $ 45.3 million.

4.4.2.1 Drilling & completion costs

Drilling and completion costs are considered significant contributors to investment costs such as 20-50 %. They can even exceed 75 % of the total investment capital cost for medium and low-grade EGS [11, 122]. Depending on the subsurface geological sequence, depth, and other factors, the drilling cost can vary drastically for different sites. Oil and gas rigs are often utilized for geothermal projects with certain modifications. These modifications are made to encounter much harder and more abrasive geothermal rocks than sedimentary formations. The situation may worsen for abnormal subsurface conditions such as under-pressured formations, which may lead to high fluid leak-off and contribute to 10-20 % of well cost. Moreover, an increased number of casing strings causes longer drilling time than hydrocarbon well completion [11]. Therefore, it is challenging to calculate the drilling cost accurately. In the last quarter of the 20th century, the oil industry started to adopt the methods of Monte Carlo simulations, uncertainty analysis, and decision trees with certain accuracy. In addition, new methods have been developed to perform drilling cost analysis with minimum error. The widely used methods for oil & gas drilling cost estimation focusing on regression-based techniques include Joint Association Survey (JAS), multidimensional attributes of drilling incorporated in Mechanical Risk Index (MRI), Directional Difficulty Index (DDI), and Difficulty Index (DI) models [123]. Not even a single such analytical tool has been developed yet for the geothermal industry to perform cost analysis independently. Due to the resemblances of equipment and materials between hydrocarbon and geothermal field projects, hydrocarbon drilling cost trends have been commonly used for geothermal wells.

Zang et al. [115] estimated the cost of one drilling well at $ 15 million, having vertical and horizontal lengths of 4500 m and 3000 m, respectively. Whereas $ 5 million could be saved

using an abandoned well in the same field. The drilling costs of Soultz EGS wells for 5100 m depth varied from $ 6.57 million for GPK3 well to $ 5.14 million for GPK4 well in 2003 and 2004, respectively [124]. Lei et al. [120] conducted an economic analysis for Qiabuqia geothermal field China and calculated the total drilling cost of approximately $ 9.36 million for three vertical and horizontal wells with vertical and horizontal lengths of 11,100 m and 1500 m, respectively. The assessment of MIT (Massachusetts Institute of Technology) in 2004 suggested the drilling cost of about $ 13.3 million in Clear Lake country for a 6 km well length with six casing strings [37].

4.4.2.2 Well Logging costs

A detailed analysis of the encountered formations through wireline logging is necessary that further helps to perform stimulation operations. The United States Department of Energy has presented a comprehensive evaluation of geothermal logging technology costs based on the critical assessment of research programs during 1976-2010 [124]. Due to the high temperature of geothermal reservoirs at greater depths, borehole conditions are relatively problematic compared to oil & gas wells. Therefore, the use of special logging devices and mud coolers becomes essential. In addition, logging cost depends on the type of logging instrument, strength, and accuracy. For high precision logging till -3700 m depth, the charge has been estimated at $ 0.45 million in Qiabuqia geothermal field, China [120].

4.4.2.3 Stimulation costs

The role of hydraulic stimulation for reservoir development is critical, especially in tight formations in an EGS field. Generally, the cost of hydraulic stimulation is relatively more minor than other operations. Stimulation cost mainly depends on the fracturing fluid and proppants used during fracturing operations. Moreover, the fluid volumes are also proportional to cost. The other expenditures include equipment costs (fracturing trucks, ancillary equipment, etc.) and operational costs. Lei et al. [120] estimated the fracturing cost at $ 0.45 million using slick-water for different reservoir scenarios. Zhang et al. [115] assumed one fracturing treatment cost to be $ 0.486 million for the Daqing oilfield at a depth of about -4500 m. Considering these field estimations for stimulation operation, $ 4.5 million is expected for this case study's excessive stimulation job.

4.4.3 Operation & maintenance costs (O&M)

Once the well is drilled and the reservoir is developed, costs of further operations are estimated through operation and maintenance costs (O&M). These costs involve internal energy consumption for injection and production pumps and reservoir maintenance. Likewise, unit capital surface equipment cost, O&M costs also decline exponentially with increasing production capacity. The frequently used approximation varies exponentially, i.e., from 20 $/MWh to 14 $/MWh for 5 MW and 150 MW plant capacity, respectively [120, 122]. The unit O&M cost can be estimated using Eq. (4.10) in $/MWh.

$$C_{O\&M} = 20 \exp(-0.0025\ (P_t - 5)) \tag{4.10}$$

According to the simulation results of this case study, the LCOE is calculated for the average plant capacity of 6.1 MW. Therefore, O&M costs are estimated to be 19.94 $/MWh. Based on the literature, the two wells' drilling cost, including horizontal and vertical sections, is estimated to be $ 20 million. Besides, exploration and logging costs are calculated at $ 4.5 million and $ 0.45 million, respectively. Consequently, the sum of drilling, stimulation, logging, and exploration costs is estimated at $ 29.45 million. While mentioning all expected geothermal power plant costs above, the total cost is calculated using Eq. (4.12).

$$C = C_{surf} + C_{sub} \tag{4.11}$$

$$C_{total} = 29.45 + 2000 * P_t + W_t * C_{O\&M} \tag{4.12}$$

where W_t is total power generation in 30 years [GWh].

The LCOE for third scenario with a flow rate of 144 L/s is calculated at 5.46 c$/kWh, which is quite economical. Figure 4.43 shows the proportions of the total cost for different segments. The major contributors in total cost are drilling and O&M costs during 30 years of power generation, and the proportion together is about 66 % of the total investment cost.

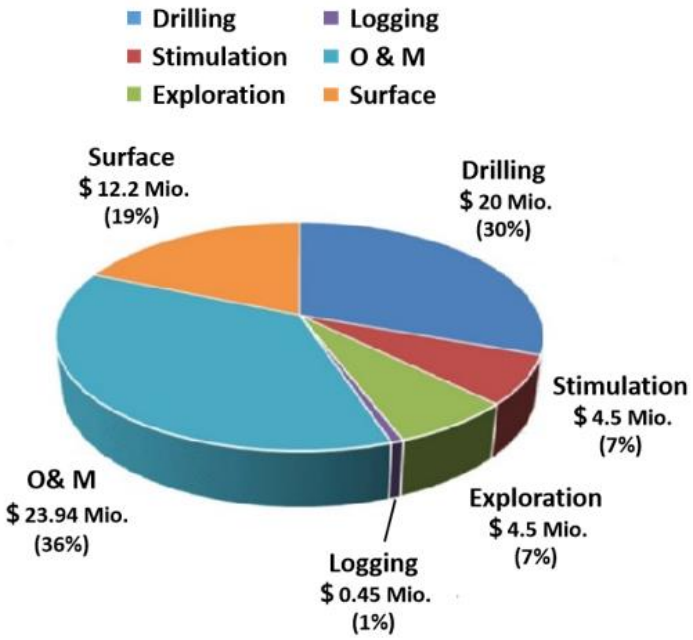

Figure 4.43 Division of total cost in different operation expenditures

The economic analysis is conducted for the study results of 12 fractures on one side of the injection well, as shown in Figure 4.11. The generated power can be doubled by creating additional 12 fractures to the opposite side using the same injection well. Furthermore, the LCOE will decrease significantly using the same vertical section of the injection well.

Summary

In this chapter, a case study is performed that integrates the production of heat and electricity using the engineering data of GeneSys, and an EGS project for the MHH-GeneSys region in the North German Basin is proposed having one injection and two production wells. The reservoir model parameters are believed to be reliable from the well-matched temporal evolution of BHP (history matching). Massive multiple hydraulic fractures are generated through a horizontal well, incorporating the stress superposition effect. Numerous simulations are conducted with different fracture spacing having the same injection plan. It is observed that stress shadow superposition enlarges in massive multiple fracturing operations, which eventually distort the fracture propagation, especially with lower fracture spacing. In addition, the shape of the newly created fracture is highly dependent on the previous fracture configuration. After the fracturing results, several simulations are performed for heat and electricity production using different well arrangements and flow rate scenarios.

The simulation results show that during continuous cold-water injection, the temperature inside the fractures as well as the surrounding of the fracture planes decreases sharply. However, less well spacing and low flow rate restrict the fluid flow within the fractional half-fracture area of each fracture, signifying the requirement of energy production optimization. The increase in flow rate enhanced the energy production results broadly; however, further simulations are conducted to acquire improved results.

Under the prevailing geological conditions, the generated fractures at higher depth attain lesser fracture lengths and higher fracture heights due to the difference in stress interference. The energy production results depict that the tendency of temperature decline in each fracture area increases with the increase in flow rate and well spacing. The optimized installed power capacity of the proposed EGS project declines from 7.17 MW to 5.08 MW for 144 L/s flow rate in a 12-fracture pattern. Moreover, the expected total cost for a multi-well multi-hydraulic fracture system is estimated to be $ 65.59 million, having significant shares of drilling and O&M costs. The LCOE is calculated at 5.46 c$/kWh, which is substantially economical compared to Germany's current electricity price. In addition, the generated power potential can be doubled by creating additional 12 fractures to the opposite side using the same injection well that can further decrease the LCOE.

5 Regenerative EGS using surplus wind & solar energy

5.1 Introduction

The energy supply from renewable energy sources like wind or solar is highly dependent on weather conditions and often mismatch the instantaneous energy demand. During times of high renewable energy production, the power transmission lines may not be adequate to carry the load and, therefore, may have to shut down the power generation plants [125]. One of the suitable options to avoid such interruption in energy production is to store surplus energy that can compensate for the energy deficit in times of low power production. Due to the favorable heat storage properties, water and hard crystalline rocks are considered suitable storage mediums with large volumes at a relatively low cost. Different methods have been used for underground thermal energy storage (UTES) that include: Aquifer thermal energy storage (ATES), Borehole thermal energy storage (BTES), Tank thermal energy storage (TTES), Pit thermal energy storage (PTES), Cavern thermal energy storage (CTES), and Fractured thermal energy storage (FTES) (Figure 5.1).

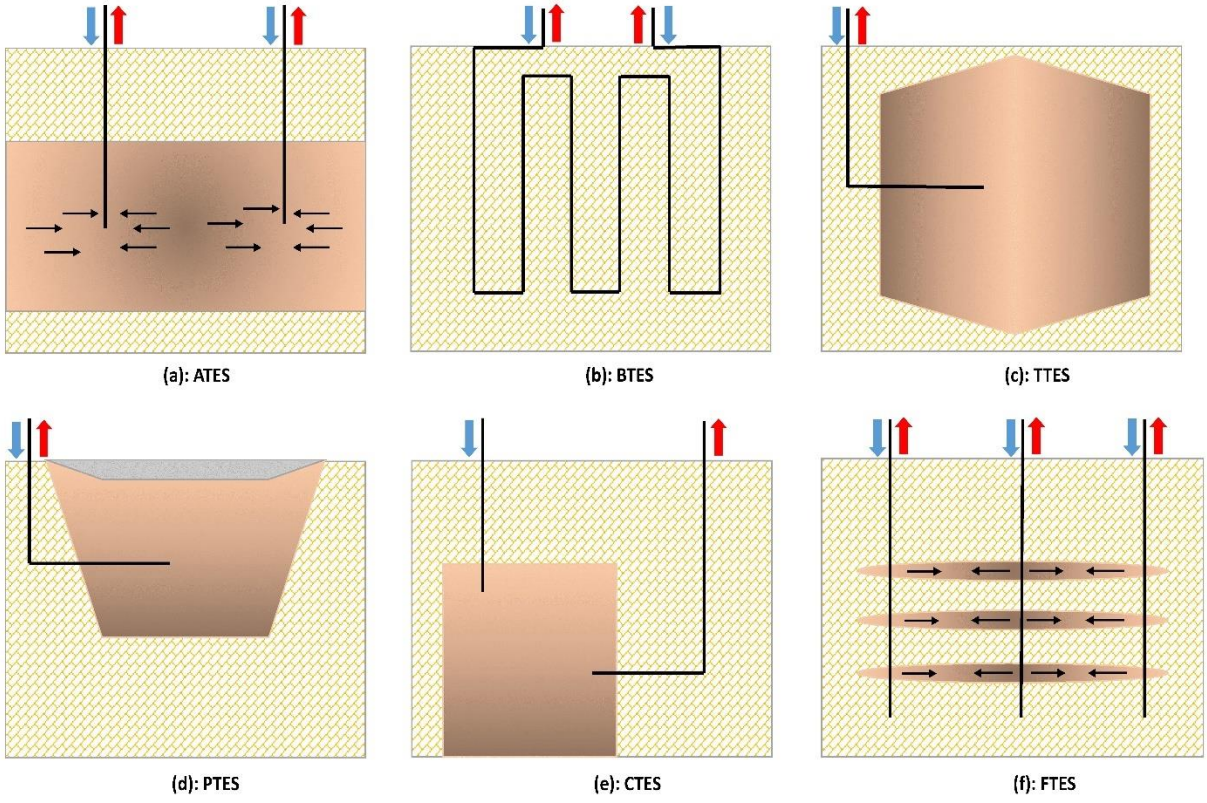

Figure 5.1 Schematic of different underground thermal energy storage methods

ATES technology involves energy storage by injecting and withdrawing the ground water through high permeable layers at shallow depths in a cost-effective way. This technology is used for the heating and cooling of buildings. For example, surplus energy produced by solar panels in summer is stored in shallow aquifers underneath the German Parliament in Berlin, and this shallow aquifer UTES has been operational since 2002 [126]. More than 2800 ATES systems are currently in operation, extracting more than 2.5 TWh of heating and cooling per year [127]. Generally, LT-ATES systems store low-temperature heat and cold in a range of 5 ºC to 30 ºC and cannot fulfill the industrial and large district heating demands [128]. In contrast, HT-ATES can store the energy of higher temperatures (> 60 ºC) but are limited due to legal and technical constraints. The injection of high-temperature water at shallow depths can cause potential contamination of drinking water and can raise environmental concerns. In addition, high energy loss due to a larger temperature gradient makes the energy storage process less efficient. However, one of the main advantages of HT-ATES is the utilization of stored energy without multiple heating pumps that can further improve energy savings. Moreover, high-temperature storage operations in the deep reservoir may not perturb near-surface ground water horizons. Therefore, high energy recovery is possible after storing high-temperature water at greater depths [129]. Some of ATES projects worldwide, along with technical and geological characteristics, are provided in Table 5.1.

Table 5.1 Overview of technical characterization of some ATES projects worldwide [127, 130]

Project name	Location	Depth [m]	Year	Injection temperature [ºC]	Heat source	Status
Neubrandenburg	Germany	1250	2004	85-90	CHP	iO
Reichstag	Germany	320	2000	70	CHP	D/iO
BMW-Dingolfingen	Germany	500-700	2016	120	CHP	E
Utrecht	Netherland	192-290	1991	90	CHP	A*
Duiven	Netherlands		2015	> 140	Waste combustion	fs
De Uithof	Netherlands	4 – 45	1991	90	CHP	D/c
Mobile	US	36-61	1976	55	Industrial	E/c
ST. Paul	US	182-244	1982	117	Industrial	E/c
Plaisir	France	500	1987	180	Industrial	E/c

CHP: combined heat and power, A*: Applied, c: closed, D: demonstration, E: explorative, iO: in operation, fs: feasibility study

The BTES systems are mostly installed for domestic heating and cooling purposes depending on solar technology, and these systems are getting rapid attention worldwide [131, 132]. In these systems, a series of vertical or horizontal U-tube pipes are placed typically with a uniform spacing to form a closed-loop heat exchanger [133]. The heat between the fluid and the ground layers is transferred and can be computed through numerical models. The BTES systems are potentially economic as these allow storage of surplus energy in a space-efficient manner. One of the best examples of the BTES technology in operation is Drake Landing Solar Community (DLSC), located in Okotoks, Canada. In DLSC, solar energy is stored seasonally in an array of 144 boreholes having approximately 34,000 m^3 subsurface BTES space [134].

In TTES, PTES, and CTES systems, heat and cold are stored in thermally stratified storage tanks, pits filled with water or water and gravel, and in naturally occurring cavities or caverns, respectively [127]. The TTES systems are constructed with concrete and steel, having size up to 12000 m^3 [135]. Due to the high heat capacity of water, thermal energy can be stored in a PTES system in a cost-efficient way. The insulation around the pit is provided to avoid any heat leakage, and heated water is sent to the consumer while cooled water is injected at the bottom. PTES systems have been constructed in a few places in Denmark, having the largest size of 75000 m^3 [135]. There are very few examples of CTES systems in the world. One of the active CTES facilities is located in Oulu, Finland, built on a converted oil storage cavern with a storage capacity of about 10 GWh [136]. HYDROCK is an application of FTES that uses hard crystalline rocks. It has advantages of increased heat transfer area and decreased boreholes compared to other UTES methods. The study results of Hellström and Larson 2001 [137] showed that a system of 25 fractures network having 5 m in radius could provide 2 GWh thermal energy seasonally.

Altogether, UTES systems are suitable for surplus thermal energy storage; however, the success of a UTES project is highly dependent on the local energy demand and in-situ geological conditions. According to an estimate, yearly storage demand in Germany varies considerably but may reach 50 TWh of electrical energy [138]. About 40 % of net electricity has been generated from wind and solar energy resources in 2020, as shown in Figure 5.2. In fact, the German Federal Cabinet has planned to expand the offshore wind energy capacity to 40 GW by 2040 [139].

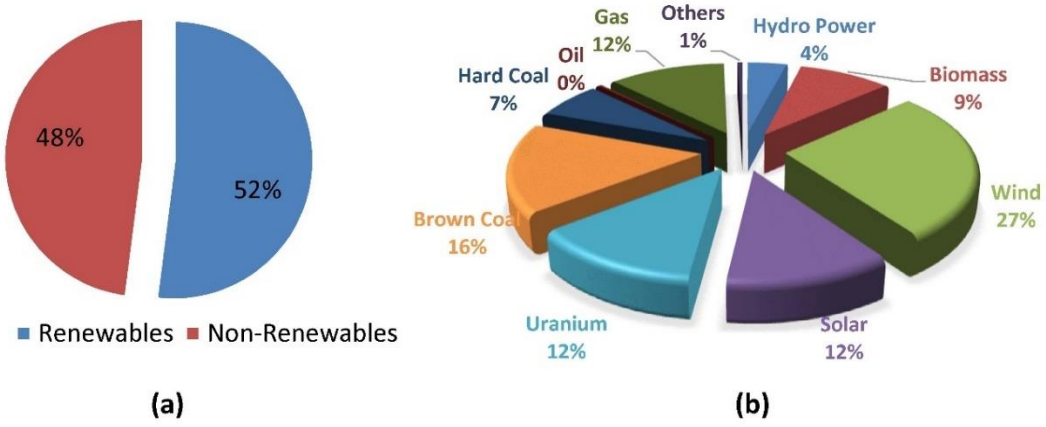

Figure 5.2 Net electricity generation in Germany-2020

5.1.1 Wind energy in Germany

Electricity from wind energy is produced with the help of wind turbines that convert the kinetic energy of the wind into electric energy by utilizing propeller-like blades which spin a generator. Wind turbines are constructed onshore or offshore like oceans and lakes, depending on wind yield and land availability. The average size of onshore wind turbines is around 2.5 to 3 MW, which can supply power to more than 1500 households. In comparison, the offshore wind turbine is around 3.6 MW. An increasing share of wind electricity generation has been observed in Germany during the last two decades (Figure 5.3). In fact, wind energy crossed nuclear and brown coal energy in electricity production in 2020 [139].

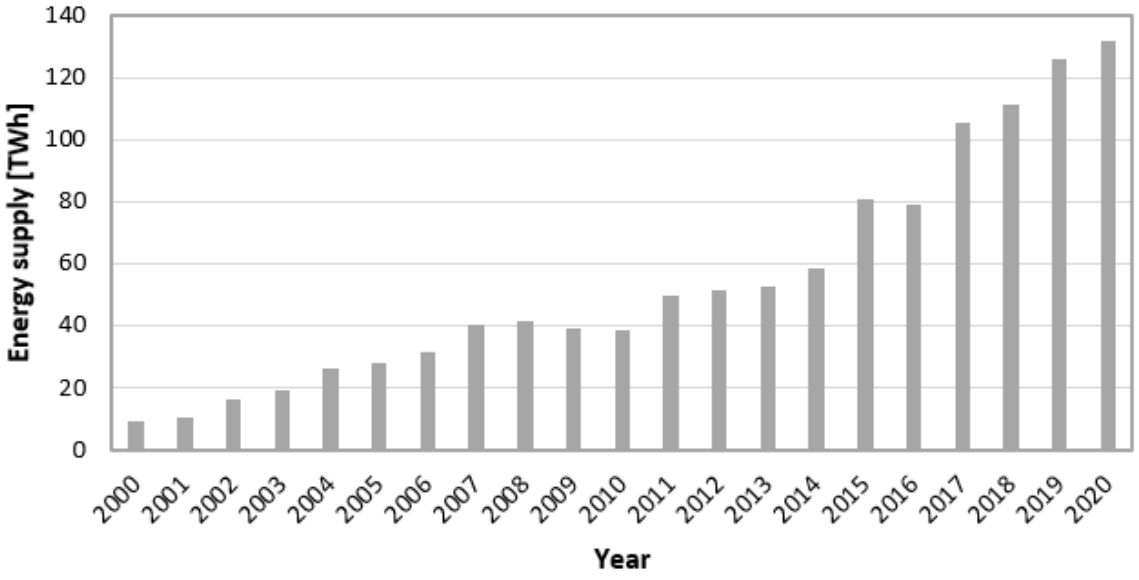

Figure 5.3 Electricity generation from onshore and offshore wind energy during last two decades in Germany

The wind power installations are much higher in the North Sea compared to the Baltic Sea due to relatively higher wind yield. Out of the total of 1460 wind turbines, 1230 are located in the

North Sea [140]. The capacity of offshore turbines has been increased successively in the past six years. In June 2020, 32 offshore wind turbines in the German Exclusive Economic Zone were added to the grid. The cumulative offshore wind capacity is about 7.76 GW which is expected to become 40 GW by the end of 2040 (Figure 5.4) [140].

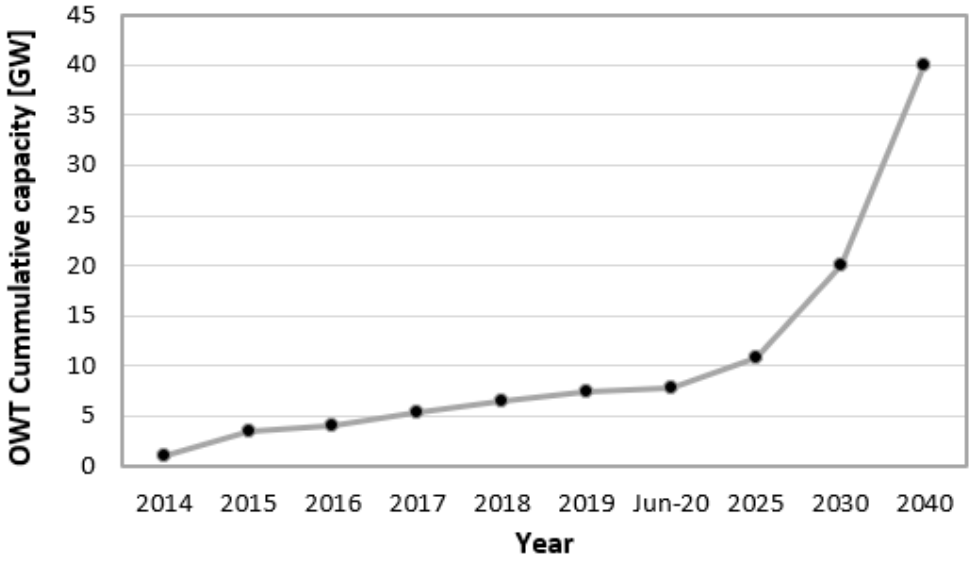

Figure 5.4 Offshore wind energy development forecast

5.1.2 Solar energy in Germany

Solar cells in photovoltaic (PV) systems convert sunlight into electricity or heat. Germany is one of the largest solar power generation countries globally despite having low sunshine hours. It had been made possible by its Renewable Energy Act (EEG) introduced in 2000. In order to accomplish maximum energy needs from renewables, the EEG provided an opportunity of guaranteed remuneration for investors to invest in solar panels that boosted solar power generation. The EEG-2021 has set a target of about 65 % gross electricity consumption from renewable energies by 2030, which requires an annual average PV addition of at least 5-10 GW along with the expansion of wind power [141]. During the last decade, a noticeable increase in solar power generation has been observed (Figure 5.5). In 2020, about 12 % of electricity was contributed to the public electricity grid with a generation power of 50.6 TWh [142].

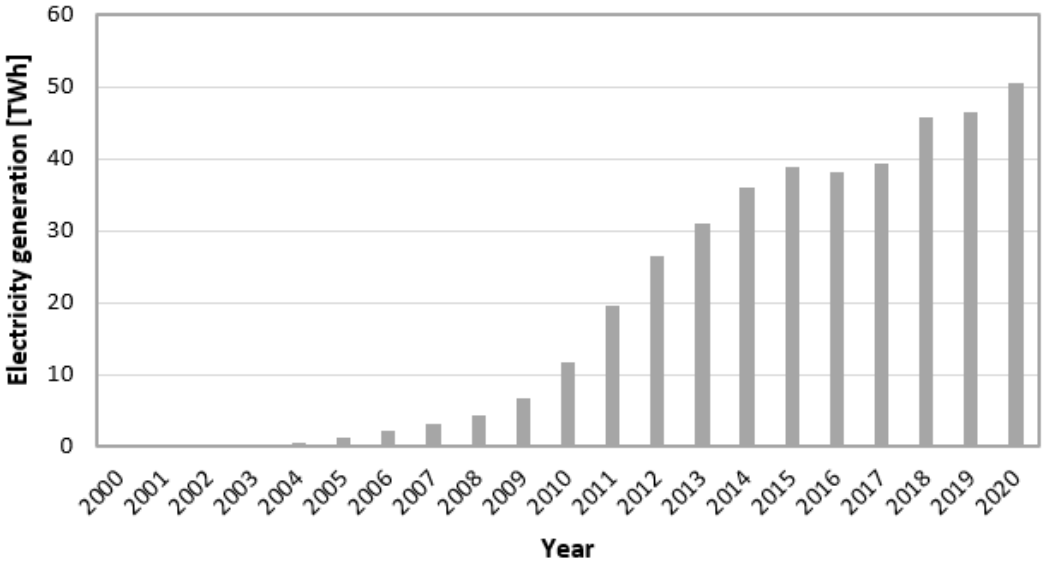

Figure 5.5 Electricity generation from solar energy during last two decades in Germany

Although a record amount of clean energy is produced in Germany today, its grid capacity is not enough to transport the power down to load centers in the south [140]. This may lead to a negative wholesale electricity price situation, where a consumer is being paid to use electricity. The surplus energy situations require the development of an energy storage mechanism through which energy can be produced back during times of low production and high demand.

5.2 Energy storage and recovery in hydraulically fractured EGS

The utilization of underground heat storage is the requirement of the recent era. It can help store energy temporarily and reduce the peak loads with intelligent handling of waste energy. In this work, an innovative concept of EGS is proposed that integrates heat and electricity production and surplus energy storage. The UTES concept for seasonal energy storage and production is used, and a deeply fractured medium is analyzed as the heat exchanger. The massive multiple fractured model of the MHH-GeneSys site that has been used initially for geothermal energy production is further investigated for the surplus renewable energy storage and recovery. Using this innovative approach, it is proposed that the life of an EGS project can be extended. The schematic of regenerative EGS under different working modes is shown in Figure 5.6.

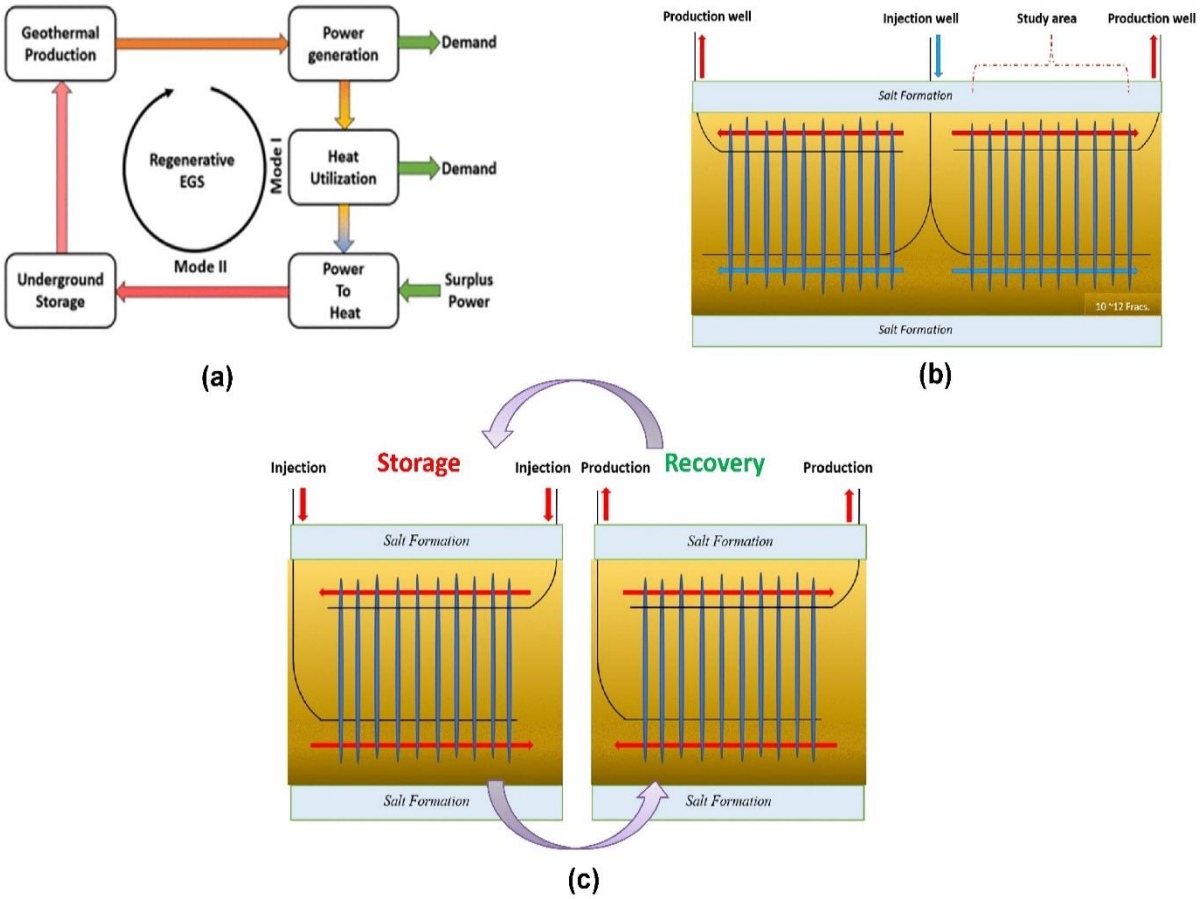

Figure 5.6 Schematics of cyclic regenerative enhanced geothermal system (a) flow chart (b) production stage - mode I (c) energy storage and recovery stage - mode II

The results of geothermal energy production for 30-years of scenario-3 in chapter 4, have been adopted as the initial model conditions for the surplus energy storage. However, this energy storage and borehole cleaning concept can be applied at any time of the EGS project's life. The temperature inside the model and surrounding the fractures has been depleted considerably. The depleted energy model is shown in Figure 5.7. In addition, different parameters of injection fluid are provided in Table 5.2.

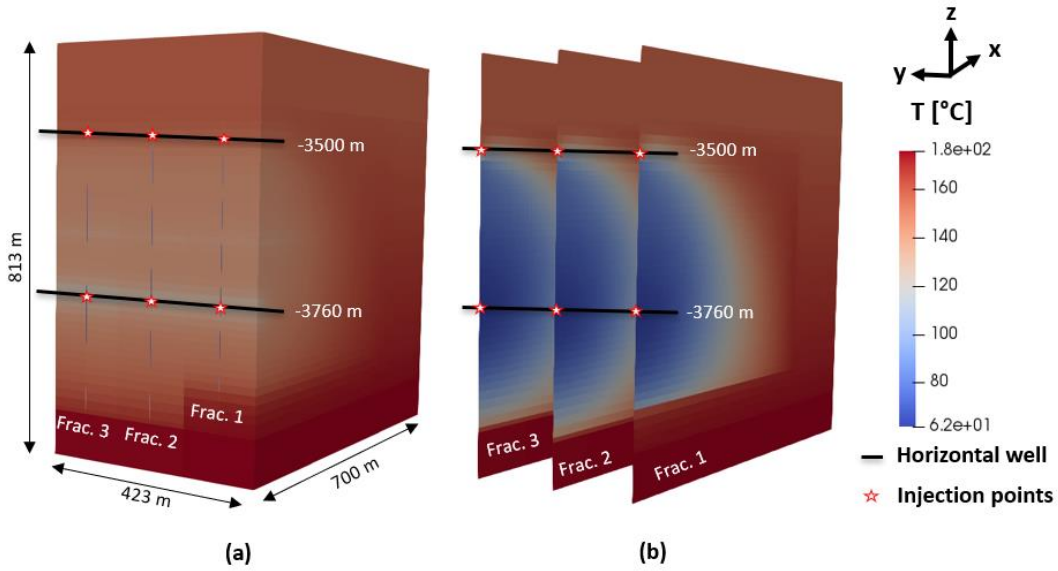

Figure 5.7 Schematic of initial conditions for energy storage (a) model and (b) 3-fractures

Table 5.2 Summary of the fluid injection parameters for energy storage and recovery

Parameter	Value	unit
Injected fluid	water	-
Injection temperature	200	[^{o}C]
Injection rate	48 (for 12 fractures)	[L/s]
Formation heat conductivity	2.5	[W/m ^{o}C]
Injection pressure	20	[MPa]

In this study, energy storage efficiency is evaluated using a recovery factor, defined as the ratio of recovered energy to stored energy with respect to ambient reservoir temperature when an equal amount of water is injected and produced [128, 143]. Mathematically, it is described in Eq. (5.1) and Eq. (5.2).

$$RF = \frac{E_{ext}}{E_{inj}} = \frac{\int_{begin}^{end} Q_t(T_{ext} - T_{nat})dt}{\int_{begin}^{end} Q_t(T_{inj} - T_{nat})dt} \tag{5.1}$$

$$VR = \frac{V_{ext}}{V_{inj}} \tag{5.2}$$

where Q_t is pumping rate [L/s], T_{ext} is extraction temperature [^{o}C], T_{inj} is injection temperature [^{o}C], T_{nat} is the ambient reservoir temperature [^{o}C], d_t is the time increment, and VR is the volume recovery [-].

The recovery factor equal to zero means none of the stored energy is recovered or produced, and the increase in recovery factor will decrease the storage efficiency and vice versa. The heat loss in the borehole is assumed as negligible. Therefore, the recovery factor calculated at production points based on extraction temperature can be considered equal at surface conditions.

In order to investigate the response of massive multiple fracture systems during energy storage and recovery, a single cycle is analyzed firstly. The single-cycle describes hot fluid injection for one-month, three-month, and six-month periods, firstly, and production of injected fluid for one-month, three-month, and six-month periods, successively. The temporal evolution of the increase and decrease in temperature in the fractured system during storage and recovery is shown in Figure 5.8. As the injection begins from the injection point, the high-temperature region is formed around the injection perforations. The hot fluid front increases outside in expansion. It can be seen that the expansion of the hot front increases with the increase in the injection period. During the recovery phase, equal volume of the injected fluid is produced; however, due to the high temperature of injection fluid, the temperature inside fractures has been increased and is shown in Figure 5.8 (b).

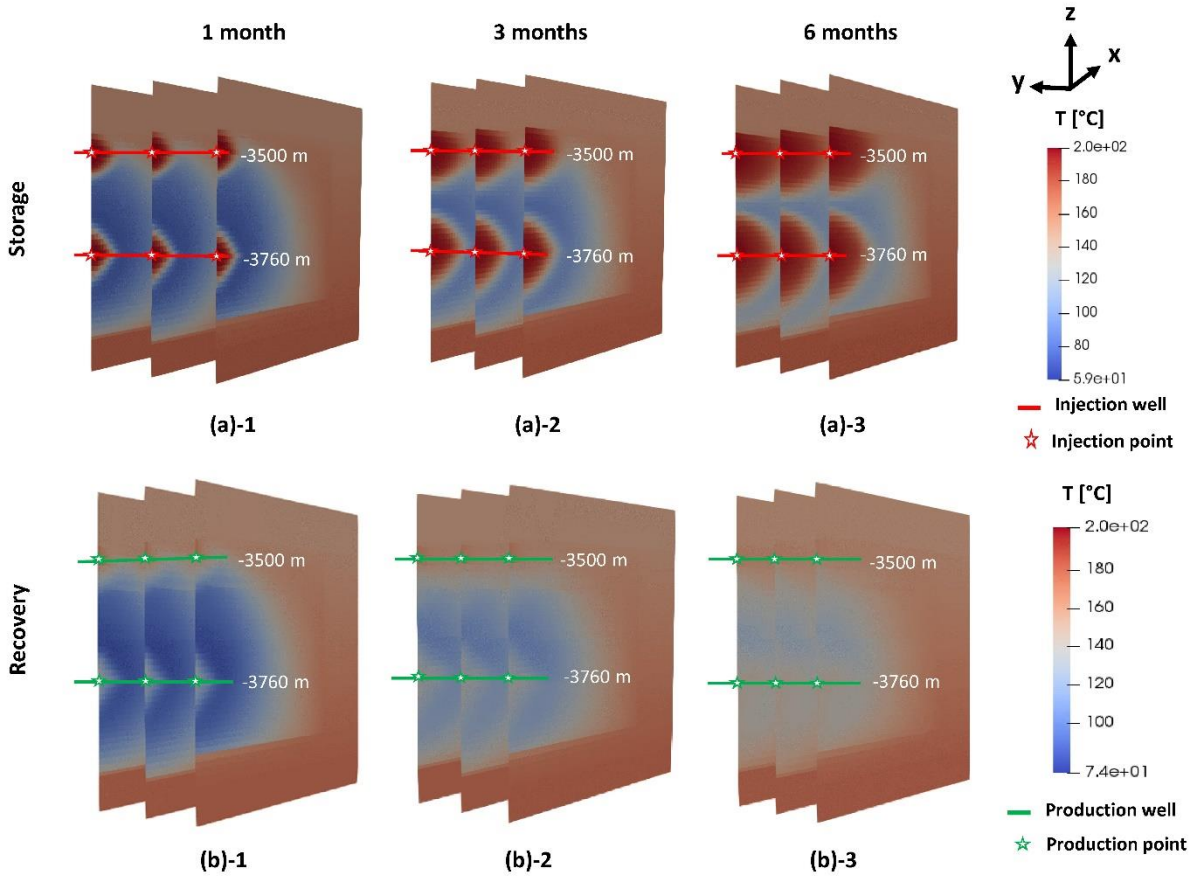

Figure 5.8 Temperature change in fractures at the end of single cycle for different periods during (a) storage phase (b) recovery phase

Figure 5.9 shows each fracture's energy storage and recovery trends for different periods. It can be seen that the heat storage decreases with the increase in the time duration of injection/production cycles. This trend is due to the injection of less energy during the one-month cycle compared to the six-month cycle. In addition, at the start of the operation, most of the heat is lost in fractures due to heat conduction/convection processes and the initial low-temperature region. As a larger amount of energy is injected during the six-month cycle, the energy recovery is more in comparison with the monthly and quarterly cycles. Furthermore, it can be observed that each fracture recovery and storage results are quite the same. Using the results of single energy storage and recovery cycles, continuous injection/production cycles are investigated further.

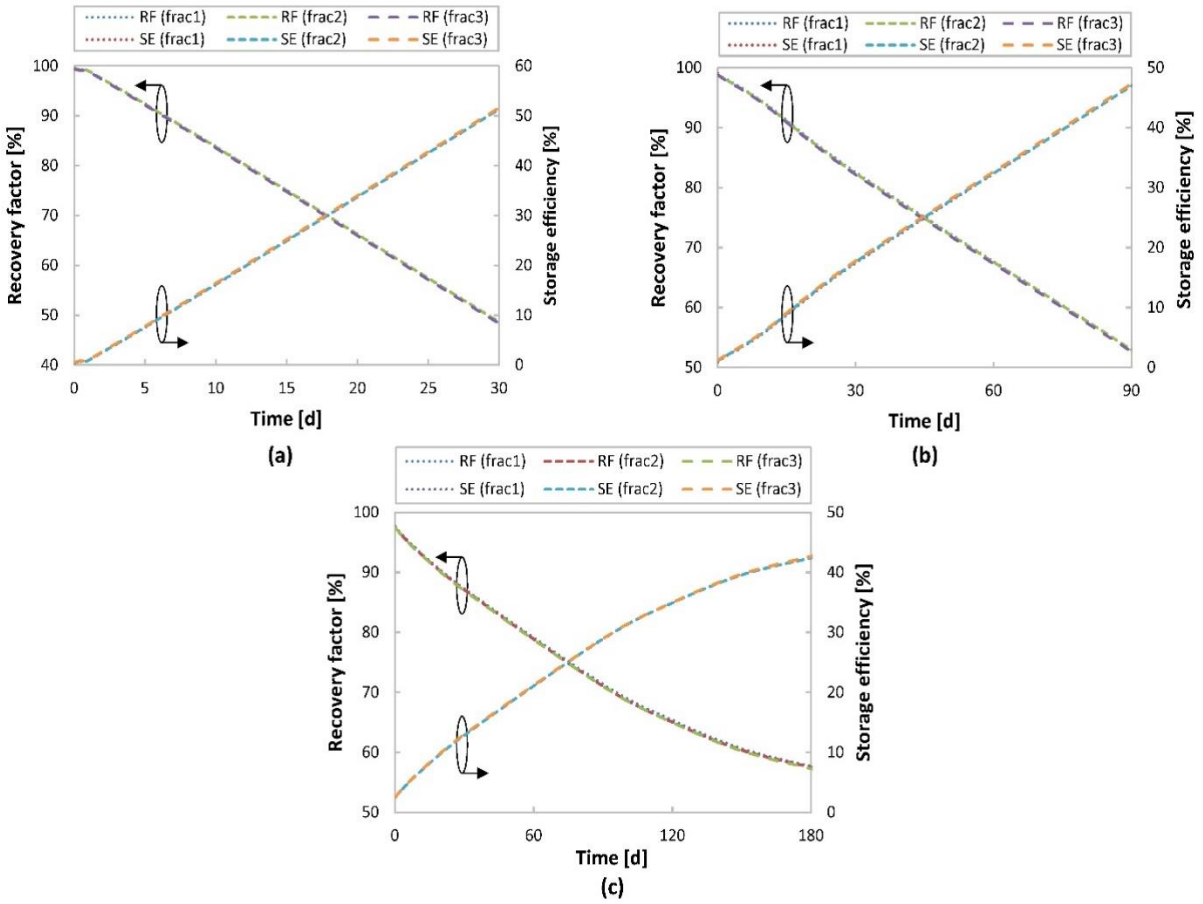

Figure 5.9 Trends of recovery factor and storage efficiency during single cycle (a) monthly (b) quarterly (c) semi-annually

5.3 Continuous injection/production cycles

Continuous injection/production cycles have been analyzed by adopting equal fluid volume and time without pause. For example, in the case of the monthly cycle, hot water is injected through both wells that flow inside the fracture at a constant injection rate. Afterward, the injected fluid is produced from both wells for one month. Figure 5.10 shows the recovery factor and storage efficiency results during five-continuous cycles for monthly, quarterly, and semi-annual periods. It is observed that after every cycle, the recovery factor increases while storage efficiency decreases. In the first cycle, maximum energy is stored in the reservoir due to initial low-temperature conditions, and therefore, the recovery factor is minimum. The recovery factor increases with the increase in cycles due to the increased injected energy. It increases from 48 % to 75 %, 52 % to 70 %, and 57 % to 65 % for monthly, quarterly, and semi-annual cycles. Contrarily, the storage efficiency decreases after every cycle. In addition, heat injection for a longer duration causes more heat loss due to heat conduction/convection processes between rock formation and fluid during continuous cycles. Therefore, less recovery is achieved for

longer period cycles. Figure 5.12 shows the change in temperature inside the fractures during different time cycles.

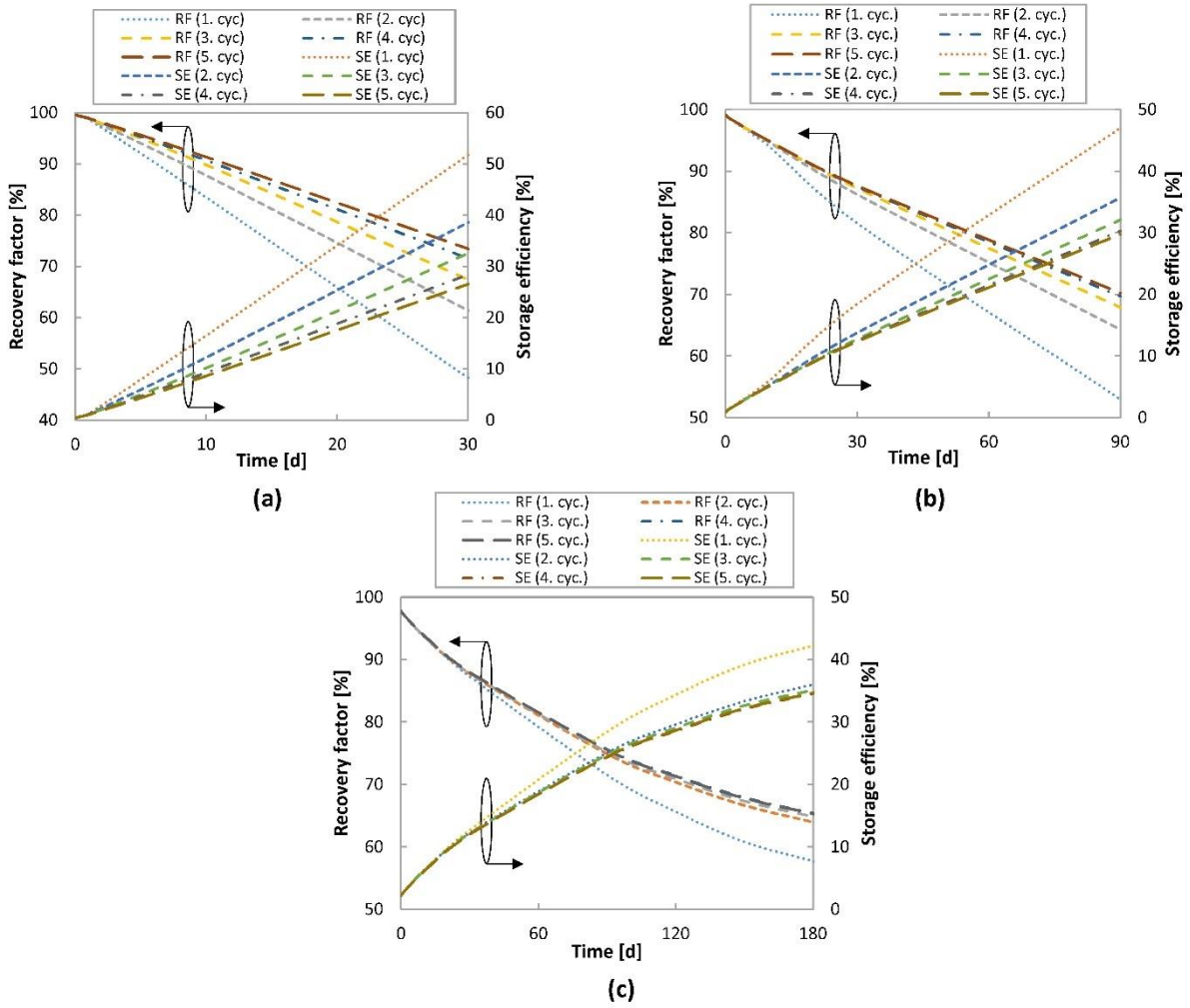

Figure 5.10 Trends of recovery factor and storage efficiency during five continuous cycles (a) monthly (b) quarterly and (c) semi-annually

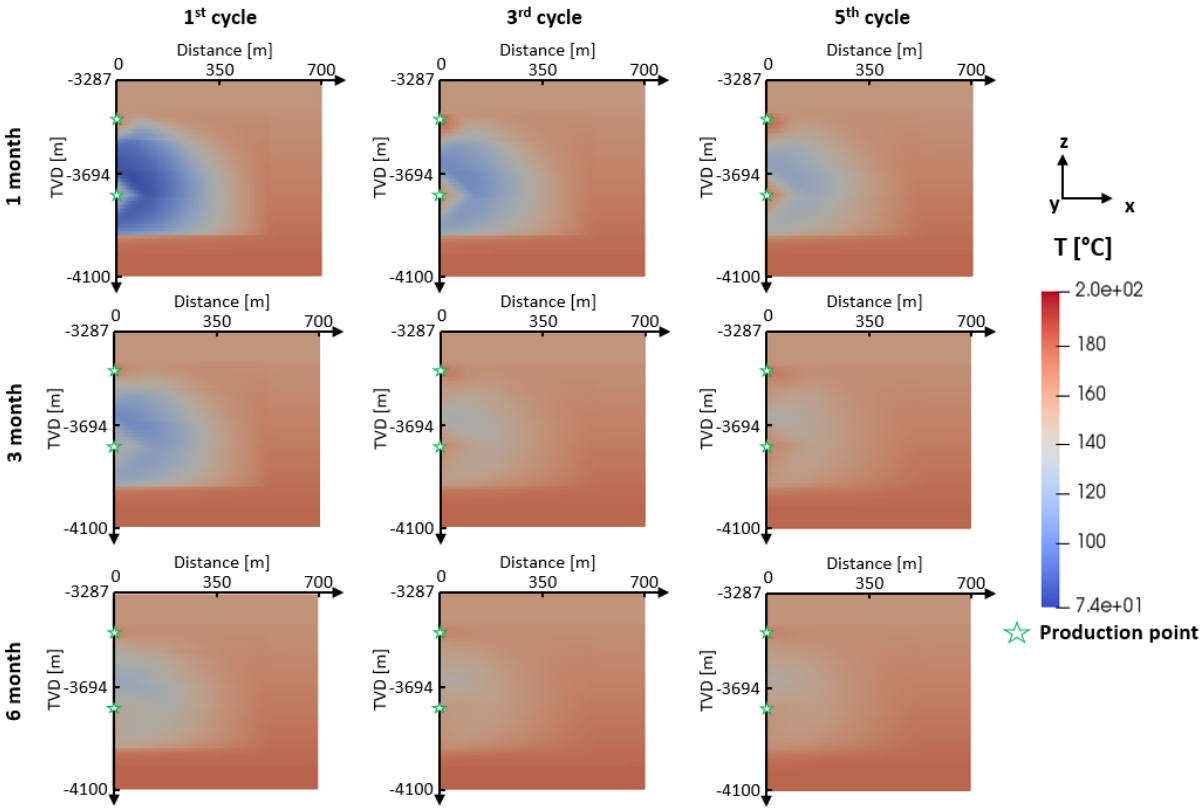

Figure 5.11 Temperature distribution after first, third and fifth cycle of energy recovery for different time duration cycles

During five continuous cycles for the 12-fracture pattern, produced net energy increases from 70 TJ to 90 TJ, 221 TJ to 260 TJ, and 462 TJ to 496 TJ for monthly, quarterly, and semi-annually cycles, respectively. In contrast, stored energy decreases gradually after every cycle, especially for the short cyclic period compared to the longer cyclic period. These results are presented in Figures 5.13 for monthly, quarterly, and semi-annual periods. It is important to highlight that one of the biggest challenges of underground energy storage is low recovery efficiency. The results of this study show that not only excess energy can be stored in a deep fractured system but also high energy recovery can be obtained, such as about 75 % in the case with monthly cycle scenario.

Figure 5.12 also shows the production temperature profile during injection and production stages for five-continuous cycles. The production temperature increases after every cycle. However, an increase in the rate of temperature decreases after every cycle. After several cycles, no significant change in temperature is observed. These results can be further elaborated using continuous cycles for five years, and it is apprehended that the reservoir is achieving temperature equilibrium (Figure 5.13).

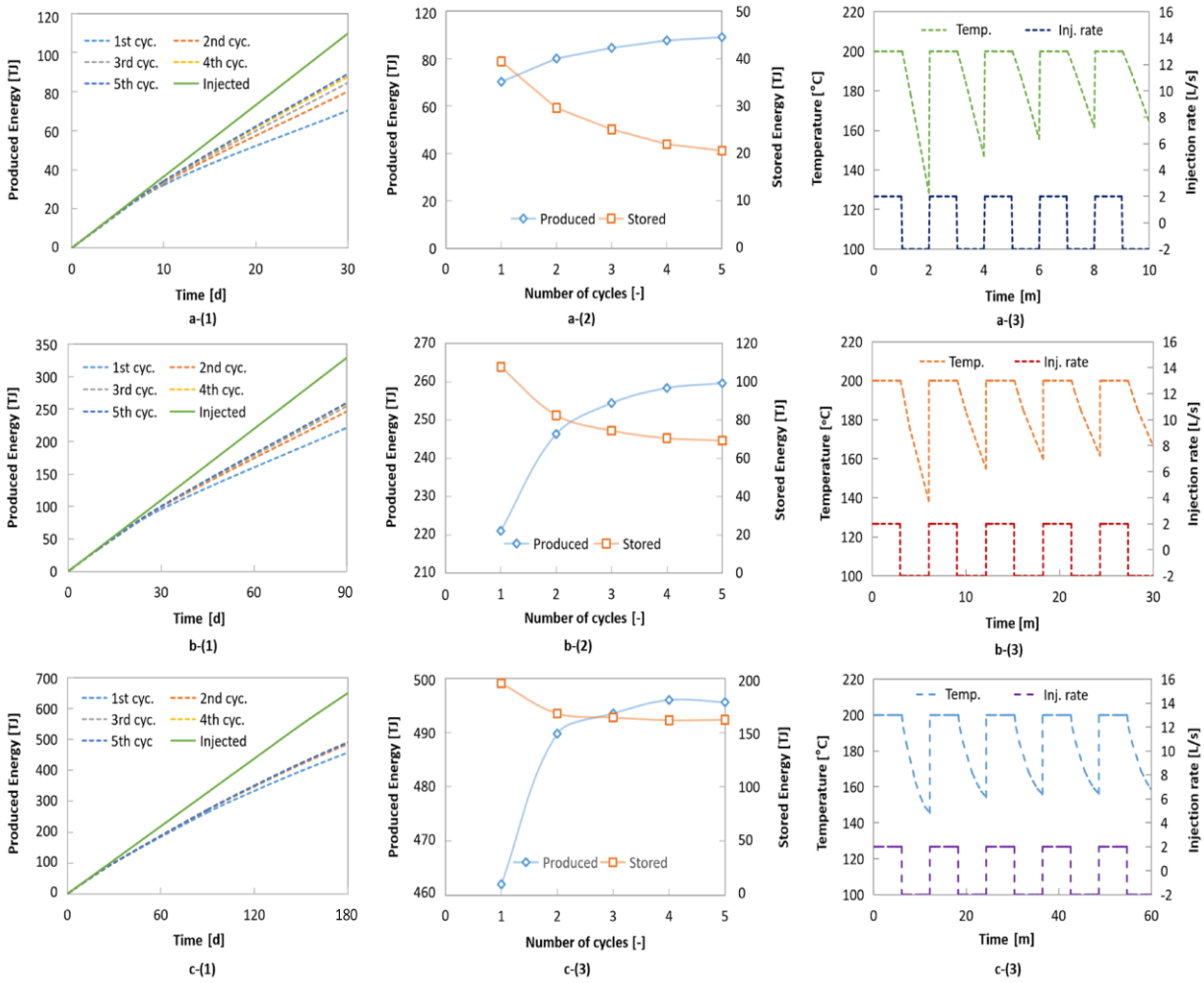

Figure 5.12 Trends of produced/stored energy and injection/production temperature during each cycle (a) monthly (b) quarterly and (c) semi-annually

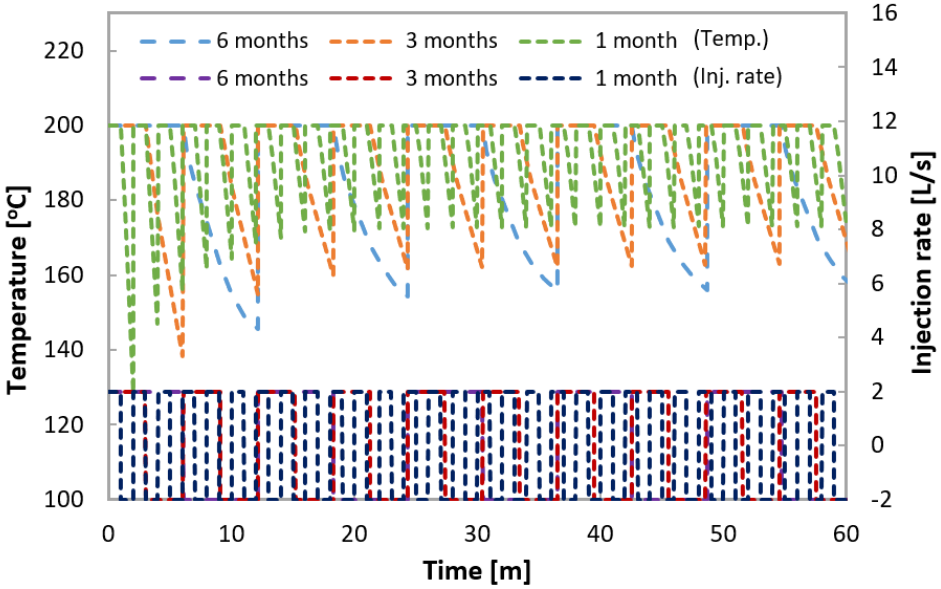

Figure 5.13 Temperature profile at injection/production points during five years for different time cycles

Furthermore, it is noticed that the number and duration of injection/production cycles are essential features that can considerably affect recovery and storage efficiency. Due to the increase in reservoir temperature, the fractured EGS is again available for geothermal energy exploitation. Therefore, by combining surplus energy storage, a regenerative EGS can be achieved in reality. In addition, this regenerative EGS concept can be applied at any time of the project's life in order to make surplus energy usable, geothermal reservoir much renewable, and clean the pipelines.

Summary

The intermittent energy supply from renewable energy sources like wind or solar often creates a disparity in direct energy demand. In this chapter, a regenerative EGS concept using surplus wind and solar energy storage is proposed. This concept can be applied in existing EGS fields as well in order to make surplus energy usable and keep a geothermal reservoir much renewable by reducing the reservoir temperature reduction rate. In addition, any salt scaling/crystallization in vertical and horizontal sections of wells could be removed using water with high injection pressure and temperature during the energy storage phase. The massive multiple fractured model that has been depleted after geothermal energy production for 30-years in chapter 4 is further investigated for the surplus renewable energy storage/recovery. Single-cycle results show that all fractures behave in a similar way during different time durations. Subsequently, continuous injection/production cycles are analyzed by adopting equal fluid volume and time. The results indicate that after every cycle, the recovery factor increases and storage efficiency decreases due to increased amount of injected energy and low fluid/thermal losses. However, less thermal recovery is achieved during longer cycles than shorter cycles. It is concluded that surplus energy can be stored in deep fractured system, and high energy recovery can be obtained by critically analyzing the continuous injection/production cycles depending upon the energy availability and demand. Consequently, the life of an EGS project with surplus renewable energy storage can be extended with a much cheaper energy production cost.

6 Conclusion

Enhanced geothermal systems (EGSs) evolved from the hot dry rock can provide a significant amount of energy and share in fulfilling the energy demands while shifting towards low to zero carbon emission. Hydraulic fracturing operations combined with horizontal drilling technology have been playing a key role in the efficient development of unconventional reservoirs and geothermal resources. The conceptual geothermal projects have been designed with single-stage fracturing focusing on shear stimulation of existing natural fractures to obtain large stimulated volume through vertical well open hole completions. However, EGSs with multiple hydraulic fractures through horizontal well have been rarely analyzed.

In this thesis, in order to investigate some targeted and important issues related to EGS, such as multiple fracturing operations, the influence of stress shadow on individual fracture geometry, the variation in fracture configuration due to difference in fracture spacing, and incorporation of individual fracture geometry for heat and electricity production along with surplus energy storage, several scenarios have been analyzed using powerful numerical tools (FLAC3D^{plus} and TOUGH2MP-TMVOC). The fundamental theories related to conventional geothermal systems and hydraulic fracturing were firstly discussed in detail. Based upon these theories, the principle of THM coupling and applied techniques for conducting the numerical simulations were further described.

Using the post-developed simulator FLAC3D^{plus}, multiple sequential hydraulic fracturing through horizontal well was carried out in a fictive model to study the influence of stress shadow on individual fracture configuration by adopting different fracture spacing cases. While conducting sequential multiple hydraulic fracturing with the same injection fluid and parameters, it was observed that the final configuration of individual fractures was different due to differences in stress shadow. In addition, with the decrease in fracture spacing, stress shadow super-position effects were raised, which ultimately changed fracture widths and fluid flow performance. Therefore, the assumption of using similar multiple fracture geometries and shapes for energy exploitation may lead to erroneous estimations. Subsequently, the fracturing results were imported to TOUGH2MP-TMVOC for energy production simulation to account for coupled THM effects in a time-efficient manner, especially in the case of multiple fracture systems. An innovative approach of one production well was also used for energy production modeling instead of two production wells to achieve additional economic benefits. Furthermore, the production well was placed at the center of fractures that provided the fluid

flow from both sides of the created fracture wings and ensured the fluid flow through each fracture. It was observed that, due to differences in individual fracture geometry, the energy contribution through multiple fractures was different. However, with the increase in fracture spacing, the same energy contribution was achieved due to a similar fracture configuration comprising less stress interference. The fluid flow analysis through variable fracture areas was performed further, which showed low energy contribution from lower fracture areas. Higher production temperature and energy contribution were observed as the fracture area increased. Therefore, it was concluded that large stimulated fracture areas are required for higher energy production. In addition, an earlier and sharp decline in production temperature was observed due to small fracture areas and less distance between the injection and production wells. It is conceivable that the distance between injection and production perforation location can set the time for a thermal breakthrough at producing end.

A case study was performed further for the MHH-GeneSys region that integrates the production of heat and electricity. The gigantic multi-fracture schemes were designed while considering stress superposition effects, and the performance for heat and electricity production was evaluated. Firstly, using the engineering data of the GeneSys project, a 3D model was generated and verified by BHP history matching with the previous fracturing job using pure water having no proppant. From the well-matched temporal evolution of BHP, the reservoir model parameters were believed to be reliable. Therefore, numerous simulations were conducted to generate massive multiple fractures with different fracture spacing. The results showed that stress shadow superposition enlarges in massive multiple fracturing, and its effect on individual fracture increases with lower fracture spacing. Furthermore, during sequential fracturing, the newly created successive fracture's configuration depended on the previous one. After the fracturing results, heat and electricity production estimations were performed using different well arrangement and flow rate scenarios while placing the production well at quarter depth from the top of the least fracture height to achieve heated fluid from each fracture. The simulation results showed that the energy-depleted fractured areas were highly dependent on the flow rate and increased with the increase in flow rate. However, these results were unsuccessful in meeting the commercial requirement. Therefore, further simulations were conducted to acquire improved production results. It was observed that under the prevailing geological conditions, the generated fractures at higher depth attained lesser fracture lengths and higher fracture heights due to the difference in stress interference. The energy production results of the optimized model depicted that the tendency of temperature decline in each fracture

area increases with the increase in flow rate and well spacing. Finally, the optimized EGS project was proposed whose installed power capacity of one side of the injection well declines from 7.17 MW to 5.08 MW for 144 L/s flow rate with 12-fracture pattern, satisfying the commercial requirement comprehensively. Moreover, the expected cost for the one side of a multi-well multi-hydraulic fracture system was estimated to be $ 65.59 million, having significant shares of drilling and operation & maintenance costs. The levelized cost of electricity was calculated at 5.46 c$/kWh, which is quite economical compared to Germany's current electricity price. In addition, the generated power potential can be doubled by creating similar fractures to the opposite side using the same injection well.

Underground thermal energy storage systems have been used broadly over the last decade and much research has been done in developing the efficient means of storing surplus energy. This is because renewable energy sources like wind or solar depend on weather conditions and often mismatch the instantaneous energy demand. An innovative concept of regenerative EGS integrating heat and electricity production as well as storage of surplus renewable energy was proposed further. This concept can be applied in existing EGS fields as well in order to make surplus energy usable, lower energy production costs, and keep a geothermal reservoir much renewable by reducing the reservoir temperature reduction rate. In addition, any salt scaling/crystallization in vertical and horizontal sections of wells could be removed using water with high injection pressure and temperature during the energy storage phase. The massive multiple fractured EGS model that had been depleted after geothermal energy production was further investigated for the surplus renewable energy storage/recovery. Continuous injection/production cycles were analyzed by adopting equal fluid volumes and time. The results showed that after every cycle, the recovery factor increased while storage efficiency decreased due to the increased amount of injected energy and low fluid/thermal losses. However, less thermal recovery was achieved during longer period cycles than shorter cycles due to excessive energy loss. It was concluded that the number and duration of injection/production cycles significantly affect energy storage and recovery and must be critically analyzed, depending on the surplus energy availability and production demand. Furthermore, the formation temperature increased with the number of injection/production cycles. Consequently, a regenerative EGS using the storage of surplus renewable energy could be achieved in reality compared to normal EGS projects.

7 References

[1] “Global Energy Review 2021,” p. 36, 2021.

[2] “Statistical Review of World Energy | Energy economics | Home,” *bp global*. https://www.bp.com/en/global/corporate/energy-economics/statistical-review-of-world-energy.html (accessed Oct. 08, 2021).

[3] “Key World Energy Statistics 2021 – Analysis,” *IEA*. https://www.iea.org/reports/key-world-energy-statistics-2021 (accessed Oct. 08, 2021).

[4] H. Ritchie and M. Roser, “Energy,” *Our World in Data*, Nov. 2020, Accessed: Oct. 08, 2021. [Online]. Available: https://ourworldindata.org/renewable-energy

[5] “An energy sector roadmap to carbon neutrality in China – Analysis,” *IEA*. https://www.iea.org/reports/an-energy-sector-roadmap-to-carbon-neutrality-in-china (accessed Oct. 08, 2021).

[6] C. Carpenter, “Study Assesses Potential of Renewable Energy in Power Sector,” *Journal of Petroleum Technology*, vol. 73, no. 07, pp. 65–66, Jul. 2021, doi: 10.2118/0721-0065-JPT.

[7] “Share of electricity production from renewables,” *Our World in Data*. https://ourworldindata.org/grapher/share-electricity-renewables (accessed Oct. 08, 2021).

[8] B. Chang and K. Starcher, “Evaluation of wind and solar energy investments in Texas,” *Renewable Energy*, vol. 132, no. C, pp. 1348–1359, 2019.

[9] P. Olasolo, M. C. Juárez, M. P. Morales, S. D´Amico, and I. A. Liarte, “Enhanced geothermal systems (EGS): A review,” *Renewable and Sustainable Energy Reviews*, vol. 56, pp. 133–144, Apr. 2016, doi: 10.1016/j.rser.2015.11.031.

[10] H. Saibi, S. Finsterle, R. Bertani, and J. Nishijima, “Geothermal Energy,” in *Handbook of Sustainable Engineering*, J. Kauffman and K.-M. Lee, Eds. Dordrecht: Springer Netherlands, 2013, pp. 1019–1042. doi: 10.1007/978-1-4020-8939-8_120.

[11] J. W. Tester *et al.*, “Impact of enhanced geothermal systems on US energy supply in the twenty-first century,” *Philos Trans A Math Phys Eng Sci*, vol. 365, no. 1853, pp. 1057–1094, Apr. 2007, doi: 10.1098/rsta.2006.1964.

[12] R. A. Crooijmans, C. J. L. Willems, H. M. Nick, and D. F. Bruhn, “The influence of facies heterogeneity on the doublet performance in low-enthalpy geothermal sedimentary reservoirs,” *Geothermics*, vol. 64, pp. 209–219, Nov. 2016, doi: 10.1016/j.geothermics.2016.06.004.

[13] P. Charlez, P. Lemonnier, C. Ruffet, M. J. Bouteca, and C. Tan, “Thermally Induced Fracturing: Analysis of a Field Case in North Sea,” presented at the European Petroleum Conference, Oct. 1996. doi: 10.2118/36916-MS.

[14] M. J. Economides and K. G. Nolte, Eds., *Reservoir Stimulation , 3rd Edition*, 3 edition. Chichester, England ; New York: Wiley, 2000.

[15] F. L. Hardin, M. D. Barry, C. E. Shuchart, R. D. Gdanski, D. W. Ritter, and D. V. Huynh, “Sandstone Acidizing Treatment of a Horizontal Openhole Completion Using Coiled Tubing From a Deepwater Floating Production Platform,” presented at the SPE Annual Technical Conference and Exhibition, Oct. 2003. doi: 10.2118/84129-MS.

[16] M. M. Sharma *et al.*, “Slick Water and Hybrid Fracs in the Bossier: Some Lessons Learnt,” presented at the SPE Annual Technical Conference and Exhibition, Sep. 2004. doi: 10.2118/89876-MS.

[17] S.-M. Lu, “A global review of enhanced geothermal system (EGS),” *Renewable and Sustainable Energy Reviews*, vol. 81, pp. 2902–2921, Jan. 2018, doi: 10.1016/j.rser.2017.06.097.

[18] G. Zimmermann and A. Reinicke, “Hydraulic stimulation of a deep sandstone reservoir to develop an Enhanced Geothermal System: Laboratory and field experiments,” *Geothermics*, vol. 39, no. 1, pp. 70–77, Mar. 2010, doi: 10.1016/j.geothermics.2009.12.003.
[19] “World Energy Resources: 2013 Survey,” *World Energy Council*. https://www.worldenergy.org/publications/entry/world-energy-resources-2013-survey (accessed May 28, 2020).
[20] H. N. Pollack, S. J. Hurter, and J. R. Johnson, “Heat flow from the earth’s interior - Analysis of the global data set,” *Reviews of Geophysics*, vol. 31, pp. 267–280, Aug. 1993, doi: 10.1029/93RG01249.
[21] “Geothermal energy,” *Wikipedia*. Oct. 08, 2021. Accessed: Oct. 15, 2021. [Online]. Available: https://en.wikipedia.org/w/index.php?title=Geothermal_energy&oldid=1048814215
[22] J. Twidell and T. Weir, “Renewable Energy Resources,” *CRC Press*. https://www.routledge.com/Renewable-Energy-Resources-3rd-Edition/Twidell-Weir/p/book/9780415584388 (accessed May 28, 2020).
[23] I. W. Johnston, G. A. Narsilio, and S. Colls, “Emerging geothermal energy technologies,” *KSCE J Civ Eng*, vol. 15, no. 4, pp. 643–653, Apr. 2011, doi: 10.1007/s12205-011-0005-7.
[24] J. Busby, “Geothermal Prospects in the United Kingdom,” p. 7.
[25] E. Barbier, “Geothermal energy technology and current status: an overview,” *Renewable and Sustainable Energy Reviews*, vol. 6, no. 1, pp. 3–65, Jan. 2002, doi: 10.1016/S1364-0321(02)00002-3.
[26] T. Agemar, J. Weber, and R. Schulz, “Deep Geothermal Energy Production in Germany,” *Energies*, vol. 7, no. 7, Art. no. 7, Jul. 2014, doi: 10.3390/en7074397.
[27] J. Weber, B. Ganz, B. Sanner, and I. Moeck, “Geothermal Energy Use, Country Update for Germany,” p. 17, 2016.
[28] J. Birner, T. Fritzer, M. Jodocy, A. Savvatis, M. Schneider, and I. Stober, “Hydraulische Eigenschaften des Malmaquifers im Süddeutschen Molassebecken und ihre Bedeutung für die geothermische Erschließung,” *Z Geol Wiss*, vol. 40, pp. 133–156, Jan. 2012.
[29] C. Dai and V. Chen, “Classification of shallow and deep geothermal energy,” *Transactions - Geothermal Resources Council*, vol. 32, pp. 270–273, Jan. 2008.
[30] “Kola.” https://www.icdp-online.org/projects/world/europe/kola-russia/ (accessed Oct. 18, 2021).
[31] “Distributed Temperature Sensing (DTS) in Geothermal Energy Applications,” *FierceElectronics*. https://www.fierceelectronics.com/components/distributed-temperature-sensing-dts-geothermal-energy-applications (accessed Oct. 18, 2021).
[32] K. Daware, “Geothermal Energy and Geothermal Power Plants.” https://www.electricaleasy.com/2015/12/geothermal-energy-and-geothermal-power-plant.html (accessed Oct. 18, 2021).
[33] G. Boyle, *Renewable Energy: Power for a Sustainable Future (3rd ed.)*. Oxford: Oxford University Press and Open University, 2012. Accessed: Oct. 18, 2021. [Online]. Available: http://ukcatalogue.oup.com/product/9780199545339.do
[34] U. Younas *et al.*, “Pakistan geothermal renewable energy potential for electric power generation: A survey,” *Renewable and Sustainable Energy Reviews*, vol. 63, pp. 398–413, Sep. 2016, doi: 10.1016/j.rser.2016.04.038.
[35] S. Han, Y. Cheng, Q. Gao, C. Yan, and J. Zhang, “Numerical study on heat extraction performance of multistage fracturing Enhanced Geothermal System,” *Renewable Energy*, vol. 149, pp. 1214–1226, Apr. 2020, doi: 10.1016/j.renene.2019.10.114.

[36] “Enhanced geothermal system,” *Wikipedia*. Sep. 26, 2021. Accessed: Oct. 18, 2021. [Online]. Available: https://en.wikipedia.org/w/index.php?title=Enhanced_geothermal_system&oldid=1046553446

[37] J. W. Tester, B. Livesay, B. J. Anderson, M. C. Moore, and et al, “The Future of Geothermal Energy – Impact of Enhanced Geothermal Systems (EGS) on the United States in the 21st Century,” *An assessment by an MIT-led interdisciplinary panel*, p. 372, 2006.

[38] K. Breede, K. Dzebisashvili, X. Liu, and G. Falcone, “A systematic review of enhanced (or engineered) geothermal systems: past, present and future,” *Geothermal Energy*, vol. 1, no. 1, p. 4, Nov. 2013, doi: 10.1186/2195-9706-1-4.

[39] D. Giardini, “Geothermal quake risks must be faced,” *Nature*, vol. 462, no. 7275, pp. 848–849, Dec. 2009, doi: 10.1038/462848a.

[40] L. Dorbath, N. Cuenot, A. Genter, and M. Frogneux, “Seismic response of the fractured and faulted granite of Soultz-sous-Forêts (France) to 5 km deep massive water injections,” *Geophysical Journal International*, vol. 177, no. 2, pp. 653–675, 2009, doi: 10.1111/j.1365-246X.2009.04030.x.

[41] S. Baisch, R. Vörös, E. Rothert, H. Stang, R. Jung, and R. Schellschmidt, “A numerical model for fluid injection induced seismicity at Soultz-sous-Forêts,” *International Journal of Rock Mechanics and Mining Sciences*, vol. 3, no. 47, pp. 405–413, 2010, doi: 10.1016/j.ijrmms.2009.10.001.

[42] “The Geysers Geothermal Field, California, United States of America.” https://www.power-technology.com/projects/the-geysers-geothermal-california/ (accessed Oct. 18, 2021).

[43] B. Bendall *et al.*, “Australian Experiences in EGS Permeability Enhancement – A Review of 3 Case Studies.,” p. 10.

[44] E. Zemach, P. Drakos, P. Spielman, and J. Akerley, “Desert Peak East Enhanced Geothermal Systems (EGS) Project,” DE--FC36-02ID14406, 1373310, Sep. 2013. doi: 10.2172/1373310.

[45] M. J. Economides, K. G. Nolte, and U. Ahmed, *Reservoir stimulation*. Englewood Cliffs, N.J.: Prentice Hall, 1989.

[46] J. Adachi, E. Siebrits, A. Peirce, and J. Desroches, “Computer simulation of hydraulic fractures,” *International Journal of Rock Mechanics and Mining Sciences*, vol. 44, no. 5, pp. 739–757, Jul. 2007, doi: 10.1016/j.ijrmms.2006.11.006.

[47] A. A. Osiptsov, “Fluid Mechanics of Hydraulic Fracturing: a Review,” *Journal of Petroleum Science and Engineering*, vol. 156, pp. 513–535, Jul. 2017, doi: 10.1016/j.petrol.2017.05.019.

[48] “Fundamentals of Rock Mechanics, 4th Edition | Wiley,” *Wiley.com*. https://www.wiley.com/en-ru/Fundamentals+of+Rock+Mechanics%2C+4th+Edition-p-9780632057597 (accessed Oct. 19, 2021).

[49] “Recent Advances In Hydraulic Fracturing.” http://store.spe.org/Recent-Advances-In-Hydraulic-Fracturing--P66.aspx (accessed Oct. 19, 2021).

[50] I. N. SNEDDON and H. A. ELLIOTT, “THE OPENING OF A GRIFFITH CRACK UNDER INTERNAL PRESSURE,” *Quarterly of Applied Mathematics*, vol. 4, no. 3, pp. 262–267, 1946.

[51] R. A. Sack, “Extension of Griffith’s theory of rupture to three dimensions,” *Proc. Phys. Soc.*, vol. 58, no. 6, pp. 729–736, Nov. 1946, doi: 10.1088/0959-5309/58/6/312.

[52] C. Liu, H. Liu, Y. Zhang, D. Deng, and H. Wu, “Optimal spacing of staged fracturing in horizontal shale-gas well,” *Journal of Petroleum Science and Engineering*, vol. 132, pp. 86–93, Aug. 2015, doi: 10.1016/j.petrol.2015.05.011.

[53] T. K. Perkins and L. R. Kern, “Widths of Hydraulic Fractures,” *Journal of Petroleum Technology*, vol. 13, no. 09, pp. 937–949, Sep. 1961, doi: 10.2118/89-PA.
[54] R. P. Nordgren, “Propagation of a Vertical Hydraulic Fracture,” *Society of Petroleum Engineers Journal*, vol. 12, no. 04, pp. 306–314, Aug. 1972, doi: 10.2118/3009-PA.
[55] “wpc-6132.pdf.” Accessed: Oct. 20, 2021. [Online]. Available: https://watermark.silverchair.com/wpc-
[56] J. Geertsma and F. De Klerk, “A Rapid Method of Predicting Width and Extent of Hydraulically Induced Fractures,” *Journal of Petroleum Technology*, vol. 21, no. 12, pp. 1571–1581, Dec. 1969, doi: 10.2118/2458-PA.
[57] G. I. Barenblatt, “The Mathematical Theory of Equilibrium Cracks in Brittle Fracture,” in *Advances in Applied Mechanics*, vol. 7, H. L. Dryden, Th. von Kármán, G. Kuerti, F. H. van den Dungen, and L. Howarth, Eds. Elsevier, 1962, pp. 55–129. doi: 10.1016/S0065-2156(08)70121-2.
[58] R. L. Fung, S. Vilayakumar, and D. E. Cormack, “Calculation of Vertical Fracture Containment in Layered Formations,” *SPE Formation Evaluation*, vol. 2, no. 04, pp. 518–522, Dec. 1987, doi: 10.2118/14707-PA.
[59] “Comprehensive Design Formulae for Hydraulic Fracturing,” p. 20.
[60] L. Zhou and M. Z. Hou, “A new numerical 3D-model for simulation of hydraulic fracturing in consideration of hydro-mechanical coupling effects,” *International Journal of Rock Mechanics and Mining Sciences*, vol. 60, pp. 370–380, Jun. 2013, doi: 10.1016/j.ijrmms.2013.01.006.
[61] W. Feng, P. Were, M. Li, Z. Hou, and L. Zhou, “Numerical study on hydraulic fracturing in tight gas formation in consideration of thermal effects and THM coupled processes,” *Journal of Petroleum Science and Engineering*, vol. 146, pp. 241–254, Oct. 2016, doi: 10.1016/j.petrol.2016.04.033.
[62] J. Rutqvist, “Status of the TOUGH-FLAC simulator and recent applications related to coupled fluid flow and crustal deformations,” *Computers & Geosciences*, vol. 37, no. 6, pp. 739–750, Jun. 2011, doi: 10.1016/j.cageo.2010.08.006.
[63] J. Rutqvist, Y.-S. Wu, C.-F. Tsang, and G. Bodvarsson, “A modeling approach for analysis of coupled multiphase fluid flow, heat transfer, and deformation in fractured porous rock,” *International Journal of Rock Mechanics and Mining Sciences*, vol. 39, no. 4, pp. 429–442, Jun. 2002, doi: 10.1016/S1365-1609(02)00022-9.
[64] Y. Gou, L. Zhou, X. Zhao, Z. Hou, and P. Were, “Numerical study on hydraulic fracturing in different types of georeservoirs with consideration of H2M-coupled leak-off effects,” *Environ Earth Sci*, vol. 73, no. 10, pp. 6019–6034, May 2015, doi: 10.1007/s12665-015-4112-5.
[65] J. Liao, Z. Hou, M. Haris, Y. Tao, Y. Xie, and Y. Yue, “Numerical evaluation of hot dry rock reservoir through stimulation and heat extraction using a three-dimensional anisotropic coupled THM model,” *Geothermics*, vol. 83, p. 101729, Jan. 2020, doi: 10.1016/j.geothermics.2019.101729.
[66] “Mtds 10 - Development Geology Reference Manual.” https://store.aapg.org/detail.aspx?id=612 (accessed Oct. 22, 2021).
[67] V. Sesetty and A. Ghassemi, “A numerical study of sequential and simultaneous hydraulic fracturing in single and multi-lateral horizontal wells,” *Journal of Petroleum Science and Engineering*, vol. 132, pp. 65–76, Aug. 2015, doi: 10.1016/j.petrol.2015.04.020.
[68] W. Yu and K. Sepehrnoori, “Optimization of Multiple Hydraulically Fractured Horizontal Wells in Unconventional Gas Reservoirs,” presented at the SPE Production and Operations Symposium, Mar. 2013. doi: 10.2118/164509-MS.
[69] “The Shale Evolution: Zipper Fracture Takes Hold,” *JPT*, Oct. 01, 2014. https://jpt.spe.org/shale-evolution-zipper-fracture-takes-hold (accessed Oct. 22, 2021).

[70] M. Rafiee, M. Y. Soliman, and E. Pirayesh, “Hydraulic Fracturing Design and Optimization: A Modification to Zipper Frac,” presented at the SPE Annual Technical Conference and Exhibition, Oct. 2012. doi: 10.2118/159786-MS.
[71] B. Guo, X. Liu, and X. Tan, “Chapter 14 - Hydraulic Fracturing,” in *Petroleum Production Engineering (Second Edition)*, B. Guo, X. Liu, and X. Tan, Eds. Boston: Gulf Professional Publishing, 2017, pp. 389–501. doi: 10.1016/B978-0-12-809374-0.00014-3.
[72] A. E. Green and I. N. Sneddon, “The distribution of stress in the neighbourhood of a flat elliptical crack in an elastic solid,” *Mathematical Proceedings of the Cambridge Philosophical Society*, vol. 46, no. 1, pp. 159–163, Jan. 1950, doi: 10.1017/S0305004100025585.
[73] M. Y. Soliman, L. East, and D. Adams, “GeoMechanics Aspects of Multiple Fracturing of Horizontal and Vertical Wells,” presented at the SPE International Thermal Operations and Heavy Oil Symposium and Western Regional Meeting, Mar. 2004. doi: 10.2118/86992-MS.
[74] J. E. Olson, “Multi-fracture propagation modeling: Applications to hydraulic fracturing in shales and tight gas sands,” presented at the The 42nd U.S. Rock Mechanics Symposium (USRMS), Jun. 2008. Accessed: Mar. 05, 2021. [Online]. Available: https://onepetro.org/ARMAUSRMS/proceedings/ARMA08/All-ARMA08/ARMA-08-327/119244
[75] N. P. Roussel and M. M. Sharma, “Optimizing Fracture Spacing and Sequencing in Horizontal-Well Fracturing,” *SPE Production & Operations*, vol. 26, no. 02, pp. 173–184, May 2011, doi: 10.2118/127986-PA.
[76] M. Haris, M. Z. Hou, W. Feng, J. Luo, M. K. Zahoor, and J. Liao, “Investigative Coupled Thermo-Hydro-Mechanical Modelling Approach for Geothermal Heat Extraction through Multistage Hydraulic Fracturing from Hot Geothermal Sedimentary Systems,” *Energies*, vol. 13, no. 13, Art. no. 13, Jan. 2020, doi: 10.3390/en13133504.
[77] N. Barton, S. Bandis, and K. Bakhtar, “Strength, deformation and conductivity coupling of rock joints,” *International Journal of Rock Mechanics and Mining Sciences & Geomechanics Abstracts*, vol. 22, no. 3, pp. 121–140, Jun. 1985, doi: 10.1016/0148-9062(85)93227-9.
[78] T. Li, S. Shiozawa, and M. W. McClure, “Thermal breakthrough calculations to optimize design of a multiple-stage Enhanced Geothermal System,” *Geothermics*, vol. 64, pp. 455–465, Nov. 2016, doi: 10.1016/j.geothermics.2016.06.015.
[79] K. F. Evans, “Permeability creation and damage due to massive fluid injections into granite at 3.5 km at Soultz: 2. Critical stress and fracture strength,” *Journal of Geophysical Research: Solid Earth*, vol. 110, no. B4, 2005, doi: 10.1029/2004JB003169.
[80] R. Parker, “The Rosemanowes HDR project 1983–1991,” *Geothermics*, vol. 28, no. 4, pp. 603–615, Aug. 1999, doi: 10.1016/S0375-6505(99)00031-0.
[81] A. Genter, K. Evans, N. Cuenot, D. Fritsch, and B. Sanjuan, “Contribution of the exploration of deep crystalline fractured reservoir of Soultz to the knowledge of enhanced geothermal systems (EGS),” *Comptes Rendus Geoscience*, vol. 342, no. 7, pp. 502–516, Jul. 2010, doi: 10.1016/j.crte.2010.01.006.
[82] K. Hayashi, J. Willis-Richards, R. J. Hopkirk, and Y. Niibori, “Numerical models of HDR geothermal reservoirs—a review of current thinking and progress,” *Geothermics*, vol. 28, no. 4, pp. 507–518, Aug. 1999, doi: 10.1016/S0375-6505(99)00026-7.
[83] M. J. O’Sullivan, K. Pruess, and M. J. Lippmann, “State of the art of geothermal reservoir simulation,” *Geothermics*, vol. 30, no. 4, pp. 395–429, Aug. 2001, doi: 10.1016/S0375-6505(01)00005-0.
[84] C.-F. Tsang, “Coupled hydromechanical-thermochemical processes in rock fractures,” *Reviews of Geophysics*, vol. 29, no. 4, pp. 537–551, 1991, doi: 10.1029/91RG01832.

[85] C. I. McDermott, A. R. L. Randriamanjatosoa, H. Tenzer, and O. Kolditz, “Simulation of heat extraction from crystalline rocks: The influence of coupled processes on differential reservoir cooling,” *Geothermics*, vol. 35, no. 3, pp. 321–344, Jun. 2006, doi: 10.1016/j.geothermics.2006.05.002.
[86] Z. Hou *et al.*, “Preliminary geological, geochemical and numerical study on the first EGS project in Turkey,” *Environ Earth Sci*, vol. 73, no. 11, pp. 6747–6767, Jun. 2015, doi: 10.1007/s12665-015-4407-6.
[87] B. Legarth, E. Huenges, and G. Zimmermann, “Hydraulic fracturing in a sedimentary geothermal reservoir: Results and implications,” *International Journal of Rock Mechanics and Mining Sciences*, vol. 42, no. 7, pp. 1028–1041, Oct. 2005, doi: 10.1016/j.ijrmms.2005.05.014.
[88] W. Cao, W. Huang, and F. Jiang, “A novel thermal–hydraulic–mechanical model for the enhanced geothermal system heat extraction,” *International Journal of Heat and Mass Transfer*, vol. 100, pp. 661–671, Sep. 2016, doi: 10.1016/j.ijheatmasstransfer.2016.04.078.
[89] S. Salimzadeh, A. Paluszny, H. M. Nick, and R. W. Zimmerman, “A three-dimensional coupled thermo-hydro-mechanical model for deformable fractured geothermal systems,” *Geothermics*, vol. 71, pp. 212–224, Jan. 2018, doi: 10.1016/j.geothermics.2017.09.012.
[90] M. Li, Y. Gou, Z. Hou, and P. Were, “Investigation of a new HDR system with horizontal wells and multiple fractures using the coupled wellbore–reservoir simulator TOUGH2MP-WELL/EOS3,” *Environ Earth Sci*, vol. 73, no. 10, pp. 6047–6058, May 2015, doi: 10.1007/s12665-015-4242-9.
[91] F. Jiang, L. Luo, and J. Chen, “A novel three-dimensional transient model for subsurface heat exchange in enhanced geothermal systems,” *International Communications in Heat and Mass Transfer*, vol. 41, pp. 57–62, Feb. 2013, doi: 10.1016/j.icheatmasstransfer.2012.11.003.
[92] C. Xu, P. A. Dowd, and Z. F. Tian, “A simplified coupled hydro-thermal model for enhanced geothermal systems,” *Applied Energy*, vol. 140, pp. 135–145, Feb. 2015, doi: 10.1016/j.apenergy.2014.11.050.
[93] Y. Zhao, Z. Feng, Z. Feng, D. Yang, and W. Liang, “THM (Thermo-hydro-mechanical) coupled mathematical model of fractured media and numerical simulation of a 3D enhanced geothermal system at 573 K and buried depth 6000–7000 M,” *Energy*, vol. 82, pp. 193–205, Mar. 2015, doi: 10.1016/j.energy.2015.01.030.
[94] Y. Zeng, J. Zhan, N. Wu, Y. Luo, and W. Cai, “Numerical investigation of electricity generation potential from fractured granite reservoir by water circulating through three horizontal wells at Yangbajing geothermal field,” *Applied Thermal Engineering*, vol. 104, pp. 1–15, Jul. 2016, doi: 10.1016/j.applthermaleng.2016.03.148.
[95] M. K. Fisher, J. R. Heinze, C. D. Harris, B. M. Davidson, C. A. Wright, and K. P. Dunn, “Optimizing Horizontal Completion Techniques in the Barnett Shale Using Microseismic Fracture Mapping,” presented at the SPE Annual Technical Conference and Exhibition, Jan. 2004. doi: 10.2118/90051-MS.
[96] D. H. Shin and M. M. Sharma, “Factors Controlling the Simultaneous Propagation of Multiple Competing Fractures in a Horizontal Well,” presented at the SPE Hydraulic Fracturing Technology Conference, Feb. 2014. doi: 10.2118/168599-MS.
[97] J. Zhao, X. Chen, Y. Li, and B. Fu, “Simulation of simultaneous propagation of multiple hydraulic fractures in horizontal wells,” *Journal of Petroleum Science and Engineering*, vol. 147, pp. 788–800, Nov. 2016, doi: 10.1016/j.petrol.2016.09.021.
[98] L. Zhou, M. Z. Hou, Y. Gou, and M. Li, “Numerical investigation of a low-efficient hydraulic fracturing operation in a tight gas reservoir in the North German Basin,” *Journal*

of Petroleum Science and Engineering, vol. 120, pp. 119–129, Aug. 2014, doi: 10.1016/j.petrol.2014.06.001.

[99] R. D. Barree and M. W. Conway, "Experimental and Numerical Modeling of Convective Proppant Transport(includes associated papers 31036 and 31068)," *Journal of Petroleum Technology*, vol. 47, no. 03, pp. 216–222, Mar. 1995, doi: 10.2118/28564-PA.

[100] E. M. E.-M. B. Shokir and A. A. Al-Quraishi, "Experimental and Numerical Investigation of Proppant Placement in Hydraulic Fractures," presented at the Latin American & Caribbean Petroleum Engineering Conference, Apr. 2007. doi: 10.2118/107927-MS.

[101] T. N. Narasimhan and P. A. Witherspoon, "An integrated finite difference method for analyzing fluid flow in porous media," *Water Resources Research*, vol. 12, no. 1, pp. 57–64, 1976, doi: 10.1029/WR012i001p00057.

[102] K. Pruess and A. Battistelli, *TMVOC, a numerical simulator for three-phase non-isothermal flows of multicomponent hydrocarbon mixtures in saturated-unsaturated heterogeneous media*. 2002.

[103] L. J. Klinkenberg, "The Permeability Of Porous Media To Liquids And Gases," presented at the Drilling and Production Practice, Jan. 1941. Accessed: Nov. 02, 2021. [Online]. Available: https://onepetro.org/APIDPP/proceedings/API41/All-API41/API-41-200/52076

[104] "(12) (PDF) TMVOC, a numerical simulator for three-phase non-isothermal flows of multicomponent hydrocarbon mixtures in saturated-unsaturated heterogeneous media," *ResearchGate*. https://www.researchgate.net/publication/255274015_TMVOC_a_numerical_simulator_for_three-phase_non-isothermal_flows_of_multicomponent_hydrocarbon_mixtures_in_saturated-unsaturated_heterogeneous_media (accessed May 28, 2020).

[105] J. B. Randolph and M. O. Saar, "Coupling carbon dioxide sequestration with geothermal energy capture in naturally permeable, porous geologic formations: Implications for CO2 sequestration," *Energy Procedia*, vol. 4, pp. 2206–2213, Jan. 2011, doi: 10.1016/j.egypro.2011.02.108.

[106] M. Franz, G. Barth, J. Zimmermann, I. Budach, K. Nowak, and M. Wolfgramm, "Geothermal resources of the North German Basin: exploration strategy, development examples and remaining opportunities in Mesozoic hydrothermal reservoirs," *Geological Society, London, Special Publications*, vol. 469, no. 1, pp. 193–222, Jan. 2018, doi: 10.1144/SP469.11.

[107] H. Feldrappe, K. Obst, and M. Wolfgramm, "Mesozoic sandstone aquifers of the North German Basin and their potential for geothermal utilization," *Z. Geol. Wiss.*, vol. 36, pp. 199–222, Jan. 2008.

[108] P. O. of the E. Union, "Atlas of geothermal resources in Europe.," Aug. 02, 2002. http://op.europa.eu/en/publication-detail/-/publication/9003d463-03ed-4b0e-87e8-61325a2d4456 (accessed Apr. 23, 2021).

[109] E. Suchi, J. Dittmann, S. Knopf, C. Müller, and R. Schulz, "Geothermie-Atlas zur Darstellung möglicher Nutzungskonkurrenzen zwischen CO_2-Einlagerung (CCS) und Tiefer Geothermie in Deutschland," *Zeitschrift der Deutschen Gesellschaft für Geowissenschaften*, pp. 439–453, Sep. 2014, doi: 10.1127/1860-1804/2014/0070.

[110] *Deep Geothermal Energy: Principles and Application Possibilities in Germany*, Second revised English edition, as At January 2017. Hannover, Germany: Leibniz Institute for Applied Geophysics, 2017.

[111] "Geothermal Installations," 2021. https://www.geotis.de/geotisapp/templates/powersumstatistic.php (accessed Apr. 23, 2021).
[112] T. Tischner *et al.*, "Massive Hydraulic Fracturing in Low Permeable Sedimentary Rock in the GeneSys Project," p. 11, 2013.
[113] E. Pechan, T. Tischner, and J. Renner, "Fracture Properties After Hydraulic Stimulation in Low-Permeability Sediments (Genesys-Project)," presented at the ISRM Regional Symposium - EUROCK 2014, Jan. 2014. Accessed: May 28, 2020. [Online]. Available: https://www.onepetro.org/conference-paper/ISRM-EUROCK-2014-232
[114] Z. Hou, T. Kracke, L. Zhou, and X. Wang, "Gebirgsmechanische Auswirkungen von Fracs im tiefen Untergrund des Norddeutschen Beckens: geologische Steinsalzbarriereintegrität und maximale Magnitude induzierter Mikrobeben anhand der GeneSys-Stimulation im Mai 2011 = Rock mechanical influences of hydraulic fracturing deep underground the North German Basin: geological integrity of the cap rock salt and maximum magnitude of induced microseismicity based on the GeneSys stimulation in May 2011," *Erdöl Erdgas Kohle*, vol. 11, pp. 454–460, Jan. 2012.
[115] Y.-J. Zhang, Z.-W. Li, L.-L. Guo, P. Gao, X.-P. Jin, and T.-F. Xu, "Electricity generation from enhanced geothermal systems by oilfield produced water circulating through reservoir stimulated by staged fracturing technology for horizontal wells: A case study in Xujiaweizi area in Daqing Oilfield, China," *Energy*, vol. 78, pp. 788–805, Dec. 2014, doi: 10.1016/j.energy.2014.10.073.
[116] S. J. Zarrouk and H. Moon, "Efficiency of geothermal power plants: A worldwide review," *Geothermics*, vol. 51, pp. 142–153, Jul. 2014, doi: 10.1016/j.geothermics.2013.11.001.
[117] R. Dipippo, "Ideal thermal efficiency for geothermal binary plants," 2007, doi: 10.1016/J.GEOTHERMICS.2007.03.002.
[118] C. Augustine, J. W. Tester, B. Anderson, S. Petty, and B. Livesay, "2006, "A comparison of geothermal with oil and gas well drilling costs," in *Proceeding, Thirty-First Workshop on Geothermal Reservoir Engineering*, 2006, pp. 1–15.
[119] T. Xu *et al.*, "Prospects of power generation from an enhanced geothermal system by water circulation through two horizontal wells: A case study in the Gonghe Basin, Qinghai Province, China," *Energy*, vol. 148, pp. 196–207, Apr. 2018, doi: 10.1016/j.energy.2018.01.135.
[120] Z. Lei *et al.*, "Electricity generation from a three-horizontal-well enhanced geothermal system in the Qiabuqia geothermal field, China: Slickwater fracturing treatments for different reservoir scenarios," *Renewable Energy*, vol. 145, pp. 65–83, Jan. 2020, doi: 10.1016/j.renene.2019.06.024.
[121] V. Stefánsson, "Investment cost for geothermal power plants," *Geothermics*, vol. 31, no. 2, pp. 263–272, Apr. 2002, doi: 10.1016/S0375-6505(01)00018-9.
[122] C. R. Chamorro, M. E. Mondéjar, R. Ramos, J. J. Segovia, M. C. Martín, and M. A. Villamañán, "World geothermal power production status: Energy, environmental and economic study of high enthalpy technologies," *Energy*, vol. 42, no. 1, pp. 10–18, Jun. 2012, doi: 10.1016/j.energy.2011.06.005.
[123] M. E. Hossain, "Drilling Costs Estimation for Hydrocarbon Wells," *Journal of Sustainable Energy Engineering*, vol. 3, no. 1, pp. 3–32, Sep. 2015, doi: 10.7569/jsee.2014.629520.
[124] M. Z. Lukawski *et al.*, "Cost analysis of oil, gas, and geothermal well drilling," *Journal of Petroleum Science and Engineering*, vol. 118, pp. 1–14, Jun. 2014, doi: 10.1016/j.petrol.2014.03.012.

[125] A. Kabuth *et al.*, “Energy storage in the geological subsurface: dimensioning, risk analysis and spatial planning: the ANGUS+ project,” *Environ Earth Sci*, vol. 76, no. 1, p. 23, Dec. 2016, doi: 10.1007/s12665-016-6319-5.

[126] B. Sanner, F. Kabus, P. Seibt, and J. Bartels, “Underground Thermal Energy Storage for the German Parliament in Berlin, System Concept and Operational Experiences,” *undefined*, 2005, Accessed: Jan. 03, 2022. [Online]. Available: https://www.semanticscholar.org/paper/Underground-Thermal-Energy-Storage-for-the-German-Sanner-Kabus/e3905ea9ec0d7b3d49ef432b1342ecd8db39065f

[127] “Dissertation: Global application, performance and risk analysis of Aquifer Thermal Energy Storage (ATES) - Fraunhofer IRB - baufachinformation.de.” https://www.baufachinformation.de/global-application-performance-and-risk-analysis-of-aquifer-thermal-energy-storage-(ates)/mobil/dissertation/2020119010247 (accessed Jan. 03, 2022).

[128] B. Drijver, M. van Aarssen, and B. de Zwart, “High-temperature aquifer thermal energy storage (HT-ATES): sustainable and multi-usable,” p. 10, 2012.

[129] B. Welsch, W. Rühaak, D. Schulte, K. Baer, S. Homuth, and I. Sass, *A Comparative Study of Medium Deep Borehole Thermal Energy Storage Systems Using Numerical Modelling*. 2015.

[130] L. Holstenkamp *et al.*, “Interdisciplinary Review of Medium-deep Aquifer Thermal Energy Storage in North Germany,” *Energy Procedia*, vol. 135, pp. 327–336, Oct. 2017, doi: 10.1016/j.egypro.2017.09.524.

[131] B. Nordell and G. Hellström, “High temperature solar heated seasonal storage system for low temperature heating of buildings,” *Solar Energy*, vol. 6, no. 69, pp. 511–523, 2000.

[132] T. Baser and J. S. McCartney, “Development of a Full-Scale Soil-Borehole Thermal Energy Storage System,” pp. 1608–1617, Mar. 2015, doi: 10.1061/9780784479087.145.

[133] N. Catolico, S. Ge, and J. S. McCartney, “Numerical Modeling of a Soil-Borehole Thermal Energy Storage System,” *Vadose Zone Journal*, vol. 15, no. 1, p. vzj2015.05.0078, Jan. 2016, doi: 10.2136/vzj2015.05.0078.

[134] “Drake Landing Solar Community.” http://www.dlsc.ca/ (accessed Jan. 03, 2022).

[135] J. E. Nielsen and P. A. Sørensen, “9 - Renewable district heating and cooling technologies with and without seasonal storage,” in *Renewable Heating and Cooling*, G. Stryi-Hipp, Ed. Woodhead Publishing, 2016, pp. 197–220. doi: 10.1016/B978-1-78242-213-6.00009-6.

[136] B. Nordell, “Borehole heat store design optimization,” 1994, Accessed: Jan. 03, 2022. [Online]. Available: http://urn.kb.se/resolve?urn=urn:nbn:se:ltu:diva-26447

[137] G. Hellstrm and K. Larson, “Seasonal thermal energy storage the HYDROCK concept,” *Bulletin of Engineering Geology and the Environment*, vol. 2, no. 60, pp. 145–156, 2001, doi: 10.1007/s100640100101.

[138] T. Klaus, C. Vollmer, K. Werner, H. Lehmann, and K. Müschen, *Energieziel 2050*. Umweltbundesamt, 2010. Accessed: Jul. 28, 2021. [Online]. Available: https://www.umweltbundesamt.de/en/publikationen/energieziel-2050

[139] B. W. e.V, “Statistics GermanyBWE e.V.,” *BWE e.V.*, 2020. https://www.wind-energie.de/english/statistics/statistics-germany/ (accessed Jul. 28, 2021).

[140] “Status_of_Offshore_Wind_Energy_Development_First_Half_of_2020.pdf.” Accessed: Jul. 28, 2021. [Online]. Available: https://www.wind-energie.de/fileadmin/redaktion/dokumente/dokumente-englisch/statistics/Status_of_Offshore_Wind_Energy_Development_First_Half_of_2020.pdf

[141] “Recent facts about photovoltaics in Germany - Fraunhofer ISE,” *Fraunhofer Institute for Solar Energy Systems ISE*.

https://www.ise.fraunhofer.de/en/publications/studies/recent-facts-about-pv-in-germany.html (accessed Jan. 04, 2022).
[142] "Germany 2020 – Analysis," *IEA*. https://www.iea.org/reports/germany-2020 (accessed Jan. 04, 2022).
[143] W. T. Sommer *et al.*, "Thermal performance and heat transport in aquifer thermal energy storage," *Hydrogeol J*, vol. 22, no. 1, pp. 263–279, Feb. 2014, doi: 10.1007/s10040-013-1066-0.